The University Of Sheffield.

Optical and Electrical Characterisation of AlGaInP Photodiodes

Aina Nur `Aalia Putri Baharuddin

A thesis submitted in partial fulfilment of the requirements for the degree of Doctor of Philosophy

The University of Sheffield
Faculty of Engineering
Department of Electronic and Electrical Engineering

Submission Date
October 2021

Acknowledgement

In the name of Allah, the most Gracious and the most Merciful.

I am beyond grateful to the One who blessed me with knowledge, health, love, time and never-ending blessings through out this journey.

This completion of thesis will never be possible without the help from my supervisor, Professor John David. I would like to thank him for all the knowledge, guidance and consistent support. Thank you for always being available for countless discussions. Thank you for being so patient for all the troubles that I have caused. Thank you for your advices and all the life lessons. Thank you for never letting me see giving up as an option. Mostly, thank you for being the most understanding and encouraging supervisor. I will always remember you saying; 'even if you have to crawl, you have to finish your PhD, Aina'.

Special thanks to Majlis Amanah Rakyat (MARA) and University of Kuala Lumpur (UniKL) for the opportunity and the scholarship. I would also like to thank my second supervisor, Prof. Jo Shien Ng for every valuable discussion on her expertise and for every little help. Thank you to Dr. Andrey Krysa for providing me the high quality AlGaInP wafer for the main work of my thesis. Thank you to Dr. Gavin William, Peter Trend, and Michael for making my days of fabrication work in the clean room feasible. Special thanks to Dr. J. S. Cheong for being very patient in assisting me since day one as a PhD student, and for all the knowledge sharing.

Thank you to other fellow members of EEE department; Hillary, Stephen, Fahmi, Dr. Liang, Dr. Xinyi, Dr. Yuchen, Dr. Simon, Dr. Pin Jern, Dr. Salman, Dr. Ben, Dr Xiao, Dr. Elizabeth, Dr. Charlotte, Dr. Leh Woon and Dr. Faezah. Thank you for every help academically and non-academically. Thank you for a fun working environment and for any random small talk that made my day. I also wish to thank my lovely friends, Fatin, Akma, Fadhilah, Wahida, Rai, Yanti, Huda, Atiqah, Zati, Ana and Syeda. Thank you for this friendship and the wonderful memories.

I am beyond grateful for my parents, Baharuddin & Fuziah. Thank you for the endless love, care and prayers along the way. Thank you for believing in me when I have given up on myself. Thank you for knowing my worth and always pushing me towards the end. You both are the reason I am pursuing my PhD, and still the reason behind every possible thing I have achieved today. I love you both.

Special gratitude to my family members; my brothers; Fitri and Ihsan, my sisters; Athira, Emee and Nasihah, my grandparents; Ishak and Fatimah, my late grandma Puteh, my aunt Rozita, my mother-in-law Siti Aishah and my in-law family. Thank you for all the love and laughs, motivation, support, and every welcomed distraction. My appreciation to my darling son, Abdul Rahman. I am sorry for the loss of time that we should have spend together. Thank you for accompanying me along this journey, and thank you for always being so lovable. Let us paint our future with beautiful memories together.

Lastly, I am especially grateful for my husband, my love, my life, my dear Amier. Thank you for always prioritising our little family first. Thank you for every sacrifices you made for us. Thank you for inspiring me to believe in my self. Thank you for all the pat on the back, the tears sharing, the late night talk, the technical support, and for many cup of coffees and wonderful food. Thank you for the countless you-can-do-it talk and for all the cheering up. Thank you so much and I love you.

Abstract

The quaternary alloy of group III-V, the $(Al_xGa_{1-x})_{0.52}In_{0.48}P$ is the widest bandgap material that can be grown lattice-matched to GaAs. Seven different aluminium compositions of x=0, 0.31, 0.47, 0.61, 0.64, 0.78 and 1.0 were grown with the same nominal i-region thicknesses of 1µm. These p-i-n photodiodes were fabricated with the standard fabrication and etching technique. The aim of this project is to characterise the optical and electrical properties of GaInP to AlInP, across the composition range for application such as top junction in multi-junction solar cell.

This work comprises of obtaining the dynamic range of absorption coefficient, α through the spectral response characterisation. The α was extracted down to the bandgap absorption region from 10^6 to as low as 10^0 cm^{-1}. The photocurrent measurement was first carried out accurately and converted to the quantum efficiency. The model of quantum efficiency derived from the current continuity equation is used to iteratively fit the experimental data. The sensitivity of the model was taken into account through the variation of the minority carrier diffusion length, the surface recombination velocity and the cladding thicknesses. Initially, the α of the direct bandgap material is rapidly blue-shifted. However, the rate of change reduces as the composition becomes indirect. From here, the bandgap is extracted through the determination of the direct and indirect bandgap between the gamma-valley and x-valley. The material started to become indirect at the aluminium content of x≥0.48, which is similar to AlGaAs.

The investigation of current-voltage (I-V) measurement across the composition range was also carried out from 300K to 600K. The heater stage system was used in the characterisation of the dark current and photocurrent. Preliminary studies of photocurrent were undertaken as a function of temperature. From the forward I-V, the activation energy through the Arrhenius plot was extracted as a function of biased voltage for GaInP and AlInP. With the ideality factor of ≈1.7, the activation energy for both ends of the composition are 1.16eV and 1.29eV respectively. The ability of the devices to function at high temperature with slight degradation and to endure multiple heating cycles, proves growth and fabrication work well for this characterisation. Subject to this temperature range, the AlGaInP is considered suitable for high temperature solar cell and space exploration applications.

Table of Content

LIST OF PUBLICATIONS i

GLOSSARY OF TERMS iii

CHAPTER 1 INTRODUCTION 1

1.1 AIM AND MOTIVATION 1

1.2 WIDE BANDGAP MATERIAL FOR VISIBLE LIGHT DETECTOR 1

1.2.1 The quaternary alloy of AlGaInP 3

1.3 TARGETED APPLICATIONS 5

1.3.1 Solar cell 5

1.3.2 Underwater Optical Communication 10

1.3.3 High Radiation Detector 12

1.3.4 High Temperature 13

1.4 PHOTODIODE PERFORMANCE 15

1.5 THESIS ORGANISATION 17

CHAPTER 2 BACKGROUND THEORY 19

2.1 SEMICONDUCTOR PROPERTIES 19

2.1.1 Band structure 19

2.1.2 Impurity Semiconductors 20

2.2 THE P-N JUNCTION 22

2.2.1 Conduction in Semiconductor 22

2.2.2 Depletion width 23

2.2.3 Ideal Diode Equation 25

2.3 FUNDAMENTAL OF ABSORPTION 27

2.3.1 Optical Transition 27

2.3.2 Absorption Coefficient 30

CHAPTER 3 DEVICE FABRICATION AND MEASUREMENT TECHNIQUES 37

3.1 LAYER DETAILS 37

3.2 DEVICE PROCESSING 42

3.2.1 Top and Back Metal Contact 42

3.2.2 Wet Chemical Selective Etching 44

3.2.3 Metal Passivation on Mesa Diode 46

3.2.4 Optimisation of Fabrication stage 49

3.3 ELECTRICAL CHARACTERISATION 50

3.3.1 *Current-Voltage (I-V) Measurement* 50
3.3.2 *Capacitance-Voltage (C-V) Measurement* 51
3.4 OPTICAL CHARACTERISATION 53
3.4.1 *Light source* 54
3.4.2 *Grating Monochromator* 55
3.4.3 *Lock-in Amplifier* 56
3.4.4 *Incident Power Estimation* 57
3.5 HIGH TEMPERATURE CHARACTERISATION 58
CHAPTER 4 CHARACTERISATION OF I-V AND C-V 60
4.1 FORWARD CURRENT-VOLTAGE CHARACTERISATION 60
4.1.1 *Dark Saturation Current* 66
4.1.2 *Ideality Factor* 71
4.1.3 *Series Resistance* 77
4.2 REVERSE CURRENT-VOLTAGE CHARACTERISATION 79
4.3 CAPACITANCE-VOLTAGE MEASUREMENT 81
4.4 SUMMARY 86
CHAPTER 5 ABSORPTION COEFFICIENT 87
5.1 ALGAINP SPECTRAL RESPONSE 88
5.1.1 *Photocurrent* 88
5.1.2 *Responsivity* 92
5.1.3 *Quantum Efficiency* 95
5.2 QUANTUM EFFICIENCY MODEL 98
5.2.1 *Parameters in Equation* 98
5.2.2 *GaInP (x=0) Model Sensitivity* 101
5.2.3 *AlInP (x=1) Model Sensitivity* 107
5.3 ABSORPTION COEFFICIENT OF ALGAINP 112
5.4 BANDGAP DETERMINATION OF ALGAINP 115
5.4.1 *GaInP Bandgap Estimation* 116
5.4.2 *AlInP Bandgap Estimation* 117
5.4.3 *Bandgap-Aluminium Relation* 118
5.5 SUMMARY 122
CHAPTER 6 TEMPERATURE DEPENDENCE OF I-V 123
6.1 FORWARD CURRENT-VOLTAGE CHARACTERISATION 123

6.1.1 Temperature Measurement Accuracy 127
6.1.2 Ideality Factor and Dark Saturation Current 130
6.2 ARRHENIUS PLOT 134
6.3 ACTIVATION ENERGY 138
6.4 REVERSE CURRENT-VOLTAGE CHARACTERISATION 141
6.4.1 Reverse Activation Energy 143
6.5 SUMMARY 146

CHAPTER 7 CONCLUSIONS AND FUTURE WORK 147

7.1 CONCLUSIONS 147
7.2 FUTURE WORK 149
7.2.1 2° and 10° Ordering of GaInP 149
7.2.2 Gallium Phosphide 150

CHAPTER 8 APPENDICES 151

8.1 XRD 151
8.2 TEMPERATURE DEPENDENCE OF PHOTOCURRENT 152
8.3 TEMPERATURE DEPENDENCE OF QUANTUM EFFICIENCY 153
8.4 TEMPERATURE DEPENDENCE OF BANDGAP 154

REFERENCES 155

List of Publications

Journal publications

1. J. S. Cheong, **A.N.A.P. Baharuddin**, J. S. Ng, A. B. Krysa, and J. P. R. David, “Absorption coefficients in AlGaInP lattice-matched to GaAs,” *Sol. Energy Mater. Sol. Cells*, vol. 164, pp. 28–31, 2017.

2. M. M. Hossain, S. Ray, J. S. Cheong, L. Qiao, **A.N.A.P. Baharuddin**, M. M. Hella, J. P. R. David, and M. M. Hayat, “Low-Noise Speed-Optimized Large Area CMOS Avalanche Photodetector for Visible Light Communication,” *J. Light. Technol.*, vol. 35, no. 11, 2017.

3. L. Qiao, S. J. Dimler, **A.N.A.P. Baharuddin**, J. E. Green, and J. P. R. David, “An excess noise measurement system for weak responsivity avalanche photodiodes,” *Meas. Sci. Technol.*, vol. 29, no. 6, 2018.

4. H.I.J. Lewis, L. Qiao, J.S. Cheong, **A.N.A.P. Baharuddin,** A. B. Krysa, B.K. Ng, J.E. Green and J.P.R. David, “Impact Ionization Coefficients in $(Al_xGa_{1-x})_{0.52}In_{0.48}P$ and $Al_xGa_{1-x}As$ Lattice-Matched to GaAs”*IEEE Trans. Electron Devices* pp. 1–6, 2021.

Paper in preparation:

A.N.A.P. Baharuddin, J.S. Cheong, X. Yi, L. Qiao, A. B. Krysa, and J.P.R. David, *“*Temperature *dependence absorption coefficient of $(Al_xGa_{1-x})_{0.52}In_{0.48}P$”*.

Conference Proceedings

1. J. S. Cheong, **A.N.A.P. Baharuddin**, J. S. L. Ong, J. S. Ng, A. B. Krysa, and J. P. R. David, "Absorption coefficients in $Al_{0.52}In_{0.48}P$," Semiconductor and Integrated Optoelectronics, Cardiff, 2015.

2. J. S. Cheong, L. Qiao, **A.N.A.P. Baharuddin**, J. S. Ng, A. B. Krysa, and J. P. R. David, "$Al_{0.52}In_{0.48}P$ photodetector for underwater communication systems," Asia Communications and Photonics Conference, Hong Kong, 2015.

3. Z. Zhou, R. D. Richards, Y. Gu, T. B. O. Rockett, F. Harun, Y. Liu, J. S. Cheong, **A.N.A.P. Baharuddin**, J. P. R. David, "Investigation of Photo-multiplication in GaAsBi Diodes," 7th International Workshop on Bismuth Containing Semiconductors, Shanghai, China, 2016.

4. **A.N.A.P. Baharuddin**, J. S. Cheong, J. S. Ng, A. B. Krysa, and J. P. R. David, "Narrow spectral response $(Al_xGa_{1-x})_{0.52}In_{0.48}P$ visible photodiodes," Semiconductor and Integrated Optoelectronics, Cardiff, 2016.

5. **A.N.A.P. Baharuddin**, J. S. Cheong, J. S. Ng, A. B. Krysa, and J. P. R. David, " High Temperature Performance of AlInP Visible Photodiodes," Semiconductor and Integrated Optoelectronics, Cardiff, 2017.

I, the author, confirm that the Thesis is my own work. I am aware of the University's Guidance on the Use of Unfair Means (www.sheffield.ac.uk/ssid/unfair-means). This work has not previously been presented for an award at this, or any other, university.

Glossary of Terms

α	:	Absorption coefficient
α_a	:	Absorption coefficient due to the photons absorption and phonon absorption
α_e	:	Absorption coefficient due to the photons absorption and phonon emission
A	:	Devices area
Abs	:	Absorbance
AlGaInP	:	$(Al_xGa_{1-x})_{0.52}In_{0.48}P$
c	:	Speed of light, 299 792 458 ms^{-1}
C-V	:	Capacitance-Voltage
C_j	:	Junction capacitance per unit area
C_T	:	Constant of the pre-exponential factor in the Arrhenius relation
D_h	:	Holes diffusion coefficient
D_e	:	Electrons diffusion coefficient
ξ	:	Electric field
ε_0	:	Vacuum permittivity
ε_r	:	Relative permittivity
E	:	Photon energy
E_a	:	Activation energy
E_f	:	Material's fermi level energy
E_g	:	Energy gap at 300K
$E_g(0)$	:	Energy gap at 0K
E_i	:	Intrinsic region's fermi level energy
E_p	:	Phonon energy
E_Γ	:	Energy gap between the lowest point of Γ valley and the highest point of valence band
E_X	:	Energy gap between the lowest point of X valley and the highest point of valence band
f_{ref}	:	Reference frequency

F : Ratio of focal length to the diameter of the mirror

G : Generation rate

h : Plank's constant, 4.1357×10^{-15} eV s

hv : Photon energy

I : Forward dark current

I-V : Current-Voltage

I_o : Saturation dark current

I_{ph} : Photocurrent

J : Current density as a function of device area

J_{Dn} : Holes' diffusion current in the n-region

J_{Dp} : Electrons' diffusion current in the p-region

J_F : Forward dark current density

J_i : Generated photocurrent from i region

J_n : Generated photocurrent due to minority holes collected from n^+ region

J_o : Saturation dark current density

$J_{0,1}$: Saturation dark current density, extrapolated using n =1

$J_{0,2}$: Saturation dark current density, extrapolated using n =2

J_p : Generated photocurrent due to minority electrons collected from p^+ region

J_{re} : Generation-recombination current

J_T : Thermal dependence current density

k : Boltzmann constant, 1.380649×10^{-23} J·K^{-1}

k_e : Extinction coefficient

k_m : Momentum

ℓ : Device thickness

ℓ_c : Critical layer thickness

LCR : Inductance-Capacitance-Resistance meter

LIA : Lock-in Amplifier

L_h : Holes diffusion length

L_e	:	Electrons diffusion length
μ_e	:	Electron mobility
m_h	:	Hole effective masses
m_e	:	Electron effective masses
M, N	:	Constant used in temperature dependence of semiconductor energy gaps; M with unit of eV/K and N with unit of K.
n	:	Ideality factor
n_i	:	intrinsic carrier density
n^+	:	electron density
n_r	:	Refractive index
n_1	:	Refractive index first material
n_2	:	Refractive index second material
N_A	:	Acceptors doping concentration
N_D	:	Donors doping concentration
Ø	:	Numbers of electron-hole pairs per incident photon
ρ	:	Resistivity
p^+	:	Holes density
P_{opt}	:	Optical power from the light source
q	:	Electronic charge, 1.602×10^{-19} C
QE	:	Quantum efficiency
QE_p	:	Quantum efficiency from p-region
QE_i	:	Quantum efficiency from i-region
QE_n	:	Quantum efficiency from n-region
r	:	Device radius
R	:	Reflectivity
R_s	:	Series resistance
R_T	:	Recombination rate
Res	:	Responsivity
S_h	:	Holes surface recombination velocity

S_e	:	Electrons surface recombination velocity
SMU	:	Source Measure Unit
τ	:	Minority carrier lifetime
t_c	:	Time constant
T	:	Ambient temperature
T_c	:	Transmission coefficient
Trm	:	Transmittance
V	:	Applied voltage
V_{bi}	:	Built-in voltage
V_{oc}	:	Open-circuit voltage
V_{p-p}	:	Peak-to-Peak voltage
V_{rms}	:	Root-mean-square voltage
w_T	:	Total depletion width
w_n	:	Depletion width into n-region
w_p	:	Depletion width into p-region
W_{OC}	:	Bandgap voltage-offset
x	:	Aluminium composition
x_T	:	Total thicknesses of p-i-n region
x_i	:	Thickness of i-region
x_n	:	Thickness of n-region
x_p	:	Thickness of p-region
λ	:	Wavelength
Z	:	Constant used in the relation of bandgap and absorption coefficient

Chapter 1 Introduction

1.1 Aim and Motivation

The absorption properties of a material can be known by characterising the absorption coefficient, which is an optical constant of material that varies with wavelength or photon energy. It indicates how far light travels in a material and how much of it is absorbed, reflected and transmitted. The in-depth understanding of absorption coefficient is important for optical modelling. From this, one can design a detector with expected efficiency for various detection applications.

This study will analyse the absorption coefficient for $(Al_xGa_{1-x})_{0.52}In_{0.48}P$ (hereafter written as AlGaInP) photodiode, through the electrical and optical characterisation of the devices. The wavelength of AlGaInP that covers the full spectrum of visible wavelength, together with the knowledge of absorption coefficient will be useful in many visible light detector applications.

1.2 Wide Bandgap Material for Visible Light Detector

The electromagnetic spectrum is a wide spread of light consisting of alternating electric and magnetic field that can be measured in energy, wavelengths or frequency. Groups of light particles move with different energy, from low energy light in radio waves to high energy light in gamma rays group. Sun is one of the electromagnetic radiation sources. But only the small portion of the sun radiation passes through the Earth’s atmosphere and the one that can be detected by human eyes is called visible light[1].

Various semiconductor has shown the ability to detect different groups of light, depending on the material bandgap energy. There are many studies with different scales for narrow bandgap (NBG) and wide bandgap (WBG) material. But refers to Owen[2] and Zaletin[3], the WBG material can be defined as a semiconductor with energy difference between conduction and valence band more than 1.4eV at room temperature.

In the early years of light detectors studies, the NBG material of Si and Ge are among the widely used semiconductors for optoelectronic technology. Si however have been universal, but Ge abilities have been challenged by other superior materials. Ge with bandgap energy of 0.67eV, initially started in the radio frequency devices and now studies has shown Ge being used as detectors for infrared[4] and gamma rays detection[5]. The InAs and InSb material with 0.35eV and 0.17eV bandgap energy respectively are also used as high speed detectors for infrared region[6]. Meanwhile for telecommunication networks, the InGaAs with 1.3eV to 1.5eV bandgap are frequently used as a receivers to detect microwaves and radio waves[7] from the transmitter.

Si with bandgap of 1.1eV is the most used semiconductor material. The material is cheap, readily available wide range of sources, very robust and can be manufactured up to 99.9999% purity[8]. Si have been used for visible sensor, remote-control application, solar cells, and many abundant range applications. It can operate comfortably to 150°C, with performance stretching up to 175°C[9]. However the generation-recombination current starts to dominates at room temperature[10] and higher, thus reducing diode performance. The absorption coefficient of Si shows a low light sensitivity of the material compared to other material. Thus, researchers agreed that Si-based material technology is fully matured and reaching its maximum performance capabilities.

There are industrial needs for WBG material to tackle the NBG material limitation. People that have interest in high temperature application are usually focusing on III-V group material, as it is suitable for heat signature application, have high resistance towards radiation exposure[11] and can cover short wavelength spectrum. The WBG material have large bonding energy and higher energy is required for defect formation. Most of WBG material are capable to work more than 300K without deterioration of the material system. WBG material can also provide high signal to noise ratio as needed to many sensitive light sensors as it can promise a low leakage current and low dark current.

Traditionally, when discussing about WBG, SiC and GaN are the prominent options[12]. Though both material system has expensive substrates to begin with, the materials can promise high efficiency, high responsivity with low power losses for various electrical systems. SiC energy gap

varied from 2.3eV to 3.3eV depending on its polytype. However, SiC material system demonstrates a high defect and dislocation, while the leakage current is increases with escalated working temperature, reported to be about at 1.8nA cm^{-2} at 22°C, and increases to 1µA cm^{-2} at 219°C at 95% of breakdown voltage[13]. GaN on the other hand, have energy gap of 3.4eV and is usually grown on lattice mismatch of Sapphire layers. It is more suitable as an emitter application rather than detector. Leakage current of GaN reported to be about 10µA cm^{-2} at 95% of breakdown voltage[14,15]. Both of these materials have cut-off wavelength at unnecessarily too short wavelength region, and do not well cover the middle range of wavelength which is not applicable for visible light detection.

The III-V group material are other alternatives for visible light detector application. AlGaAs has the advantages of varying the aluminium composition to suit various application even at high temperatures, and can maintain low leakage current. The bandgap for $Al_{0.2}Ga_{0.8}As$ is 1.67eV[16] with recorded leakage current density of 5.5nA cm^{-2}, while $Al_{0.8}Ga_{0.2}As$ with 2.09eV[17] bandgap energy is reported to have leakage current density of 2.2nA cm^{-2}. This inexpensive and widely used material system however is known to have low surface quality.

1.2.1 The quaternary alloy of AlGaInP

The combination of the two-extreme end of ternary materials, GaInP and AlInP, offers a wide range of tailored wavelength application, by forming a quaternary alloy of AlGaInP. The two ends of this composition have different formations of bandgap. The GaInP is reported to have direct bandgap, in contrast of AlInP of having indirect bandgap, while the indirect-direct crossover point exist at $x \approx 0.5$[18]. The AlGaInP offers the widest bandgap that can be grown lattice matched to GaAs.

Figure 1-1 shows AlGaInP located on the same x-axis of lattice constant of 5.65A as the GaAs material. If indium is replacing some of gallium fractions in GaAs, and phosphorus replacing the arsenic, the $Ga_{0.5}In_{0.5}P$ will be formed at the same lattice constant of GaAs. AlP and GaP have very small variation of lattice constant at about 5.45Å which means aluminium and gallium have the same atomic radii size. Thus, it allows the formation of AlGaInP with variation of zero Al to full range of Al to be growth lattice matched to GaAs.

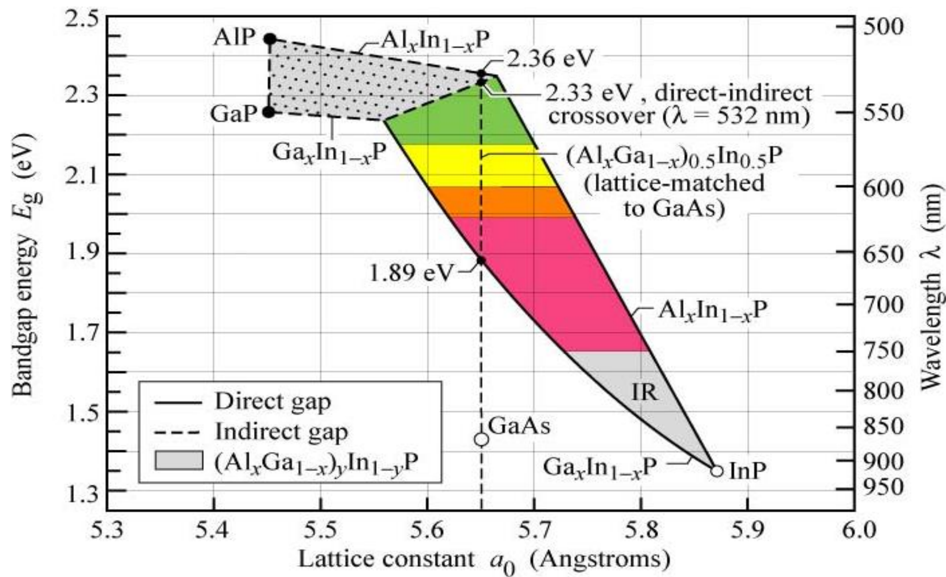

Figure 1-1 Lattice constant for various material with their respected bandgap energy (*attributed to E. Schubert, "Visible-spectrum LEDs", 2006*) [19]

The AlGaInP is a simple and inexpensive material system, which has a narrow FWHM spectrum. This then leads to promising filterless detector, and have shown to work well under high temperature and can maintain low dark current up to breakdown voltage. The formation of AlGaInP from group III-V material have been introduced around 1990s for visible spectrum of light-emitting and light detection application[20].

The advantages of varying the aluminium composition give the opportunity of this material to be used in many applications where bandgap tunability is required. Based on variety of aluminium composition in this alloy, the AlGaInP can be tailored for a specific range of wavelength wanted, and gives an excellent visible spectrum coverage. The other optical constant of AlGaInP have been discovered by various methods for different alloy fractions[21,22]. However, minimal works have been shown on extracting accurate data for AlGaInP absorption coefficient across a visible spectrum, especially near the cut-off wavelength and weak detection region.

1.3 Targeted Applications

1.3.1 Solar cell

Since the 1990s where coal and burning fossil fuels have been extensively used, the increase in carbon emission has caused many destructive problems across the globe. The increase in this greenhouse gas emission contributed to temperature imbalance that eventually lead to rapid climate change, consequently causing global warming. However, recent studies show the reliability towards fossil fuels has started to decrease, as more efficient technology arise.

From 1990 to 2020, UK reported to have carbon emission reduction by 46%[23]. This impressive feat is achieved through the transformation in electric generation by coal to oil and natural gas, and eventually to the recent increase in usage of renewable energy. Following the government action to ban the coal-electricity generation starting in 2024 as part of their green recovery plan, massive expansion on renewable resources especially at home has taken place. By 2020, UK reported to have 43% of their power generated by renewable energy, where 28% is contributed by solar energy[24]. Increase interests toward solar energy help in further research in improvising current solar technology.

The three generations of solar cell evolved from Si photovoltaics to thin film solar cell, and subsequently the most efficient multi junction solar cell. The first solar cell studies were carried out by Bequerel in 1839 where he observed a current generation from platinum electrodes separated by a thin membrane. The history of photovoltaics were expanded in 1870s by Smith[25], Adam[26], and Fritts [27] on the Selenium solar cell. Si starts to dominate the single junction solar cell technology due to its benefit of cost and availability of raw material, and followed by the wide bandgap semiconductor solar cell which is a popular option for elevated temperature environment[28].

The second generation of thin film solar cell became an interesting alternative due to its low cost and flexibility in size and weight[29]. Recent achievements by crystalline Si and thin film GaAs single junction solar cell recorded 26.7% and 29.1% efficiency respectively, when measured under global AM1.5 for terrestrial application[30].

The third generation of multi junction solar cell works with different single junction solar cell growth from wide to narrow bandgap stack from top to bottom. Theoretically, a solar spectrum is divided into several ranges of wavelength which will be absorbed by corresponding material, and the lower photon energy is captured by the next adjacent layer. The III-V semiconductor group material offers a promising solar cell option compared to single junction Si solar cell, as it can cover the whole solar spectrum range as shown in Figure 1-2[31].

However, there are major concerns following the increasing number of junctions which are to minimise the lattice-mismatch of different material and maintaining current matching. Since the multi junction cell are connected in series, the generated output current is constrained by the lowest current through the cells. Thus, it is important to ensure each stackable cell can generate current matching to reach the optimum device efficiency.

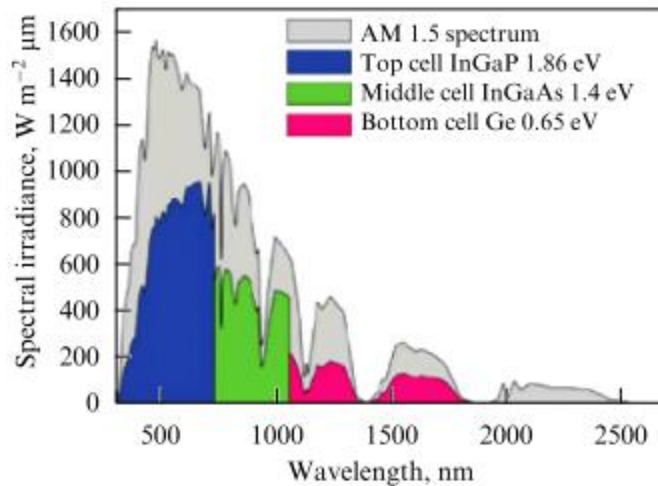

Figure 1-2 The spectrum of triple-junction solar cell
(*attributed to V. Milichko, "Solar photovoltaics: current state and trends", 2007*) [32]

The Fraunhofer Institute for Solar Energy Systems have shown studies on GaInP-GaInAs-Ge triple-junction solar cell, with engineered metamorphic Ge substrates. The double layer anti-reflection coating is applied on the structure and manage to increase the efficiency to 35.2% under AM1.5D 443sun[33]. The same structure of 3-junction solar cell by National Renewable Energy Laboratory (NREL) reported 37.3% efficiency measured under AM1.5D 175sun[34].

The Optoelectronics Research Centre have shown the lattice-matched 4-junction solar cell grown monolithically from narrow to wide bandgap, to make the stackable junctions of GaInP-GaAs-GaInNAsSb-GaInNAsSb solar cell[35]. These solar cell covered the spectrum from 0.93eV to 1.88eV with 39% efficiency under illumination of 560sun. They then improvised the structure by introduce 60% of aluminium on the widest bandgap material and also increase the nitrite content by 8% for the narrowest bandgap material which consequently expanded the spectrum coverage from 0.7eV to 2.2eV[36].

The same study suggests that instead of GaInP, the increase in aluminium concentration by 10% and 26% provide optimal current match between the top and lower cells. This is applicable for 5 and 6 junctions solar cell respectively, with advantages of larger voltage output. The better spectrum coverage on shorter wavelength region can also be observed when using higher aluminium composition. For example, at 400nm, the 70% IQE can be increased to 85% when using $(Al_{0.3}Ga_{0.7})_{0.52}In_{0.48}P$ instead of GaInP.

Study by X. Zhang et al demonstrated higher efficiency can be achieved by implementing the heterojunction instead of the homojunction of AlGaInP for the first window of 4-junction solar cell. The heterojunction of n-type emitter of $Al_{0.13}Ga_{0.37}In_{0.5}P$ with p-type base of $Al_{0.19}Ga_{0.31}In_{0.5}P$ enhanced the coverage of the short wavelength light. The rest of the junctions were grown on Ge substrate beginning with 2.13eV of AlGaInP followed by AlGaInAs-GaInAs-Ge. The adopted heterojunction from homojunction structure recorded an increase from 12.5% to 14% efficiency, and cumulatively the 4-junction structures obtained 30.45% efficiency under AMO[37].

The other study by X. Huang et al have implemented the polyimide film solar cell with 1.9eV AlGaInP as a first layer, followed by 3 layers of AlGaAs-$In_{0.17}Ga_{0.83}As$-$In_{0.47}Ga_{0.53}As$. This inverted metamorphic multijunction flexible 4-junction solar cell is grown for space exploration. The solar cell is fabricated with 50µm thickness without anti reflection coating, with mass density of 467g/m^2. This produced 25.76% efficiency under AM1.5G illumination[38].

The 5-junction solar cell by SpectroLab have shown a reliable technology of semiconductor bonding, to increase the interface transmission and reducing resistance across materials without being mechanically destructed. Initially, the first three junctions of 2.2-1.7-1.4eV were grown inversely by MOVPE on lattice match of GaAs. Subsequently, the 0.73eV material were grown on InP, followed by 1.05eV. The separate wafer's structure of GaAs and InP with pre-polished surface roughness to <0.5nm then are directly bonded to make a multijunction solar cell, ranging from 2.2eV to 0.73eV. The system demonstrated 35.1% and 37.8% efficiency measured under AM0 and AM1.5 respectively[39].

Recently, NREL have shown the latest 6-junction solar cells which promotes an achievement of 47.1% efficiency under direct spectrum of 143 solar concentrator[40]. Meanwhile, 39% efficiency is recorded under 1 sun global spectrum from the same structure. The 6-junction structure shown in Figure 1-3(a) optimises the III-V semiconductor materials with AlGaInP as the top window, followed by AlGaAs, GaAs and the other 3 layers of different composition of InGaAs.

The AlGaInP structure used has 18% of aluminium composition, with 2.1eV bandgap and 1.2µm absorber region thickness. The external quantum efficiency (EQE) under 1 sun from each material is in average of over 80%, where the peak of AlGaInP reaches about ~90%. The forward current density measured under 1 sun on AlGaInP layer recorded to be 8.5mA cm^{-2} and 8.7mA cm^{-2} for AM1.5D and AM1.5G respectively. Meanwhile, under higher concentration performance at 500sun and 1000sun, the current density at 0V is 4.23Acm^{-2} and 8.47Acm^{-2} respectively.

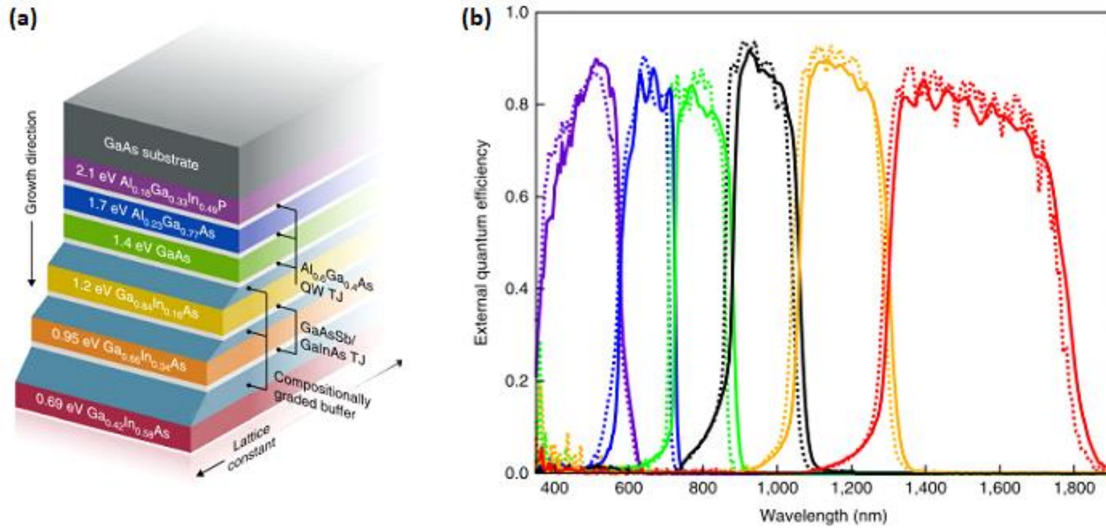

Figure 1-3 (a) Six junction solar cell structures and (b) their respective external quantum efficiency measured under 1 sun condition, for AM1.5D (solid lines) and AM1.5G (dashed lines). (*attributed to J. Geisz, "Six-junction III–V solar cells with 47.1% conversion efficiency under 143 Suns concentration", 2020*)[40]

Another study by Bernades S. shows a smart improvement on the top junction of solar cell, by creating the subcell of GaInP that is sandwiched in between n-type AlInP and p-type AlGaInP[41]. The AlInP layer acts as a front surface window, optimising the photon capture with its wider bandgap advantages. Meanwhile, the formation of AlGaInP as the back surface window reduces the loss of minority carrier due to reflection. The sharing of the applied voltage across this AlInP-GaInP-AlGaInP structure manages to reduce the dark current and consequently improve the short-circuit current output.

1.3.2 Underwater Optical Communication

The optical communication systems need narrow full-width half-maximum (FWHM) spectrum sizes to ensure less crossover of noise during data transmission. Studies demonstrate that the system is able to transmit more than 1 Gb/s at a very short distance (100m) and consumes less power, thus reducing the cost of the transmitter-receiver system[42,43]. However, the solar radiance is one of the primary noise sources which cause interference towards the efficiency of a communication system.

In designing a low-noise underwater communication system, a detector can be made to specifically respond in Fraunhofer[44] dark lines and in less turbidity region. Fraunhofer in his studies discovered lots of black lines appears in solar spectrum due to the absence of light as shown in Figure 1-4[45].

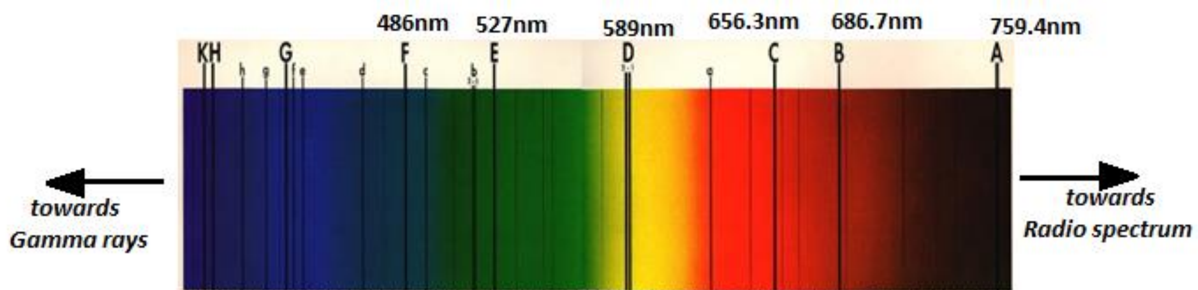

Figure 1-4 Dark absorption lines existed in visible solar spectrum wavelength (*attributed to A. Larson, "Learning Astronomy by Doing Astronomy," 2019*) [45]

Meanwhile, Jerlov[46] has studied the classification of water effects on signal transmittance for underwater nature. As shown in Figure 1-5, as the turbidity level in seawater increases from Type I to 9, the transmittance of light at respected wavelengths decreases. It illustrates that Type 1 of seawater allowed the maximum transmittance of 400-500nm light. The peak transmittance is shifted towards the longer wavelength with an increase in turbidity level. Moreover, Morel and Prier classified the seawater into two different groups with respect to the turbidity level and its pigment content[47]. Group 1 consists of high chlorophyll concentration whereas Group 2 consists of high inorganic particles. For Group 1, the maximum chlorophyll absorption is recorded at 440nm and the second maximum is at 665nm. However, the reflectance of light for Group 2 is higher due to low purity levels, and dominant at wavelength longer than 550nm[48].

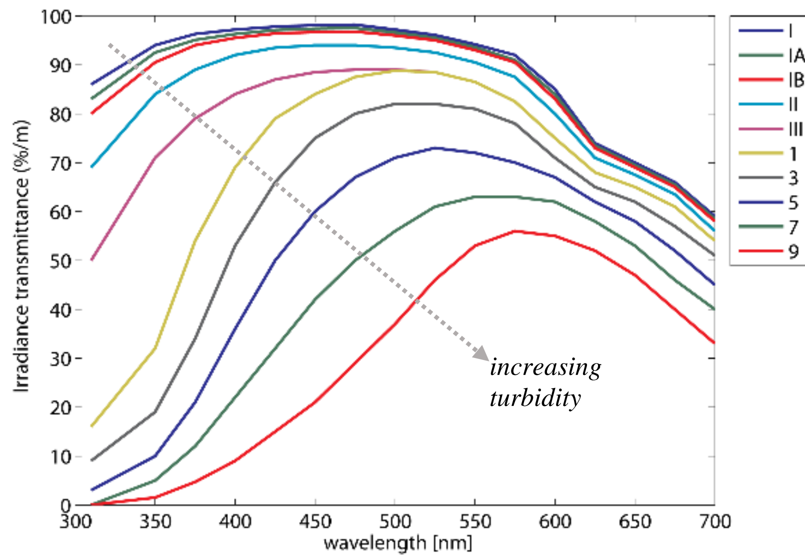

Figure 1-5 Transmittance of visible light under different types of seawater
(*attributed to N Jerlov, "Marine Optics", 1976*)[46]

Based on the above consideration, a receiver for underwater communication system is practically best to work within the dark lines existed in visible range of wavelength, provided the detector has a narrow FWHM spectrum. The ability of AlGaInP material system to detect wide range of visible light will be beneficial in building the underwater detector. Together with the accurate knowledge of material optical absorption coefficient, the detector can be designed to operate at specific dark-lines, and the desirable FWHM can be tailored.

1.3.3 High Radiation Detector

X-ray detector

The abilities of wideband gap material to tolerate high radiation emission have been considered in detection of X-rays. X-rays can be classified in two groups, either soft X-ray or hard X-ray with more than 5keV photon energy. Many recent researches have intensified ionising radiation detectors based on wide bandgap detectors such as in SiC and AlGaAs. Si has pioneered the X-ray detector field, however the limitation of the material system has been resolved by SiC with three times wider bandgap and better breakdown voltage up to eight times higher[2]. The advantage of low thermally generated leakage current and minimum dark current helps in measuring the total charge created by absorbed photons as reported by Bertuccio[49] for SiC detector. Barnett[50] and Whitaker[16] have characterised GaAs and AlGaAs photodiodes that operate with uncooled function at temperature higher than 20°C and manage to measure the peak output from the absorbed photon energy. There is recent work shown using GaInP and AlInP avalanche photodiodes in detection of low X-ray phonons with charge sensitive preamplifier, demonstrated by Auckloo[51].

Scintillation coupled detector

The visible-light detector coupled with Bismuth Germanate (BGO) scintillation material can be used to detect gamma rays that are emitted from the scintillator. This crystal structure material have high absorption efficiency towards gamma ray radiation, and converts the high energy particles to visible light spectrum ranging from 375nm to 645nm with peak intensity at 480nm as in Figure 1-6[52]. Other than BGO, other scintillators such as NaI[53], TlCl[53] and CsI[54] are also emitting visible light after irradiated by high energy rays with peak intensity spectrum at 420nm, 465nm and 540nm. There are extensive studies on using BGO in the medical field, nuclear detector radiation and space exploration. Therefore, a detector can be designed to detect the scintillator output spectrum which is beneficial in confirmation of the presence of gamma-rays.

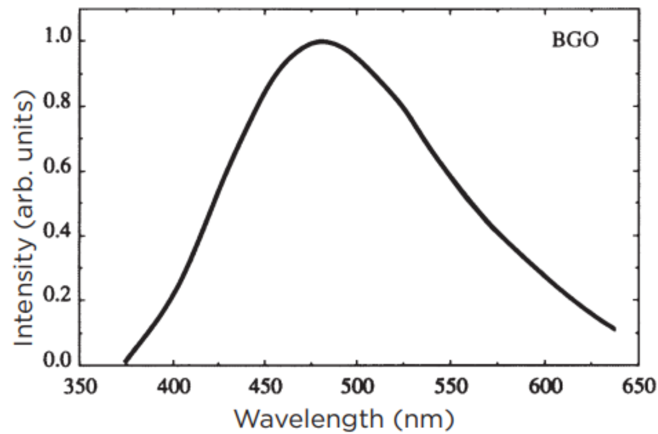

Figure 1-6 BGO scintillation emission spectrum when irradiated with Gamma-ray (*attributed to Saint Gobain, "Bismuth Germanate Scintillation Material", 2004*)[52]

1.3.4 High Temperature

High temperature can be classified based on the targeted application. Up to 70˚C is usually needed for daily electrical equipment, while up to 85˚C is commonly needed by automotive industries. Solar cell applications work up to 120˚C, while military and space exploration commonly need more than 200˚C[55,56].

Long wavelength detection is in high demand for space exploration, from visible to long-wavelength Infrared (up to 15µm)[57]. The fundamental is to detect the reflected or emitted light by planets, the earth, or stars for their atmospheric analysis. The devices should be able to withstand harsh space environment with fluctuating temperatures, minimal in size and weight, and able to maintain a long lifetime without deteriorating the system.

The wide bandgap materials are suitable for a large range of working temperature due to the ability to reduce efficiency loss with increasing temperature[58]. Waltereit in his study designed a high performance of AlGaN/GaN integrated circuit with the ability to withstand 200°C temperature with 10^5 hours of lifetime[59]. Banu in his work shows SiC diode as a protection device for a satellite to orbit Mercury at a temperature of 280°C[60]. Diamond has become a new generation of detectors for harsh environment as it has superior properties towards radiation hardness and able to operate up to 250°C[61].

For high intensity high temperature (HIHT) applications, analyses are carried out up to 500K. A recent spacecraft mission to Mercury, the Bepi Columbo, carried the main mission of orbiting the planet for over two Earth years[62]. The system consists of solar arrays, aimed to analyse the topography, the atmosphere and the interior of the planet. Therefore, the solar arrays will be exposed extensively to high infrared radiation from Mercury. At the same time, the solar arrays have to operate close to its maximum temperature limit due to direct heat flux from the sun. The capabilities of the solar arrays in the Bepi Columbo have become the pioneer and model for extensive studies on solar cell behaviour towards HIHT[63].

Following the NASA mission in developing the photovoltaic power for high temperature environment, the main objectives were improving the material efficiency and their lifetime[64]. These goals require further development on wide bandgap semiconductors such as GaP, GaInP, GaN and SiC. Advanced technology for SiC[65], GaN[66] and Diamond[56] have been proven to sustain high temperature working environment. However, researchers are attempting to find other alternatives in terms of simpler material structures. As shown by the 5 junctions solar cell by Spectrolab, the cells have excellently performed under AM0 solar irradiance with efficiency of 35%[39]. The cells utilise the advantages of wide bandgap AlGaInP as the top junction, which is lattice matched to GaAs. This high quality substrate is reported to achieve the V_{oc} of 4.78V and J_{sc} of 12mA/cm^2.

1.4 Photodiode Performance

There is no definitive standard in judging the performance of a photodiode as each photodiode are designed for different operating conditions. However, in setting the standard performance metrics of a photodiode, one has to start with the ability of the detector in absorbing the photons and to produce an electrical output[67]. Photodiode, which acts as a sensor or receiver for any transmitter system can be characterised and compared based on the following parameters.

Wavelength coverage

Photodiode, as a detector should have a strong coverage of a spectrum of interest, to ensure most light with photon energy greater than the bandgap is absorbed by the device. A cut-off wavelength needs to be considered in optimising device performance, as too short nor too long cut-off wavelength will be unnecessary.

High efficiency

Highly efficiency photodiode is preferable as it can absorb more photons and therefore, convert them to greater electrical output. The ideal photodiode has a unity efficiency, but it is common for photodiodes to departs from 100% efficiency due to many losses occurred during the absorption process. The efficiency of a device is another way of determine the device sensitivity towards light.

Low dark current

Photodiode in theory, should not have a current flowing through it in the absence of light. However, the dark current which is a background noise that usually exists in a small value is activated by thermal energy even at room temperature. The non-radiative current can be minimised by reducing temperature. The ability of a good device to maintain low dark current until near breakdown voltage is needed to ensure most photons still can be absorbed by the material even at low intensity. Low dark current characteristic and high device efficiency will help in reducing the noise of the system, thus improving signal to noise ratio.

Physical properties

A robust photodiode that can withstand harsh environment are in demand for various applications. These devices should be able to work under extreme temperature, vibration and vigorous activity while maintaining the devices' performance. External cooling aid are usually used to ensure the absence of overheating problems during operation. The impedance and resistance between packaging and measurement setup have to be kept as low as possible to maximise the device performance. Furthermore, other devices might need anti reflection coating on their window, or bigger absorption area to reach the expected output.

Repeatable results

Photodiode characterisation should provide repeatable and consistent results to avoid misinterpretation of data and ensuring the results are free from uncertainties. The ability of a device to replicate uniform characterisation results after repeated tests is the key to a convincing result.

1.5 Thesis Organisation

Chapter 1 presents the motivation behind the studies of absorption coefficient of AlGaInP photodiode. The chapter includes the background about wide and narrow bandgap material, and the suitable wide bandgap material application that can be beneficial from the knowledge of this optical property. The comparisons with industrial-ready material are discussed, and suggestion for better diode performance are included.

Chapter 2 starts with the introduction to semiconductor bandgap energy, the direct and indirect semiconductor. The formation of p-i-n photodiode together with the physics behind the electric field created in the junction is discussed. The ideal diode equation, the equation behind the dark current measurement are introduced here. Lastly, for better understanding of the result analysis in the later chapter, the absorption details process is covered and compared with several known materials.

Chapter 3 briefly describes about the layer details, where all seven layers have nominal thickness of 1µm i-region growth by MOVPE technique. The XRD results of each layer are also included, used for determining the aluminium composition percentage. The fabrication process in making top and back metal contact for the p-i-n devices is discussed, with specific steps from cleaning the wafers to evaporating the thin metal layer. This is then followed by the passivation of device edge using negative and positive photoresist. All device processing stages that end with selective etching are illustrated for better figuration of steps involved.

There are various measurement techniques involved in this study to contribute in extracting the absorption coefficient of AlGaInP. They include current-voltage (I-V), capacitance-voltage (C-V), photocurrent and high temperature measurement. The critical steps and specific assumption made throughout the measurement are discussed here.

Chapter 4 reports the I-V and capacitance-voltage C-V on AlGaInP, under dark environment at room temperature. Results of measurement under forward and reverse bias of different sizes area are shown to observe on how it scales with area. From I-V measurement, the analysis on ideality factor, series resistance and dark current density with respect to aluminium composition

are also included. The C-V characterisation were done to extract information about the background doping and depletion width as a function of voltage. Results are then compared with nominal layer structure growth by MOCVD.

Chapter 5 demonstrates the optical characterisation of AlGaInP photodiode at room temperature. From the photocurrent measurement using a monochromator, the quantum efficiency can be calculated with a known value of the power input of each photon. Then, by using current-continuity equation, the quantum efficiency results are modelled and the value of the absorption coefficient can be extracted. For sanity check, the reverse calculated quantum efficiency using the extracted absorption coefficient are compared to experimental results. The details in calculation and assumption made for the model are elaborated in details here. The work also presents comparisons of previously published material absorption properties, and the characteristics that correlate back to the semiconductor geometry. The bandgap energy of each composition is then determined by existing theory discussed in chapter 2. Subsequently, the bandgap relation with aluminium composition is shown, where the crossover point between direct and indirect bandgap energy is discovered.

Chapter 6 analyses the temperature dependence of I-V characteristics for AlGaInP under forward and reverse bias. The Arrhenius plots which consist of current versus inverse in temperature are plotted for every voltage increment. The fitting through the Arrhenius plot gives the value of activation energy.

Chapter 7 summarises the contribution of the research and discuss the possible future works for research advancing in visible light detection. We discuss about the other alternatives of wide bandgap material for visible light detection. The characterisation of 2µm i-region GaP devices show blue-green spectrum detection, and make a good set of detectors from 350nm to 700nm when plotted on the same axis with AlGaInP. The quantum efficiency of 2° and 10° offset ordering of GaInP are also shown to understand the effect of ordering towards spectrum coverage. Results show the peak shifting towards short wavelength for 2° sample.

Chapter 2 Background Theory

2.1 Semiconductor Properties

2.1.1 Band structure

Bandgap energy can be used to classify groups of material into metal, semiconductor and insulator. Each material has energy gap, E_g defined as the minimum energy needed to excite an electron from the highest state in valence band to the nearest empty state in conduction band. The conduction band is the higher energy level that is occupied with electrons, while the valence band is an empty state full of holes indicating the absence of electrons. It should be noted that no charge carriers are allowed to be within the gap, thus it also known as the forbidden gap. The bandgap energy with respect to temperature in Kelvin can be expressed as Equation 2.1 where $E_g(0)$ is energy gap at 0K, while A with unit of eV/K and B with unit of K is constant[68].

$$E_g(T) \approx E_g(0) - \frac{MT^2}{T + N}$$ **Equation 2.1**

Figure 2-1 illustrates the difference of band structure for each material, emphasising the difference in size of band gap and fermi level position at 0K. Fermi level represents the highest position of available electron state, with the levels above it are full of holes. The bandgap in metal is considered non-existent as the conduction and valence bands are overlapping. This allows the conduction of current in metal, as the electron can move freely between the band, excited from any level and fall back to any empty level. Numerically, insulators' band gap energy starts from 6eV or higher[69], while narrow than that are considered as semiconductor material. The insulators are considered to be electrically poor conductive material, as the band gap is very wide and leads to inability of free carriers to excite into the conduction band. Even thermal energy at room temperature is not enough to excite the electron to the first empty level in conduction band. At 0K, the semiconductor will behave just like insulators. Nevertheless, at certain temperature, the electrons are able to excite into the conduction band due to the narrow size of the band gap.

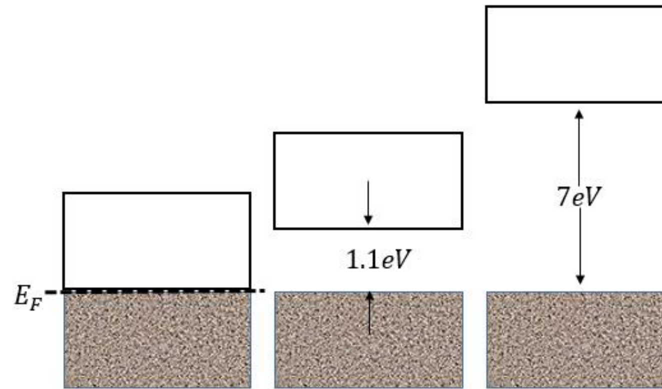

Figure 2-1 Band structure representation of metal, semiconductor and insulator

2.1.2 Impurity Semiconductors

A semiconductor material of intrinsic, p and n type region are determined by the absence and presence of dopants. Intrinsic semiconductor is a pure semiconductor with a small, neglected amount of impurities. To have an excess of carriers in either valence or conduction band, an equal number of holes and electron from intrinsic materials have to be perturbed. Dopants are usually used to create free carrier charges. The p-type semiconductor is a pure semiconductor which has been doped by positive-charged holes created in valence band called acceptors. While the n-type semiconductor is doped with negative-charged electrons called donors which sits on the conduction band lattice[70].

For example, in making a n-type Germanium semiconductor from group I and group V, dopant such as Phosphorus from group V can be introduced to modify the covalent bond of Germanium. With only four electrons needed for covalent bonding, the fifth electron becomes weakly bounded to the nucleus, thus creating free electron. Now, the number of electrons in a semiconductor is increasing and outnumbers the number of holes, creating the n-type semiconductor. The electron can then be called as the majority carriers, while the holes are the minority carriers. The same process can be used to create a p-type semiconductor. The impurities from group III such as Gallium can form incomplete covalent bonding to the Germanium. This leads to one free hole available in the semiconductor, with the same electron numbers as before, creating a p-type semiconductor.

In intrinsic semiconductor, the fermi level lies in the middle of the band gap, while the fermi level of p and n type of semiconductors lies near to the heavily doped region. With increase in carrier concentration, the fermi level shifts upward towards the conduction band for n-type semiconductor, and shifts downward near to the valence band for p-type semiconductor. The difference in energy band is illustrated in the Figure 2-2.

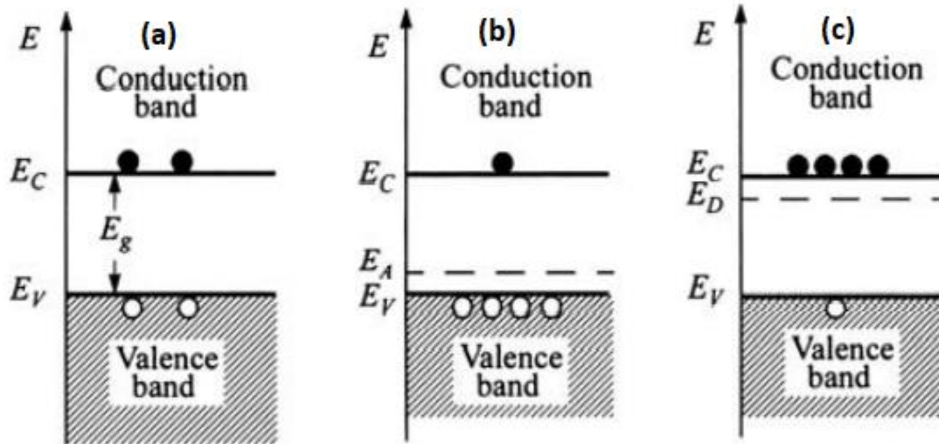

Figure 2-2 Energy band diagram for (a) Intrinsic, (b) p-type and (c) n-type semiconductors (*attributed to S. M. Sze, "Semiconductor Devices: Physics and Technology", 2006*)[68]

The intrinsic carrier density, n_i is given by $np = n_i^2$ where the proportion of electrons density, n is said to be equal to holes density, p. The carrier concentrations of n and p are expressed as;

$$n = n_i \exp\left(\frac{E_f - E_i}{kT}\right)$$ **Equation 2.2**

$$p = n_i \exp\left(\frac{E_i - E_f}{kT}\right)$$ **Equation 2.3**

where E_f is the material's Fermi level energy. It should be noted that in intrinsic or doped semiconductor, the number of carriers represented by $np = n_i^2$ are always true for each type, as n_i is a material constant that varies with either band gap energy or the temperature.

2.2 The p-n Junction

2.2.1 Conduction in Semiconductor

Electrons and holes, as free charge carriers can propagate in a semiconductor in two different ways; either through drift motion or diffusion motion. When the junctions from p and n semiconductor are brought together, a gradient of carrier concentration is created with an inequilibrium condition. The majority carriers, either electrons in n-type semiconductor or holes in p-type semiconductor are roaming freely in the crystal. Near the p-n junction, there is a diffusion current flow due to the non-uniformity of carrier concentration. The electron for example, from the n-region diffuse to the p-side, leaving behind the positive charge donor ion in the n-side. However, the positive ion is bounded to the nucleus of crystal and cannot freely moved. The electron will reach to the p-side to recombine with the abundant number of holes, resulting in the formation of a negative charge ion in the p-side junction. The positive and negatively charged stationary ions form a region with depleted numbers of freely moved carriers. Thus, this region is called the depletion region as shown in Figure 2-3.

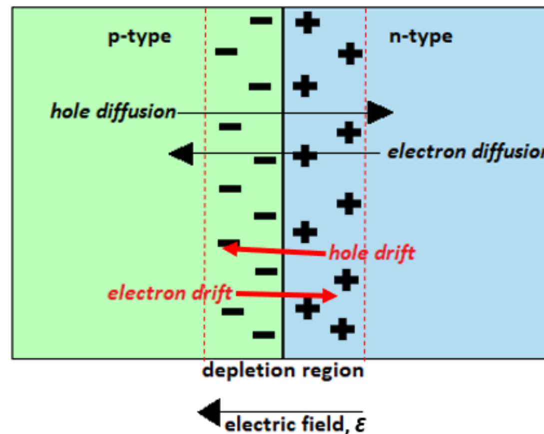

Figure 2-3 Formation of depletion region between p and n junction

The depletion region creates a built-in voltage that allows a drift current to flow to the opposite direction of the diffusion current. In equilibrium of semiconductor, the electric field in the depletion region sweeps the free carriers across it and balance the number of carriers throughout the semiconductor, resulting in the net current to be equal to zero[71]. Therefore, there is no current flow in an absence of external bias, and the p-n junction will maintain the equilibrium state.

2.2.2 Depletion width

The Poisson's equation explains that the derivation of built-in potential as a function of the depletion width yields the electric field of the device. However, assumptions have to be made in the derivation of the Poisson's equation, shown in Equation 2.4.

$$\xi\,(w) = -\frac{dV}{dw} = -\frac{q}{\varepsilon_0 \varepsilon_r}[{N_D}^+(w) - n(w) - {N_A}^-(w) + p(w)] \qquad \textbf{Equation 2.4}$$

Figure 2-4 shows the electric field distribution function of a p-n junction diode, with the highest electric field, ξ is at $w = 0$ (junction of p and n), and $\xi = 0$ at the end of a depletion width for both regions where $-w_p \leq w < w_n$. One of the junctions is assumed to be highly doped, leaving abrupt junction or steep doping profile on one side. Electric field will sweep all the free carriers, so no free carriers left in the depletion region, $n(w) \approx p(w) \approx 0$. There is also no generation or recombination occurred in the depletion region and all dopant is ionised, ${N_A}^+ = N_A$ and ${N_D}^+ = N_D$.

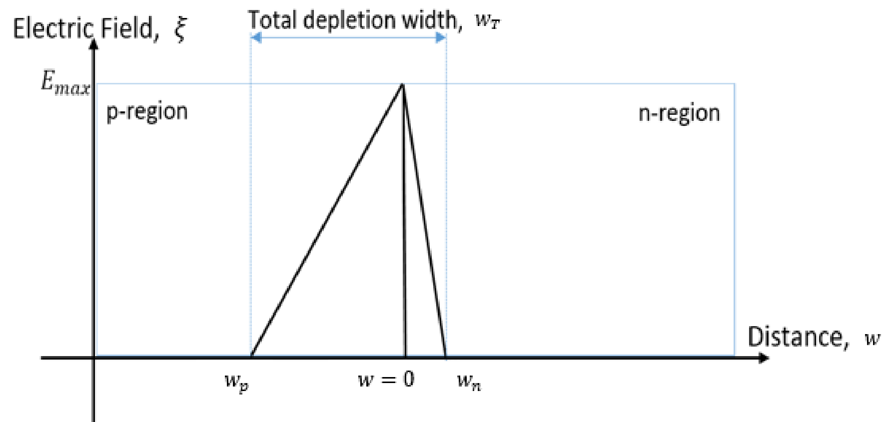

Figure 2-4 Electric field distribution of a p-n junction diode

At the p-n the junction, the maximum electric field now is;

$$\xi_{max} = \frac{qN_A w_p}{\varepsilon} = -\frac{qN_D w_n}{\varepsilon} \qquad \textbf{Equation 2.5}$$

Integration of $\xi(w)$ results in the potential, V across the diode as a function of width of depletion. Note that the total charge at both junctions is equal, thus $N_A w_p = N_D w_n$. When $N_D \geq N_A$, w_p must be much wider than w_n to balance the total charge. In this case, w_n is neglected ($w_n \approx 0$), leaving total depletion width, $w_T = w_n - w_p = -w_p$.

$$V = \frac{1}{2}(\xi_{max})(w_T) = \frac{qN_A {w_p}^2}{2\varepsilon}$$ **Equation 2.6**

The depletion-layer capacitance (per unit area) can be considered as the derivative of depletion charge with varying value of applied voltage. For one-sided abrupt junction, the junction capacitance can be simplified as;

$$C_j = \frac{\varepsilon}{w_T} = \sqrt{\frac{qN_A\varepsilon}{2V}}$$ **Equation 2.7**

Under forward bias condition, the direction of applied bias opposes the direction of built-in voltage across the junction, leading to a reduction of electric-field. This causes an interruption in the equilibrium state of the material, and results in the lowering of the slope between the two junctions. Consequently, more diffusion current can flow to the opposite junction, while drift current is kept constant as it depends on the thermally generated minority carriers.

Contrarily, under reversed biased the depletion region is widened due to increase in electric field. This increases the potential barrier and causes diffusion current to drastically reduce as the majority carriers have to overcome a much larger slope than in equilibrium. However, the drift current of minority carriers is kept constant as before, termed as a reverse saturation current, I_0 in ideal diode equation.

2.2.3 Ideal Diode Equation

The ideal diode equation by Shockley in definition is the total current flows through the semiconductor devices due to diffusion current, and includes the relation of Boltzmann's constant and the approximation of highly doped region abrupt junction[68]. This deduces the Equation 2.8, where the current is represented in current density, J as a function of device area.

$$J = J_o \left[exp\left(\frac{qV}{kT}\right) - 1 \right] \qquad \textbf{Equation 2.8}$$

The saturation dark current density, J_o is a summation of electrons' and holes' diffusion current in the p and n region, as shown in Equation 2.9 and Equation 2.10. The T is the ambient temperature, while q and k are constant value of electron charge and Boltzmann's constant respectively. It should be noted that even when measuring the hole diffusion from p to n region, the magnitude of current is determined by the electron diffusion parameters from the n-side. Similarly, the same process takes place in measuring the electron diffusion current. The D_e and D_h are electrons and holes diffusion coefficient related to $D_{e(h)} = \frac{kT}{q}\mu_{e(h)}$ whereas, L_e and L_h are electrons and holes diffusion length, related to the minority carrier lifetime,τ as in $L_{e(h)} = \sqrt{D_{e(h)}\tau_{e(h)}}$.

$$J_{Dp} = \frac{qD_h {n_i}^2}{L_h N_D} \left[exp\left(\frac{qV}{kT}\right) - 1 \right] \qquad \textbf{Equation 2.9}$$

$$J_{Dn} = \frac{qD_e {n_i}^2}{L_e N_A} \left[exp\left(\frac{qV}{kT}\right) - 1 \right] \qquad \textbf{Equation 2.10}$$

The generation-recombination current, J_{re} is another dominating current that flows under forward bias when devices start to departs from ideal characteristics. J_{re} is due to the current emission collected from the depletion region, thus explaining the inclusion of depletion width,W_D in J_{re} characteristic, shown in Equation 2.11.

$$J_{re} = \frac{qW_D n_i}{2\tau} exp\left(\frac{qV}{2kT}\right) \qquad \textbf{Equation 2.11}$$

By assuming the abrupt junction of p⁺-n devices as initially discussed, the summation of diffusion current and generation-recombination current will deduce the total dark current flow in forward bias, J_F as shown Equation 2.12.

$$J_F = \frac{qD_h n_i^{\,2}}{L_h N_D} exp\left(\frac{qV}{kT}\right) + \frac{qW_D n_i}{2\tau} exp\left(\frac{qV}{2kT}\right)$$ **Equation 2.12**

Numerically, the forward dark current can be portrayed as;

$$J_F \propto exp\left(\frac{qV}{nkT}\right)$$ **Equation 2.13**

where the ideality factor plays an important role in determining the dominating current. The ideality factor, n measured in range 1 to 2 indicates how much the device deviates from the ideal characteristics. Diffusion current can be represented by $n = 1$, whereas with $n = 2$, the generation-recombination current will lead the I-V slope to stray from Ohm's Law. Devices with ideality factor that lies in between 1 to 2 indicate that each current mechanism are involved in total dark current measurement.

At the higher forward bias region, the effects of series resistance, R_s can disturb the linearity of the current-voltage characteristics, which alters the diffusion current to Equation 2.14. While in reverse biased condition, the series resistance is assumed to be very high, and the increment in negative voltages turn the exponential factors to zero. This reduces the equation to be dominated only by saturation current[68]. The series resistance which can be contributed by the doping level, or surface contacts, tend to increase with increases in bias. The R_s effect will be more prominent at high forward voltage supplied regime. The significant amount of voltage drop can be observed on I-V characteristics of devices, when large amounts of current flow through the device. The R_s can be measured from the voltage drop across the resistor, or iterative fittings between the ideal I-V curve to experimental data.

$$I = I_o \left[exp\frac{q(V - IR_s)}{nkT} - 1\right]$$ **Equation 2.14**

2.3 Fundamental of Absorption

2.3.1 Optical Transition

The Beer's Lambert Law describes the attenuation of light that travels through a material will have a dependency on the absorbance and the concentration of the material. It can be described as Equation 2.15 where Abs is the absorbance and Trm representing the transmittance. Materials that allow most of the light to pass through can be valued to have $Trm = 100\%$ and $Abs = 0$. Nevertheless, a very good absorbing material with high absorbance value i.e $Abs = 5$, will still allow 0.001% of light to transmit. However, light as an energy can be lost in the form of heat, or some of it may even be reflected or transmitted[72].

$$Abs = -\log_{10} Trm$$ **Equation 2.15**

In a semiconductor diode, the photons that impinge on a surface of a device are absorbed by the electrons at the lower band. Provided the energy is larger than the material bandgap energy, the electrons excite to the conduction band and creates a carrier. However, not all the generated carriers are able to contribute to photocurrent. Photon energy, E measured in eV can be described as in Equation 2.16 where h is Plank's constant, c is the speed of light, and λ is wavelength in µm[70].

$$E = \frac{hc}{\lambda}$$ **Equation 2.16**

Absorption coefficient, α is the principal mechanism for photodetectors which is defined as the ratio of light intensity being absorbed by a material after travelling a certain distance, x measured in unit cm^{-1}. The inverse of α determines the penetration depth of the photon through the devices. Light travelling through the device is reduced to $1/e$ of its initial intensity, at a distance of 1/α. The absorption coefficient strongly depends on the extinction coefficient, k_e and wavelength, λ as shown in Equation 2.17[73].

$$\alpha = \frac{4\pi k_e}{\lambda}$$ **Equation 2.17**

Ideally, a device should absorb all photons with higher energy than its bandgap, making the $\alpha = \infty$. In addition, a material is practically transparent when $\alpha \approx 0$, showing the light travelling without being absorbed and thus not contributing to the excitation of electron from the valence to the conduction band. The bandgap directness will also determine the electron-hole pair generation in the material. Figure 2-5 shows the energy versus momentum diagram, commonly known as $E - k_m$ diagram, illustrating in a simple way of electron position in a material.

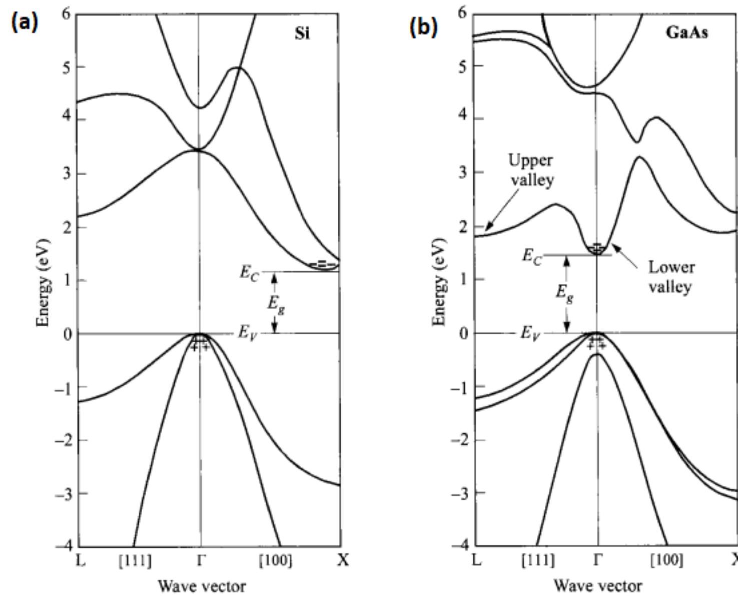

Figure 2-5 $E - k_m$ diagram for (a)indirect and (b) direct semiconductor
(*attributed to S. M. Sze, "Semiconductor Devices: Physics and Technology", 2006*)[68]

The bottom of conduction band consists of many sub bands that can be aligned or misaligned to Γ-valley, at $k_m = 0$. In GaAs, the conduction band minima are symmetry to the valence band maxima at the same momentum of $k_m = 0$, indicating a direct bandgap structure. Hence, with higher photon energy than the bandgap, the band-to-band interaction happens easily for direct material, and rapidly increase the absorption coefficient. The transition of inbound electron at the same k_m value that depend on the available empty states indicate a direct material, where the bandgap can be extracted from Equation 2.18.

$$\alpha(hv) = Z \times \left(hv - E_g\right)^{1/2}$$

Equation 2.18

The constant Z is given as Equation 2.19 where q is the electron charge, m_h, m_e are the hole and electron effective masses, n_r is the refractive index, c is the speed of light, and h is the Plank's constant.

$$Z \approx \frac{q^2 \left(2\frac{m_h m_e}{m_h + m_e}\right)^{3/2}}{n_r c h^2 m_e}$$

Equation 2.19

Hence, the absorption coefficient can be correlated to direct bandgap energy as in Equation 2.20.

$$\alpha(hv) \propto Z \times \left(hv - E_g\right)^{1/2}$$

Equation 2.20

For indirect bandgap such as in Si, the conduction band minima are positioned at a higher momentum towards 100, off-set from $k_m = 0$. The different momentum in indirect material creates a difficult path for carrier generation, compared to a direct material. Energy from photon along with phonon have to be conserved in order to create the transition of electron-hole pair[74]. This indirect transition involves phonon together with either emitted or absorbed photons. The absorption coefficient then is given as Equation 2.21 for transition with phonon absorbed, or as in Equation 2.22 for transition with phonon emitted.

$$\alpha_a(hv) = Z \times \frac{\left(hv - E_g - E_p\right)^2}{exp\frac{E_p}{kT} - 1}$$

Equation 2.21

$$\alpha_e(hv) = Z \times \frac{\left(hv - E_g + E_p\right)^2}{1 - exp\left(-\frac{E_p}{kT}\right)}$$

Equation 2.22

When $hv \geq E_g + E_p$, both transitions possibly occurred and consequently lead to $\alpha = \alpha_a + \alpha_e$. Thus, the relation of indirect energy gap and absorption coefficient can then translated as in Equation 2.23 where hv is the photon energy and E_p is the phonon energy[75].

$$\alpha(hv) \propto \left(hv - E_g \pm E_p\right)^2$$

Equation 2.23

The linewidth in semiconductors at high temperatures is largely determined by the interaction of carriers with phonons and hence has a dependence on kT. Measurements undertaken in Chapters 6 involve temperatures that go from 300K to 600K, hence kT will vary between about 26meV to 52meV. As the AlGaInP alloys being investigated have band gap energies that vary from 1.7eV to 2.27eV over this temperature range, the maximum uncertainty of any optical transition due to thermal broadening effects is less than 3% and so has been ignored.

2.3.2 Absorption Coefficient

A photodetector performance can be measured by measuring the efficiency of the device in converting the amount of light absorbed to photoexcitation and therefore the photocurrent. In an ideal world where quantum efficiency, QE is equal to 1, each incident photon is assumed to generate one electron hole pair. Undoubtedly, 100% efficiency is impossible in the real world as QE significantly depends on the absorption coefficient value that varies with material optical properties.

Figure 2-6 shows absorption coefficient of various material properties at temperature of 300K which portrays a strong wavelength relation characteristic. The spectrum started with high α at a short wavelength region, and started to reduce when approaching a longer wavelength. The direct bandgap materials, the GaAs and InP show steep increments in α. Whereas, the indirect bandgap materials of Ge and Si show gentle slopes of increment in α. Studies have shown several ways in extracting absorption properties of material, either (a) Spectroscopic, (b) Transmission or through (c) Photocurrent measurement.

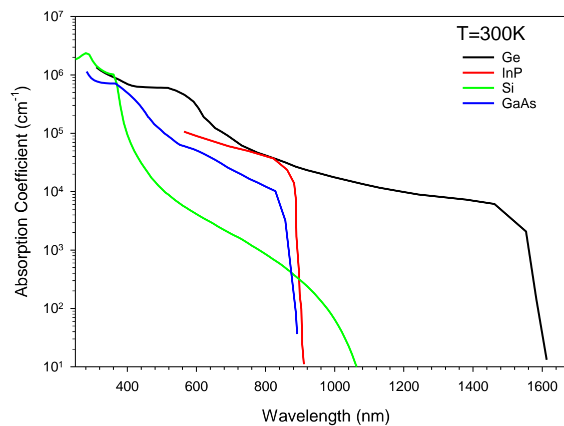

Figure 2-6 Optical absorption coefficient of semiconductor material[76]

Spectroscopic Ellipsometry Method

The spectroscopic ellipsometry method has been widely used in determining the material properties of either optical or surficial properties for homojunction and heterojunction material, for bulk material or ternary-quaternary alloy material or for thin film structure. Ingersoll[77] in his studies showed how this method works in a way of a linear polarized light is shined on a well-polished metal. The reflected elliptical polarized beam then will be analysed for its optical properties. The value of refractive index and extinction coefficient can be measured by this method and subsequently the absorption coefficient can be calculated as in Equation 2.17.

Based on Azzam's reviewed on spectroscopic ellipsometry history[78], Augustin Fresnel has made a significant contribution to polarisation studies. He introduced the two planes of beam from a linearly polarised light of electric wave, parallel (p-plane) and perpendicular (s-plane) which becomes the core of advancing the spectrometer nowadays. Further work only started to take place when computer is available in helping the analysis process. The null configuration is the usual method that has been used in calculating the refractive index and extinction coefficient.

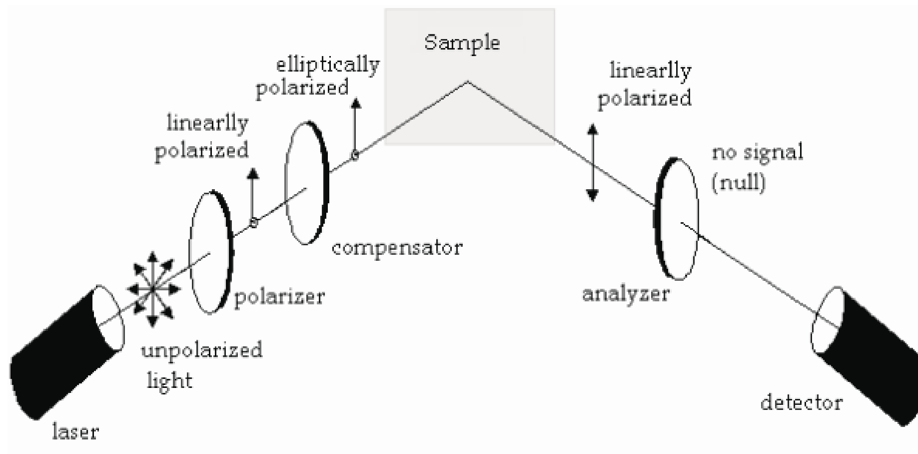

Figure 2-7 Schematic diagram of null-configuration of ellipsometer.
(attributed to D. Gonçalves, "Fundamentals and applications of spectroscopic ellipsometry" 2002)[79]

Figure 2-7 shows the schematic diagram of the null-configuration of ellipsometer. From the entrance arms, the polariser turns the unpolarised light to linearly polarised light at an angle of ${P_{entrance}}^0$. The light then turns into elliptically polarised light after passing through a compensator plate fixed at 45° and falls onto a tested sample. The reflected light at the exit arm forms a linearly polarised light and passes through the analyser at an angle of ${P_{exit}}^0$ before detected by a photodetector. The user will adjust the ${P_{entrance}}^0$ so that the phase between s-plane and p-plane will be 180° elliptically apart before hitting the sample. The angle ${P_{exit}}^0$ is also adjusted until the photodetector can read the minimum intensity of the light[80].

The spectroscopic ellipsometry is well known for its advantages of non-contact and non-destructive measurement method with repeatable and reproducible result. However, the fundamental of the measurement depends on the surface of a material. Kato showed in his study the AlGaInP absorption coefficient value from 1.2eV to 5.5eV measured by spectroscopic ellipsometry method[81]. However, the low absorption value at about $2 \times 10^6 cm^{-1}$ cannot be distinguished for composition of x=0 to x=1. The oxide layer that is usually formed at the AlGaInP photodiode surfaces will give an impact on measurement near the low detection region especially near the band-edge.

Transmission Method

The transmission method involves a study on how light behaves after being transmitted through a material with respect of wavelengths that cover a wide range of light from visible, near-infrared to infrared light region. Various studies on germanium[82,83] and silicon[84,85] have been employing this method by observing the radiation intensity of the light transmitted. Barnes has shown us how to measure the transmission coefficient, T_c and reflectivity, R of an antimony that is deposited on a mirror[86] and Braittain in his study has measured the transmission of germanium based on the difference of light wave maxima and minima amplitude after transmitted through a material[87].

$$T_c = \frac{(1 - R^2)(e^{-\alpha x})}{1 - (R^2 \times e^{-2\alpha x})} \qquad \textbf{Equation 2.24}$$

Both transmission and reflection maxima and minima wave values should be corresponded to each other when plotted. Multiple transmission measurement is done on the same material for different thickness, different spots where the light shined, and different wavelengths to ensure the uniformity of the results. The sample is tested on two condition; first where the light is transmitted at normal incident to record the transmission value, and second at 45° to study the reflection value.

The spectrum range of light is tested from a very short wavelength where the absorption is too large and extended far beyond the cut-off wavelength of a material where the absorption value is zero. Thus, a very thin material is needed to understand the transmission at a very large absorption region, but it involves tedious and particular steps. Researchers always opted for depositing a thin film on a glass rather than preparing a thin bulk material[83]. The material is weighed before undergoing thermal evaporation process where a very thin layer will be evaporated on a glass sample in a vacuum pressurised chamber.

There are several assumptions to be taken into when expecting a thin film sample will yield the same data as the bulk material which are; (i) the uniformity of the thickness deposited on a film, (ii) the purity of a weighed raw material and (iii) the chamber pressure should be very low to ensure absence of other gases. However, the AlGaInP is normally grown on a thick buffer layer, such as GaAs. The difference of optical constant between the two materials will complicate the transmission measurement, unless the thick substrate is removed before the measurements were taken. Another drawback of this material are the possibilities of oxide layer forming on a surface of crystalline material such as in AlGaInP material. Philip in his study shows a rapid drop of reflectance with respect to wavelength are seen on aged sample compared to a new sample, proving the discrepancy of the result due to the oxidised layer[85].

Spectral Response Method

This study will later show the extraction of the absorption coefficient, α using the spectral response method. The photocurrent of a material will first be measured by a monochromator as will be discussed in chapter 3. Provided the details of layers are known, the α can be modelled by using the current continuity equation. We first consider the generation rate, G of electron-hole pairs per incident photon, hv from a surface of a device with a distance of x, expressed as Equation 2.25. The α, ∅, and R are the absorption coefficient, number of incident photons, and reflectivity on device surfaces respectively.

$$G = \alpha \emptyset (1 - R) \times exp(-\alpha x)$$ **Equation 2.25**

Since absorption coefficient and generated carriers are directly proportional, the short and long wavelength relation can be portrayed as Figure 2-8 . Higher α at shorter wavelength leads to rapid decrease in generation rate. Contrarily, the generation rate reduces slower with longer wavelength.

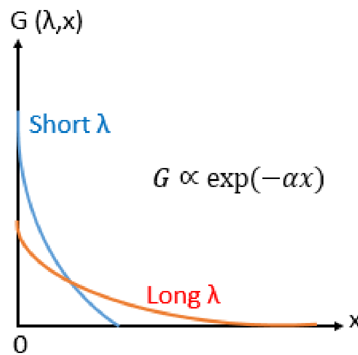

Figure 2-8 Generation rate as a function of wavelength[68]

The photogenerated carriers are measured from diffusion and drift carriers, collected separately from 3 regions of devices as shown in Figure 2-9. First is the top surfaces of the p-region with thickness of x_p, followed by the i-region with thickness of x_i and the neutral region of n with thickness of x_n.

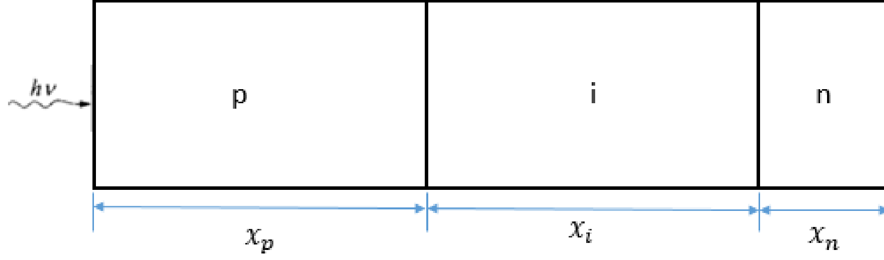

Figure 2-9 Schematic of p, i and n region with a present of hv injection

By assuming a uniform doping density throughout the whole region with a constant diffusion length and carrier's mobility, the generated photocurrent due to minority electrons collected near the depletion edge of p+ region can be expressed as Equation 2.26.

$$J_p = \frac{q\emptyset(1-R)\alpha L_e}{(\alpha^2 {L_e}^2 - 1)} \times \left[\frac{\left(\frac{S_e L_e}{D_e} + \alpha L_e\right) - \exp(-\alpha x_p)\left(\frac{S_e L_e}{D_e}\cosh\left(\frac{x_p}{L_e}\right) + \sinh\left(\frac{x_p}{L_e}\right)\right)}{\left(\frac{S_e L_e}{D_e}\right)\sinh\left(\frac{x_p}{L_e}\right) + \cosh\left(\frac{x_p}{L_e}\right)} - \alpha L_e \exp(-\alpha x_p) \right]$$

Equation 2.26

Similarly, the generated photocurrent due to minority holes collected near the depletion edge of the n+ region can be expressed as Equation 2.27. The S_e and S_h are electrons and holes surface recombination velocity.

$$J_n = \frac{q\emptyset(1-R)\alpha L_h}{(\alpha^2 {L_h}^2 - 1)} \times \exp[-\alpha(x_n + x_p)] \times \left[\alpha L_h - \frac{\left(\frac{S_h L_h}{D_h}\right)\left[cosh\left(\frac{x_n}{L_h}\right) - \exp(-\alpha x_n)\right] + sinh\left(\frac{x_n}{L_h}\right) + \alpha L_h \exp(-\alpha x_n)}{\left(\frac{S_h L_h}{D_h}\right)\sinh\left(\frac{x_n}{L_h}\right) + \cosh\left(\frac{x_n}{L_h}\right)} \right]$$

Equation 2.27

The number of photogenerated carriers from depletion region is assumed to be 100% collected, giving out to 100% efficiency. This defines that each number of injected photons being absorbed creates a number of electron hole pairs, and can be represented by Equation 2.28.

$$J_i = q\emptyset(1-R)\exp(-\alpha x_p)\,[1-\exp(-\alpha x_i)]$$ **Equation 2.28**

Then the total photocurrent, from each region as a function of wavelength can be deduced by the summation of each region generated carriers.

$$J_{total} = J_p + J_i + J_n$$ **Equation 2.29**

Instead of further characterising in photocurrent density, the result is converted to the external quantum efficiency. Thus, the summation of photocurrent from Equation 2.29 is used as the numerator and divided with the denominator of $q\emptyset$, to deduced the QE of a device.

$$QE = (1-R)(QE_p + QE_i + QE_n)$$ **Equation 2.30**

The QE_p measures the minority electrons that travels from the top layers of p^+ to the depletion region. The QE_i measures the electron-hole pairs generated within the depletion region, x_i and the QE_n measures the diffusion of minority holes from the bottom n^+ region to the depletion region. Since QE varies with wavelength, an ideal QE plot should show a steep function from the energy bandgap, saturated at unity value when photon energy ≥ E_g. From the measured QE, the absorption coefficient, α can then be extracted.

Cheong have shown details of absorption measurement on AlInP and proven that this method will give an acceptable accuracy of α with respect to wavelength of interest[88]. This method will be used in extracting the α for seven compositions of AlGaInP, covering the visible spectrum and measured down to the band edge region. The sensitivity of this method is discussed in 5.2 and compared to other published data for convincing results.

Chapter 3 Device Fabrication and Measurement Techniques

3.1 Layer details

The metal organic vapour phase epitaxy (MOVPE) growth method is used in MR reactor for the growth of the quaternary alloy of $(Al_xGa_{1-x})_{0.52}In_{0.48}P$ wafers. Seven layers with different aluminium composition (x) ranging from x=0 to x=1 is grown lattice matched to the GaAs substrate, by Andrey B. Krysa. A thin layer of about 50 to 100nm of p^+ GaAs cap is grown on top of the AlGaInP wafers to optimise the ohmic contact formation between metal and semiconductor material. The nominal layer of 1µm of p-region and 1µm of i-region are growth together with 0.3µm layer of n-region, creating the p-i-n structure wafers. The AlGaInP are grown on GaAs buffer layer, as shown in Figure 3-1 .

GaAs (50nm)
p^+ AlGaInP (1µm) (N_A=10^{18}cm^{-3})
i AlGaInP (1µm) (n_i=10^{15}cm^{-3})
n^+ AlGaInP (1µm) (N_D=10^{18}cm^{-3})
n^+ AlGaAs reference layer
n^+ GaAs buffer
n^+ GaAs substrate

Figure 3-1 The schematic diagram of the p-i-n device structure

All layers were grown on a 10° offset angle towards the 111 plane while another x=0 composition was grown on 2° offset angle on the GaAs substrate. The layers of 10° orientation are characterised in this thesis, as the effect of Copper Platinum (Cu-Pt) can be minimised[89]. The 2° wafer was omitted in this study to maintain understanding on 10° samples only, and kept for future characterisation.

Table 3-1 summarise the layers details.

Table 3-1 Growth and nominal layer details of $(Al_xGa_{1-x})_{0.52}In_{0.48}P$ wafers

$(Al_xGa_{1-x})_{0.52}In_{0.48}P$								
Offset angle (^{0})	10							2
Aluminium fraction(x)	1	0.78	0.64	0.61	0.47	0.31	0	0
Reactor	MR							
Wafer	3924	3917	3916	3919	3920	3921	3925	3925
Structure	p-i-n							
Growth Details								
Growth Temperature	660 (^{0}C)							
p^+ / n^+ doping density ($x10^{18}$ cm^{-3})	0.5 / 1.0							
Peak splitting (arcsec)	300	367	258	110	62	278	310	310
Lattice mismatch ($x10^{-3}$)	1.3	1.58	1.1	0.47	0.27	1.2	1.3	1.3
Strain	compressive	tensile	compressive	tensile	compressive	compressive	compressive	compressive
Nominal Thickness								
GaAs cap (nm)	50							
Top cladding thickness (µm)	1							
Intrinsic width (µm)	1							
Bottom cladding thickness (µm)	0.3							
GaAs substrate thickness (µm)	0.3							

The structure of the p-i-n homojunction layers of $(Al_xGa_{1-x})_{0.52}In_{0.48}P$ consists of highly doped p^+ cladding with Zn dopants, highly doped n^+ cladding with Si dopants, and pure i-region in the middle. The same flow rate ratio of group III sources was used for all layers and both p^+ and i-region were grown at 660°C. Dr. Andrey Krysa reported that the p^+ doped layer is 45° shifted towards the tensile strain. As much as highly doped p^+ region is needed for better performance of a photodiode, Zn dopants on the other hand are known to abundantly diffuse into the intrinsic region and reduce the lattice constant of the material[90]. Research show that increase in Al composition in AlGaInP will lead to increase in lattice constant shift to active layers[91].

The X-ray Diffraction (XRD) results provided by Dr. Andrey Krysa (who grew the samples studies) shows the lattice mismatch between the AlGaInP and GaAs layer. Figure 3-2 shows the results of XRD for GaInP, and the results for the rest of the wafers are attached in the appendix. In order to unambigiously determine the composition of the AlGaInP, an n+ layer of AlGaAs was initially grown before the subsequent growth of the AlGaInP with the same Al:Ga flow rates. By determining the Al composition of this AlGaAs layer from XRD, the Al composition in the AlGaInP layer could be deduced. This AlGaAs layer was not needed for the GaInP and AlInP layers.

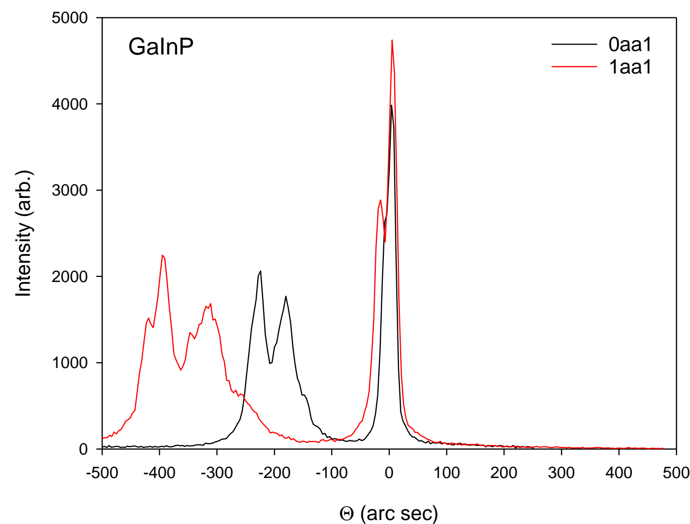

Figure 3-2 XRD results for MR3925 GaInP, where the black line and red line shown different rotation degree of X-ray scan

The XRD measurement is usually carried on a bulk semiconductor to generate the information of mismatch and determine the composition of the material. The XRD scans were done at 180° each to care for the misoriented substrate. If the axis were grown perfectly on axis, the differences between scans would yield a systematic error, in an opposite direction.

The two peaks observed in Figure 3-2 indicate the spacing between the substrate and epilayer. The highest peak represents the substrate and the epilayer is represented by the second peak. A narrower peak is one of the indicators for a good material. The space between the two peaks (black and red) is calculated as $\frac{420+200}{2}$, which yields the 310 ϴ spacing for this composition. The average relaxation of 300 ϴ is almost as close as GaAs lattice constant. Thus, growing reasonably thin layers would not cause any problem.

Based on critical limit theory by Matthew and Blakeslee[92], the mismatch during growth can be accomodated by the strain until a specific amount of critical layer thickness is reached. In the same studies, it is reported that the layers of thicknesses above 350Å are prone to generate the dislocation. Up to this point, the strain and dislocation will propagate towards the surface and disturb the lattice relaxation. Meanwhile, the dislocations are not found in thinner layers.

The amount of mismatch allowed is directly correlated to the epilayer thickness. The fraction of lattice mismatch can be calculated as; $\Delta = \frac{\alpha_e - \alpha_s}{\alpha_e}$ where α_e is the epilayer lattice constant and α_s is the substrate lattice constant[68]. Meanwhile, the critical layer thickness can be calculated as, $\ell_c = \frac{{\alpha_e}^2}{2|\alpha_e - \alpha_s|}$. In this case, the lattice mismatch between GaInP and GaAs were reported to be less than 2×10^{-3}, which are considered low. In addition, the Nomarski image of AlGaInP wafers are shown in Figure 3-3, and are used to observe the surface contamination and wafer defects.

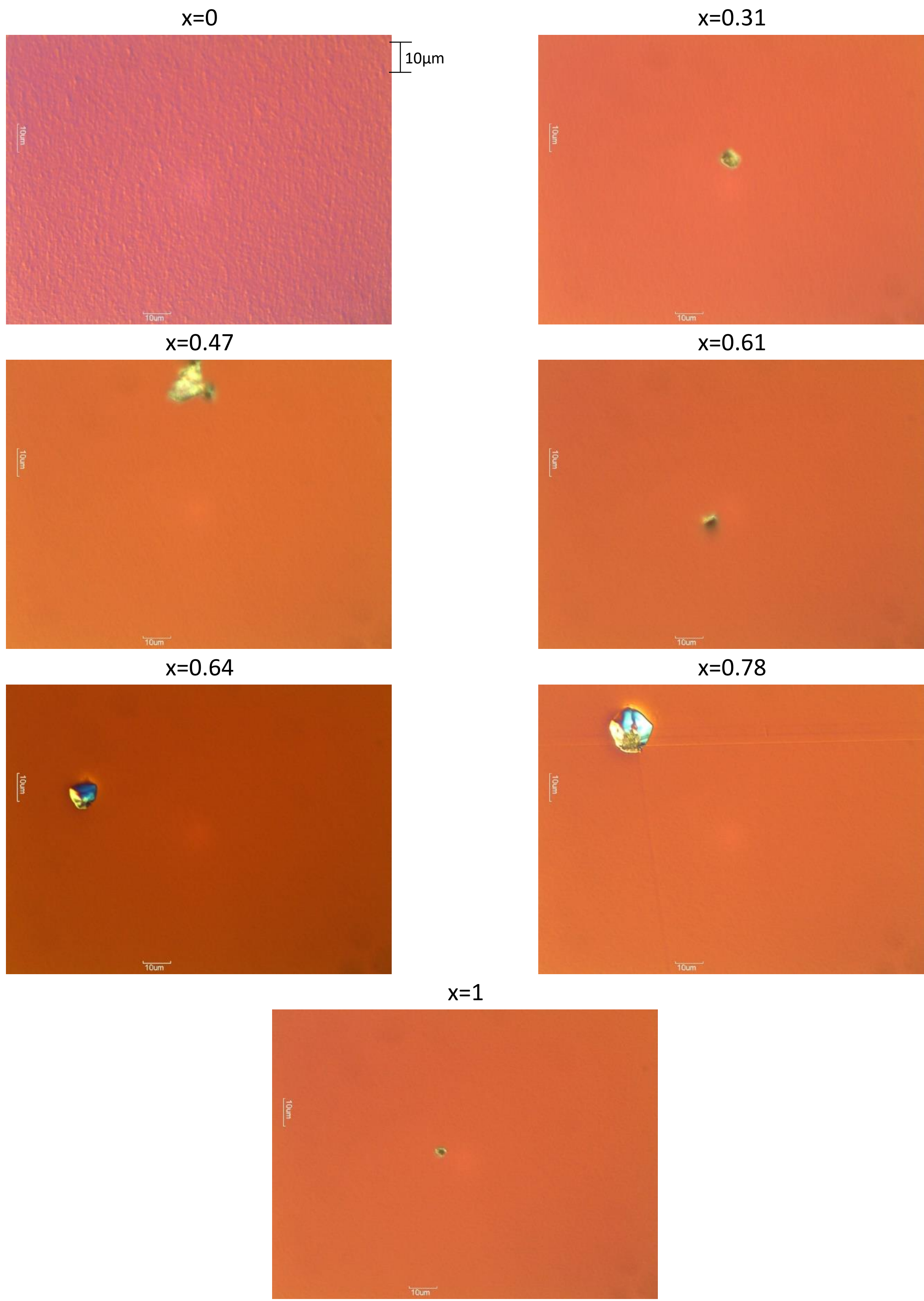

Figure 3-3 Nomarksi image of AlGaInP wafers surface

3.2 Device Processing

The fabrication processes described in this chapter were performed in a clean room for p^+-i-n^+ photodiode on AlGaInP wafers. A standard chemical etching process were involved in forming different sizes of devices.

3.2.1 Top and Back Metal Contact

Firstly, the wafer is cleaved into a smaller size sample, followed by the 3-stage solvent cleaning using n-Butyl Acetate ($C_6H_{12}0_2$), Acetone (C_3H_60), and Isopropyl Alcohol (C_3H_80). The sample surface should be clean from any dirt and dust without confusing it with permanent growth defects. The fabrication stages start with the back-contact metallisation, involving the evaporation of InGe-Au using high vacuum evaporator, with pressure less than $1x10^{-6}$ torr. Two metallisation evaporations are necessary, first for InGe and second for Au. For ohmicity test, the thin strip of Molybdenum is placed across the edge of the sample to create a separation between the metal side. Annealing process then takes place for 1 and a half minute at temperature range from 350°C to 420°C, to make sure the metal diffuses into the semiconductor and forms a good ohmic contact.

Prior to top contact metallisation, photolithography is first conducted on a top surface of a sample covered with a thin layer of photoresist (BPRS200). The mesa patterns of 200µm, 100µm, 50µm and 25µm radius of circles are aligned to the sample area to fit in as many devices as possible. The samples are then exposed under UV light by using a mask aligner. The samples are then immersed in the MF26A developer diluted in distilled water (ratio 1:0.7; MF26A:DIW) to remove the exposed positive photoresist. Finally, the evaporation of Au-Zn-Au takes place. The whole surface area is now covered with metal as a p-type contact.

The fabrication stages resume with lift-off process to dissolve the undeveloped photoresist. The sample will be slowly agitated in a beaker of acetone. A pipette is sometimes used to introduce air bubbles and small pressure to remove the unwanted metal. After ensuring the device active area is clear from metal deposition, the annealing process takes place and followed by transmission line measurement (TLM).

The second stage of photolithography was carried out to create the mesa pattern that isolates one device to another. The second mask of deep mesa etch pattern was used and another 10µm radius was added on each devices resulting in 210µm, 110µm, 60µm and 35µm. The UV is exposed on the remaining sample area excluding the device area. The exposed photoresist will then dissolve in developer, and this part will undergo etching process. Figure 3-4 shows the radii of the mesa mask. In chapter 4.3, the capacitances scaled with the device area, confirming the values of these radii.

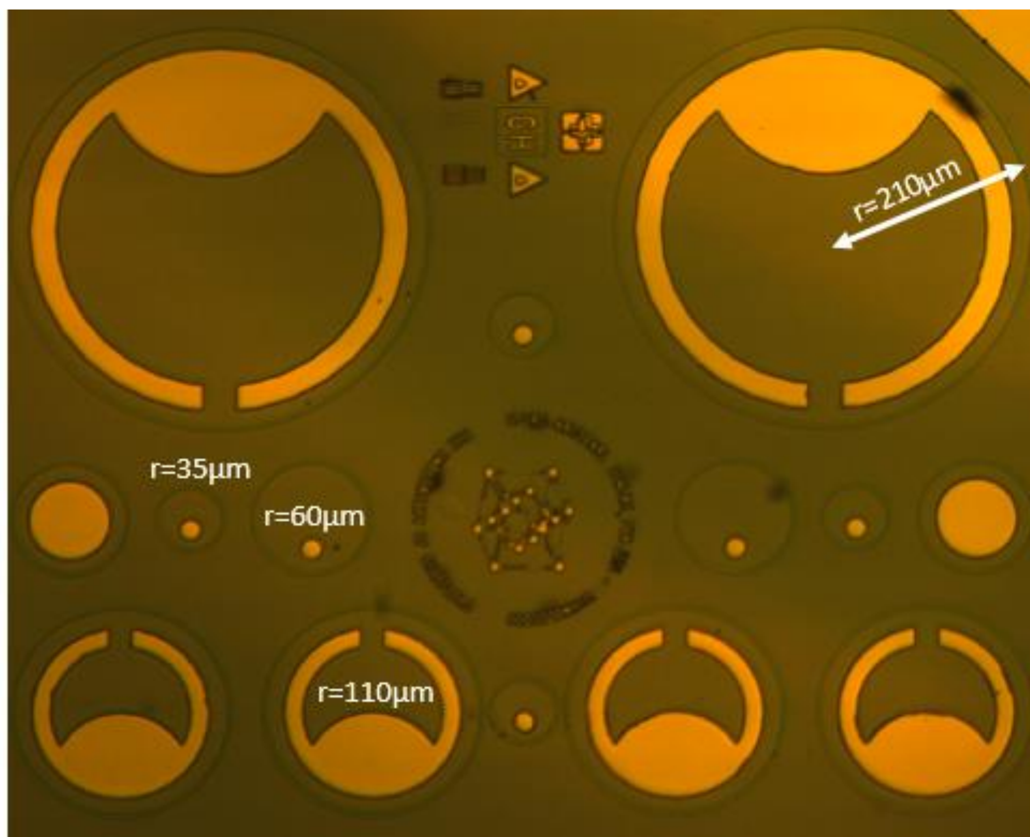

Figure 3-4 Metal contact of Au-Zn-Au on top surfaces of mesa diodes. The radii mentioned are for the mesa.

3.2.2 Wet Chemical Selective Etching

The selective etching is the process of removing specific material, without perturbing on any other material. Figure 3-5 (a) shows the device with metal contact fabricated on top and bottom surfaces, before the etching stages. Firstly, the positive photoresist covers the whole surface area, before exposed under deep mesa mask pattern as Figure (b). Followed by immersing in developer, the exposed area under UV light will dissolve, leaving the photoresist to cover optical window only, as shown in (c).

The sample mounted on a glass slide is then fully immersed in 1:1:1 etchant containing a part of each Hydrobromic acid, Acetic acid, and Potassium Dichromate solutions as shown in (d). The mixture of dark-green colour will react with AlGaInP without attacking the photoresist. A minute in this isotropic etchant solution will etch ~2μm depth. After ensuring the sidewalls of devices has been etched with a desired thickness, the photoresist on the optical window area is now removed.

The etching stages recommences with the removal of the GaAs cap with 1:8:80 etchants as shown in (e). The mixture of one part of Sulphuric acid and 8 parts of Hydrogen peroxide is then diluted in 80 parts of DIW, will give the etch rate of ~300nm/min. The GaAs layer with thickness of about 50-80nm are assured to be etched off when soaked for 30seconds. The thickness removed is measured using the Dektek Stylus Profiler. The etching process can be repeated until the desired thicknesses is removed. Finally, as shown in Figure (f), the optical window area is now free from the thin GaAs layer, with a separated distance created between neighbouring devices.

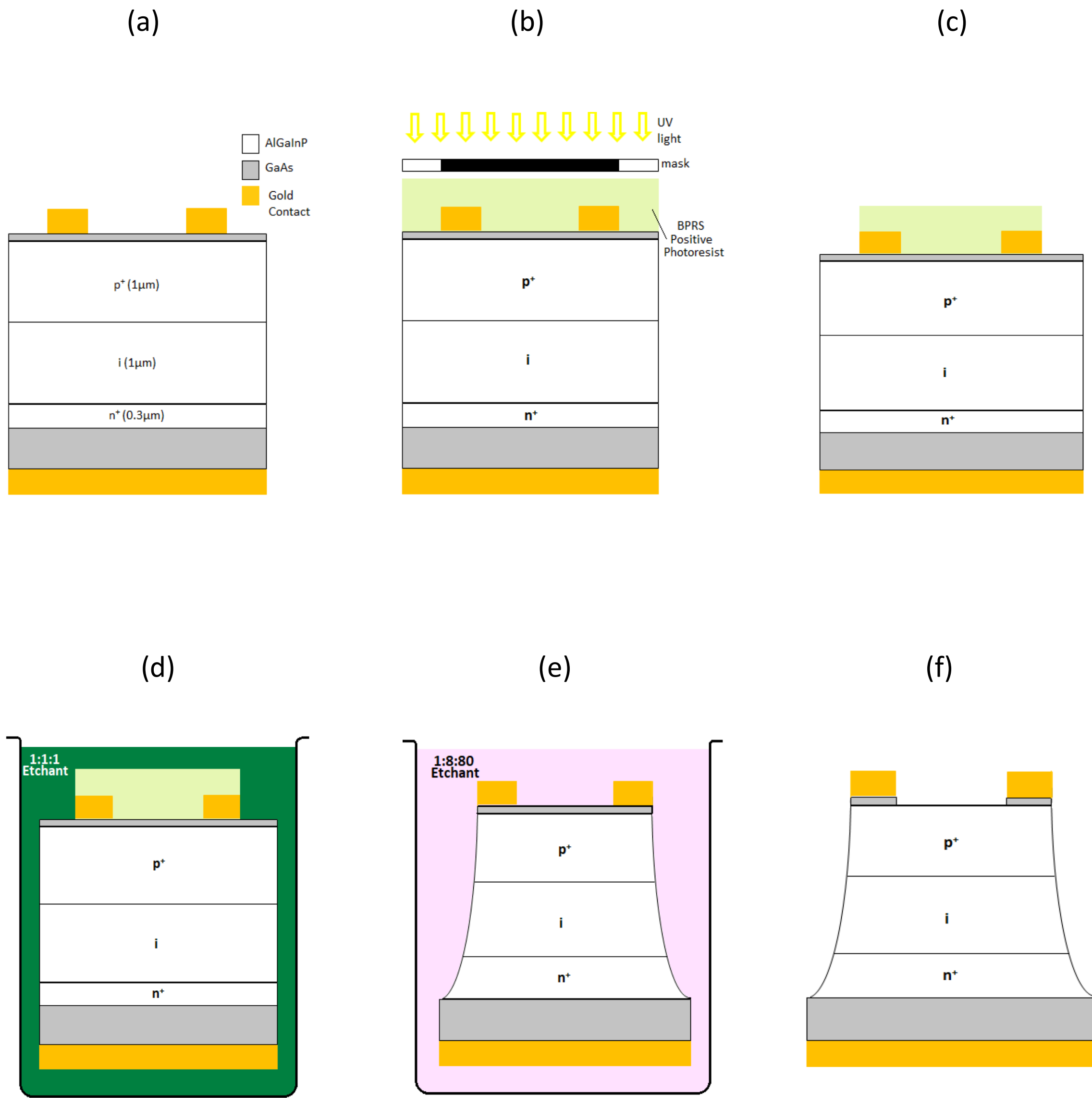

Figure 3-5 Flow chart of wet etching process of removing the side walls of device followed by removing the thin layer of GaAs cap

3.2.3 Metal Passivation on Mesa Diode

The metal passivation process is aimed to cover the exposed area of the devices' edges, and to prevent the penetration of light through the side walls. It is with this process that, the amount of photocurrent measured from a device can be ensured to be coming from the light that fall onto active area. J. Ong studied the choice of material that can lessen the transmission of 442nm wavelength which is part of the strong wavelength absorption for AlGaInP[93]. The study demonstrated that AuZnAu and InGeAu combination of metal can block up to 98% of light. Figure 3-6 shows the top view of the AlGaInP photodiode after being passivated with Zn-Au.

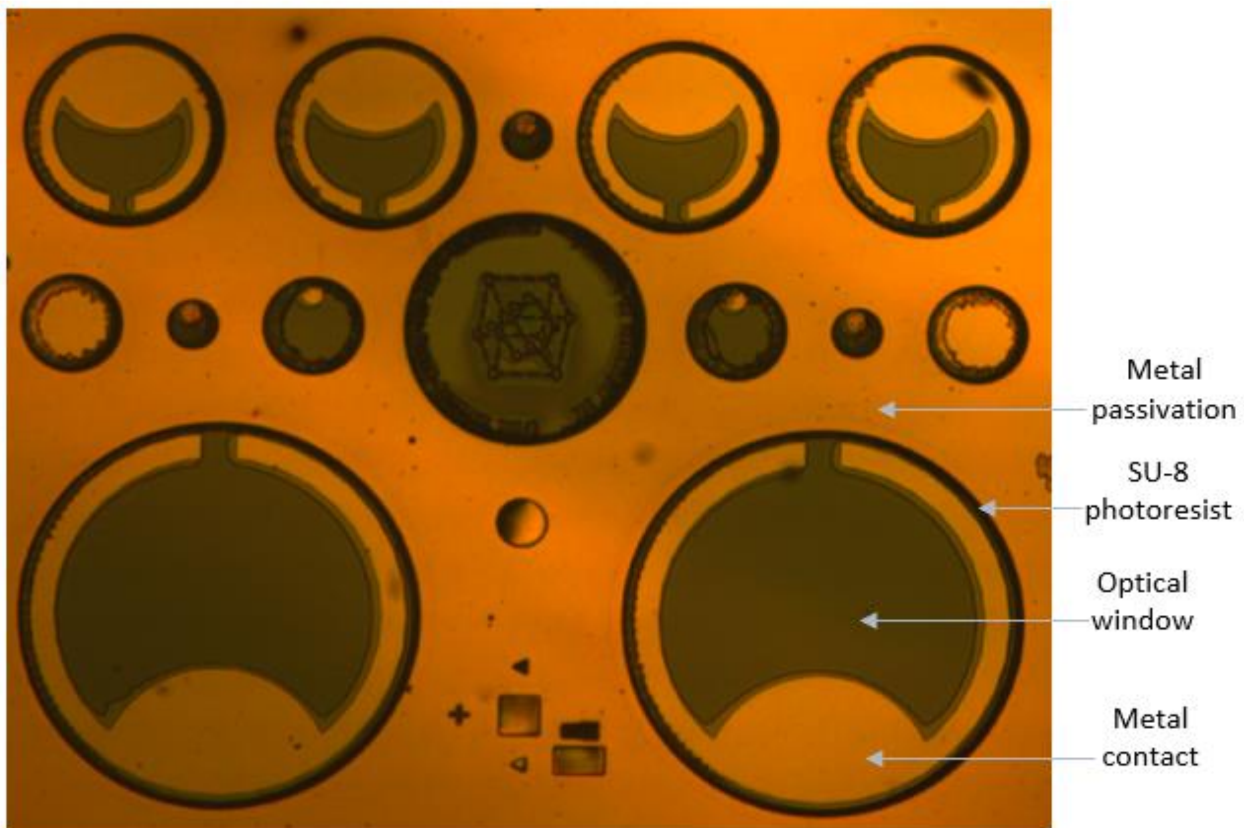

Figure 3-6 Top view of mesa diode sample without GaAs layer and with Zn-Au passivation on a side wall of each device

The stages involved in sidewalls passivation are schematically shown in Figure 3-7. Figure (a) shows the sidewall of the devices are exposed to air after the etching process took place. To prevent further oxidisation, the samples were initially spun with the SU8-5 negative photoresist, followed by a mesa mask pattern, and exposed to UV light as shown in (b). The negative photoresist hardens with more exposure of UV light. Therefore, the SU8 developer penetrates and distorts the photoresist on an unexposed area and leave behind the photoresist in the surrounding of the optical window, as shown in (c). To avoid short circuit between the metal passivation and the metal contact of the device, the thickness of the photoresist must be thicker than the gold contact of the device.

The top surfaces are then covered with BPRS200 positive photoresist, and exposed to UV light after the mask alignment has been made as shown in (d). After it develops, the positive photoresist covers the optical window as shown in (e). In this stage, the BPRS thickness must be ensured to be thicker than the expected gold deposition on the next steps.

The passivation steps proceed with depositing a thin layer of Zn (10mg) and Au (200mg) on the surface of the sample, shown in (f). The distance between the sources of evaporants and the samples have to be accurately positioned to ensure correct thickness of gold is deposited. After evaporation, the gold layers are expected to cover the whole surface of the sample as shown in (g).

The process is wrapped up by lifting off the gold that covered the active area of the device. The BPRS developer attacks the photoresist through a small gap between the gold deposition on the mesa sidewall and the gold deposition on the optical window area. This then leaves a clear passage for photons to impinge onto the centre of the optical window, and avoid penetrating through the sidewalls which has already been covered with metal as shown in (h).

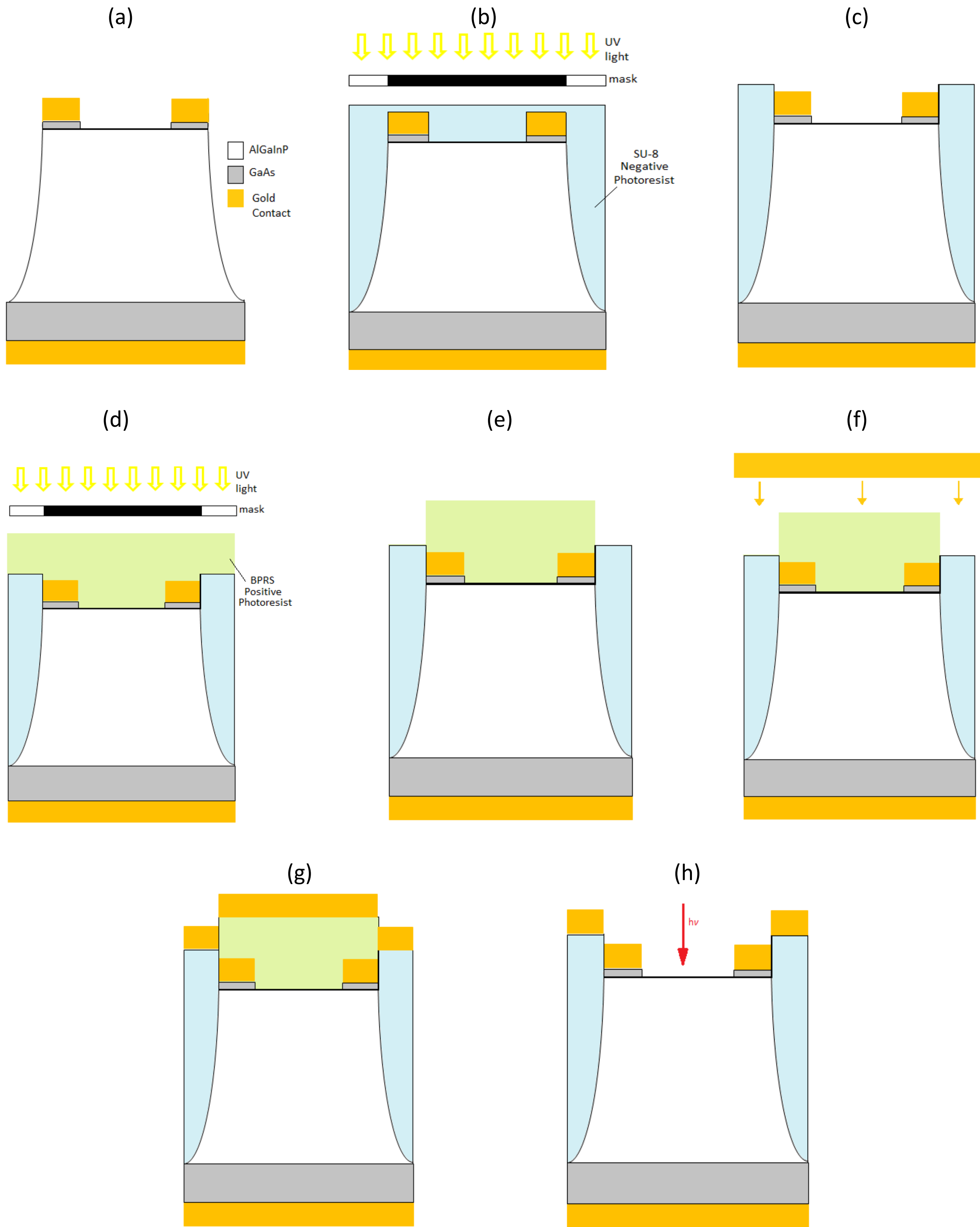

Figure 3-7 Flow chart of metal passivation on side wall of AlGaInP

3.2.4 Optimisation of Fabrication stage

Sanada has proven in his works that contact evaporation using the metal combination of Au-Zn-Au will result in a low series resistance[94]. Discussion below is to learn on how sensitive the first layer of Au thickness corresponding to its weight, the annealing time and its temperature are towards the resistance value. Table 3-2 summarises the variable parameters' effects on series resistance. The d1, d2, and d3 indicate the distance between one end of the probing to the other end during the TLM measurement. The series resistance increases with increase in distance between cells. Summarising the results, there are few options in getting the low series resistance; with most of it can be achieved by annealing at 420°C. However, the lowest series resistance across each device are recorded by the combination of 20mg weigh of gold annealed in 3 minutes.

Table 3-2 Device resistance value as a result of varying gold thickness, annealing time and annealing temperature. The best obtained values are highlighted in blue

Weigh of Au	Annealing Time	360°C			420°C		
		d1	d2	d3	d1	d2	d3
20mg	1min	12.5Ω	16.67Ω	25Ω	12.5Ω	21.25Ω	25Ω
	3min	12.5Ω	16.67Ω	21.67Ω	8.75Ω	10Ω	13.33Ω
	5min	12.5Ω	16.67Ω	25Ω	18.75Ω	20Ω	25Ω
10mg	1min	50Ω	50Ω	60Ω	35.7Ω	76.92Ω	250Ω
	3min	60Ω	60Ω	80Ω	12.5Ω	13.89Ω	25Ω
	5min	50Ω	50Ω	53.33Ω	10Ω	14.29Ω	16.67Ω
6mg	1min	-	-	-	125Ω	140Ω	250Ω
	3min	16.67Ω	20Ω	22.73Ω	16.67Ω	27.78Ω	50Ω
	5min	20.83Ω	27.78Ω	35.71Ω	6.67Ω	12.5Ω	15Ω

Annealing Temperature ← (360°C / 420°C row); Cell's distance ← (d1, d2, d3 row)

3.3 Electrical Characterisation

3.3.1 Current-Voltage (I-V) Measurement

The I-V measurement was carried out in a dark environment where the device is enclosed from any stray light. This measurement aims to measure the device dark current in forward and reverse bias, without any optical carrier generation. The HP4140B Picoammeter is used to supply the voltage source and measure the device current using LabView software installed in the PC. The HP4140B able to source up to ±100V, and measure down to about 10^{-15} A[95]. This voltage and current range are suitable for measuring AlGaInP photodiodes, as wide bandgap materials offer low dark current values of picoAmps, and breakdown voltage below 100V.

The same amount of current density is expected to flow through different devices' areas. However, the etching stage in fabrication may lead to less resistive edges and allows current to flow through the junction surface. The edge leakage current will cause the I-V results to scale more with perimeters, indicating the surface current density, K are flowing $\left(K = \frac{I}{2\pi r}\right)$. However, if the device current shows independent result from various area, then the bulk current may dominate in this device. The bulk current measured in volume current density, J $\left(J = \frac{I}{\pi r^2}\right)$ is contributed by diffusion, generation-recombination, and/or tunnelling current[96].

In reverse biased, the leakage current is expected to be low. The device breakdown voltage is determined when the dark current increases rapidly to several orders of magnitude within small increments of applied voltage. Due to very low dark current, precaution must be taken to minimise the noise. The high resistance BNC cables are used and kept short to minimise the parasitic resistance. The undesirable vibration is eliminated by placing the device and measuring equipment on a vibration free probing station. Probe needles are cleaned with Isopropyl alcohol to avoid dirt on devices, and replaced regularly to prevent deep scratches on the metal contact due to the blunt needles.

3.3.2 Capacitance-Voltage (C-V) Measurement

The LCR meter as the name indicates is designed to measure the inductance (L), capacitance (C) and resistance (R) of a device. The C-V measurement using LCR meter helps in calculating the device capacitance, built-in voltage, doping density and depletion width. HP4275A LCR meter works by connecting the device with DC voltage and subjecting it to AC bias[97]. Other equipment specifications are tabulated in Table 3-3 below.

Table 3-3 The LCR meter of HP4275A specifications

Internal DC Voltage	0 to ±35V
AC Voltage	0.001V to 1V
Frequency range	10kHz to 10MHz
Capacitance	0.0001pF to 100µF

The LCR meter works by internally measuring the impedance value of the device and phase angle between voltage and current, then convert it to capacitance or inductance. Theoretically in a purely capacitive AC circuit, the phase angle of voltage is sinusoidally lagging at 90° behind current. The phase angle however starts to deviates from its nominal value due to low shunt resistance value. This normally happens on a defected layer or when high leakage current starts to dominates. This issue can be minimised by applying a high-test frequency signal. Throughout the measurement for all samples, the phase angle of 88° to 89° are recorded.

There are two available modes to help in accurate C-V measurement, which are resistor-capacitor series mode and resistor-capacitor parallel mode. The high capacitance device usually employed a series circuit, while low capacitance measured in parallel circuit. In this study where measured capacitance is in the range of $10^{-12}F$, parallel circuit at frequency of 1MHz is applied with 50mV steps of AC signal.

The capacitance relation as in Equation 3.1 enables us in characterising the reverse bias effect towards the depletion width, $W.$ The $\varepsilon_o = 8.85 \times \frac{10^{-12}F}{m}$ is the permittivity of vacuum, while the relative permittivity, ε_r for different aluminium compositions in AlGaInP can be extracted from interpolation between ε_r of AlP ($\varepsilon_r = 9.8$)[98], InP ($\varepsilon_r = 12.6$)[99] and GaP ($\varepsilon_r = 11.2$)[100].

Tests are done on different devices area, A to ensure independent capacitance value with respect to the device sizes. Prior to the measurement, parasitic capacitance that exist between all connections and the device are zeroed out to avoid misinterpretation of capacitance value.

$$C = \frac{\varepsilon_o \varepsilon_r A}{W}$$ **Equation 3.1**

By solving the Poisson equation and assuming a one-sided abrupt junction occurs in a device, the built-in voltage, V_{bi} value can be extracted. The equation is rearranged as in Equation 3.2 and a graph of $\frac{1}{C^2}$ versus applied voltage V is plotted. From the graph, the x-intercept from a linear line is extrapolated to the x-axis to show the V_{bi} value. Then by differentiating Equation 3.2, the doping densities, N_D of depletion region can be calculated as in Equation 3.3.

$$\frac{1}{C^2} = \frac{2}{qN_D \varepsilon_o \varepsilon_r A^2}(V_{bi} - V)$$ **Equation 3.2**

$$N_D = -\frac{2}{q\varepsilon_o \varepsilon_r A^2 \frac{d\left(\frac{1}{C^2}\right)}{dV}}$$ **Equation 3.3**

3.4 Optical Characterisation

The aim of the spectral response measurement is to measure the device optical characteristics and evaluate the responsivity, quantum efficiency, absorption coefficient, and bandgap of the device. The setup schematic diagram is shown in Figure 3-8.

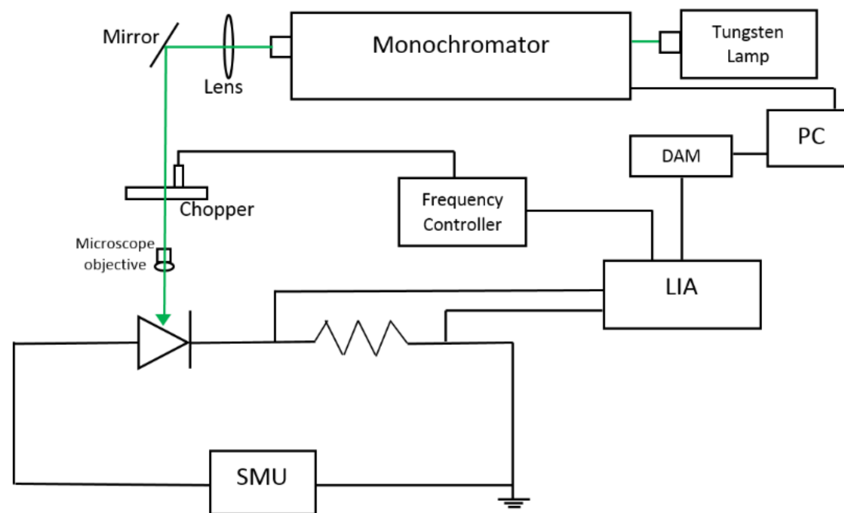

Figure 3-8 Schematic diagram of spectral response measurement setup

The light from the tungsten source will enter the monochromator and will then be diffracted by the chosen grating, and chopped at 180kHz. The frequency chopper is used to differentiate between dark current and photocurrent. To prevent the cross interferences between surrounding electrical appliances, the frequency of multiple of 50Hz signal must be avoided. The size of the beam spot from the monochromator can be adjusted by size of the exit slit. The beam is then focused by a microscope objective to create a small spot that shines onto the optical window of the device. The output generated by the diodes will be collected by an SR830 lock-in amplifier (LIA), which measures the value of voltage drop across the resistor that is positioned in series with the diode. The results are then digitised using the data acquisition module (DAM) and SCADAS software installed in the computer. The diode is connected to a Keithley 236/237 Source Measure Unit (SMU) for biasing purpose when needed, but most of the measurement are done on 0V connection.

3.4.1 Light source

The tungsten lamp[101] is used as the light source in the setup and the black body radiation is replicated. The Stefan-Boltzmann Law conclude that energy radiated by a black body is proportional to the fourth magnitude of temperature. An opaque non-reflective body fully absorbs all the incident electromagnetic radiation within it, and the heated bodies then generate a temperature dependence spectrum light[102].

As shown in Figure 3-9, the increase in temperature leads to higher intensity and shifts the peak to the shorter wavelength. Tungsten is the most preferable material with the advantages of low cost and better life span. The melting point (3383°C) of tungsten limits the movement of peaks from reaching the visible light region. Nonetheless, the spectral curves are stably uniform throughout the visible light region, which is the working range for devices under test in this thesis.

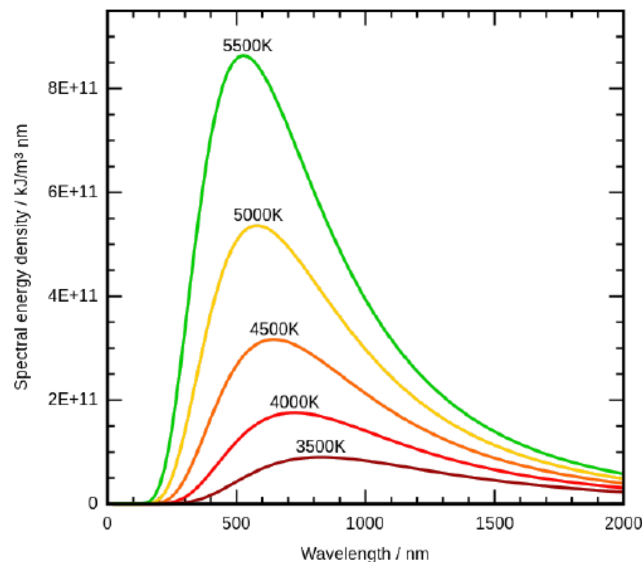

Figure 3-9 Black body radiation with respect to wavelength, as a representation of tungsten light source used in spectral response measurement
(*attributed to M. Fowler, "Blackbody Radiation Cannot Be Explained Classically",2020*) [102]

3.4.2 Grating Monochromator

The 1681 Jobin Yvon monochromator is an optical measurement instrument that transmits selectable narrow and specific wavelengths from the broad band wavelength source. The light that enters a monochromator through the entrance slit located in front of lamp housing is directed towards the collimating mirror. It then forms a parallel beam that falls onto a diffraction grating. The narrow wavelength selected depends on the grating angle, which is then diffracted towards another concave mirror, before being converged and focused to the exit slit.

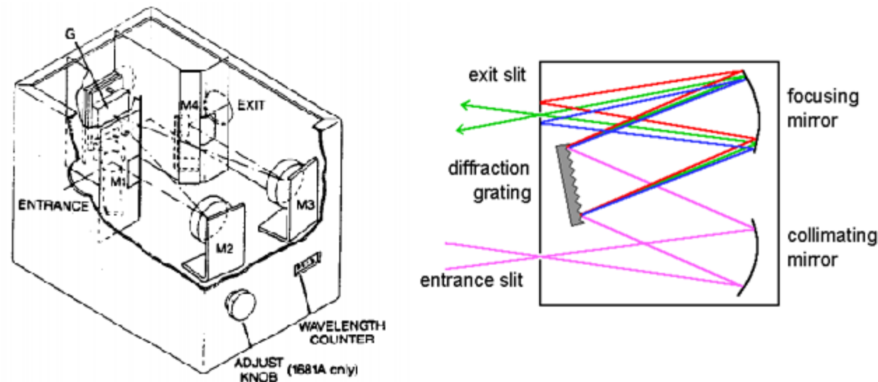

Figure 3-10 Model of 1681b monochromator with the emphasize diagram of light flow from entrance to exit slit
(*attributed to J Yvon, "SPEX 1681 Monochromator User Manual", 1980*) [103]

F number is the ratio of focal length to the diameter of the mirror. The F number between the entrance slit to the concave mirror, and concave mirror to the exit slit have to be equal to maximise the light transmitted. Large F number is more preferable, as it can aid to differentiate narrower wavelength, resulting in high resolution wavelength. To maintain a consistent result, both entrances are operated at a same width. In this measurement, 2mm slits are used for both entrances, with 3.7nm/mm dispersion and ±0.5nm accuracy.

A grating has a periodically grooved surface which splits the white light to a range of spectral colours. Diffraction grating can be described as in Equation 3.4;

$$m\lambda = d(\sin i + \sin r) \quad \textbf{Equation 3.4}$$

where *m* is diffraction order, *d* is grooves periodic distance, *i* is angle of incident and *r* is the reflection angle[103].

3.4.3 Lock-in Amplifier

The SR830DSP Lock-In Amplifier amplifies the weak signal within its working bandwidth. Moreover, it generates a sine wave with a reference frequency, f_{ref} supplied by the frequency chopper. The chopper initiates the square-wave signal differentiating between dark current and photocurrent. The signal is then multiplied by the sine-wave of LIA and the photocurrent is amplified. The signal is maintained at the respected f_{ref} by the phase-locked-loop, while the noise at other frequencies is removed using low pass filter. Multiple peak-to-peak, V_{p-p} value of sine wave components will be detected by LIA, indicating strong photocurrent signal from diodes. The display in LIA will show the first V_{p-p} in terms of root-mean-square (RMS) terms which is gained by the optically chopped square wave at f_{ref}.

The conversion of digitised data by DAM to LIA's displayed voltage can be calculated using Equation 3.5, and the photocurrent can be calculated by converting V_{rms} to V_{p-p} as in Equation 3.6.

$$V_{LIA} = \frac{Arbitary\ value\ of\ LIA}{1 \times 10^5} \times Sensitivity\ of\ LIA$$ **Equation 3.5**

$$I_{ph} = V_{LIA} \times \frac{\sqrt{2} \times \pi}{2} \times \frac{1}{R} \approx \frac{V_{LIA}}{0.45R}$$ **Equation 3.6**

To have a better and stable reading, the resistor, R and time constant, t_c value can be increased during measurement. By increasing the R, the voltage-drop across the resistor will increase and is useful in measuring low photocurrent signal. The value of R is chosen until the display voltage in LIA gives a significant reading. A longer time constant variation is also useful in reducing the bandwidth of the band-pass filter, thus extracting low signal from the noise and increasing the signal-noise ratio. By increasing the t_c, the integration time which is set in the PC has to be long enough to integrate the reliable final value. In most measurements, the integration time is set to be at least $3t_c$.

3.4.4 Incident Power Estimation

As a black body radiation is wavelength dependent, the output power is expected to vary with wavelength. In this measurement, Silicon commercial p-i-n photodiode, model S5973-02 from Hamamatsu with a known value of responsivity shown in Figure 3-11 is used as a reference device[104]. The reference device has a broad spectrum that covers the wavelength of interest from 400nm to 700nm, requirable for all seven composition devices.

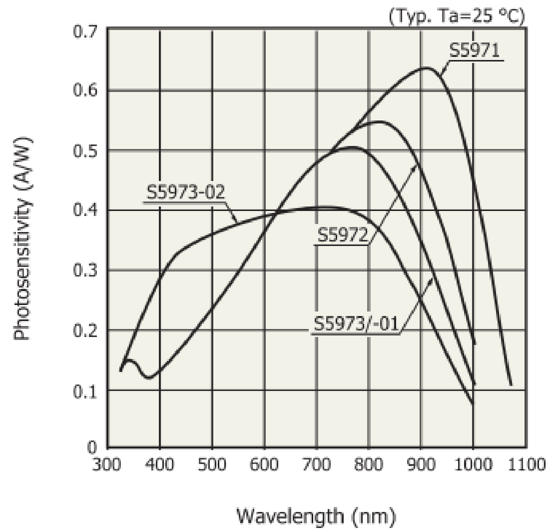

Figure 3-11 Responsivity of Silicon p-i-n photodiode S5973-02 with full coverage of visible wavelength region. (*attributed to Hamamatsu, "Si PIN photodiode"*)[104]

Responsivity measures the absorption output of a device in a unit of A/W as shown in Equation 3.7 where I_{ph} is the photocurrent and P_{opt} is the light source power. By knowing the value of responsivity and the measured photocurrent, the value of optical power can be reverse calculated. With all the information extracted, the quantum efficiency for each device is calculated using Equation 3.8 for further optical characterisation.

$$Res = \frac{I_{ph}}{P_{opt}}$$ **Equation 3.7**

$$QE = \left[Res \times \left(\frac{1240}{\lambda}\right)\right] \times 100$$ **Equation 3.8**

Knowing the actual size of area that allowing the light to travel in a device is useful for accurate estimation of photocurrent flowing from a device. Two ways of estimating the correct optical area of the device are; (i) captured the magnified image of devices, prints it out on grids paper, and manually calculated the ratio of optical window to the total area or (ii) cuts the printing magnified image devices, separated the area covered with gold and uncovered, and weigh using sensitive (mg) digital scale to get the ratio. Both methods satisfyingly show the same results with the percentage of active area of a biggest device of 210µm, are 71% out of the whole device area.

$$\frac{Optical\ window\ area}{Total\ area} = 71\% \qquad \textbf{Equation 3.9}$$

$$Optical\ Power = \frac{71\% \times \pi \times {r_{DUT}}^2}{\pi \times {r_{Si}}^2} \times P_{Si} = 78\% \times P_{Si} \qquad \textbf{Equation 3.10}$$

The Silicon reference diode active area is 200µm in radius, which is comparable to the biggest AlGaInP device's size of 210µm in radius. By assuming the light output is uniformly absorbed, the illuminated power on a device is scaled with the power measured on reference diode. Thus, as shown in Equation 3.10, the optical power from the light source is estimated to be 78% of the total power measured by the reference diode.

3.5 High Temperature Characterisation

The electrical characterisation as a function of temperature presented in this work was measured on 110µm in radius devices, meanwhile devices of 210µm in radius were used for optical characterisation. The high temperature dark I-V and photocurrent characterisation were carried out by using the same measurement setup as discussed in 3.3 and 3.4 with a copper heater stage placed on the probing station. Figure 3-12 shows the schematic diagram of the temperature setup.

The devices under test were probed on the copper stage, that has a built-in heater element and the thermocouple. The ceramic capsulated cartridge heater element comes with Nickel-chromium resistance wire which is able to withstand high temperatures up to 450°C. The attached thermocouple is used as a temperature sensor, to monitor the working temperature before and during the measurement. The temperature is controlled by the variac, which works by adjusting the voltage range to suit the intended operating temperature.

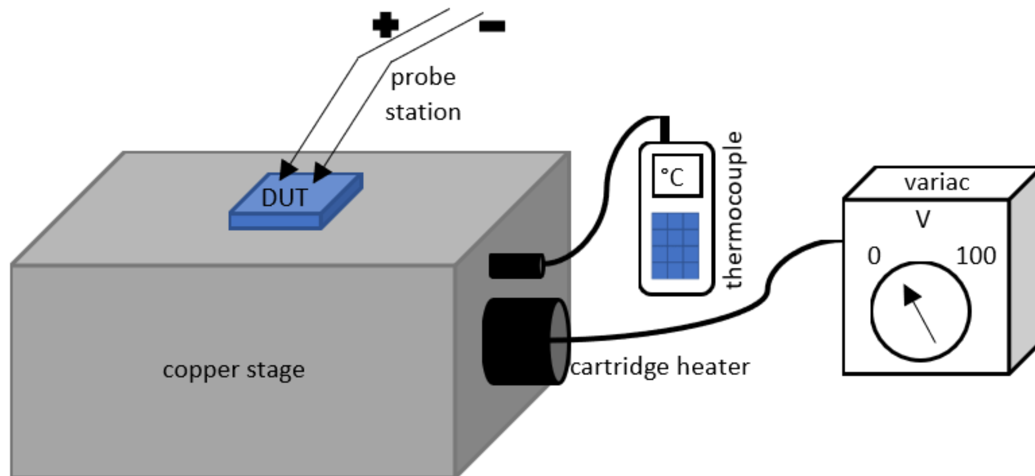

Figure 3-12 Schematic diagram of the temperature setup measurement

At each increment of temperature, the unprobed devices are let to sit on the metal stage for about 10 minutes to ensure correct and stable temperature is reached. The measurement then is carried out on temperatures range of 300K to 600K with accuracy of ±5K. Temperature recorded by the thermocouple is corroborated with an infrared thermometer. Even though a difference in temperature may exist between the top and bottom surfaces of a device, the bulk temperature is assumed to be constant throughout the devices, considering the total devices thickness are about 3µm in total.

Chapter 4 Characterisation of I-V and C-V

4.1 Forward Current-Voltage Characterisation

The current – voltage (I-V) measurement was carried out on each sample under controlled dark environment. The dark current generated from forward bias was measured on 210µm, 110µm and 60µm devices' radius on each composition. The I-V behaviours associated to diffusion and recombination current as described by Shockley diode equation are expected to ensue. By normalising the measured dark current to the device area (πr^2) or device circumference ($2\pi r$), the source of the dark current flowing from either bulk or edge can be identified. The bulk current flow comprises of diffusion current and generation-recombination current. Meanwhile the edge current is due to leakage current flowing from the mesa side walls. Figure 4-1 shows the dark current density between different devices areas for GaInP. There are minimal disagreements observed on low voltage ranges, suggesting the surface recombination currents were dominating. Whereas from 1.4V to 1.5V, the agreement between different areas can be observed. The slope of J-V at this region becomes steeper, suggesting an ideal ideality factor is expected. Constant currents beyond 1.5V are the current compliances limit that has been set up prior to measurement, to avoid overshoot of current.

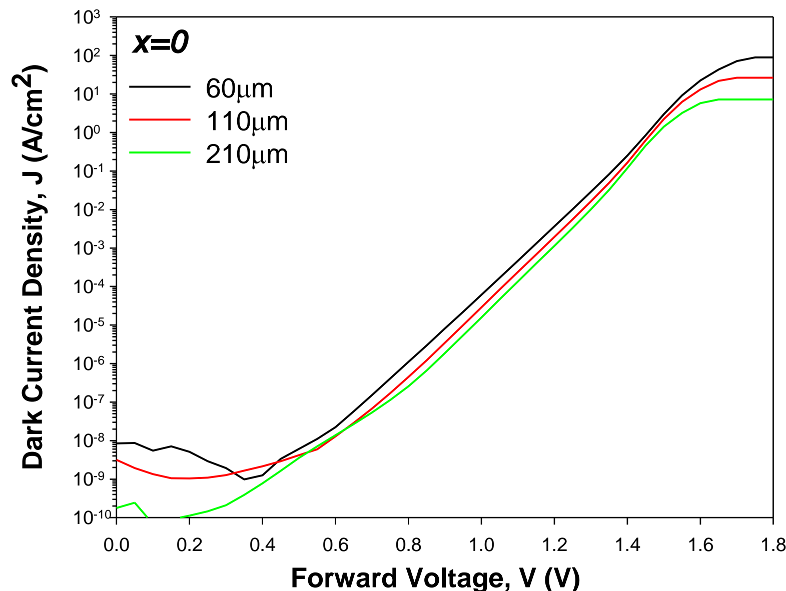

Figure 4-1 Dark current as a function of devices area for GaInP versus forward voltage

The same measurement was repeated on x=0.47 and x=1 samples as shown in Figure 4-2. Comparing to GaInP, the I-V slopes of the intermediate composition and the other end of composition show better current agreement between different devices area. The sensible dark current reading for x=0 device starts at 0.6V, whereas 0.8V and 1V onwards for x=0.47 and x=1.

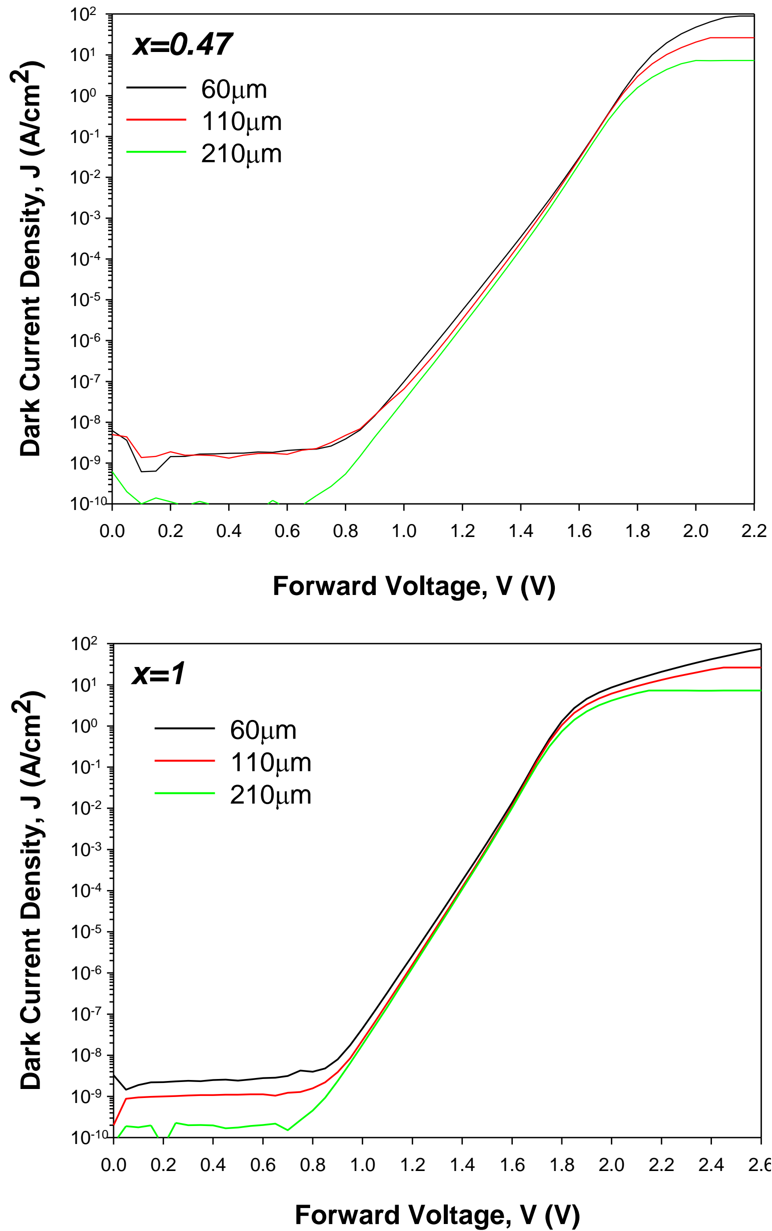

Figure 4-2 Dark current as a function of devices area for x=0.47 and x=1 versus forward voltage

The same measurement was repeated for the rest of the compositions of x=0.31, x=0.61, x=0.64 and x=0.78. The agreement of devices current with different area can be seen for all of the compositions, with x=0.31 showing a small discrepancy in results. The disagreement at lower voltages for x=0.31 are also seen in x=0 as previously mentioned. Hence, devices with more aluminium compositions are expected to scale better with area. The sensible data for x=0.31 can be seen from 0.7V onwards, while the rest of composition show sensible data from 0.9V onwards. The very low bias region data is due to the noise floor and the minimum capability of the measurement setup.

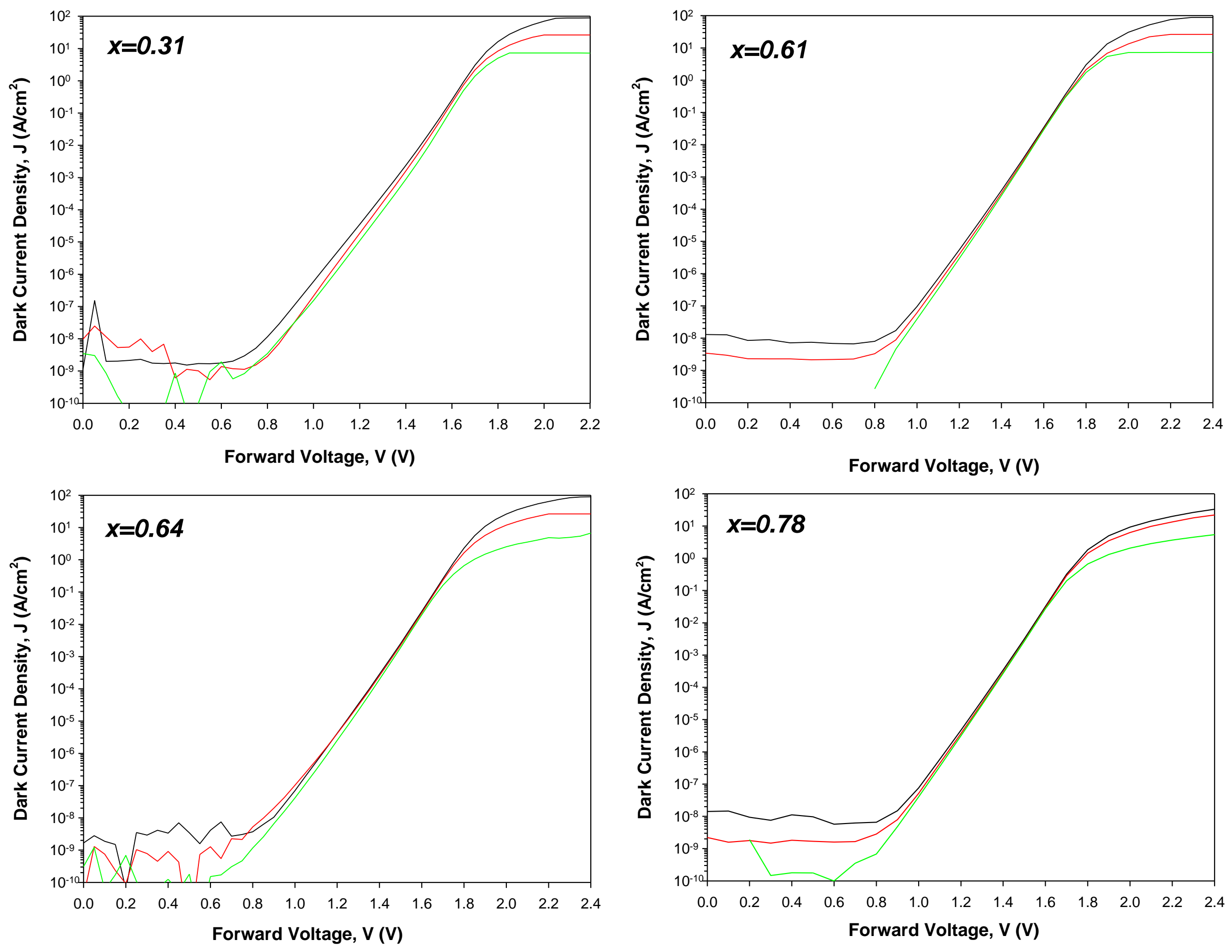

Figure 4-3 Dark current as a function of devices area for x=0.31, x=0.61, x=0.64 and x=0.78 versus forward voltage

Figure 4-4 shows all seven compositions of dark current density, J versus forward voltage. With increase in aluminium composition, the J-V slopes shift towards the higher voltages. The x=0 current firstly deviates from the linear increase slope and saturates at 1.6V. Meanwhile, the x=0.31 and x=0.47 saturates at 1.8V and 2V respectively. The rest of the composition devices saturate around 2.2V onwards.

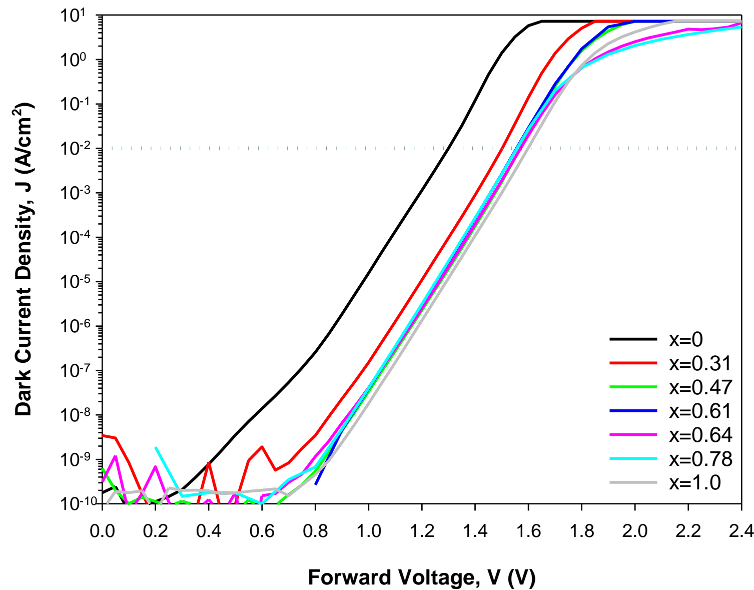

Figure 4-4 Dark current density as a function of forward bias

The 10 mA/cm^2 mark is included in the figure to emphasise the limiting factor for solar cell, and have been used in many published data as an indication for solar cell performance. From this I-V measurement, the solar cell performance can be characterised. The desirable of high fill factor can be achieved by maintaining low dark current and high operating voltage. The large value of open-circuit voltage, V_{OC} can be accomplished by controlling the devices dark current. This ideal characteristic however is difficult to achieve, but multi junction solar cells are able to offer higher efficiency output.

Figure 4-5 shows the J-V of AlGaInP in a linear plot together with published data of the same material. The 2.05eV of AlGaInP used as a subcell in multijunction solar cells records J_{dark} of $10\mathrm{mA/cm}^2$ at V_{OC} of 1.1V[105]. The bigger V_{OC} of 1.32V recorded at the same dark current was measured on x=0.16 devices[106]. From the same studies, the increase in J_{SC} and V_{OC} are recorded

when the n-type emitter dopants of Si are replaced with Se. By switching the dopants, the J_{SC} increases from 6.7 to 7.9mA/cm^2, while the V_{OC} develops from 1.51 to 1.54V. The effect of Se dopants are also associated with the increase of 8% to 10% of QE, while reducing the degradation of the devices.

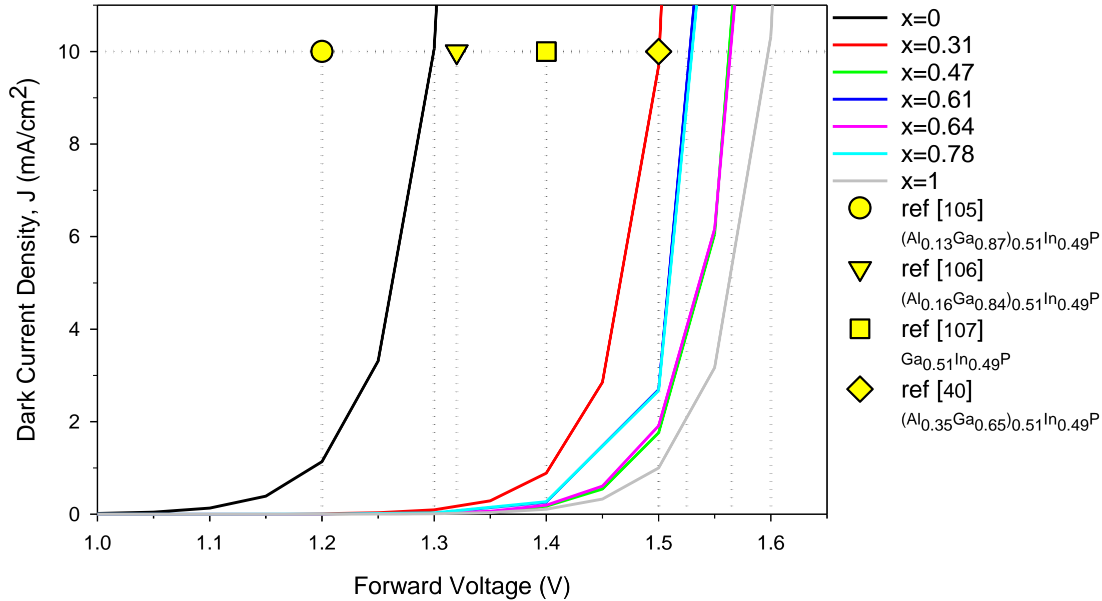

Figure 4-5 J-V characteristics of AlGaInP along with published data of $(Al_{0.13}Ga_{0.84})_{0.51}In_{0.49}P$ [105], $(Al_{0.16}Ga_{0.84})_{0.51}In_{0.49}P$ [106], GaInP [107] and $(Al_{0.35}Ga_{0.65})_{0.51}In_{0.49}P$ [40]

Meanwhile, studies by ISE show that using GaInP as the top layer of a 4-junction cell produces similar current at 1.4V, which is better than our GaInP[107]. In addition, the latest highly efficient 6-junction solar cell by NREL records the V_{OC} of 1.5V measured on the top junction of x=0.35[40], which is comparable to the V_{OC} of our x=0.31 devices. The other devices of x>0.47 achieved the same range of dark current with bigger V_{OC} and broader bandgap. The AlInP with bandgap of 2.27eV reached the same dark current at the biggest operating voltage of 1.6V.

The higher the fraction of ${V_{OC}}/{Bandgap\ Energy}$, the better the solar cell performance. From the measured data, the GaInP and AlInP shows the percentage of $\frac{1.3}{1.89}(\%) = 68\%$ and $\frac{1.6}{2.27}(\%) = 70\%$ respectively. If $n = 1$ is applied for both devices, the existing I-V curve will be shifted to the right, and will yield much lower dark current and bigger voltages. The fraction of ${V_{OC}}/{Bandgap\ Energy}$ will then increase.

Alternatively, the bandgap voltage-offset, $W_{OC} = {}^{E_g}/_{q} - V_{OC}$ can be used as the benchmark of the material quality. Small W_{OC} represents a better quality of substrate. The GaInP and AlInP W_{OC} are 590 mV and 670 mV respectively. Meanwhile, published data have shown various W_{OC} data. Studies by Masuda on 2eV AlGaInP growth by MBE reported a W_{OC} of 620 mV[108], whereas study by Hongbo reported a W_{OC} of 593 mV on 2.05eV AlGaInP growth by MOVPE[105]. The lowest W_{OC} to date is 440 mV recorded by 2eV AlGaInP growth at 780°C by MOVPE[109]. This shows that our AlGaInP samples are comparable to published data, and suitable for the application of solar cell.

As the key of choosing the material for each layer in multi junction cell would be the wavelength coverage and the V_{OC}, the AlInP could be the better option for this application. The V_{OC} of x=0.61, 0.64 and 0.78 are not following the increasing trend, due to the noise during measurement. However, the V_{OC} from x=0, 0.31, 0.47 and x=1 show sensible V_{OC} for further analysis. The relation of V_{OC} and aluminium composition is summarised in Figure 4-6. The dotted-line are included as a reference on expected V_{OC} with respect to the aluminium composition.

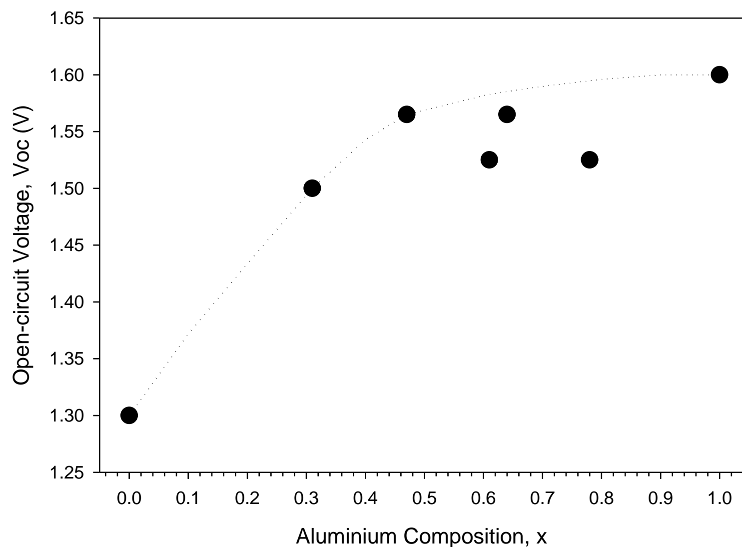

Figure 4-6 Open-circuit voltage recorded at 10mA/cm^2 for respected composition

4.1.1 Dark Saturation Current

The knowledge of dark current at 0V is important for detector characterisation. The dark saturation current in definition is the diffusion of dark current in both p and n region, in a bulk semiconductor device. Based on the diode equation of $J = J_o\left[exp\left(\frac{qV}{kT}\right) - 1\right]$, the -1 term must be ignored for approximation of the ideality factor and dark saturation current. When log function is applied to both sides of the equation, the gradient of $\ln(J)$ versus V will result in $\left(\frac{q}{nkT}\right)$ shown in Equation 4.1.

$$\ln(J) = \left(\frac{q}{nkT}\right)V + \ln(J_0)$$

Equation 4.1

The variation of the ideality factor with voltages will offer multiple linear plots across the J-V curve, and the extrapolation to 0V results in various J_o value. Figure 4-7 shows the linear fitting plot across the experimental J-V for GaInP by using the nominal ideality factor of 1 and 2.

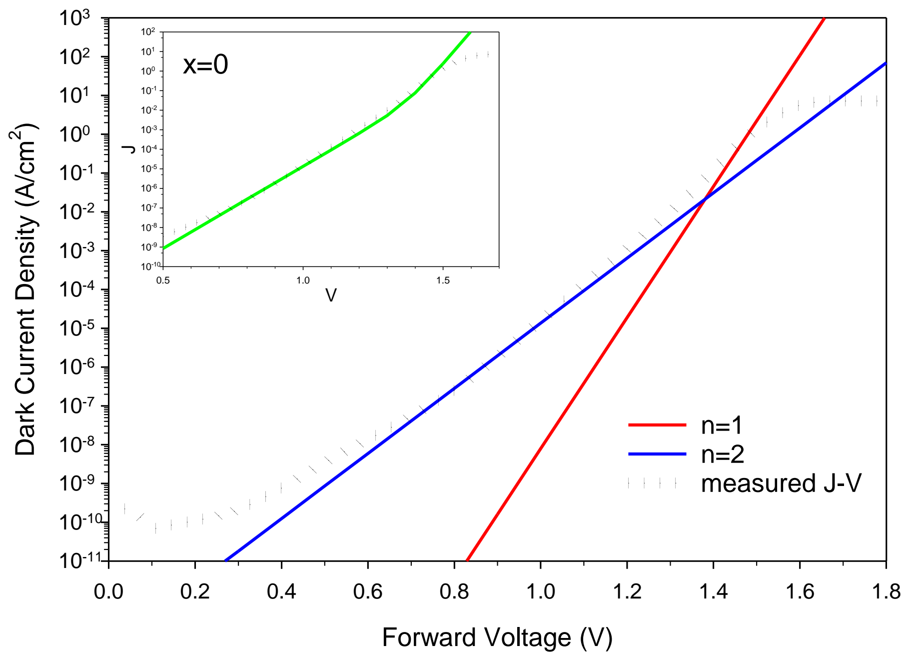

Figure 4-7 Extrapolation of J_o with n=1 and n=2 on GaInP J-V curve

The ideality factor of 2 shown in blue line fits the experimental data from 0.7V to 1.1V. The extrapolation to V=0 gives $J_{0,2} = 1 \times 10^{-25} A/cm^2$. Furthermore, the fitting with $n = 1$ only agrees with 1.45V experimental result and stray away from most of the J-V slope. The extrapolation of n =1 yield the $J_{0,1} = 5 \times 10^{-14} A/cm^2$.

The assumption of $n = 1$ positioned at 1.45V can be explained by the inset figure in Figure 4-7. The green line represents the summation of the J_{dark} from $n = 1$ and $n = 2$. The combination shows a well fit result between the experimental and the linear plots. This signifies the generation-recombination current dominates at low voltage region, whereas diffusion current dominates at high voltage region. The current from 1.45V onwards are expected to keep increasing and following the $n = 1$ plot, but deviates due to the series resistance effect.

The same analysis as GaInP was then carried out on x=1 device, shown in Figure 4-8. For AlInP, the $n = 2$ linear plot fits the region between 0.8V and 1.2V, while $n = 1$ fits at 1.65V. The ideality factors of 1 and 2 result in $J_{0,1} = 3 \times 10^{-30} A/cm^2$ and $J_{0,2} = 9 \times 10^{-17} A/cm^2$ respectively. From this analysis, both GaInP and AlInP are showing different ideality factors representing different voltages region.

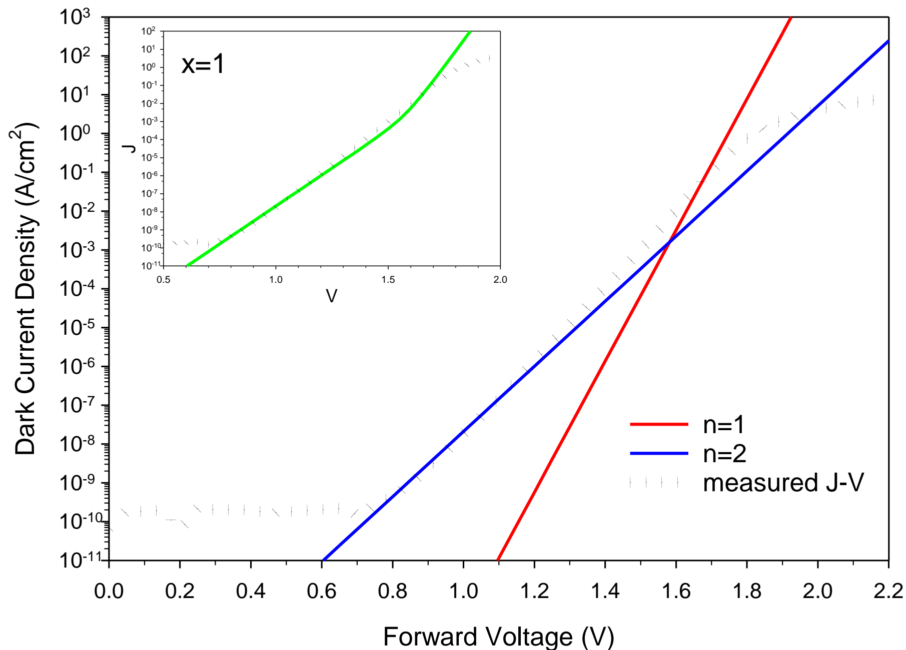

Figure 4-8 Extrapolation of J_o with n=1 and n=2 on AlInP J-V curve

Research by both E. Perl[109] and J. Faucher[110] on 2eV and 2.2eV AlGaInP respectively, demonstrated the same trend of fitting with ideality factor of $n = 1$ started at 1.4V onwards. The 2eV AlGaInP slope of $n = 2$ started from 0.8V to 1.5V, whereas $n = 1$ slope dominated from 1.5V up to 1.7V. Meanwhile, the 2.2eV AlGaInP annealed samples have the transition between $n = 2$ to $n = 1$ at 1.4V, before deviating due to the series resistance effects at 1.5V.

The product of J_0 is governed by two terms of equation, consisting of n_i and ${n_i}^2$ shown in Equation 4.2. The ${n_i}^2$ plays the main role in the first part of the equation whereas the depletion width and lifetime dominates the second part of equation.

$$J_0 \approx \frac{qD_h}{L_h N_D}{n_i}^2 + \frac{qW_D}{2\tau}n_i$$

Equation 4.2

The intrinsic carrier concentration, n_i is the number of electron and holes involved in thermal agitation of electron to excite into the conduction band, and consequently creating a hole in the valence band. Many textbooks simplified J_0 relation to ${n_i}^2$, which is sensible for p-n junction analysis.

The fermi level positioned in p-n junction is far from either conduction or valence band due to the absence of an intrinsic region or the existence of a very small depletion region. For p-i-n junction diode, the nominal thickness of depletion width is usually wide. By ignoring the second part of Equation 4.2, the total of the dark current will be underestimated. However, under very high forward bias, the depletion region collapses, making p-i-n to behave like a p-n junction.

Since the defects or traps are only active in the depletion region, thus assuming the ideality factor of 1 is sensible at this high voltage region. It is then sensible to compare J_0 with $n = 1$ for AlGaInP, to the conventional p-n junction semiconductor as shown in Figure 4-9. The published data of experimental J_0 with respect to their bandgap energy for Si, InP and GaAs p-n junction are taken from study by Neville on solar energy conversion[111].

The $J_{0,1}$ for x=0, 0.31, 0.47 and 1 are extrapolated using $n = 1$ shown in red circle symbols while the $J_{0,2}$ from $n = 2$ are shown in blue circle symbols. The dotted lines across each symbols are manually plotted for observation purposes. The green square symbols are the theoretical J_0 value for respected material calculated by assuming the devices work as a p-n junction.

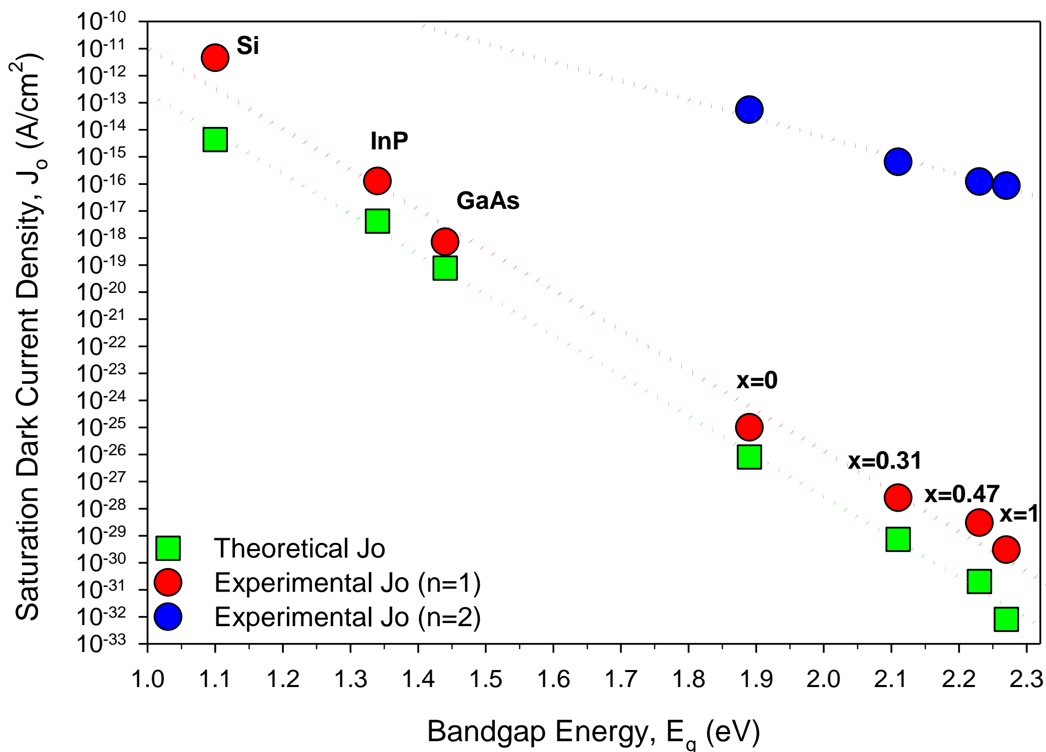

Figure 4-9 J_o with respect of bandgap energy

From this assumption, the Equation 4.2 is reduced to the first part that is dominated by the n_i^2 and calculated by Equation 4.3. The relation of $D_{e(h)} = \frac{kT}{q}\mu_{e(h)}$ and $L_{e(h)} = \sqrt{D_{e(h)}\tau_{e(h)}}$ are used in the equation.

$$J_0 = \frac{qD_h}{L_h N_D} n_i^2 = \frac{kT\ \mu_e}{\left(\sqrt{\left(\frac{kT}{q}\mu_e\right)\tau_e}\right) N_D} \times n_i^2$$

Equation 4.3

The n_i with respect to the bandgap energy are referred from studies on solar cell parameters changing with temperature by Vaillon[112]. The minority carrier lifetime and mobility for Si[113,114], InP[115] and GaAs[116] are from the information of their electrical properties at 300K. Furthermore, the lifetime and mobility for AlGaInP are extracted from studies by Schultes on temperature dependence effects towards various parameters[117].

The relation between J_0 and the bandgap energy portrayed a decreasing trend. The literature shows Si has a higher J_0 value compared to InP, GaAs and AlGaInP, agreeing to the theory of narrower bandgap energy paired with higher J_0[111]. Experimentally, the AlGaInP devices record about 100 times higher J_0 than theoretical J_0 calculation. The same range of gap between theoretical and experimental is also seen in Si, InP and GaAs, which gives us confidence in the quality of our samples.

In short, the effect of bandgap shrinkage due to the reduce in aluminium contents is associated to the increase of the dark saturation current. It is impossible to grow the perfect material to reach the theoretical J_0. Neville in his study suggested that it is practically normal to expect about one or two orders of magnitude of higher dark current than the minimum theoretical dark current[111]. However, with a reasonably low J_0, devices still able to perform well for the rest of characterisation. This has been the best J_0 of AlGaInP experimentally reported, even though much lower J_0 can be expected. There is a possibility to have lower dark current by increasing the minority carrier lifetime of a material, achievable through the optimisation of material growth and junction fabrication.

4.1.2 Ideality Factor

Theoretically, ideality factors, n of a working diode should be in between 1 to 2 and can never be zero. Forward biasing the p-i-n diode will depart the ideality factor from the unity value as several combinations of current flow existed. The doping density, the external bias and the existence of traps could influence the value of the ideality factor.

The recombination rate, R_T assisted by traps in the depletion region can be explained by the Shockley-Read Hall equation, given as;

$$R_T = \frac{n(w)p(w)}{\tau_0[n(w) + p(w)]}$$

Equation 4.4

The maximum recombination rate occurred at $w = 0$, meaning that the most effective recombination is due to the existence of traps at the half way point of the forbidden gap. This explains the value of 2 in the denominator of the diode equation. With increase in w, the R_T changes from being proportional to $\left(\frac{qV}{2kT}\right)$ to $\left(\frac{qV}{kT}\right)$[118]. The assumption from theoretical books suggests that any recombination in depletion layer will be approximated to the maximum recombination rate[68]. This makes $n = 2$ unrealistic for working diodes as the number of traps existing in the forbidden gap and the exact position of the traps' fermi level are not exactly known.

The variation of ideality factor indicates different mechanism of current flowing through the diode at different bias. Figure 4-10 shows the ideality factor of GaInP with respect to voltage, plotted on the same x-abscissa with dark current density for different device sizes. All three devices show sensible ideality factors of n<2 starting from 0.7V onwards. The dark current below this voltage is largely due to the surface leakage current, thus omitted from further ideality factor analysis. It appears that, all three devices exhibit a similar trend of ideality factor variation with voltages. The 210µm device shows the lowest ideality factor at a range of 0.9V to 1.45V compared to 110µm and 60µm devices.

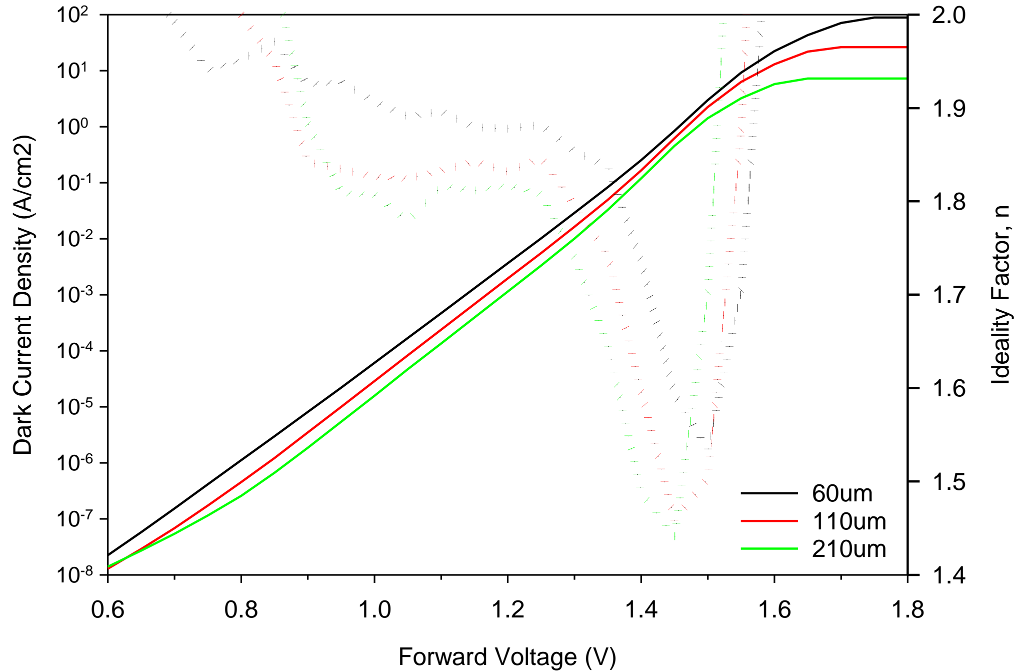

Figure 4-10 Ideality factor and J_o as a function of voltages for GaInP

By observation, the ideality factor of GaInP reduces from $n = 2$ to a constant range of about 1.8 at the intermediate voltage range. The ideality factor then shows a rapid decrease to $n = 1.4$ near 1.4V to 1.5V. The ideality factor is expected to decrease to $n = 1$ with increase in voltage however, the series resistance causes bigger voltage drop at the higher bias region, and suppresses the increase in dark current value. This series resistance causes the ideality factor to increase to beyond $n = 2$ at the higher bias region. Based on GaInP, the best ideality factor is yielded by the larger device. Thus, the same analysis on other compositions are characterised on the 210µm devices, shown in Figure 4-11.

All compositions portrayed a similar trend found in GaInP as discussed before. The shifting of n to higher voltages is associated with increase in aluminium composition. The lowest ideality factor is recorded for x=0 and x=0.31, followed by x=0.47. The rest of composition samples seem to have the lowest ideality factor accumulated at ~1.6-1.7. The ideality factors of x=0, 0.31 and 0.47 show a gradual decrease of n before starting to drop rapidly. The rate of change in ideality factor indicates the I-V characteristic of a diode started as recombination-current and tries to reach the ideal ideality factor at the intermediate voltage range. However, due to the larger voltage drop, the dark current does not increase rapidly as it should with $n = 1$.

Meanwhile, the same observations are not replicated on x>0.47. The rapid reductions in ideality factor are not obviously shown in most of indirect material (x>0.47). It is either the higher aluminium content or the fact that it is an indirect bandgap material could be the reason behind different trends of ideality factor compared to GaInP. The devices seem to struggle to reach much lower ideality factor, and remain constant at $n = 1.8$ over a larger voltage range, before increasing again to $n = 2$.

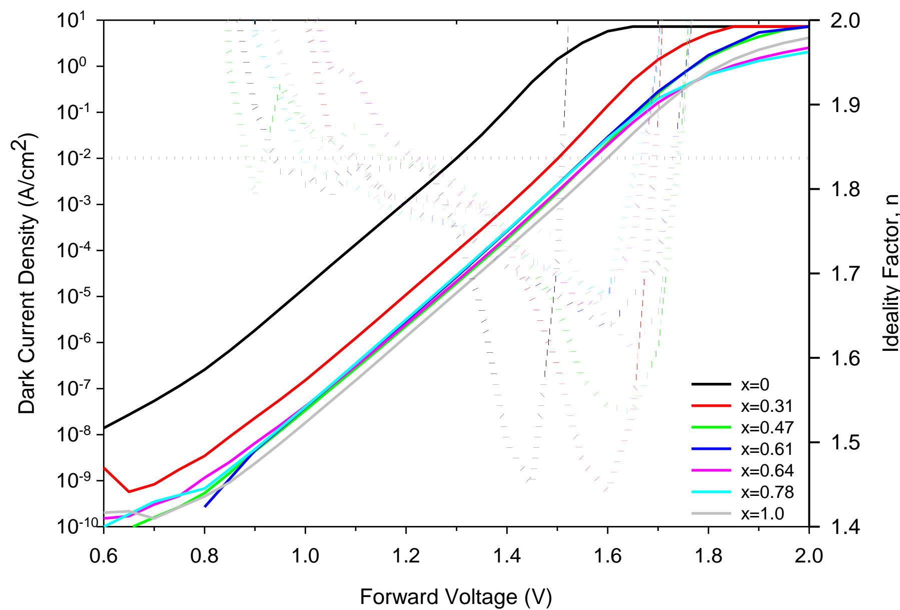

Figure 4-11 Ideality factor and J_o as a function of voltages for AlGaInP

Figure 4-11 shows that the ideality factor is not constant at $n = 1$ or $n = 2$ over any significant part of the forward voltage for any of the samples. Consequently, if a single ideality factor value is proposed to represent the material, the slope is taken in the region where the ideality factor does not change rapidly with forward bias voltages. For AlGaInP, the ideality factor of 1.8 manages to fit most of the middle region of the forward IV characteristic as shown in Figure 4.12. The $n = 1$ red line shown in Figure 4-12 is more an indication of what we would expect to see if the series resistance did not dominate at the higher forward voltages. The best ideality factor at the higher voltages is shown instead by the green line.

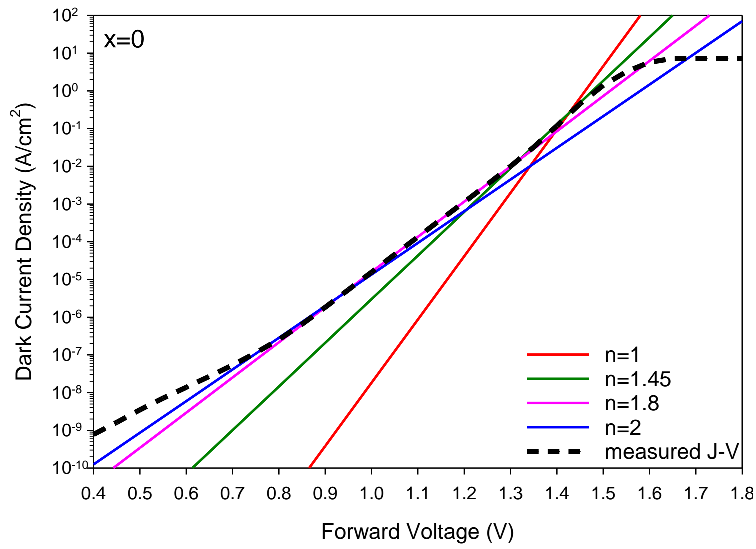

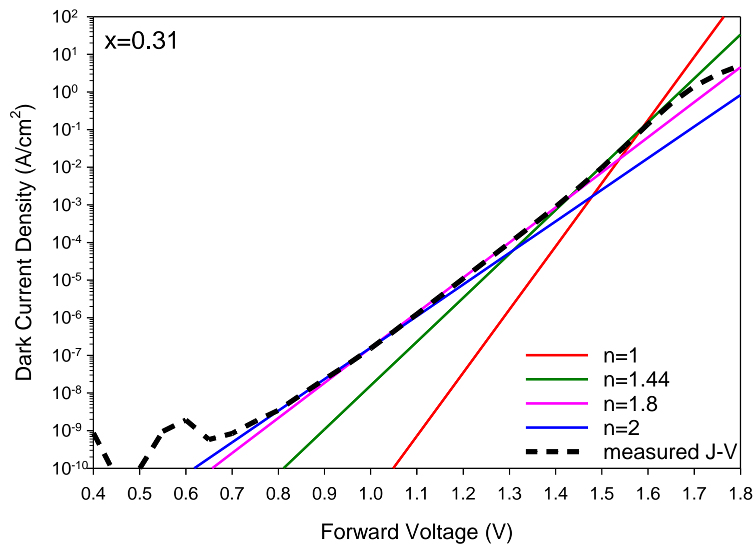

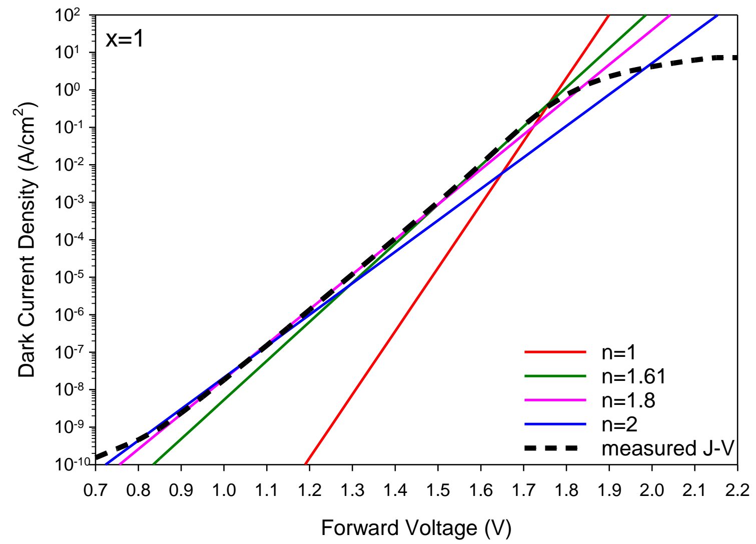

Figure 4-12 Linear plot through the experimental J-V with different ideality factor

The material with higher aluminium content is known to have a problem of oxygen contamination due to the deformation of energy bond between oxygen and aluminium. This dissociation bond introduces defects of deep-level traps, which contribute to the non-radiative recombination[106]. This eventually leads to the non-ideal I-V characteristic. Similar challenges are also reported in AlGaAs samples. Studies by Dimroth show the impurity of oxygen significantly increase in AlGaAs compared to GaAs, due to the volatility of A_2O_x[119]. The oxygen impurities become larger with higher aluminium content, but start to become independent with aluminium higher than 45%.

Therefore, the expectation of n to reduce from 2 and eventually reaching 1 is not achievable in this material. Some material are reported to have higher ideality factor up to $n = 3$[120], whereas devices across the composition of AlGaInP can be represented by $n \leq 2$.

The relation of J_0 and ideality factor are summarised in Figure 4-13.The desirable characteristics for photodiodes are lower J_0 value that comes in a pair with lower ideality factor. However, a higher ideality factor is a better representation for the intermediate voltage region of AlGaInP, which then comes with higher J_0.

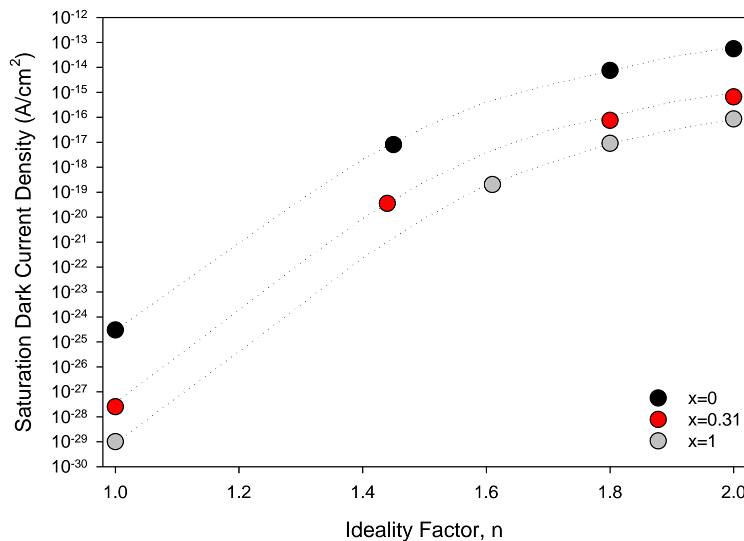

Figure 4-13 J_0 relation with ideality factor

Both J_0 and n_i are temperature and bandgap dependant properties, expressed in Equation 4.5 and Equation 4.6. In wide bandgap material, electrons have to gain higher energy for recombination to take place. Contrarily, lesser energy is needed in narrow bandgap material. Thus, n_i decreases as bandgap widens. From this justification, J_0 relation to bandgap energy are similar as in n_i.

$$J_o \propto exp\left(-\frac{E_g}{2kT}\right)$$ **Equation 4.5**

$$n_i \propto exp\left(-\frac{E_g}{2kT}\right)$$ **Equation 4.6**

Literature shows that with doping density more than $10^{17} cm^{-3}$, the ideality factor starts to astray from unity value and J_0 will rapidly increase[68]. However, it is not applicable for AlGaInP as it is grown with the same nominal range of doping. The J_0 is higher in lower aluminium composition across the ideality factor of 1 to 2. The higher J_0 in GaInP compared to AlInP explains that the material bandgap influences the difference in J_0.

4.1.3 Series Resistance

Series resistance, R_S is another factor that leads to the deviation of the ideality factor from the unity value. High R_S value is undesirable as it will limit the device's performance. Nevertheless, it is possible to have a lower R_S with better diode design. The R_S in a device is introduced by parasitic elements during I-V measurement, such as from between substrate, between internal and external connection, through wire bonds or through ohmic contact.

Studies show R_S in a solar cell can be calculated as a different component with respect to the contributing element[121]. For simplification, the sum of R_S is considered in this study. Once R_S effects start to dominate, the Rs absorbs a substantial amount of voltage, and reduces the value of dark current significantly[68]. As discussed previously, the term of IR drops in Equation 2.14 can be used on comparison with ideal I-V slope. The fitting started at the high bias region, from where an ideal I-V slope starts to deviate. The estimation of R_S is iteratively run until a comparable I-V fitting is reached as to measured I-V.

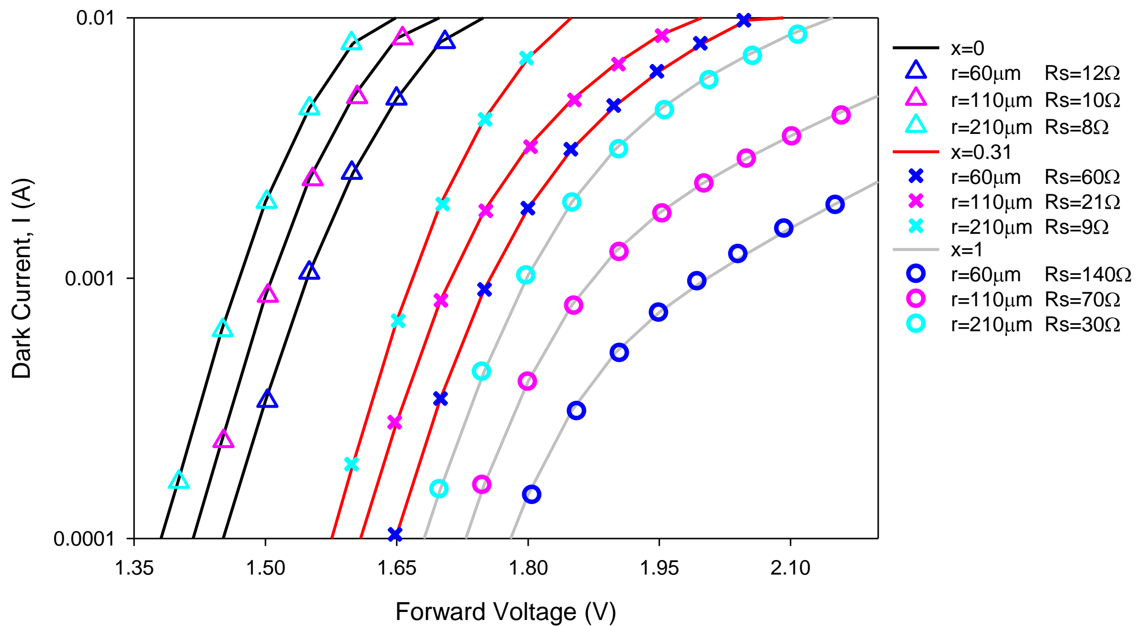

Figure 4-14 I-V for x=0, x=0.31, and x=1 shown in black, red and grey solid-lines. The blue, pink and cyan symbol colours represent 60µm, 110µm and 210µm radius devices sizes, for respected composition

From Figure 4-14, all compositions record the highest resistance from the smallest size areas. This concurs with the relation of $R_S = \frac{\rho \ell}{A}$, where ρ represents resistivity, ℓ as device thickness and A is the device surface area. With constant device nominal thickness, one should expect higher R_S on the smaller areas of devices, as summarised in Figure 4-15. Wider device area allows more electrons to pass through, thus reducing the device resistance.

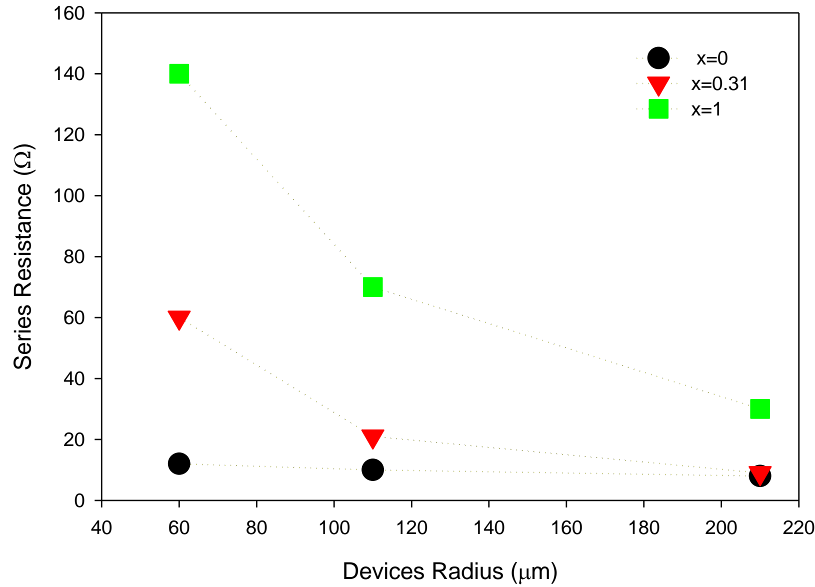

Figure 4-15 Series resistance measured on 210µm, 110µm and 60µm radius devices, shown in black, red and green symbols representing x=0, 0.31 and 1 respectively

The variation of R_S for GaInP is much smaller compared to devices with increasing aluminium content. This validates the increase in R_S with increases of material bandgap. This relation correlates to how resistivity changes with number of carriers in a semiconductor, as shown in Equation 4.7. From C-V measurement, the doping density of GaInP is an order of magnitude higher than AlInP, which explains the lower resistivity range found in GaInP. Study by SM Sze demonstrated with the same doping concentration, GaAs has higher resistivity than Si. This coincides on how narrow bandgap energy has lower resistivity value[122].

$$\frac{1}{\rho} = q(\mu_e n + \mu_h p)$$

Equation 4.7

4.2 Reverse Current-Voltage Characterisation

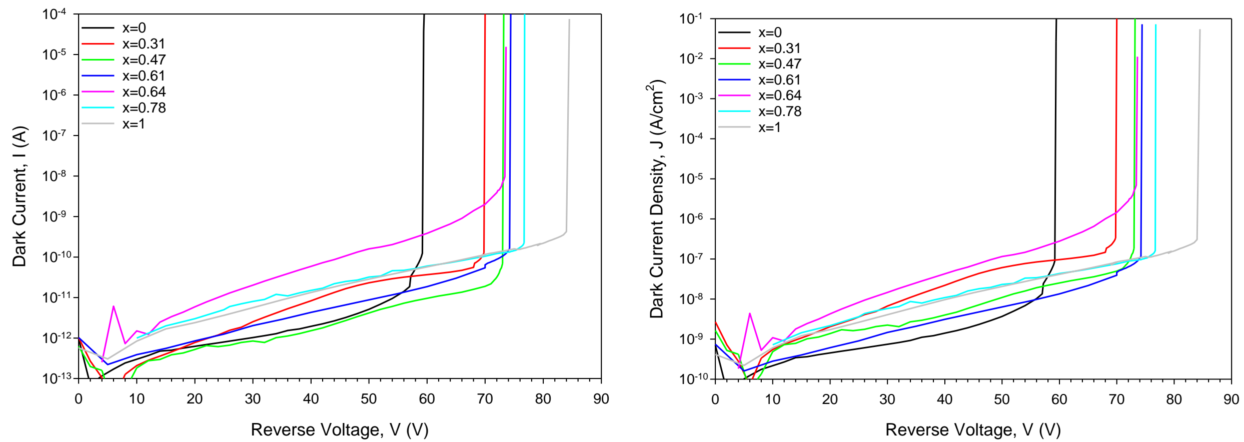

Figure 4-16 Reverse I-V (left) and Reverse J-V (right) of AlGaInP

Figure 4-16 shows the junction breakdown of AlGaInP shifting to higher voltages as aluminium content increases. The AlGaInP is wide bandgap material which offers low and stable reverse dark current density of ≤1.5μ Acm^{-2} up to 5% below breakdown voltage. The exponential rise of dark current near the breakdown voltage is due to the deep level trap, introduced by Zn-doped material. Commonly, III-V material with Zn dopants will face oxygen contamination problem. This issue is more obvious in higher aluminium content devices. Oxygen contamination introduces deep donor-like traps and causes the free-carriers to fall on the mid-energy traps. This leads to non-radiative recombination, increasing the resistivity of devices and reducing their efficiency[123].

At zero voltage, either probing in forward or reverse connection, the measured current should be zero in an ideal diode under absence of light. In this measurement however, the dark current in a range of pico amps are recorded. Much lower dark current measurement is restricted by the setup noise limitation. The noise level from the open circuit setup is measured by probing one side of BNC cable and leaving the other side disconnected. The result shows a noise level in the range of pico amps of dark current.

Theoretically, in reverse biased connection, specifically for wide bandgap material, the increase in depletion width will oppose the flow of current due to very high value of reverse resistance. Experimentally, there is still small current that insists on flowing through any possible path with the least resistance. The measured current could possibly flow down through the side of the mesa. This explains the unscaled results of reverse dark current density as shown in Figure 4-17 for x=0.61. Meanwhile, the reverse current results of different device sizes scale better with perimeter, explaining the surface leakage current are contributing to higher reverse current.

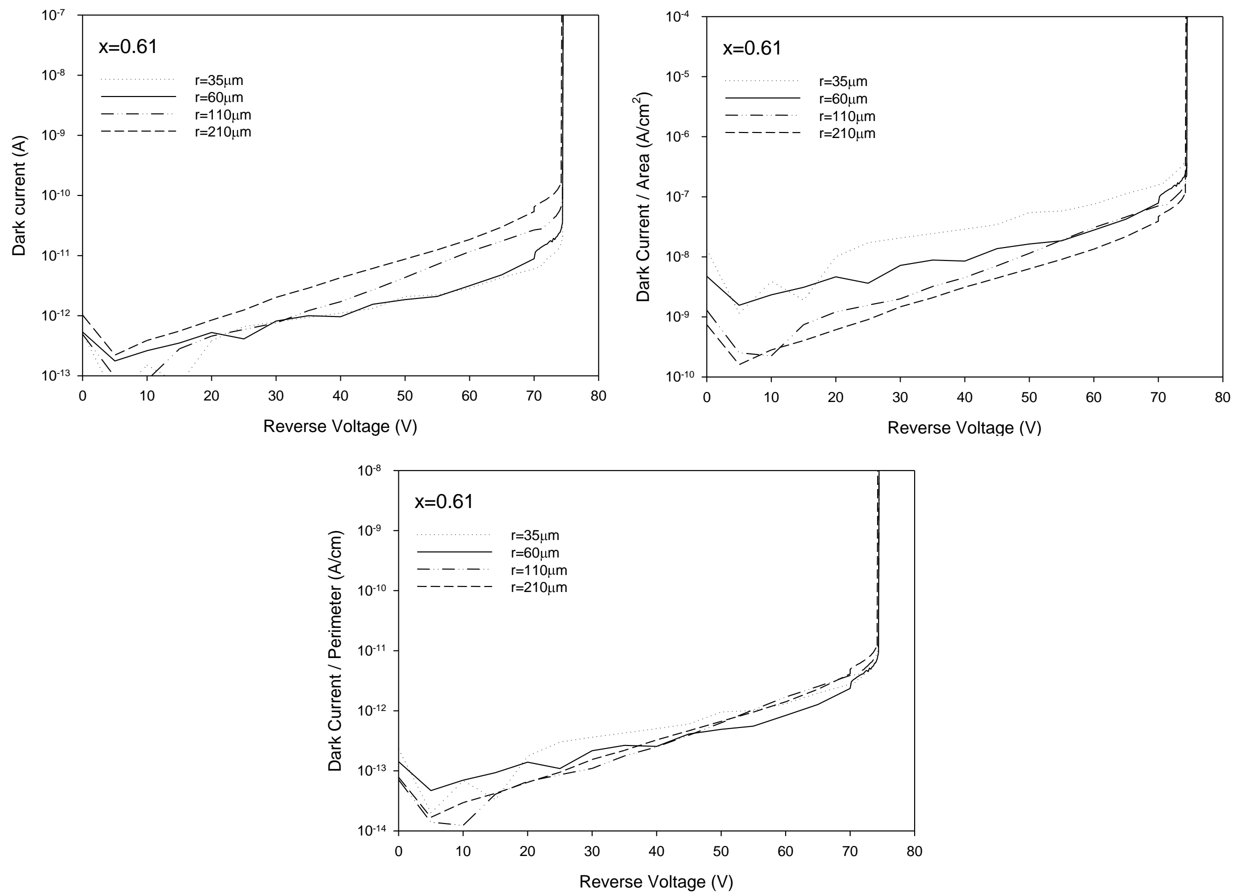

Figure 4-17 Current, Current/Area and Current/Perimeter versus reverse voltage for x=0.61. The dotted, solid, dashed-dotted, and dashed lines represent devices radius of 35µm, 60µm, 110µm, and 210µm respectively.

4.3 Capacitance-Voltage Measurement

The capacitance-voltage (C-V) measurement was performed on AlGaInP samples under a dark environment to prevent external energy applied to the junction. In reverse bias, the p-n junction builds a region filled with charges, and acts as a dielectric region. The aim of C-V measurement is to determine the depletion width and the doping concentration. Figure 4-18 shows the $\frac{Capacitance}{Area}$ measured on 60µm, 110µm, and 210µm radius devices with inset image of doping profile for respected devices. All compositions show an agreement of capacitance value despite difference in sizes, suggesting the bulk capacitance is measured instead of edge capacitance.

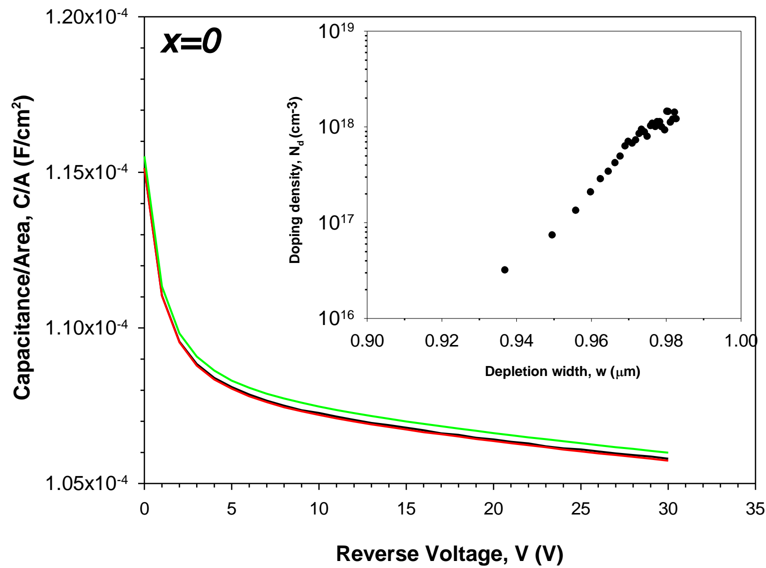

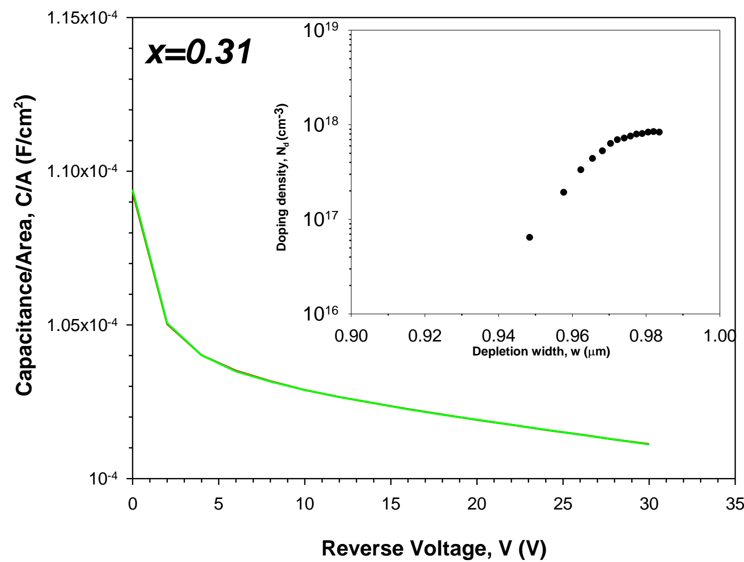

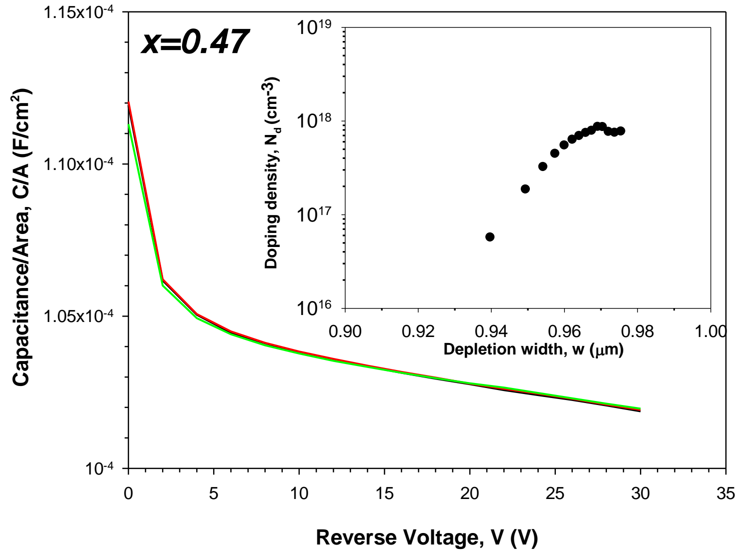
x=0.47
Capacitance/Area, C/A (F/cm^2)
Reverse Voltage, V (V)
Doping density, N_d (cm^{-3})
Depletion width, w (μm)

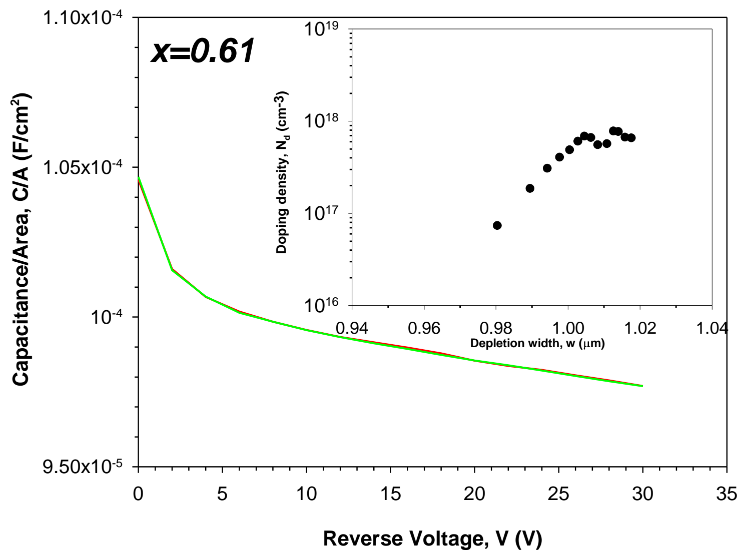
x=0.61
Capacitance/Area, C/A (F/cm^2)
Reverse Voltage, V (V)
Doping density, N_d (cm^{-3})
Depletion width, w (μm)

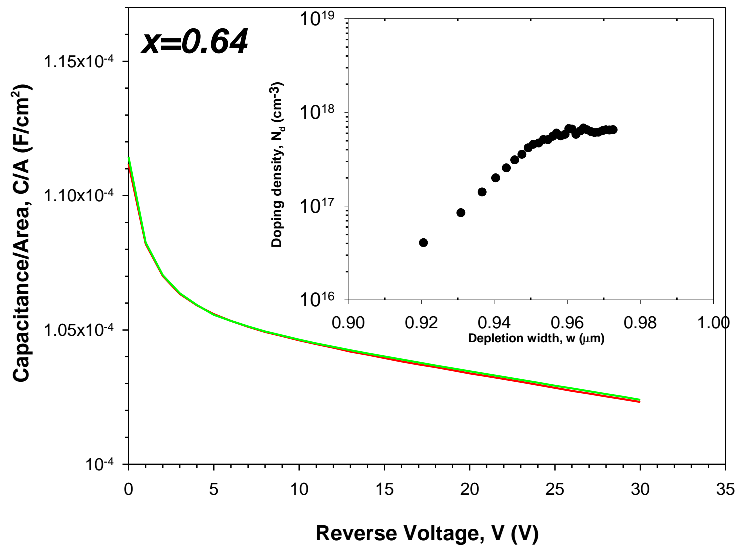
x=0.64
Capacitance/Area, C/A (F/cm^2)
Reverse Voltage, V (V)
Doping density, N_d (cm^{-3})
Depletion width, w (μm)

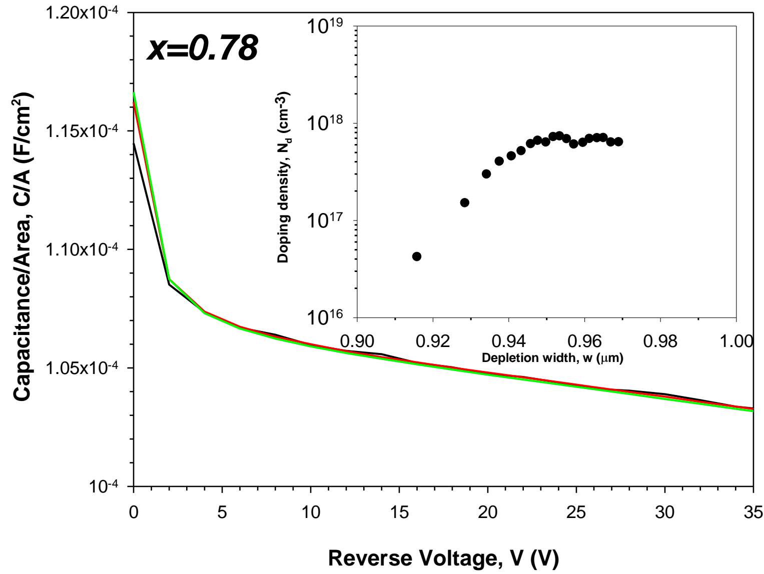

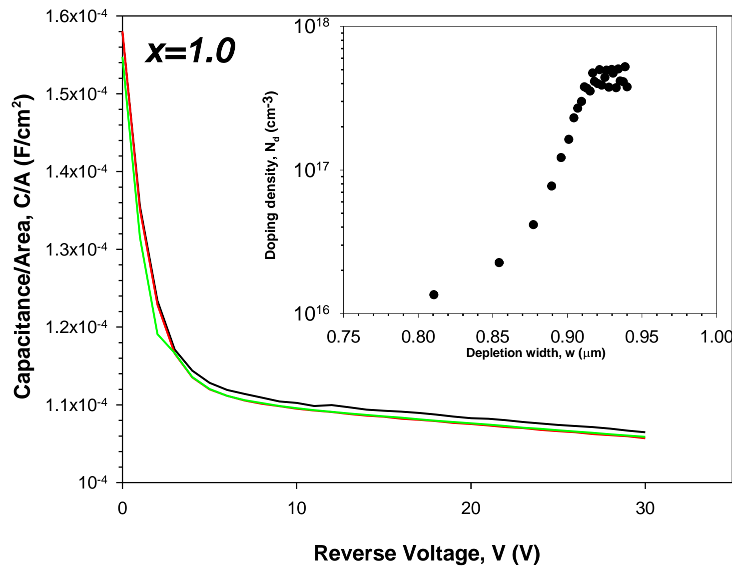

Figure 4-18 Capacitance/Area versus reverse voltage for AlGaInP with inset image of doping profile for respected composition labelled at the top left graph. Different colours of line represent the sizes of the device's radius, with black for r=60µm, red for r=110µm and green for r=210µm

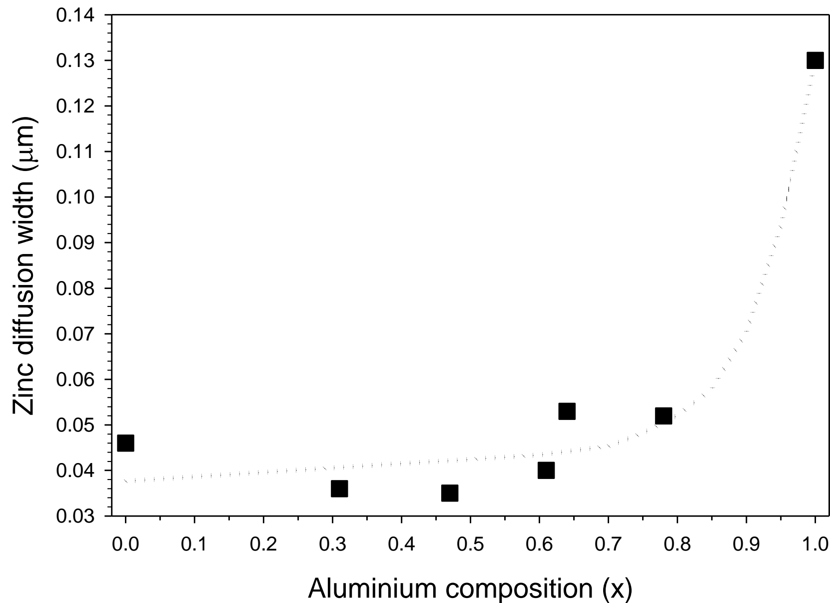

Figure 4-19 Depth of zinc diffusion through the p-type junction of AlGaInP, extracted from doping profile of each indicated material

Ideally, a doping profile should have a vertical line indicating an intended abrupt junction, opposing the depletion width movement. However, the experimental results show the evidence for zinc diffusion to extend into the low doped p-region, as plotted in Figure 4-19. The relation of zinc diffusion with aluminium content are vaguely shown but there is a big difference of diffusion depth between x=0 and x=1. The dotted-line is included, plotted manually as reference for the zinc diffusion relation with aluminium composition.

Research suggests that a Si dopant would make a very highly doped region. This causes the movement of depletion to widen to the p-type junction instead of the n-type Si doped region. Zinc, which is knowns as a vigorous diffuser material, is commonly used as p-type dopants for III-V group materials. This complicates the growth of intended doping. Studies show a slow increase of doping profile movement towards the p-type junction as the doping increases. Contrarily, some minor zinc diffusion is observed on undoped GaInP and AlGaInP material profile. The constant increase of zinc dopants will perturb the metastable lattice arrangement of group III elements. This either disrupts the bandgap of the alloy system, or increase the defects in the material[124].

Based on Poisson equation discussed in Chapter 2 and the dielectric constant value interpolated between GaInP[125] and AlInP[126], the depletion thickness of i-region and doping concentration of the cladding thickness can be registered as in Table 4-1.

Table 4-1 The parameters extracted from C-V measurement for AlGaInP photodiode.

Aluminium composition (*x*)	Dielectric constant	p^+ doping level ($x10^{17}cm^{-3}$)	i-region doping level ($x10^{15}cm^{-3}$)	n^+ doping level ($x10^{18}cm^{-3}$)	i-region thickness (µm)
0	11.8	18	2		0.97
0.31	11.63	10	2		0.99
0.47	11.54	9	3		0.93
0.61	11.46	8	2	~2	1.00
0.64	11.45	8	2		0.96
0.78	11.37	10	2		0.94
1.0	11.25	3.5	3		0.96

The results extracted from C-V measurement show the doping concentration reduce as aluminium composition increases. However, the deviation from the trends for x=0.78 could be caused by high tensile strain and cross-hatching strain relaxation shown in Chapter 3, Figure 3-3. The increase in temperature during growth of wafers could also increase the doping concentration. It is however not applicable in this case as the temperature growth is maintained throughout the composition at 660°C.

The doping density of GaInP compared to AlInP, show a one order of magnitude higher in number of holes' concentration in p^+ region. Ohba et al. in his study of the same material, shows the zinc solubility reaches its maximum at $5 \times 10^{18} cm^{-3}$ for x=0, and decreases to $5 \times 10^{17} cm^{-3}$ for x=1[127]. It is a challenge to maintain high doping in high aluminium composition due to presence of oxygen contamination during the growth process. The oxygen-related defects may reduce the quality of wafer and consequently lessen the devices' efficiency[128].

4.4 Summary

Chapter 4 comprises of I-V and C-V measurements at room temperature for all seven compositions. Starting with forward I-V measurement, the current scaled with area is first shown before further analysis on 110µm devices are done. The series resistance dominated at very high voltage region, thus stopping further increases of the dark current. The comparison of open circuit voltage at 10 mA/cm^2 is shown with other published data for solar cell application. Devices under this study performed reasonably well, where the AlInP shows the largest V_{OC} of 1.6V while GaInP V_{OC} is 1.3V. The J_0 of devices are 100 times higher than the theoretical calculation, however still lies in the same range as in Si and InP published results. The ideality factor of 1.8 is shown to fit the intermediate voltage region of experimental data for all compositions. The reverse current voltage characteristics are stable and maintained at about ≤1.5µ Acm^{-2} before breakdown voltage. The capacitance-voltage for each device are shown together with their doping profiles. Most of the devices have their depletion width close to nominal thicknesses of ~1µm.

Chapter 5 Absorption Coefficient

The absorption coefficient is a material property constant that varies with wavelength and energy of the incident photons, composition of the semiconductor material and operating temperature. The knowledge of absorption coefficient can be used in optimising device performance by calculating the efficiency of the conversion of photon to photocurrent for various applications mentioned in Chapter 1. Many studies have shown different ways to analyse the absorption coefficient including the well known spectroscopic ellipsometry, transmission and photocurrent method as described in Chapter 2. In this thesis, the photocurrent method is used, as it can deliver an accurate figure of absorption coefficient in wavelength range of interest.

Figure 5-1 shows the flow chart that summarises the steps involved in extracting the absorption coefficient of any material, provided the growth material and structure is properly known.

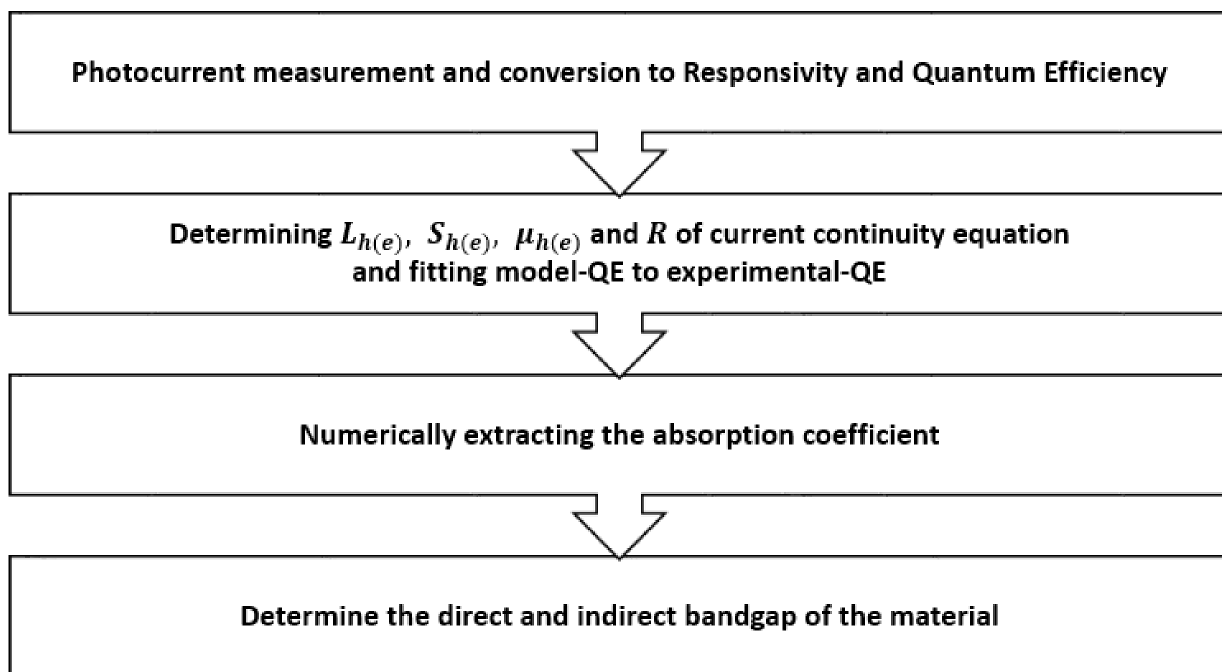

Figure 5-1 Steps involved in extracting the absorption coefficient

5.1 AlGaInP Spectral Response

5.1.1 Photocurrent

Photocurrent measurement is the first step in modelling the absorption coefficient of the respected devices. With a proper measurement setup, a spectrum of a device from a peak to about 3 orders of magnitude below can be measured provided the device has a very low dark current value. The measurement was carried out on a bigger device area with a mesa radius of 210µm and with the GaAs cap removed. 0V applied voltage was maintained throughout the measurement, and repeated for all seven compositions.

The unpassivated devices are used for optical characterisation in this chapter, to avoid any light reflection or any other effect due to the passivation that may affect the accuracy of the photocurrent measurement. Both passivated and unpassivated samples show very similar photocurrent from 450nm onwards, as shown in Figure 5-2. However, there is an enhanced short wavelength response on the unpassivated sample, whereas the short wavelength gets more strongly absorbed by the passivation sample. This difference is very minimal to be differentiated on the absorption coefficient analysis later.

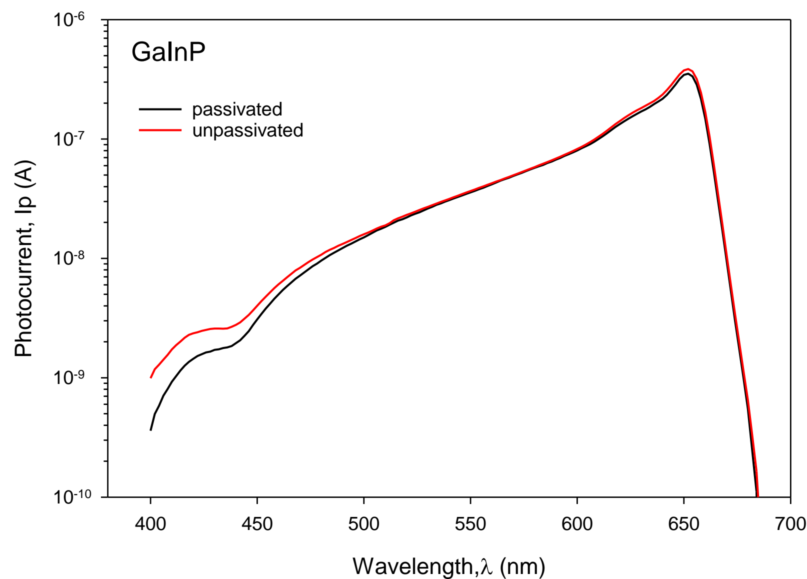

Figure 5-2 Passivated and unpassivated devices photocurrent of GaInP

The light passing through a monochromator was illuminated on a device and the photocurrent was then measured by lock-in amplifier (LIA). Referring to Equation 3.5 with the appropriate range of voltage sensitivity, a full scale of signal reading was obtained from the LIA. Different voltage sensitivity of LIA's were used in order to extract an accurate spectrum. Thus, multiple LIA scans were done on a material and a typical reading is shown in Figure 5-3.

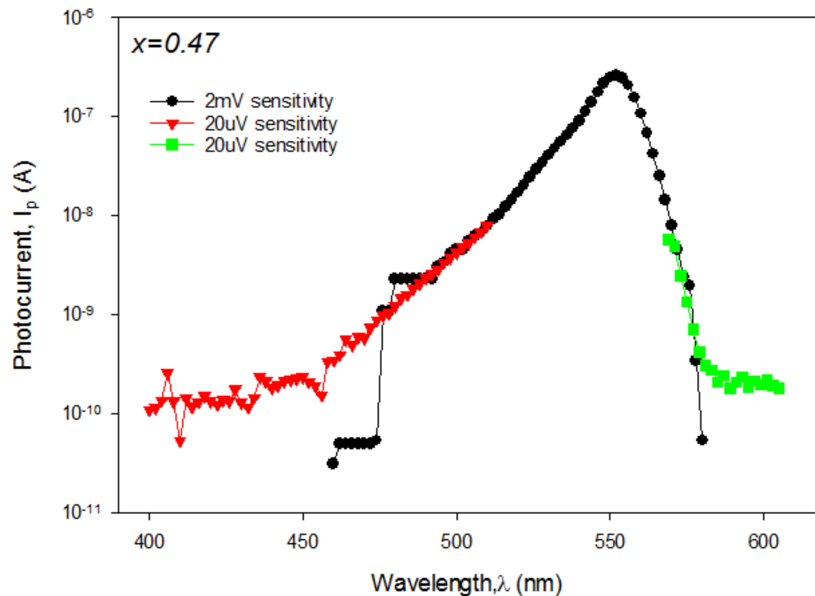

Figure 5-3 Photocurrent of x=0.47 by different sensitivity value of Lock-in Amplifier

For x=0.47 device, a full range scan was done initially using a standard setting of 2mV sensitivity, which yields a reliable spectrum from the peak to a two magnitude below it. However, it provides a false cut-off wavelength where in this scan, it cuts off at 470nm and 580nm. Other scans with higher sensitivity of 20µV were repeated as shown in red and green lines. The measurement was run until the photocurrent reaches the flat curve where the noise floor started to limit the measurement. Results of different sensitivities were overlapped at the wavelength where the photocurrent of different scans are at the same value. For this material, the overlapping scans between high and low sensitivity can be concluded to have a reliable reading from 460nm to 590nm.

The short cut-off wavelength at 460nm is due to very large α which generated more carriers at the surface. In such cases, the photon-generated carriers are less likely to diffuse to high electric field region and there were losses due to surface recombination. On the other hand, the longer cut-off wavelength at 590nm, the α value is too small to generate a practical amount of carriers[68].

Photocurrent measurement as a function of reverse bias was also carried out to observe peak photocurrent changes from 0V to -20V shown in Figure 5-4. For GaInP, a reduction of 5% on C-V measurement from 0V to -2V should give an expected increase of photocurrent by 5%. However, the peak photocurrent for GaInP start to decrease at higher reverse voltage and increase in long wavelength region, due to electroabsorption effect called Franz-Keldysh (FK)[68].

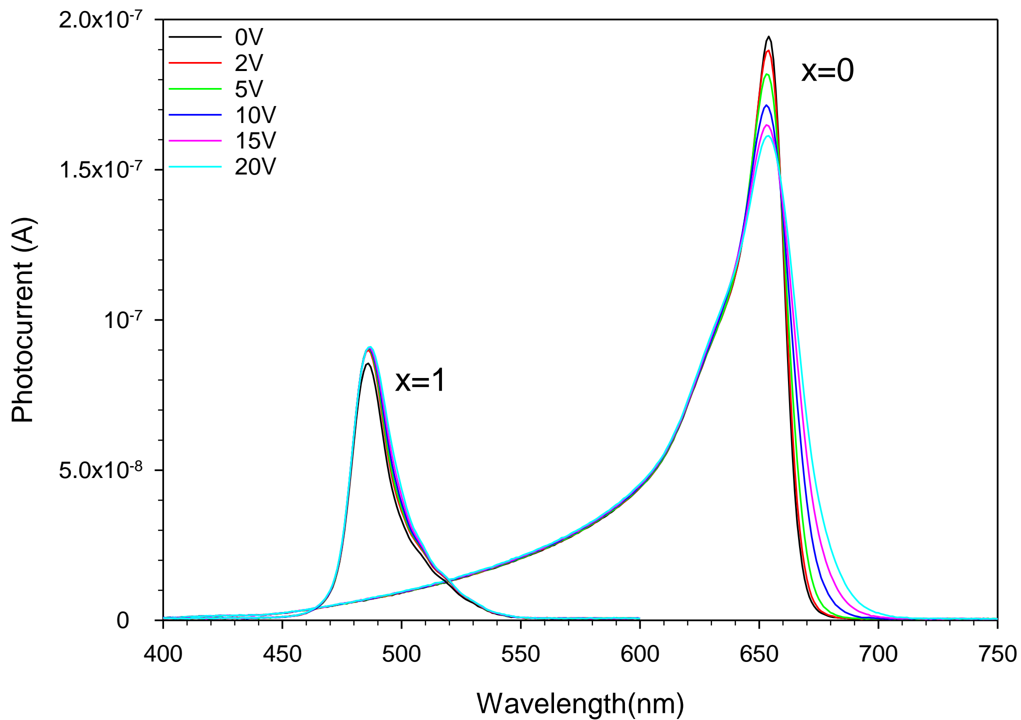

Figure 5-4 Photocurrent of GaInP and AlInP as a function of reverse bias

The FK effect is more prominent near the band edge region in bulk semiconductor and in high doping cladding layers. With the presence of electric field, the tunnelling of electron and hole wave function leaks to forbidden band gap, and overlap each other. This causes strong optical absorption even at energy lower than the bandgap. As reverse voltage increases, the FK effect affects the long wavelength for GaInP more compared to AlInP. This relates to uncomplicated process of recombination of carriers in direct bandgap material compared to indirect material.

Nevertheless, all further measurement was taken at 0V for all compositions, thus the FK effect towards photocurrent are presumed to be negligible. The same method of measuring the full spectrum is applied to other compositions and plotted in Figure 5-5.

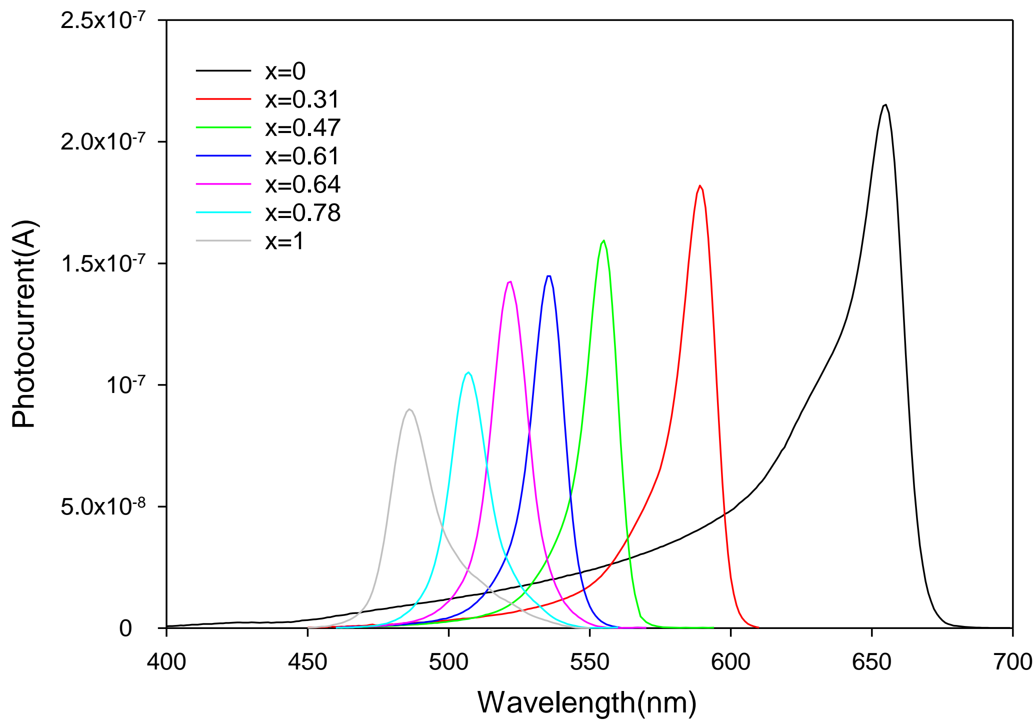

Figure 5-5 Photocurrent of AlGaInP measured at 0V

5.1.2 Responsivity

The intensity of photocurrent measured is correlated to the intensity of the light source, that governed by the black body radiation. The 100W tungsten bulb was chosen as a light source for this measurement, as it comes with enough intensity and broad spectrum that covers the whole wavelength of interest.

A commercial Si photodiode, Hamamatsu S5973-02[104] model was used as a reference diode to extract the optical power density per unit area (P_{opt}) from the light source. Figure 5-6 shows the photocurrent from 400nm to 700nm, measured on the Si photodiode which is 400µm in diameter. Subsequently, the P_{opt} is calculated from $Res = \frac{I_{ph}}{P_{opt}}$, by using the provided value of Si responsivity (Res). By assuming the light output is uniformly absorbed, the power of the Si was then scaled to the AlGaInP devices. Since the AlGaInP devices area is partly covered by gold metal contact, the optical window area is only 78% of the total area.

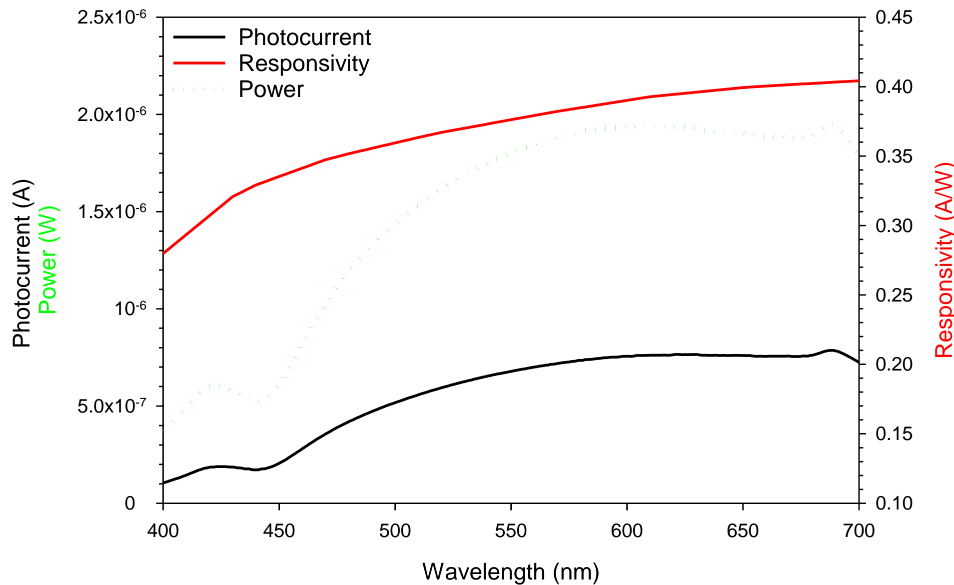

Figure 5-6 Photocurrent, Responsivity[104] and Optical Power of Si Photodiode

The ability of the light source to maintain the power output after prolong use was also recorded. After 30 minutes, the light source power output recorded shows only 1% decrease in initial power. After 90 minutes, only 4% of decrease in power was observed, indicating a stable power output. To gain confidence in responsivity data where it should be independent of sizes and intensity of power sources, two other measurements were carried out as shown in Figure 5-7.

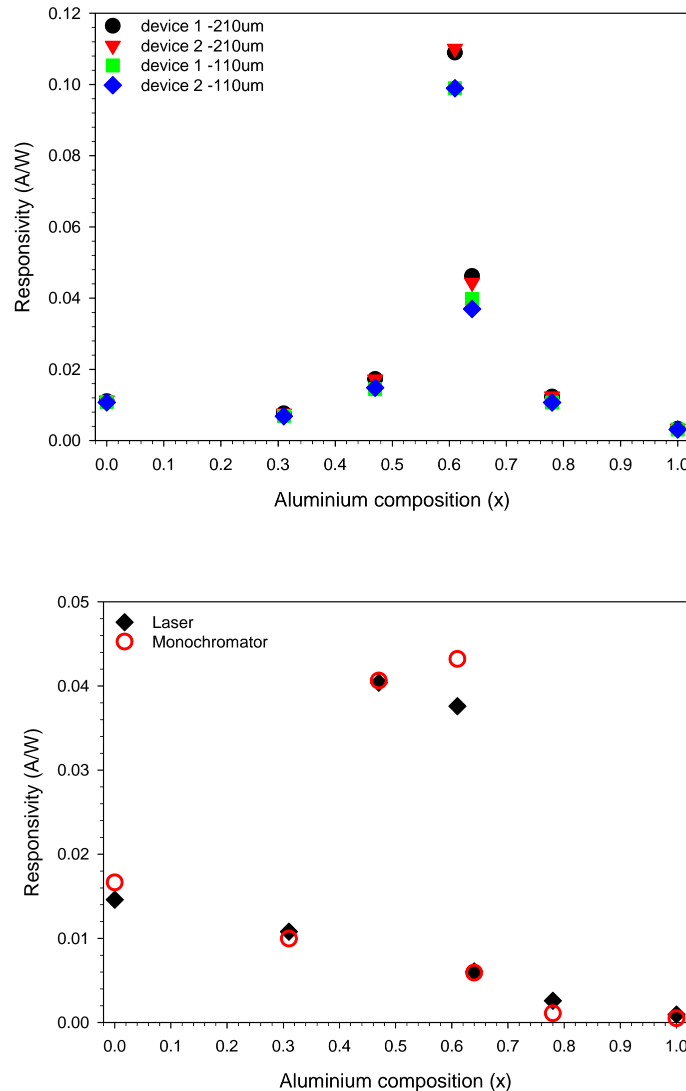

Figure 5-7 Responsivity for different devices sizes (top graph) measured with 532nm-Laser, and Responsivity comparison between 543nm-Laser and 543nm-Monochromator (bottom graph)

The first measurement is the responsivity at 532nm by double-frequency laser measured on 210µm and 110µm radius devices. The laser spot of 20µm in diameter size is focused onto the middle of the optical window so all light is collected by the devices. The power of the laser spot is measured using a power meter. Observing where 532nm locates in Figure 5-8, the uniformity in Res data of various sizes devices only occurred for compositions that have Res<0.02 A/W. There might be discrepancies in low value of Res, but it is too small to be distinguished. In an event of unfocused laser, or laser being block by probe tips, dirt or shadows, underestimation of Res value could be recorded. This could be the reason in inconsistency results of x=0.61 and 0.64 for various sizes devices. Similarly, the same observation can be seen on x=0.61 when measured using a 543nm He-Ne laser. For x=0.61, the discrepancies between 543nm monochromator and laser could be contributed by light collected around the mesa edge.

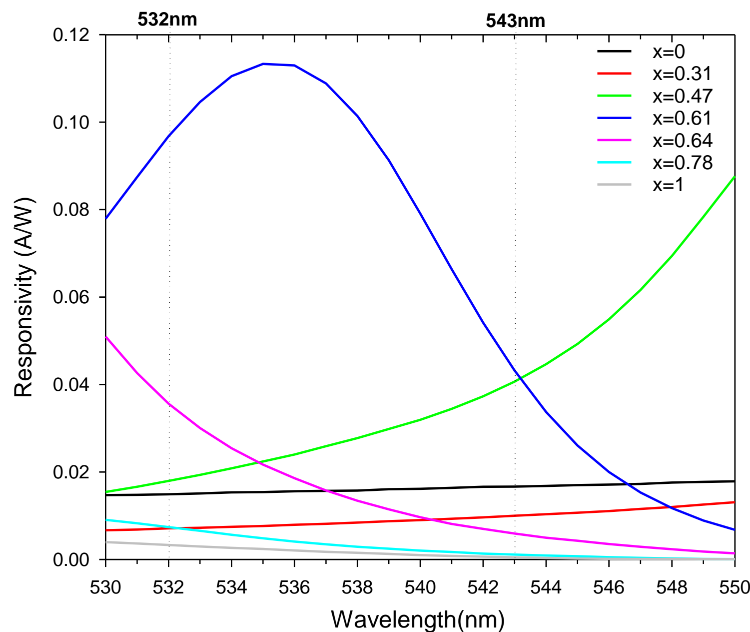

Figure 5-8 Responsivity spectrum emphasising the 532nm and 543nm

5.1.3 Quantum Efficiency

Quantum efficiency can be defined as how much carriers produce as an output per number of photons absorb as the input. The ideal diode should have unity quantum efficiency. However, real conditions where many events of carrier losses, reflection, recombination and defect on device can cause lesser efficiency output[68]. The quantum efficiency can be calculated from responsivity data by $QE = \left[Res \times \left(\frac{1240}{\lambda}\right)\right] \times 100$. The QE of AlGaInP p-i-n photodiodes for x=0, 0.47 and 1 are plotted in log scale for better comparison. They are shown in Figure 5-9 and the QE were calculated based on the measured photocurrent of the devices at applied voltage of 0V.

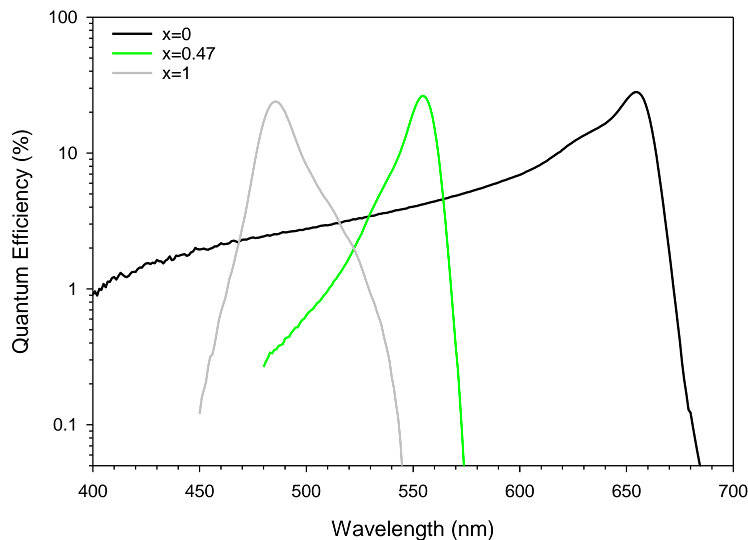

Figure 5-9 Quantum efficiency of x=0, 0.47 and 1 calculated from photocurrent

The remarkable differences between the two ends of compositions are the broadness of the spectrum where GaInP (x=0) have longer cut-off wavelength compared to AlInP (x=1) with short cut-off wavelength. The short carrier's diffusion length for aluminium-based alloy semiconductor leads to weak absorption at short wavelength and is the reason behind its narrow spectrum[88]. A carrier with longer diffusion length can also travel far before recombining, thus explain why GaInP have a broader spectrum and higher efficiency. GaInP is reported to have a direct bandgap around 1.8-1.89eV, while AlInP has indirect bandgap material with energy level of 2.2-2.3eV[129]. The composition of x=0.47 lies almost in between direct-indirect transition of x=0.48, thus the long wavelength sharp roll-off replicates the direct bandgap.

The same processes of measurement were repeated on other compositions and full spectrums are shown in Figure 5-10, both in linear and log plot. Noticeably, the spectrums are blue shifted to narrow wavelength with increasing in aluminium percentage. This corresponds to an increase in bandgap as the number of aluminium increases. However, research shows that this comes with lower electron mobility that leads to the decrease of QE which can be observed on a linear plot[38].

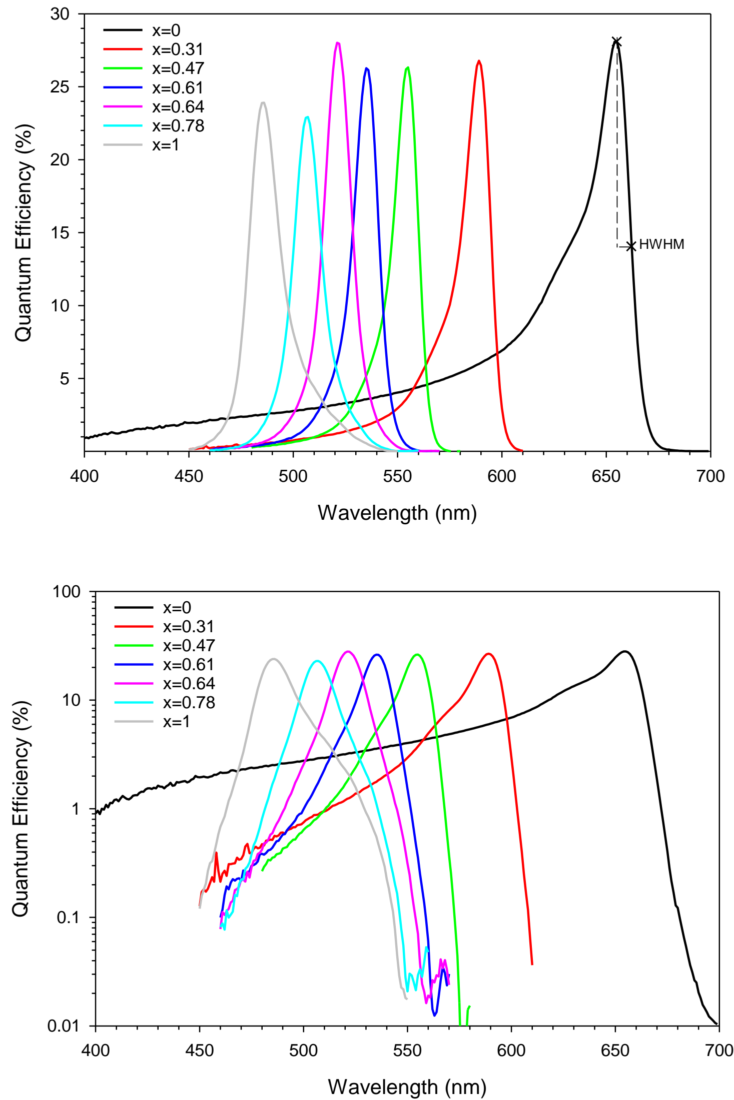

Figure 5-10 Quantum Efficiency versus wavelength plotted in linear-plot (top) and log-plot(bottom)

Table 5-1 registers the significant figures extracts from Figure 5-10. Half-width half-maximum are calculated from width of the wavelength (or energy) from peak down to half of the peak value, on the long wavelength (or lower energy) side. The key takeaways from QE plot shows increasing aluminium content will blue-shifting the peak emission and reducing the efficiencies.

Table 5-1 Parameters obtained from Quantum Efficiency analysis

Aluminium composition, x	External Quantum Efficiency (%)	Peak wavelength (nm)	Peak wavelength (eV)	Half Width Half Maximum (nm)	Half Width Half Maximum (meV)
0	28.11%	655	1.89	7	24.7
0.31	26.78%	589	2.11	6	23.3
0.47	26.19%	554	2.24	6	23.5
0.61	26.23%	535	2.32	7	28.2
0.64	27.91%	521	2.38	8	37.6
0.78	22.94%	506	2.45	8	41.5
1	21.88%	482	2.56	9	48.4

5.2 Quantum Efficiency Model

5.2.1 Parameters in Equation

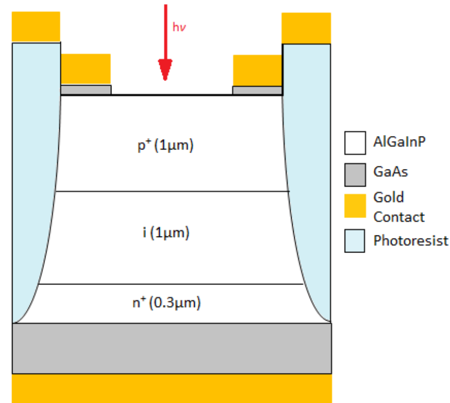

Figure 5-11 Schematic diagram of AlGaInP devices

When a light from the monochromator is illuminated on a surface of a device, the photocurrent is measured from the number of carriers collected per incident photon at each region of p^+-i-n^+ as shown in Figure 5-11. The quantum efficiency model, QE derived from current continuity equation shown in Chapter 2, then is used to extract absorption coefficient, α for each composition as in Equation 5.1[68]. The accuracy in measuring the photocurrent and also converting it to QE are the initial steps in ensuring the data accuracy of α. However, to model QE, it requires the knowledge of R, S_e, S_h, μ_e, μ_h, L_e and L_h.

$$QE = (1 - R)\left(QE_p + QE_i + QE_n\right) \quad \textbf{Equation 5.1}$$

The reflectivity, R is the number of photons reflected from the device surface and can be expressed as Equation 5.2. The refractive index, n is the real part of calculating the reflectivity while the extinction coefficient, k_e is the imaginary part. The extinction coefficient measures the loss of light due to attenuation, whereas the refractive index is defined as the speed of light travel in a material in comparison to vacuum. Both vary with wavelength, throughout the full electromagnetic spectrum.

$$R = \frac{(n_2 - n_1)^2 + {k_e}^2}{(n_2 + n_1)^2 + {k_e}^2} \quad \textbf{Equation 5.2}$$

The increase in n indicates slower speed of light travelling in material, and can be measured by the spectroscopic ellipsometry method, which is suitable for surface sensitive measurement[130]. The increase in reflectivity will reduce the absorption of light by the material. Anti-reflection coating could be applied on the top surfaces to increase the photon absorption. However, without anti-reflection coating on devices under studies, the amount of reflectivity has to be carefully considered to avoid higher photocurrent estimation which leads to inaccurate absorption coefficient. For the reflectivity at the top surface, the n and k_e studied by Kato[81] at each incident wavelength are used in absorption calculation as it covers the whole wavelength of interest, shown in Figure 5-12.

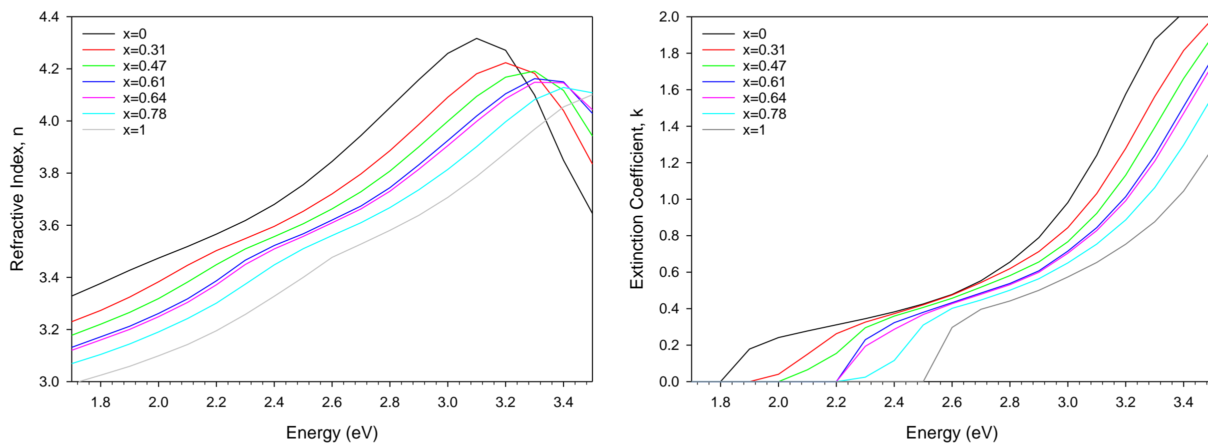

Figure 5-12 Data by Kato[81] for the refractive index, n and extinction coefficient, k_e for different aluminium composition, x as a function of photon energy

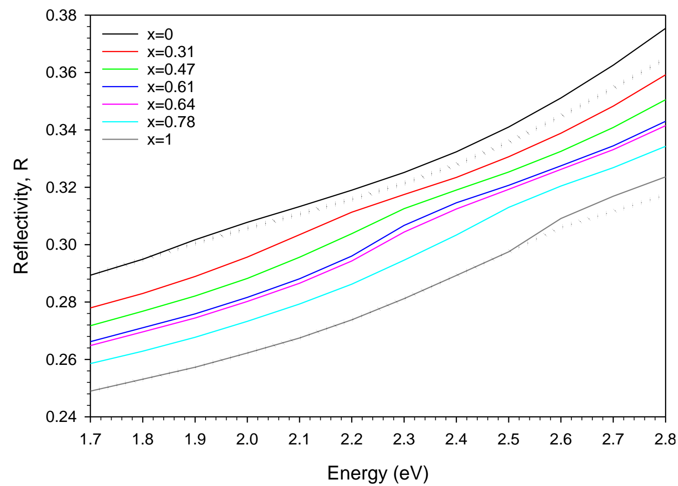

Figure 5-13 Reflectivity of AlGaInP shown in solid lines. The dotted lines shown for GaInP and AlInP are the reflectivity calculated without k_e

The significance of the extinction coefficient can be shown in Figure 5-13. The dotted lines shown for GaInP and AlInP are the reflectivity calculated without k_e, thus reducing Equation 5.2 to $R = \frac{(n_2-n_1)^2}{(n_2+n_1)^2}$. Since most measurements were taken at wavelengths of 450nm (2.75eV) and longer, the differences in the reflectivity at this wavelength are <3%, for GaInP and AlInP. **Error! Not a valid bookmark self-reference.** shows the difference of reflectivity value when the k_e is included and excluded from the reflectivity equation. Therefore, for measurements within this range, the contribution of k_e is negligible. However, when the spectrum of interest moves to the shorter wavelength region, the absence of k_e leads to an increasing underestimation of the material reflectivity.

Table 5-2 Effect of extinction coefficient, k_e on reflectivity equation for GaInP and AlInP, both measured at 2.7eV

Material	$R = \frac{(n_2-n_1)^2+{k_e}^2}{(n_2+n_1)^2+{k_e}^2}$	$R_{\not{k}} = \frac{(n_2-n_1)^2}{(n_2+n_1)^2}$	% difference
GaInP	$R = 0.3626$	$R_{\not{k}} = 0.3546$	$\frac{0.3626-0.3546}{0.3626} \times 100 = 2.2\%$
AlInP	$R = 0.3169$	$R_{\not{k}} = 0.3117$	$\frac{0.3169-0.3117}{0.3169} \times 100 = 1.64\%$

Meanwhile, the reflectivity between AlGaInP and buffer layer of GaAs can also be considered negligible as the amount of reflectivity are minimal as shown in Table 5-3. Both reflectivity amount is calculated at the band edge of absorption for respected composition.

Table 5-3 Parameters use for reflectivity calculation between AlGaInP and GaAs interface

Aluminium composition	**λ (nm)**	**n_1 (AlGaInP)** [81]	**n_2 (GaAs)** [131]	**k_e (GaAs)** [131]	**R (%)**
x=1	550	3.2	4.1	0.68	2.4
x=0	680	3.8	3.7	0.45	0.4

5.2.2 GaInP (x=0) Model Sensitivity

To begin with, the task on modelling the experimental QE is done on x=0 sample, on 210µm in radius devices. Literature shows the minority electron mobility for GaInP[132], for p⁺ region at 300K is $\mu_e = 3 \times \frac{10^2 cm}{Vs}$. The S_e and S_h are electrons and holes surface recombination velocity, and are assumed to have a large value of $S_{e(h)} > 10^{10} ms^{-1}$. The L_e and L_h are electrons and holes diffusion length before carriers recombines. The approximation value of L_e, L_h and α are varied iteratively until the perfect fit between the QE model and QE experimental are gained.

Figure 5-14 shows 10 points of fitting that are done initially across the spectrum of GaInP with thickness of each region are known by C-V measurement described in Chapter 0. With several simulations, $L_{e(h)} = 0.27\mu m$ shows the best fit to the experimental data. After an agreeable result between model and experimental is reached, the interpolation between points are made to have a full spectrum from 400nm to 700nm.

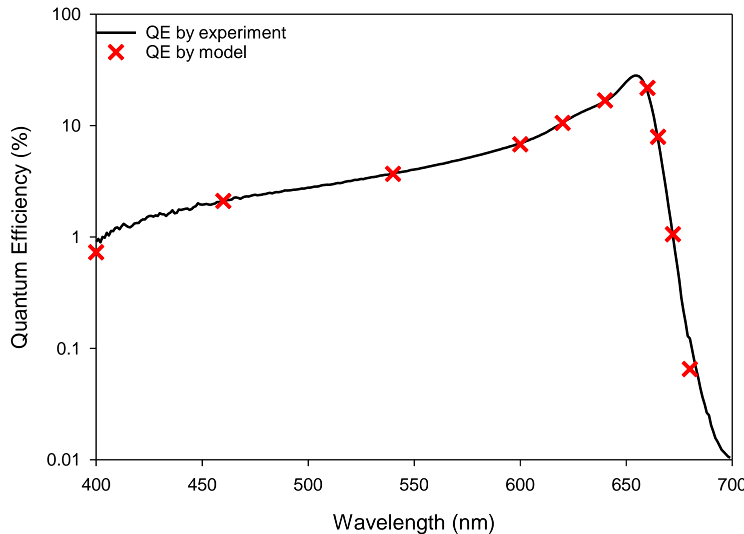

Figure 5-14 Fitting of GaInP (cross-red) to the experimental QE (black line) by approximation of L_e and α value

To evaluate the parameters chosen in deducing α, value of QE contributes by each region of p⁺, i and n⁺ have to be understood. Simulation of multiple sets of QE are run with different variable varied one at a time. The QE from p⁺ region will be influenced by minority electron diffusion length, L_e. Meanwhile, the minority holes diffusion length, L_h will influence the absorption in n⁺ region. Although some light can be absorbed in the layers below the n⁺ AlGaInP, like in the n⁺ AlGaAs and n⁺ GaAs substrate, minority holes cannot diffuse to the n⁺ region of AlGaInP, as the large valence band discontinuities act as a barrier, even at high temperatures. We can therefore ignore the contribution of carriers generated in these regions to the photocurrent that is measured.

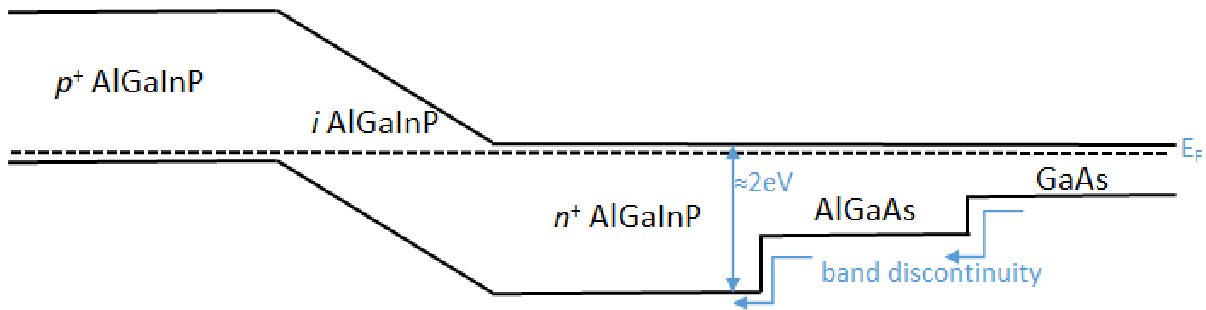

Figure 5-15 Band alignment of AlGaInP-AlGaAs-GaAs

Figure 5-16 shows the contribution of L_e that varies from 0.1 µm to 10µm towards the spectrum of QE_p, where the thickness of $x_p = 1\mu m$ and $x_n = 0.3\mu m$. When the $L_e = 0$ makes the $QE_p = 0$. The $S_e(S_h) \approx 10^{10} ms^{-1}$ and $\mu_e(\mu_h) = 10^0 m^2 V^{-1} s^{-1}$ is used for this simulation.

Longer L_e increases the QE_p in short wavelength region, while very minimal changes are seen on long wavelength sides. This explains that L_e is not a vital parameter in governing a longer wavelength absorption. The simulated results give the range of possible value of L_e, which in variation of ±5% will still emulate the experimental QE. The dotted lines in Figure 5-16 also show the contribution of the n+ photocurrent (QE_n) to the overall photocurrent with hole diffusion lengths of 0.1 µm to 10µm. The contribution of n+ photocurrent to the overall photocurrent is very small, especially at the shorter wavelengths.

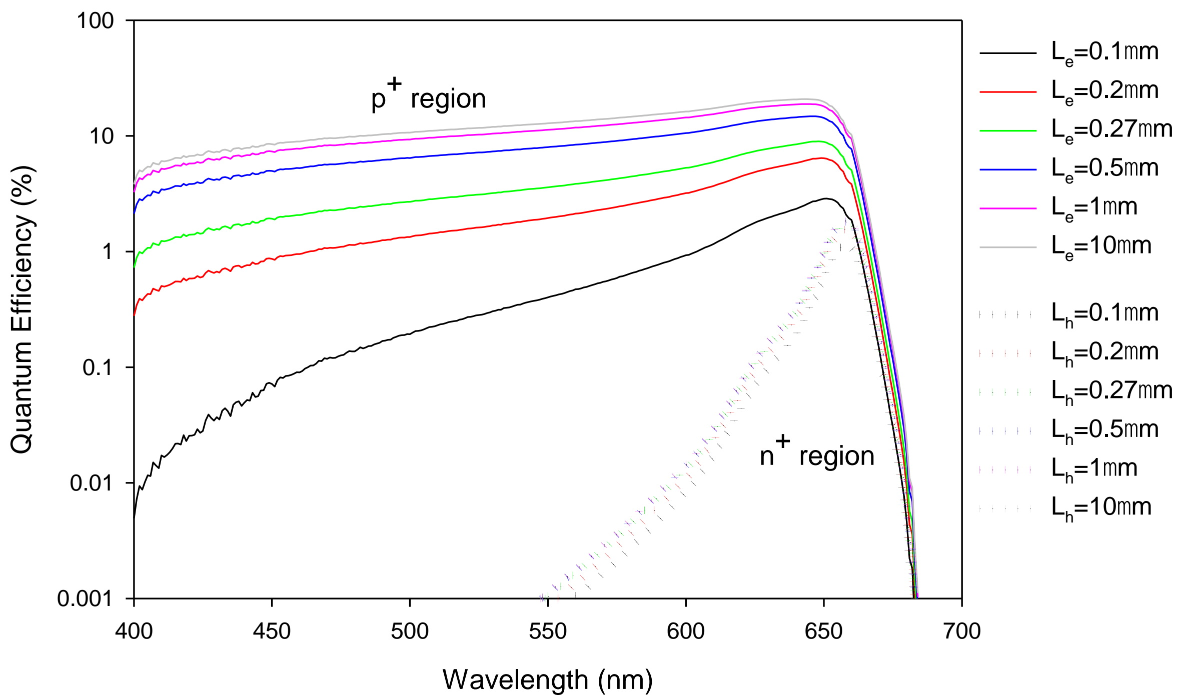

Figure 5-16 QE_p for GaInP contributes by p⁺ region (solid lines) and QE_n contributes by n⁺ region (doted-lines)

The QE_i shows an increase in spectrum broadness and efficiency with variation of i-region thickness, shown in Figure 5-17. The green line of 0.97µm represents the GaInP depletion region width, measured from the C-V measurement. Even with very narrow thickness of 0.01 µm, the efficiency from i-region still contribute significantly compared to contribution by n-region. There is a large increase in short wavelength QE with i-region thickness widening from 0.01 µm to 0.97 µm.

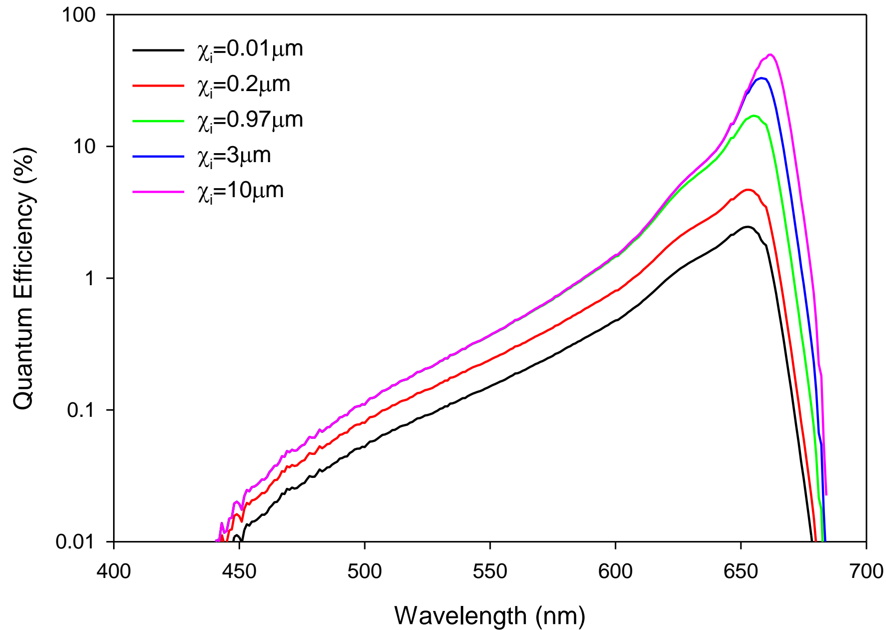

Figure 5-17 QE_i contributes by variation of i-region thickness

However, very minimal change in absorption is seen with thicknesses >0.97µm. This suggests that all photo generated carriers are able to be fully absorb within ~1µm width. Therefore, there are no advantages in increasing the i-region thickness further.

Studies by Perl portrayed a similar trend on 2eV AlGaInP solar cell[106]. The study shows the cell with 2µm thick, absorbs most of the long wavelength photons. On the other hand, increasing the cell thickness up to 3µm shows no benefits towards the QE. When the absorber region is wider than the diffusion length, carriers are unable to reach the junction to contribute to QE, and could possibly cause device degradation. Therefore, knowing the right width of absorption region is important as a small variation will lead to over or under estimation of the whole efficiency spectrum.

The sensitivity of S_e and μ_e on QE of p⁺ region is also studied, while the variations of S_h and μ_h are not demonstrated here as the contribution of it is very minimal towards the spectrum with the same trends as L_h. From Figure 5-18, the $S_e < 10^4 ms^{-1}$ gives too similar results that overlaps each other data. Meanwhile, higher S_e reduces the short wavelength QE, resulting in narrow spectrum. The $L_e = 0.27\mu m$ and $\mu_e = 10^0 m^2V^{-1}s^{-1}$ is used for this simulation.

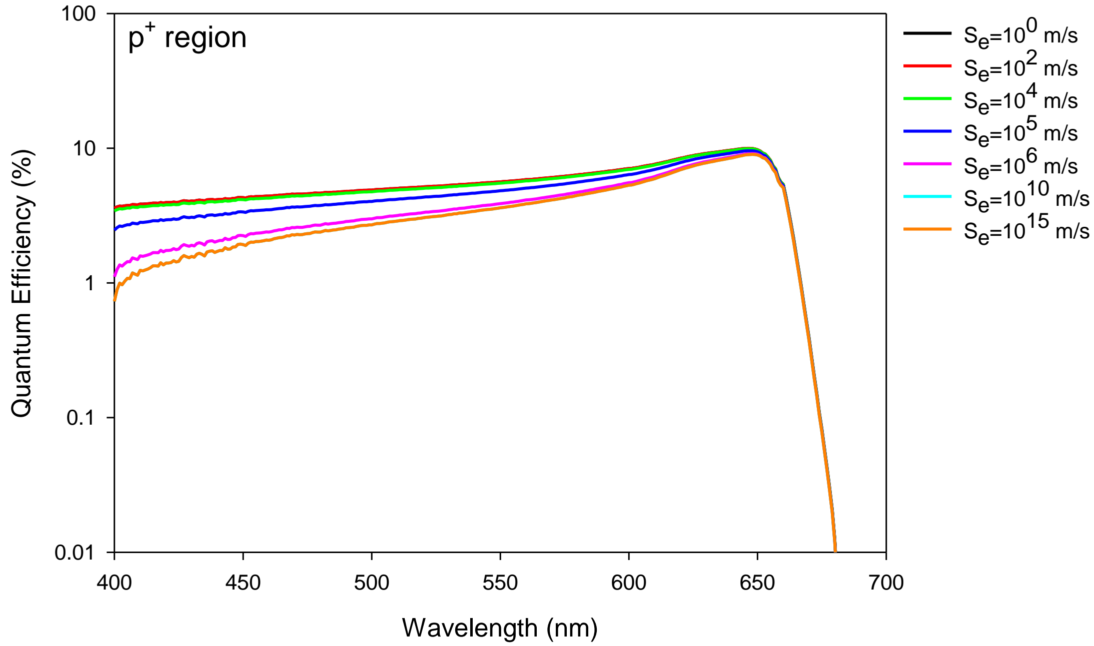

Figure 5-18 GaInP QE_p contributes by p⁺ region with variation of S_e

The surface recombination velocity of S_e and S_h vary linearly with doping density and lattice mismatch of the material, and decrease with quality of the surface preparation and treatment technique of a material[133]. High α and large S_e cause most of carriers created near the surface to be lost to deep trap recombination due to the dangling bond, instead of diffusing to the depletion width[72]. This would lead to oxidation forming on a device surface and consequently cause defect in the active region.

The μ_e is the electron speed diffusion, that measures the time taken for the carrier to reach the material. Most of III-V semiconductor are reported to have small μ_e. As summarised from literature, the μ_e for GaInP and AlInP are 0.5 and 0.1 respectively[134]. The μ_e of other materials of Si, Ge, GaAs, InP and InSb are 0.14, 0.39, 0.85, 0.54 and 7.7 $m^2V^{-1}s^{-1}$ respectively[135]. However,

from the sensitivity simulation for GaInP as shown in Figure 5-19, the variation of $\mu_e < 10^3 m^2 V^{-1} s^{-1}$ gives insignificantly change on the QE spectrum. The L_e =0.27μm and $S_e = 10^{10} ms^{-1}$ is used for the following simulation.

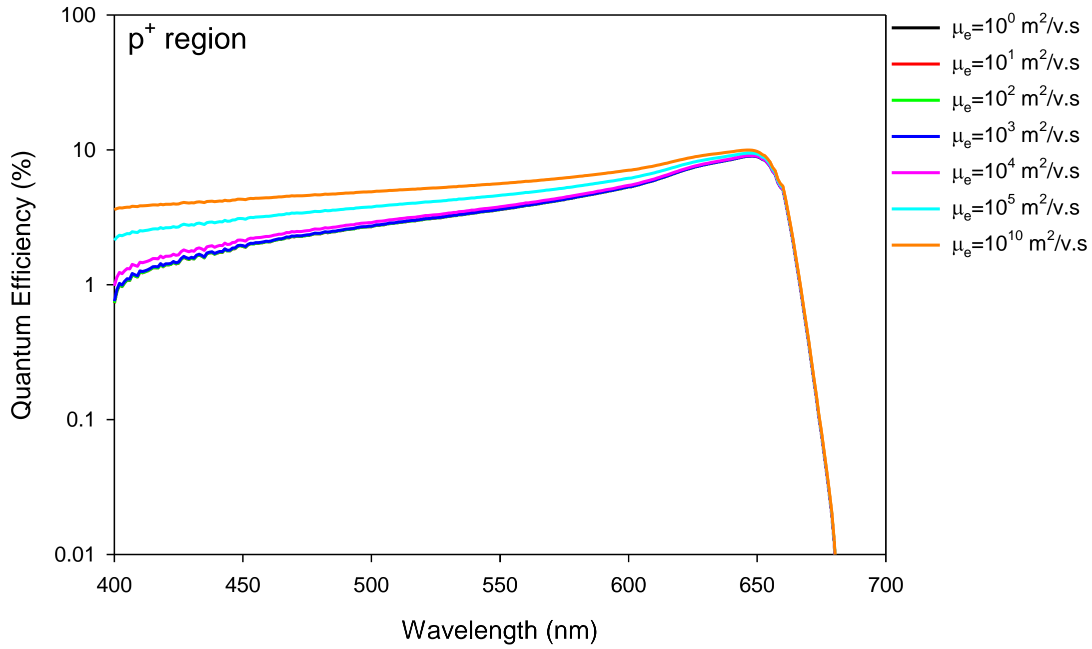

Figure 5-19 GaInP QE_p contributes by p+ region with variation of μ_e

5.2.3 AlInP (x=1) Model Sensitivity

To model the QE of AlInP of x=1, the same steps taken in modelling the experimental QE as in GaInP are repeated. Being on the extreme end of the composition, variables effects are expected to vary differently. Contrarily, most of the variables showing similar simulation effect as in GaInP, as shown in Figure 5-20. For each analysis, the variables are varied one at a time, and other parameters are kept constant. In variation of L_e and L_h, the $S_{e(h)} \approx 10^{10} ms^{-1}$ and $\mu_{e(h)} = 10^{0} m^2 V^{-1} s^{-1}$ is used for this simulation. And for simulation of S_e and μ_e, $L_e = 0.12\mu m$ is used for this simulation. $x_p = 1\mu m$, $x_i = 0.96\mu m$, and $x_n = 0.3\mu m$ are the thickness for AlInP region devices.

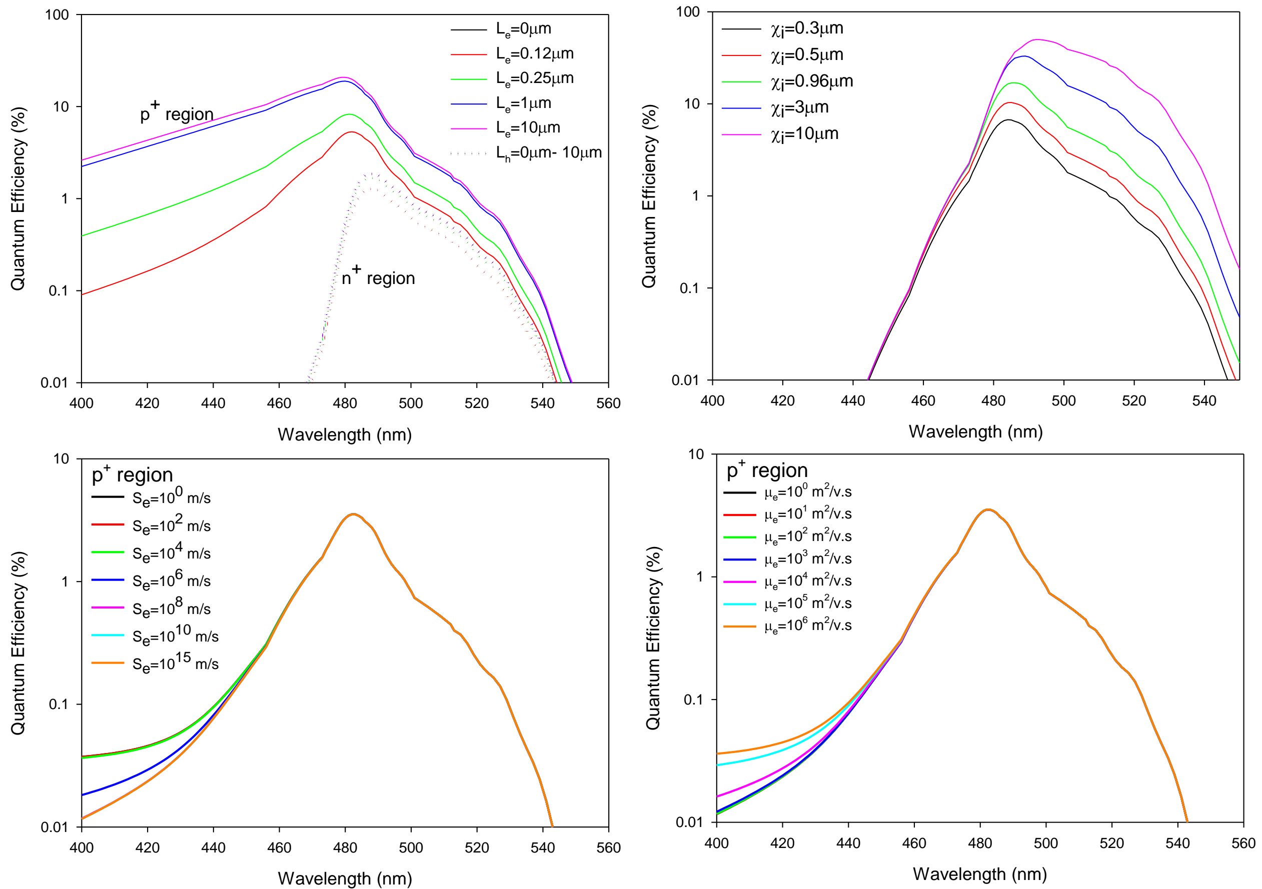

Figure 5-20 Simulation of QE for AlInP, where variables are varied one at a time

Figure 5-21 shows the QE converted from photocurrent formerly measured from (i) diffusion of minority electron carriers from p^+ to depletion region shown in black-solid line, (ii) electrons-holes pair created in depletion region shown in red solid line, and (iii) diffusion of minority holes carriers from n^+ to depletion region shown in green-solid line.

At short wavelength and high α, most carriers were created near the devices surface. Those carriers travelling from p to i region are getting lesser before reaching to n region. Furthermore, with short diffusion length, carriers created far from the depletion region are unable to contribute to photocurrent. However, at long wavelength with low α, some carriers are able to reach the n region and be collected as photocurrent. Nevertheless, it has very tiny contribution in total photocurrent, making the total of QE from p^++i $\approx$ p^++i+n^+.

This demonstrates low involvement of minority holes from n region towards total QE, and by assuming $L_e = L_h$, $S_e = S_h$, and $\mu_e = \mu_h$ for the rest of analysis is acceptable. With sensitivity measurement shown before, and discussion of variable value chosen, both x=0 and x=1 QE modelling results manage to reproduce the same QE by experiment.

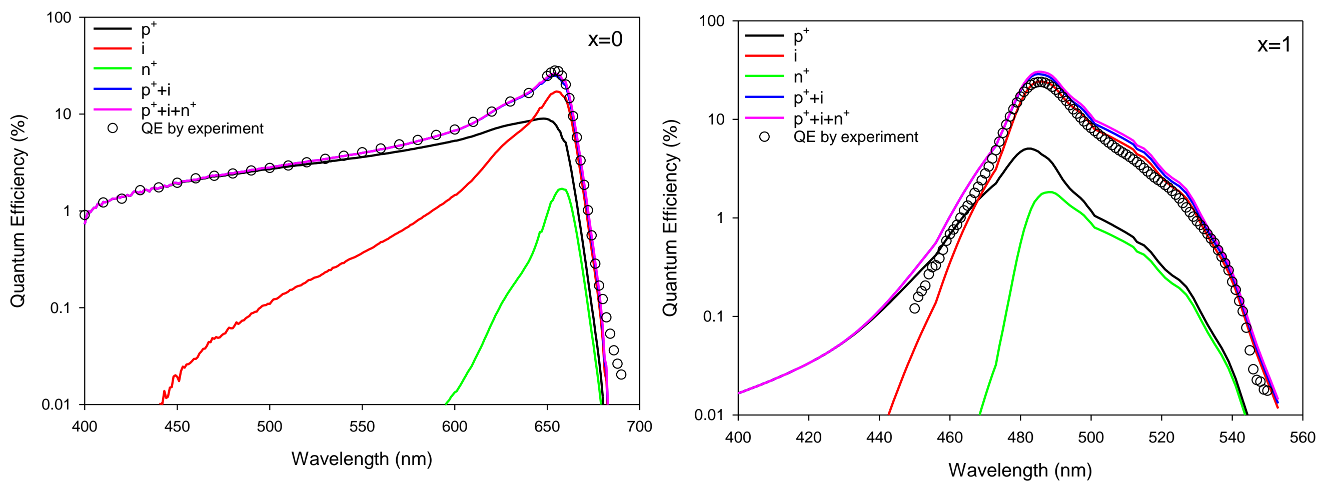

Figure 5-21 QE for GaInP (top) and AlInP (bottom) from each region of p, i, and n

The quality of the fitting of the photocurrent depends on the knowledge of the structure, the layer thicknesses, the surface recombination velocity, the reflectivity, the diffusion lengths and the absorption coefficient. The layer structure and the thicknesses are well known from growth calibrations and CV measurements. The surface reflectivity has also been calculated accurately over the wavelength range of interest. The surface recombination velocity, electron and hole diffusion lengths in the doped cladding regions, and the absorption coefficients are the only remaining unknowns. The hole diffusion length makes very little difference to the overall photocurrent measured as shown in Figure 5-16, leaving only the surface recombination velocity, electron diffusion length and the absorption coefficients as the main variables. These three alter the shape of the photocurrent that would be expected in different ways as shown by the sensitivity analysis in Figure 5-16, Figure 5-17 to Figure 5-18, consequently we can get only one set of these material parameters that will agree with the measured results.

To gain confidence in the fittings, α from literature is used in comparison to α extracted by QE model, shown in Figure 5-22. For GaInP, data by M. Schubert[136] and H. Kato[81] are plotted on the same axis, while for AlInP, data by Cheong[88] is used. Both show an agreeable result for the middle range of the spectrum, while an extrapolation has been made for the rest of the spectrum.

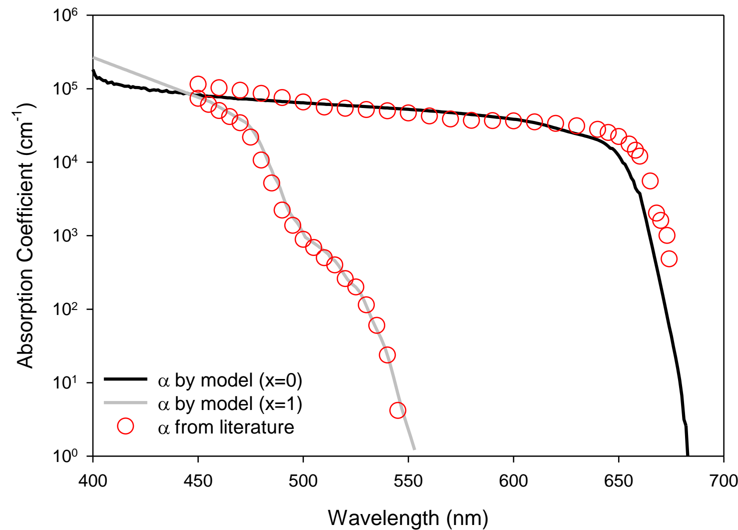

Figure 5-22 Comparison of absorption coefficient with published data for GaInP[136] and AlInP[88]

For the other compositions, the same steps taken in getting the absorption coefficient as mentioned for GaInP and AlInP are repeated. Value of $L_{h(e)}$, $S_{h(e)}$, $\mu_{h(e)}$ and R are tabulated in Table 5-4, and are used for the other composition analysis. Diffusion length however is not a constant material property, as it differs with doping densities, temperature, and band structure. AlGaInP for this study shows a small range of diffusion length that varies between 0.12µm to 0.27µm. The increase in aluminium composition is known to increase the oxygen contamination due to strong bonds of Al and O. This increases the non-radiative recombination and leads to short diffusion length that relates to lower carrier lifetime. Consequently, there will be less photon generated carriers collected, thus reducing the quantum efficiency[37].

Table 5-4 Device variables for extracting absorption coefficient for AlGaInP

Equation variables	X						
	0	0.31	0.47	0.61	0.64	0.78	1
$\boldsymbol{L_{h(e)}}$ (µm)	0.27	0.25	0.22	0.20	0.20	0.15	0.12
$\boldsymbol{S_{h(e)}}$ (m/s)	10^{10}						
$\boldsymbol{\mu_{h(e)}}$ (m^2/Vs)	10^{0}						
$\boldsymbol{R}$	from Equation 5.2 where n_r and k are from Kato[81]						

Figure 5-23 shows how diffusion length change with aluminium composition and are in the same trend as how much carriers absorbed at a peak wavelength. A similar trend is found in AlGaAs [137], where GaAs (x=0) has the longest minority carrier lifetime, which relates to diffusion length of $L_e = \sqrt{Dt_e}$. AlGaAs shows reduction in diffusion length from x=0 to 0.4, but starts to increase when the composition band structure change to indirect bandgap[138]. It is reasonable to have a long diffusion length for indirect bandgap, provided the material growth is in high quality. In a similar study, Hooft[137] shows independent effect of high and low doping towards the minority carrier lifetime. Hence, variation of doping in each region of AlGaInP will not impose a problem towards the modelling of absorption coefficient results.

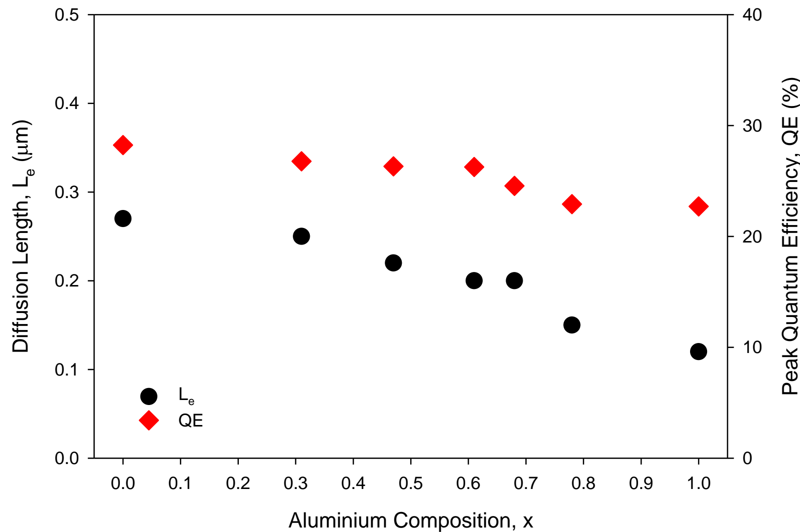

Figure 5-23 The electron diffusion length (left axis) and the peak quantum efficiency value (right axis) as a function of aluminium fraction in AlGaInP

5.3 Absorption Coefficient of AlGaInP

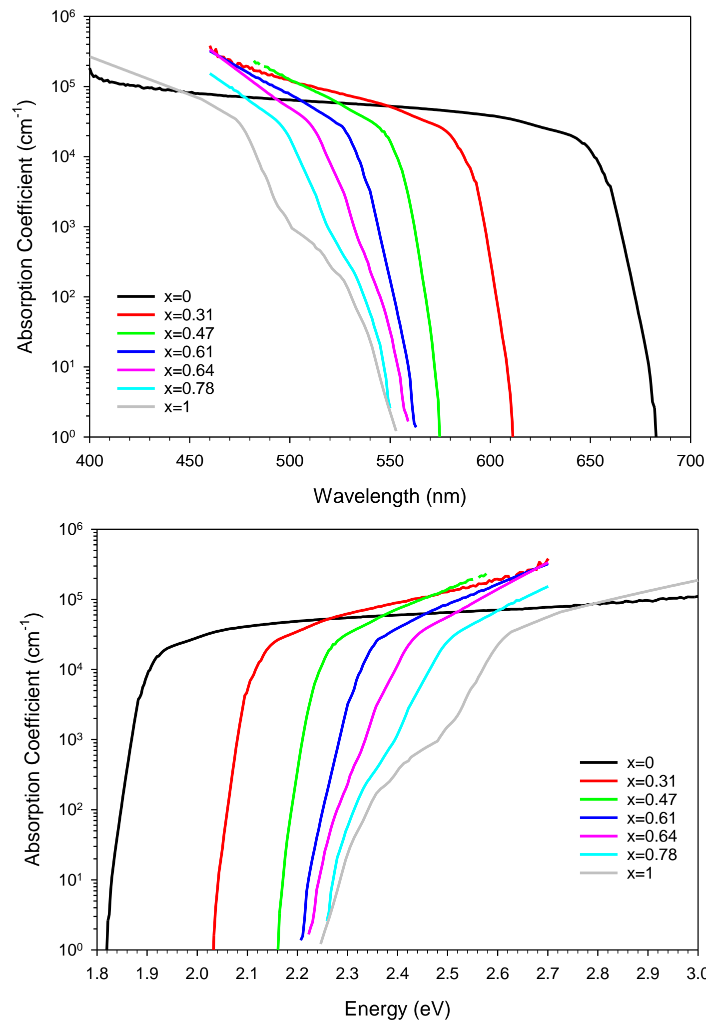

Figure 5-24 Absorption coefficients versus wavelength (top) and energy (bottom) based on QE measurement. The value of aluminium composition shown in graph are denoted as x

Figure 5-24 shows the AlGaInP absorption coefficient modelled by the QE result. The curves are blue-shifted to the shorts wavelength with increase in aluminium composition as observed in spectral response measurement. The trends of α from AlInP to GaInP are found to have steep increase from the band edge absorption region, before starting to increase gradually and saturate at shorts wavelength. The absorption below the band-edge region which is caused by Urbach tail are due to the material structure disorder and thermal disorder[139].

Figure 5-25 shows overlapping of QE and α, where the QE peak position lies at the turn-over point between low slope of α and roll-off slope towards the bandgap energy. GaInP demonstrated a smooth steep slope compared to a knee-like curve shown in AlInP. The absorption coefficient increases rapidly beyond the bandgap due to the availability of the density of states in conduction band to allow the transition of the carriers.

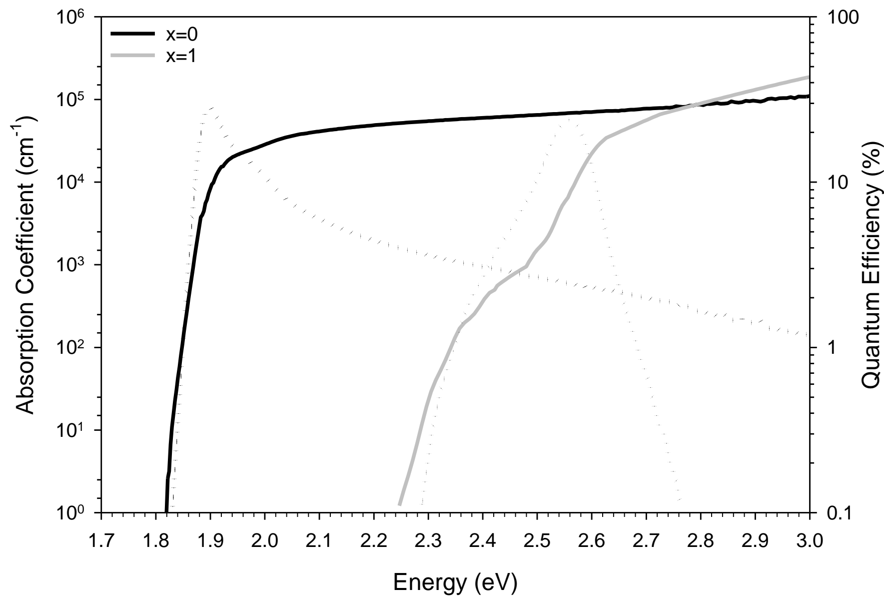

Figure 5-25 Absorption coefficients (bold-lines) versus Energy on the left-axis and Quantum Efficiency (dotted-lines) versus Energy on the right-axis.

When the absorption coefficient of other materials' are plotted together in Figure 5-26, different behaviour of various materials are shown. The orange X-symbols in Figure 5-26 signify the band gap energy for respected material. For better visualisation, materials are grouped as direct bandgap and indirect bandgap as shown in Figure 5-27. The steeper rise in α near the band edge can be seen as a common trend in direct bandgap materials.

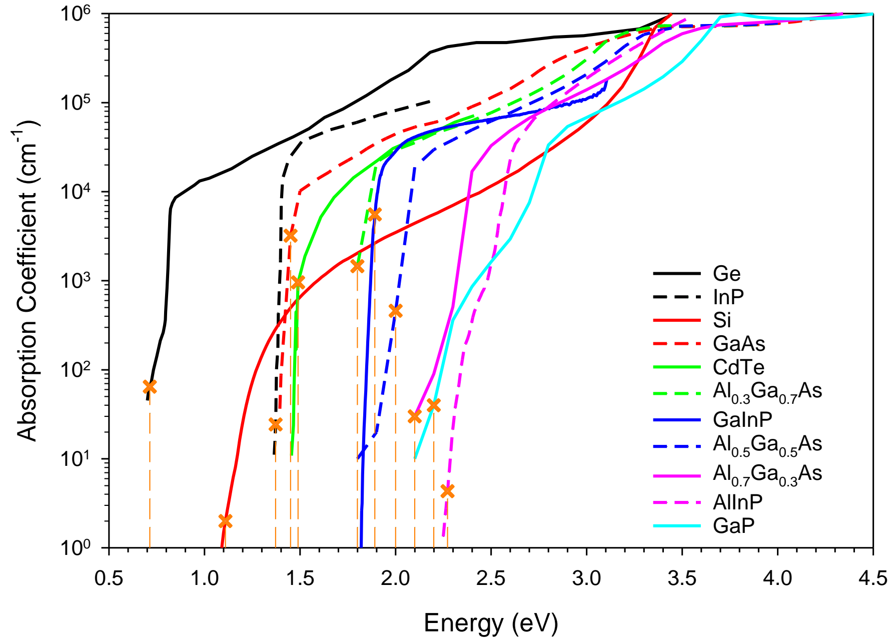

Figure 5-26 Absorption Coefficient of GaInP and AlInP from this study plotted together with other semiconductor material of Ge[140], InP[141], GaAs[141], GaP[141], Si[142], CdTe[74] and AlGaAs[143]

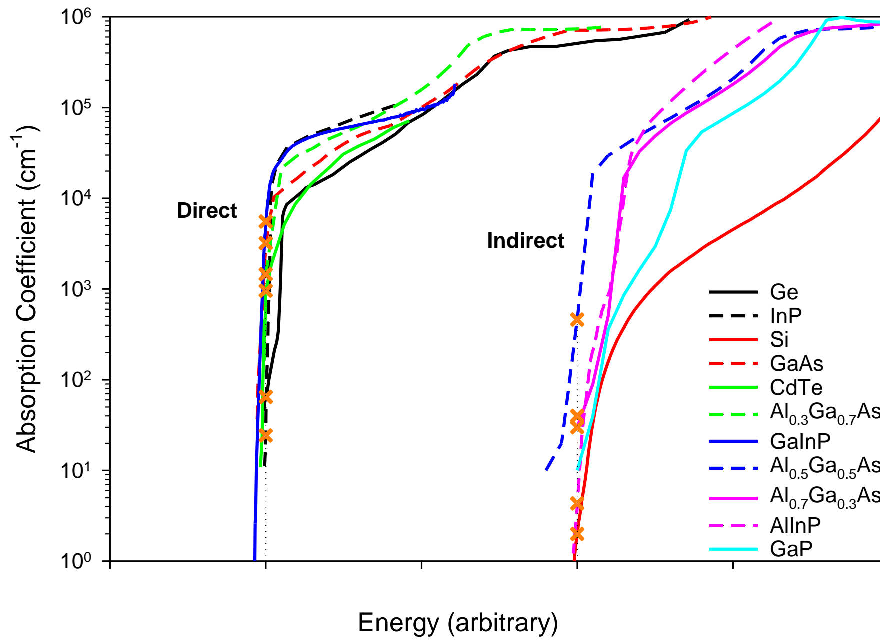

Figure 5-27 Absorption Coefficient versus Energy of semiconductor materials, separated by direct bandgap and indirect bandgap material

5.4 Bandgap Determination of AlGaInP

The bandgap of material can be referred to as the lowest energy needed to excite the electron from valence to conduction band, and the longest wavelength that is absorb by a material. An accurate knowledge of bandgap energy will be useful in applicability prediction and understanding the material optical properties. Conventionally, the estimation of band gap value from the x-intercept of α^2-E will indicate the energy value between the bottom of Γ-valley and the maximum of valence band[75]. Meanwhile, the x-intercept of $\alpha^{0.5}$- E represent the energy value between the bottom of X-valley and the maximum of valence band[75]. The narrowest valley separation energy either between valence band to Γ-valley or X-valley will characterise the band structure of the material to be either direct or indirect.

The foundation of this bandgap estimation is initially studied by Tauc on Ge and Si[144]. It is widely used since then in estimation of bulk semiconductor material. Tauc found that in energy dependant of absorption spectrum, there exist a linear photon energy (hv) dependents region with increase in energy beyond the band edge. Tauc plot however is arbitrary performed with neglection of absorption near-and-under the band edge[145].

Researchers are trying to justify and generalise Tauc plot function to overcome the grey regime in Tauc plot. Instead of one linear extrapolation towards x-intercept, Makula[146] introduced another linear abscissa just under the fundamental spectrum curve. The intersection point between those two linear lines were extrapolated to the x-axis, to get the energy gap value. Meanwhile, Ming D.[147] suggested two ways of extracting bandgap, either thru improvised Tauc plot or merging the method of Cody and Tauc plot. Both of these methods include refractive index, n as a variable dependent together with absorption coefficient data. Figure 5-28 shows the estimation of bandgap on GaInP by 4 methods described before, names as method (a)Conventional (b)two-linear plot (c)nαE-Tauc and (d) nα/E- Cody.

5.4.1 GaInP Bandgap Estimation

The bandgap,E_g recorded for each method are 1.89eV, 1.902eV, 1.85eV and 1.85eV respectively. Method (a) provides the clearest and most comprehensive way of extrapolating the direct-bandgap value through the absorption-squared relation. However, method (b) gives more confidence in E_g estimation as low-and-high slope of absorption spectrum are taken into consideration. Method (c) and (d) both show similar E_g estimation, despite having contrast of factor in the y-axis data, which are $n_r \times E$ and n_r/E respectively. The results between all methods yield a small variation of about 3% from 1.85eV to 1.902eV. This concludes that any method of E_g estimation is valid for direct bandgap material. The same analysis is done on AlInP, to observe the E_g variation on indirect bandgap material, shown in Figure 5-29.

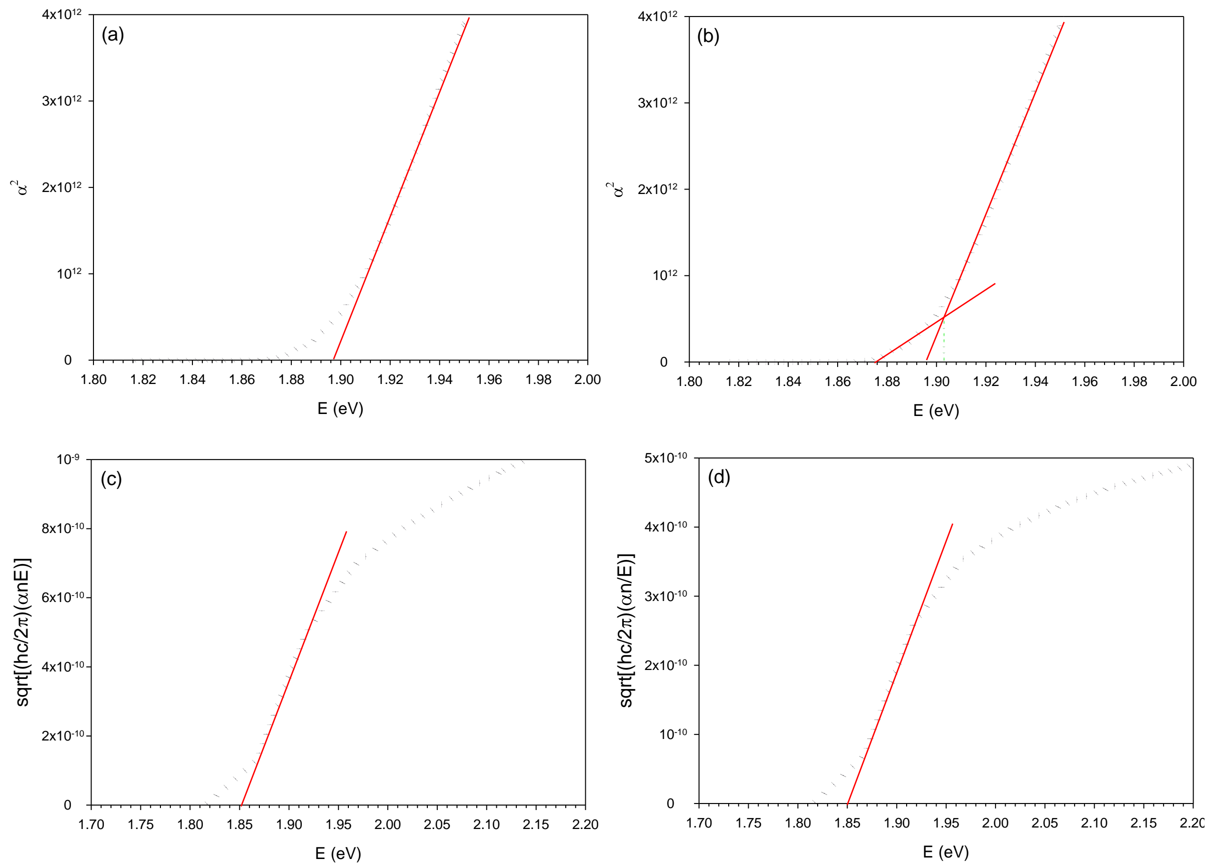

Figure 5-28 Bandgap estimation of GaInP by methods labelled as (a)Tauc (b)two-linear plot (c)n-α Tauc and (d)n-α Cody. The black-dotted line is the y-axis data that varies with Energy. The red-line are extrapolation made to x-intercept, as an estimation of bandgap value, except for Figure (b). The green dotted-line on Figure (b) represent the intersection point of two linear plots that giving out the bandgap estimation value

5.4.2 AlInP Bandgap Estimation

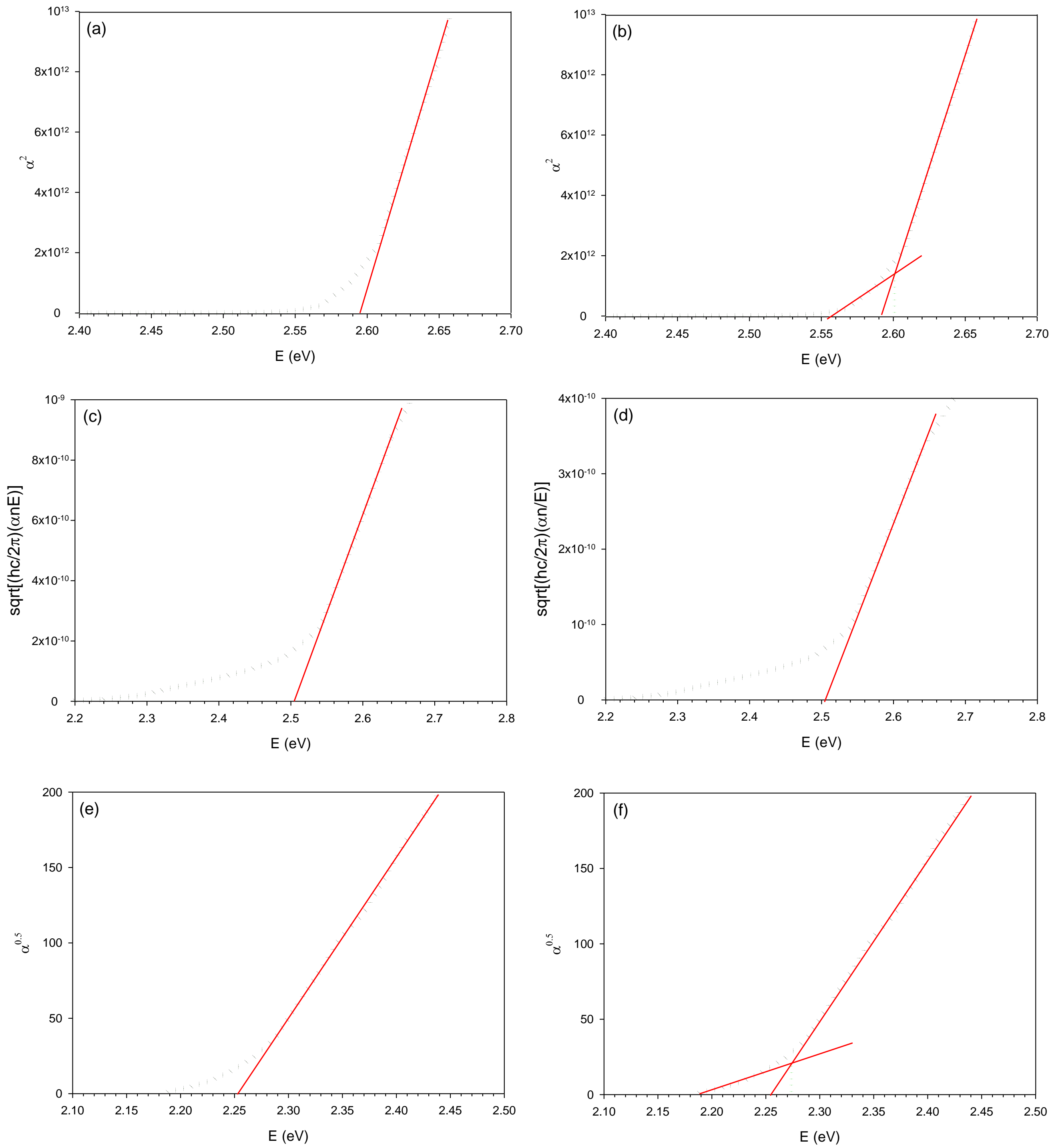

Figure 5-29 Bandgap estimation of AlInP by various method labelled as (a)Tauc (b)two-linear plot (c)n-α Tauc and (d)n-α Cody. Figure (e) and (f) using same method as (a) and (b) respectively, but with y-axis is in $\sqrt{\alpha}$ instead of α^2

Referred to Figure 5-29, the E_g estimation from Figure (a) to (d) are 2.596eV, 2.6eV, 2.5eV and 2.5eV respectively. However, Figure (e) gives E_g=2.255eV and Figure (f) gives E_g=2.275eV. This explain that method (a) to (d) can be used in estimation of Γ-valley gap. Hence, to estimate E_g of X-valley, the $\alpha^{0.5}$ versus Energy function has to be used. With narrower energy of X-valley compared to Γ-valley, the band structure for AlInP is identified as indirect bandgap material.

5.4.3 Bandgap-Aluminium Relation

Judging from the various methods of GaInP and AlInP E_g estimation, Tauc plot is found to be the simplest way of estimating the E_g. Thus, for the rest of the compositions, the E_g estimation is done by using method (a) shown in Figure 5-30 for Γ-valley, and X-valley as shown in Figure 5-31.

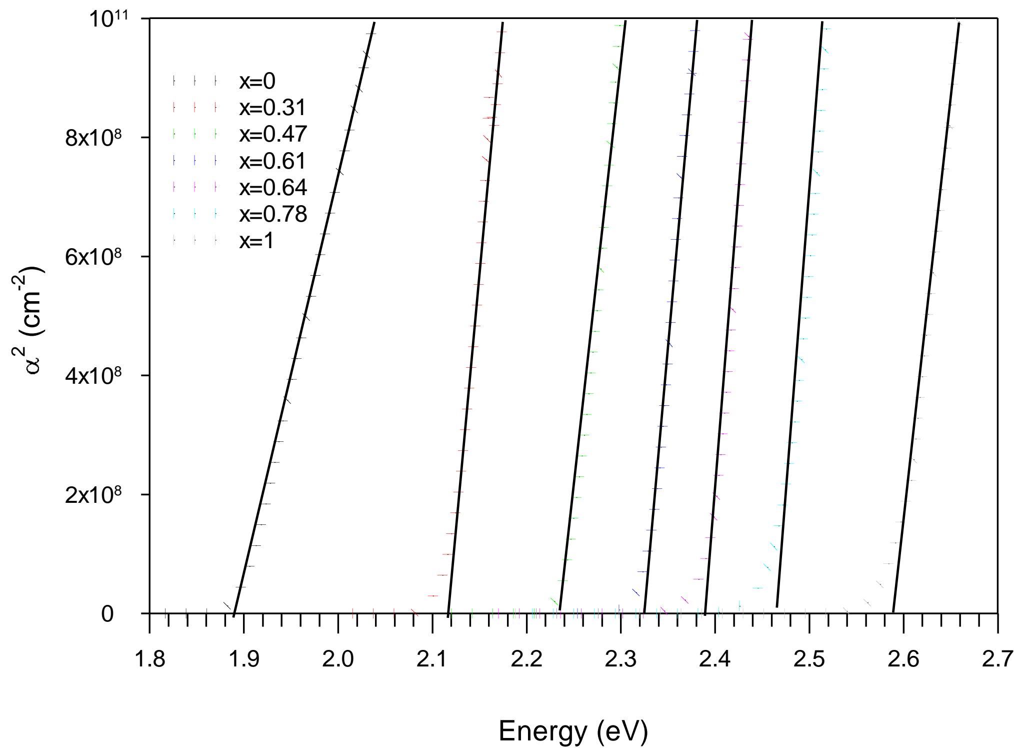

Figure 5-30 Extrapolation analysis of Γ-valley for determination of direct bandgap energy of AlGaInP

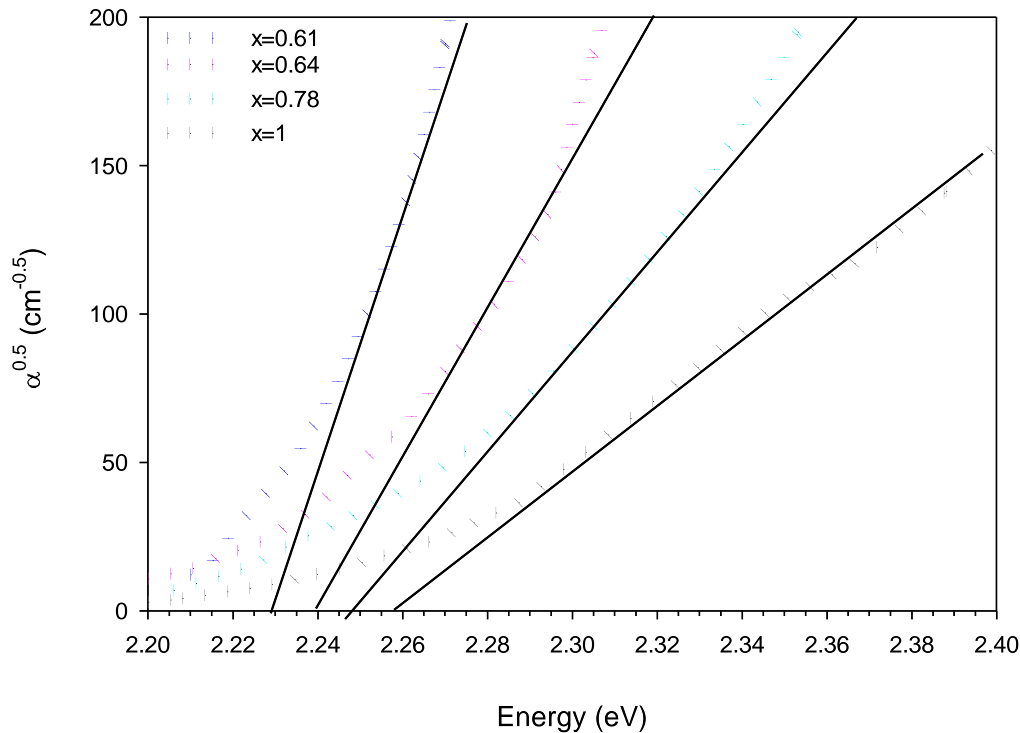

Figure 5-31 Extrapolation analysis of X-valley for determination of indirect bandgap energy of AlGaInP

At direct-indirect bandgap crossover, the minimum conduction band of Γ-valley and X-valley positioned on the same energy level, as shown in Figure 5-32 (b). When aluminium content is higher than 48%, the gap between Γ-valley maximum at valence band, and Γ-valley minimum at conduction band, becomes wider than energy gap between Γ-valley maximum at valence band, and X-valley minimum at conduction band. Thus, the E_g after x>0.48 are recognised as indirect bandgap material energy, while E_g for x<0.48 are grouped as direct bandgap material energy.

However, the mechanism that influenced the transition of directness of bandgap remain vague. Studies by Yuan suggested that the foundation of direct bandgap material is the existence of occupied cationic d orbital. The semiconductors of group I-V (except Si, Sn, C), most of group III-V (except GaP and Al-containing alloy) and all group II-VI are possessing occupied cation d bands, subsequently all the bandgaps are direct. On the other hand, either the absent of d orbital, or lack of occupied d orbital, or low-lying position of cation d bands are making the rest of material structure indirect. This theory, however, applies for x>48% in AlGaInP, but the theory behind direct bandgap material with lower aluminium composition were left unanswered[148].

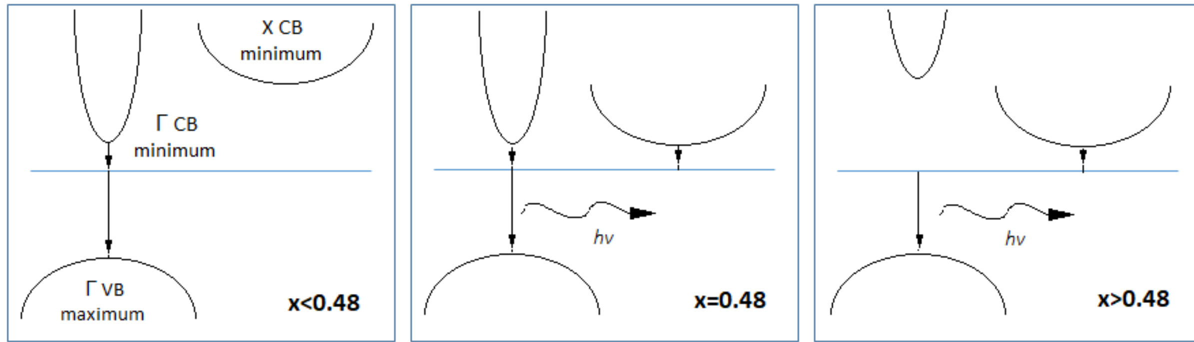

Figure 5-32 Band structure to represent x<0.48 for direct bandgap, x=0.48 for cross-over, and x>0.48 for indirect bandgap

Beaton in his studies of AlInP material suggested that the material ordering is strongly affected by CuPt effect during growth. This effect lowers the Γ-valley conduction band edge, but leaves the X-valley unaffected.[149] Due to difference in atomic sizes and arrangement between the atom and its neighbouring atom, material with lower aluminium compositions is known to have a long-range order. These repetitive atoms positioned in a crystal structure creates well-defined valence and conduction band. Increase in aluminium atoms however, perturbed the arrangement between atoms in the lattice and thus the short-range order existed, as in Si. This extends the wave function to other directions, causing asymmetry of valence and conduction band, leading to indirect bandgap structure.

The extracted bandgap energy from absorption coefficient data is summarised in Figure 5-33. The influence of Al and Ga composition in AlGaInP shows the bandgap bowing from direct to indirect structure at x=0.48. The results are compared to Mowbray[129] and Donati[150], where 4K data are converted to 300K by reducing 80meV from the photon energy. All results portrayed a fair agreement, with a similar crossover point. The same trend is observed in AlGaAs[151], with lower crossover point at x=0.45. Each material shows similar rate of E_Γ change, which increases linearly with aluminium content. Meanwhile, the E_X is showing a saturated value after crossover point.

In a conclusion, for $(Al_xGa_{1-x})_{0.52}In_{0.48}P$, Γ-valley energy can be expressed as;

$$E_\Gamma = 1.89 + 0.71x\ eV$$

while X-valley energy is approximated to $E_x \approx 2.24eV$.

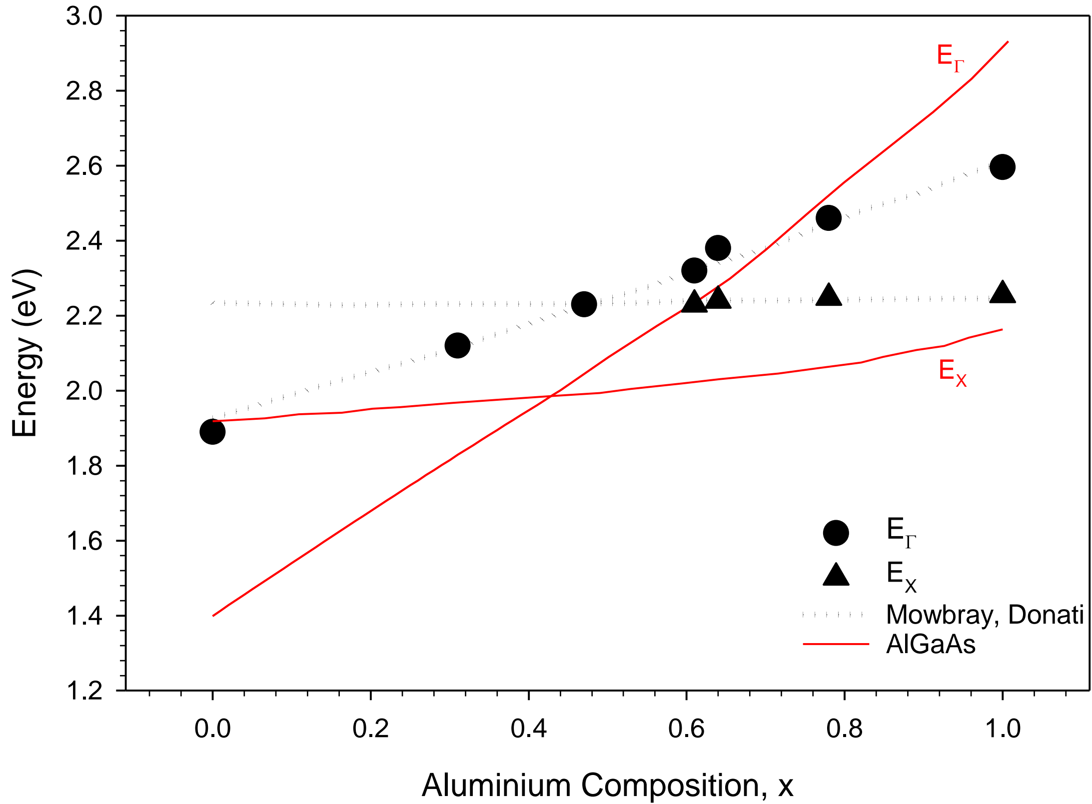

Figure 5-33 Γ and X-valley of AlGaInP shown in circle and triangle black symbols respectively. Results from literature by Mowbray[129] and Donati[150] of the same material are shown in black dotted line. The AlGaAs result for Γ and X-valley by Adachi[151] are shown in red lines

5.5 Summary

Chapter 5 presents the mechanisms in extracting the absorption coefficient of AlGaInP. The work starts with measuring the photocurrent in detail, converting it to responsivity and then quantum efficiency. The confidence in responsivity data was confirmed with different range of lasers. The multiple scans help in ensuring the uniformity of the results. Next, the sensitivity analysis towards parameters involved in current continuity equation is discussed. With the available idea of R, S_e, S_h, μ_e, μ_h, L_e and L_h, the absorption coefficients were iteratively extracted until the efficiency of the model fit the experimental efficiency. The absorption coefficient across the visible wavelength for GaInP and AlInP are compared with published data and shown consistent results. The absorption coefficients across the composition are then used for bandgap analysis. Through the α^2-E and $\alpha^{0.5}$-E relation, the determination of direct and indirect bandgap energy is calculated. The classification of the material can be summarised as direct bandgap for aluminium composition of ≤0.48 and indirect bandgap are for aluminium composition of ≥0.48.

Chapter 6 Temperature dependence of I-V

Many parameters are expected to vary with temperature according to theory. However, none of these devices are ideal, thus the variance in parameters can be observed by experimental studies. The benefits of higher working temperature have different effects on different activities. For many applications such as solar cell technology, understanding the temperature dependence parameter is critical. In this chapter, the analysis of forward voltage current characteristic was carried out from room temperature to high temperature, for both ends of the compositions.

6.1 Forward Current-Voltage Characterisation

Figure 6-1 shows the temperature dependence of dark current density as a function of forward bias for GaInP. The J-V measurements were done on three different 110µm radius devices across the sample, to ensure the uniformity in results. Except for the very low current, the agreements between different devices are generally very good. The same measurement was also carried out on different area devices, and the results show J-V that are scaled with area. Further analysis was done as a function of area (current density) to make the comparison with literature easier.

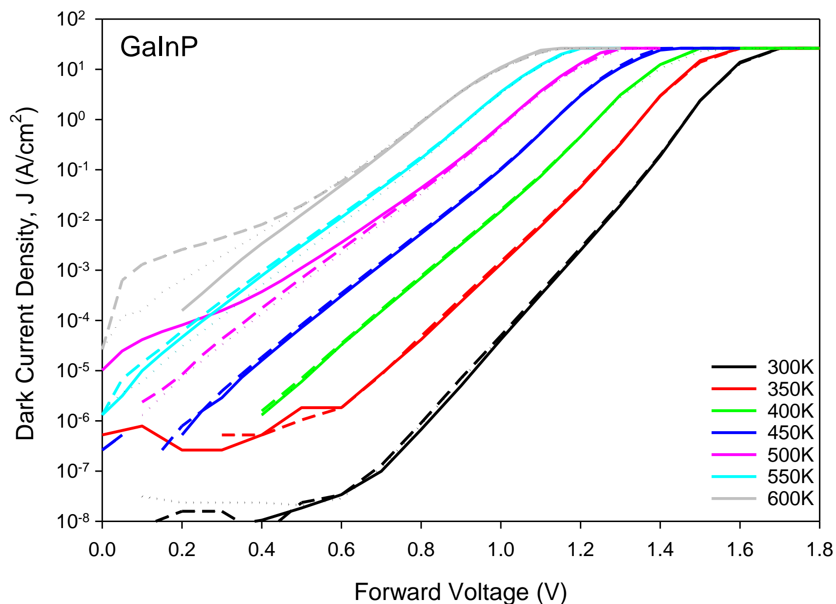

Figure 6-1 J-V characteristics of GaInP measured on three different 110µm radius devices as function of temperature

The J-V of AlInP was done on 210µm and 110µm radius devices, shown in Figure 6-2. The dark current for both sizes at the intermediate voltage region are mostly scaled with area. This indicates that the bulk current is flowing through the p-i-n region up to 600K. However, the slight variation can be seen at the low current region and also at the very high current region, caused by the effect of series resistance on different contact area. From these different ways of measurement, the results provide confidence in J-V characteristics for these materials. Similar analysis was done on the rest of the compositions, shown in Figure 6-3. Compared to room temperature J-V measurement discussed in chapter 4, some devices show different J-V results. This could be due to multiple probing at elevating temperatures, which leads to unintentional annealing. The discrepancies in results however are minimal.

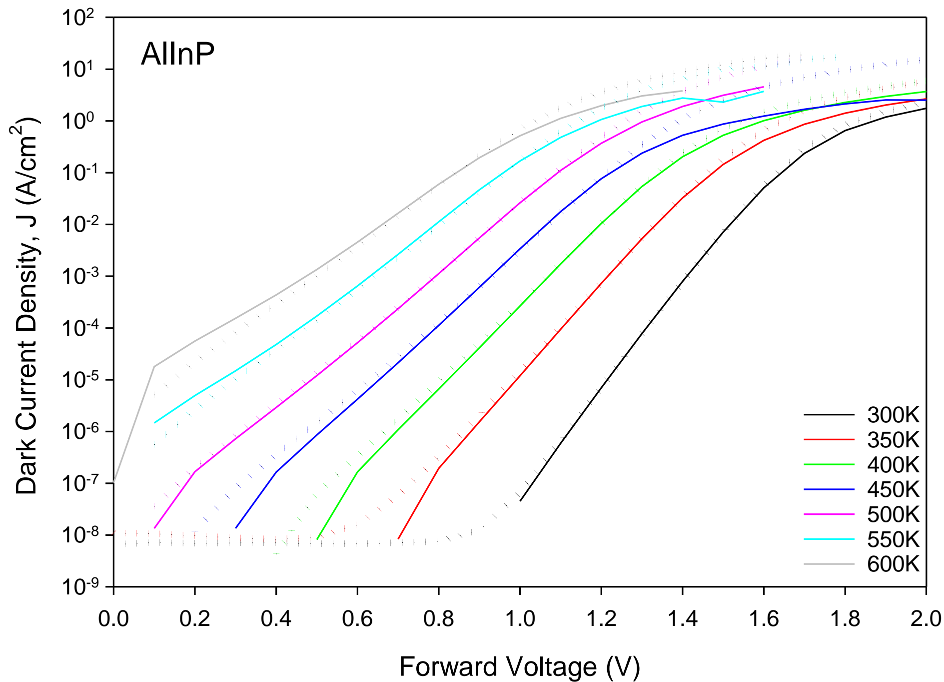

Figure 6-2 J-V characteristics of AlInP measured on 210µm and 110µm radius devices, shown in solid and dotted line respectively, as a function of temperature

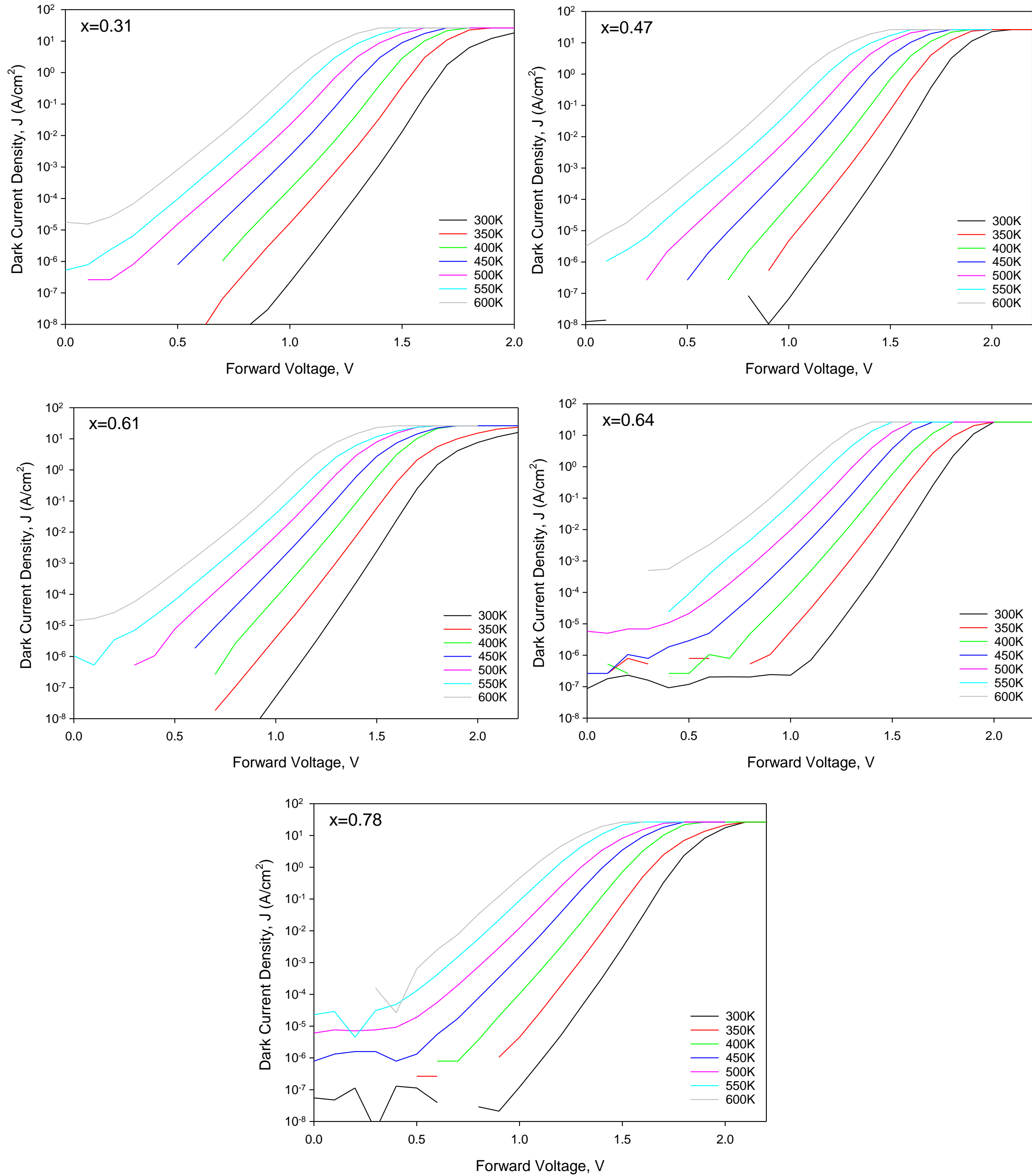

Figure 6-3 Temperature dependence of dark current density measured under forward bias. The composition value denoted on top-left of each graph

The I-V measurement from 300K to 600K was done after the photocurrent measurement at the same temperature range. Therefore, the samples have undergone multiple higher temperature measurement. Figure 6-4 shows the J-V in solid lines, used as a controlled result of 300K, which is measured before high temperature measurement. Meanwhile, the dotted-lines shows the J-V of similar devices, measured at 300K after several temperature measurements.

Upon observation, devices are not able to deliver the expectation of maintaining the same dark current. Most devices show deterioration that cause higher dark current than the preliminary measurement, with the exception for x=0.31. The inset figure emphasises on the middle voltages region of x=0 and x=1, to highlight the difference between the highest and the lowest aluminium compositions. The considerable degradation is obvious in the highest aluminium composition of x=1.

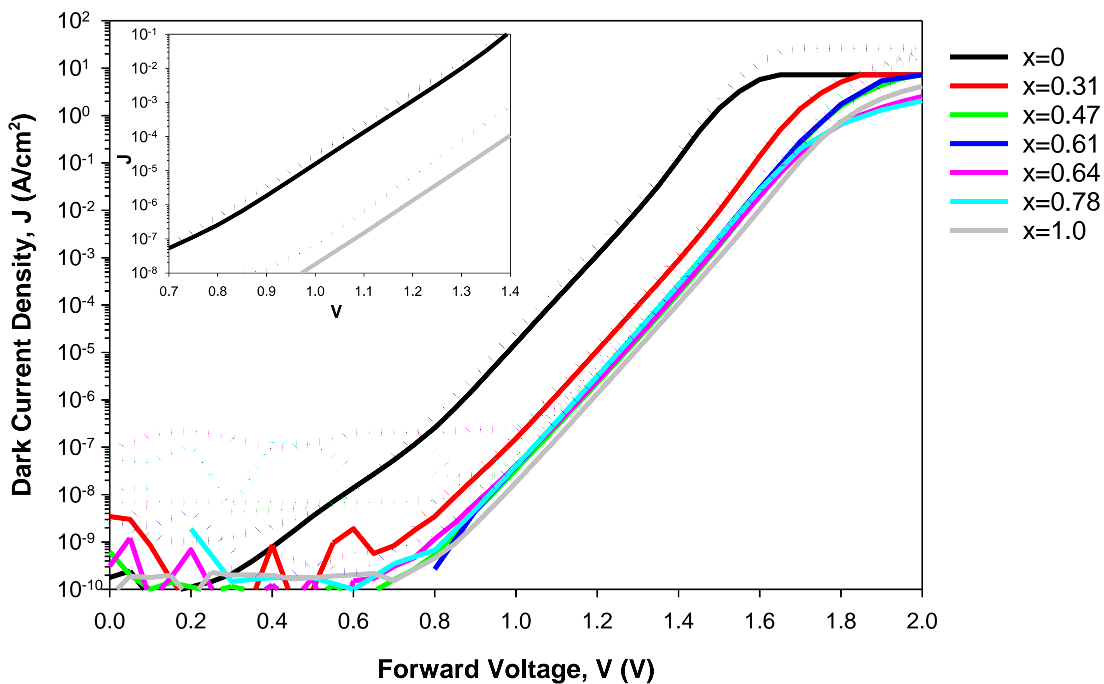

Figure 6-4 J-V differences for before(solid) and after(dotted) high temperature measurement at 300K

Initially, x=1 started with having the lowest dark current. After undergoing multiple heat measurements, the x=1 dark current is now positioned at the same range as x=0.31. The existence of gallium could possibly stabilise the alloy system even at high temperature. In addition, by replacing the gallium with aluminium and heating up the sample in air, severe oxidisation occurred. This introduces defect that yield the irreversible changes on the I-V characteristic.

In short, the bandgap and the composition have major influences toward the changes in temperature dependant dark current. The increase of dark current up to two times higher than the preliminary measurement is observed in this set of alloy system. Despite the degradation, the dark current is scaled with area from 300K to 600K, giving the assurance for the following analysis. If devices are passivated properly during fabrication, the surfaces can be protected from exposure to air. Then, even after multiple high temperature cycles, the devices are expected to maintain their performance. For this chapter analysis, the sets of results measured at the same time in the same environment from 300K to 600K are used for further characterisation.

6.1.1 Temperature Measurement Accuracy

The working temperature is recorded by the thermocouple that is embedded in the copper stage. There exists a small gap between the devices which is probed on the copper stage and the thermocouple. Throughout this chapter, temperature for both devices and thermocouple are assumed to be similar. Here, the verification of temperatures is shown.

Firstly, through the diode equation with ideality factor of 2, the J_o are extrapolated across each temperature as shown in Figure 6-5. The first three temperatures fitting looks reliable. The linear fits agree to most of experimental data from 300K to 450K, mostly at the intermediate voltage region. From 450K onwards, only several experimental data can be fit with n=2. As the temperature increases, the ideality factor is expected to reduce to represent the domination of diffusion-recombination current.

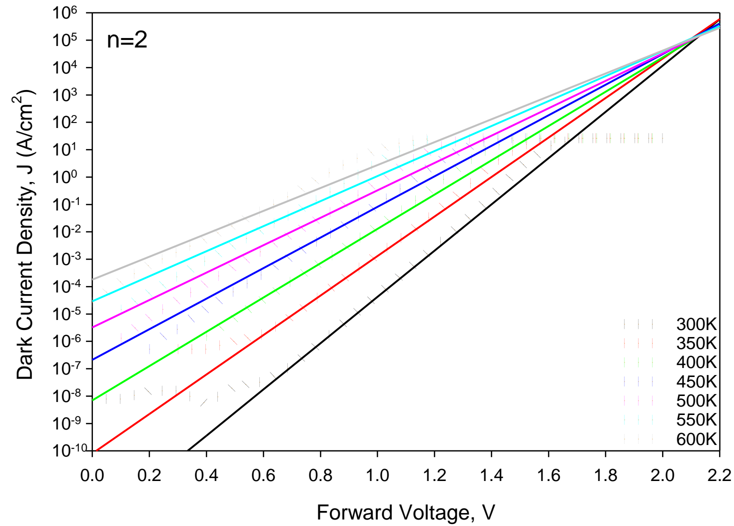

Figure 6-5 Fitting through J-V of GaInP by ideality factor of 2

However, for comparison purposes, the n=2 are kept constant for all temperatures and are plotted versus 1/T as shown in Figure 6-6. In the same figure, the J_o of 2eV AlGaInP studied by E Perl from room temperature to 400°C are included[152]. Perl in his studies also extracted the J_o with n=2, thus making the gradient between GaInP and AlGaInP comparable. The fact that GaInP's J_o positioned at the same gradient as Perl devices, proves that temperatures are valid up to 600K. The GaInP devices show higher dark current at the same temperature, due to narrower bandgap than the 2eV AlGaInP.

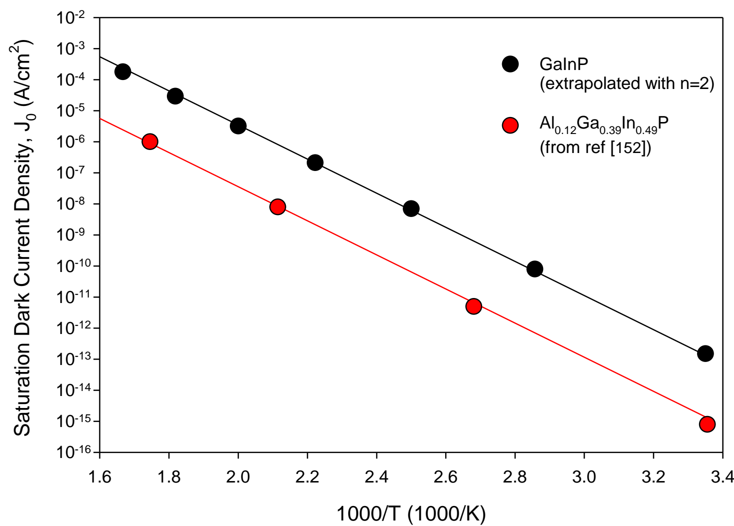

Figure 6-6 J_o versus 1/T for GaInP and $Al_{0.12}Ga_{0.39}In_{0.49}P$[152]

Other ways to confirm the temperature is through the Varshni relation between bandgap energy and the temperature. From photocurrent measurement and the analysis of absorption coefficient, the bandgap for GaInP at each temperature can be extracted. The bandgaps of the same material between 0K until 200K studied by DeLong[153] are also included in the same figure. The results are then proven with the Varshni relation given as; $E_g(T) = 1.99 - \frac{(6.25\text{x}10^{-4})T^2}{T+290}$ and shown in Figure 6-7.

Based on the Varshni fittings and the comparison with lower temperature bandgap, it can be concluded that the temperature accuracies are acceptable. A few degrees of about ≤5° off are expected but more than that may not be the case in this study. This gives a good sense and confidence towards the temperature accuracies. Therefore, further analysis on this chapter will correspond to the thermocouple temperatures.

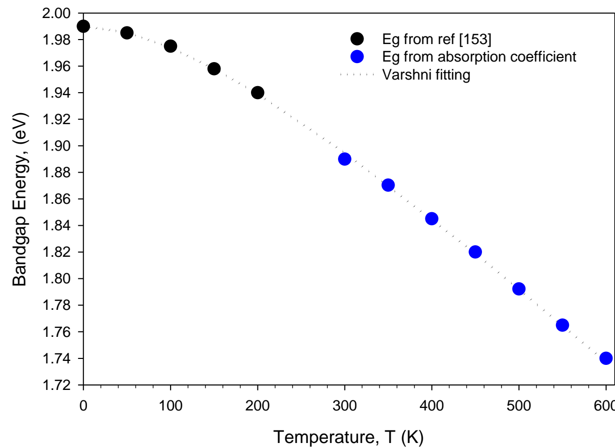

Figure 6-7 Temperature dependence of GaInP bandgap energy

6.1.2 Ideality Factor and Dark Saturation Current

The variations of ideality factors with voltages at each increment of temperature are studied prior to further I-V characterisation. Figure 6-8 shows the dotted line representing the ideality factors from 1 to 2 plotted on the right abscissa on the same plot of GaInP J-V characteristics. The gradients between 2 voltage steps are calculated to obtain the ideality factor between voltages, and are repeated for each temperature.

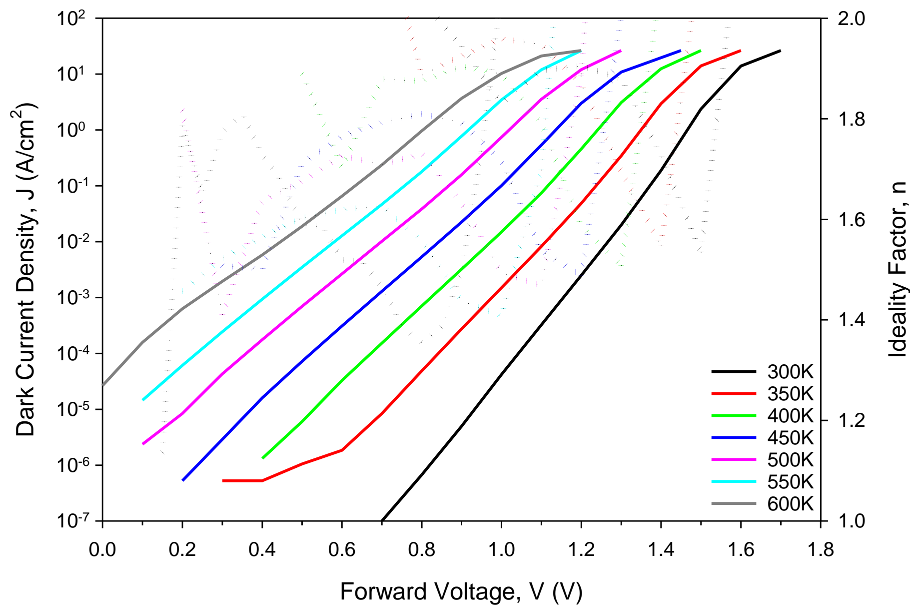

Figure 6-8 Ideality factor as a function of voltage and temperature, on J-V of GaInP

In average, from 300K until 600K, the ideality factors show a decreasing trend. Contrarily, the carrier's mobility is expected to become worse with temperature, and the series resistance is expected to increase. This leads to the prediction of the ideality factor at higher temperature to be greater than the room temperature's ideality factor. However, the effect is small compared to other strongly temperature dependant parameters that dominated the whole forward dark current.

The lowest ideality factor of 1.5 at 300K reduces to 1.38 at 600K. Upon observation on Figure 6-9, the lowest ideality factor at 300K until 550K are all located at the same range of dark current of 10 A/cm^2. From this voltage onwards, it is expected for the ideality factor to continually decrease and reach $n = 1$, as the current increases. However, the series resistance supresses the increases

in current, and causes the ideality factor to increase and reach $n = 2$. At 600K, the lowest ideality factor recorded is at 1 A/cm^2. With the same temperature, the average ideality factor of 1.7 fits the voltages from 0.45V to 0.7V only. Meanwhile, wider voltage region can be represented by 1.7 ideality factor from 300K to 400K, and become much wider from 450K to 550K.

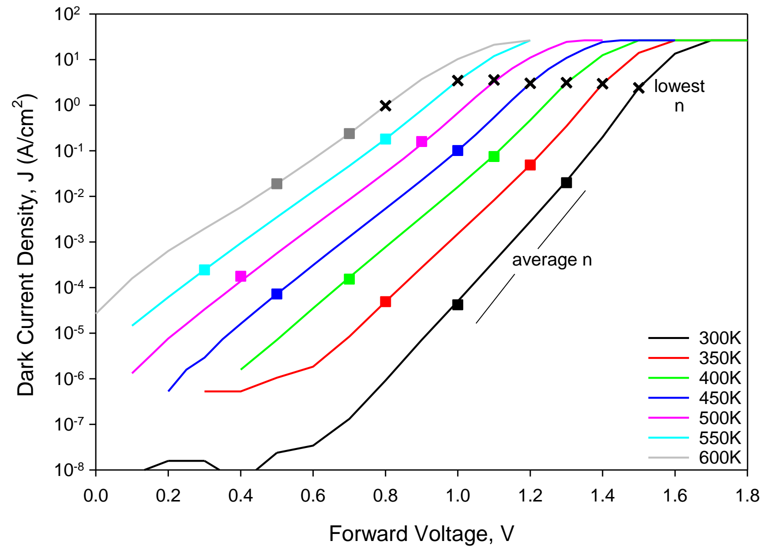

Figure 6-9 Position of lowest and average ideality factor on J-V of GaInP

Based on forward biased measurement on 110µm GaInP devices, the result at each temperature is then analysed by using the Shockley diode equation. The linear analysis at each temperature can be iteratively fitted, to fit well with the measured data. The high voltage region is excluded from the fitting due to the effect of parasitic series resistance that yields lower dark currents than what was expected.

Through the linear fittings, the dark saturation current density, J_0 is allowed to vary freely as long as most of the experimental data are fitted. The linear fit with $n = 2$ have been shown with very minimal experimental data that are well fitted. Thus, $n = 2$ is not the best representative for this material.

Here, two other cases on the relation of n and J_0 are going to be analysed. First, the ideality factor is kept constant through the increase in temperature, with average of $n = 1.7$. Second, the ideality factor is varied according to the temperature from $n = 1.8$ to $n = 1.6$. Both fitting are shown in Figure 6-10. From observation, the variation of ideality factor fits the experimental data much better compared to a constant ideality factor. However, with $n = 1.7$, most of the data in intermediate voltage region still agreed well with the linear fit.

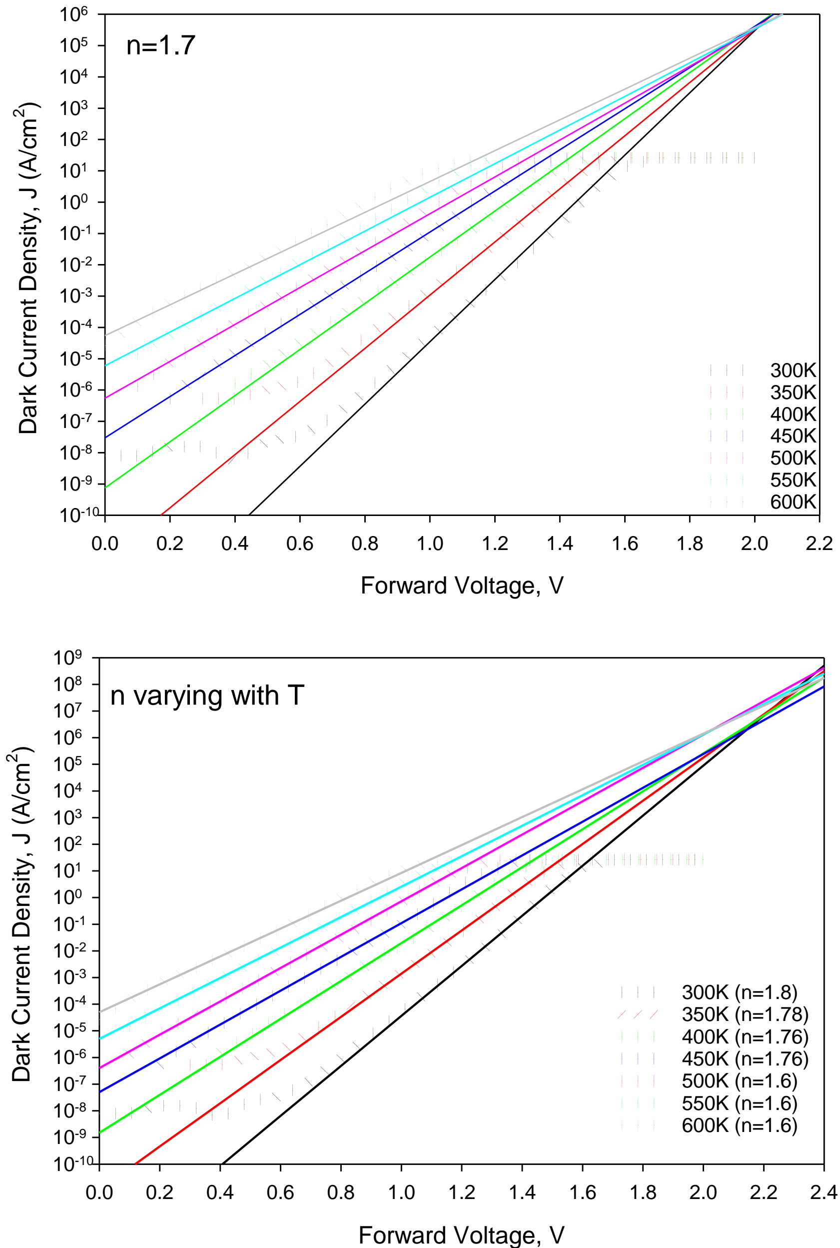

Figure 6-10 The multiple fitting through the measured data by using variation of ideality factor from 1 to 2 at 300K, 450K and 600K

Based on single n plots, the extrapolation of all the linear fit to higher voltages creates the intersection point at 2V. On the other hand, in variation of n plots, there are two intersection points. One for 300K to 450K, located at 2.1V. Another point at 1.9V is from the linear fit between 500K to 600K. From this point of view, the pair of n and Jo value are presumed accurate when each fitting lines converged at a same point. The same direction of converging point is seen at 2.3V in AlInP devices, with n of 1.75 is kept constant from 300K to 600K. By using this as a benchmark, further analysis is going to be based on the single n of 1.7 and 1.75 to represent GaInP and AlInP respectively, from 300K to 600K.

The gradients of J-V characteristics are observed to become steeper with decrease in temperature and shifts to higher forward voltages. This explains that J_0 of a diode is a strong function of temperature. The extrapolation of the diode equation to the y-axis provides the saturation dark current density value as shown in Figure 6-11. The J_0 for GaInP with $n = 1.7$ has a significant increase from 10^{-15} to 10^{-5} A/cm^2, from room temperature to 600K. Meanwhile, the increase in J_0 with variation of n is recorded to be from 10^{-14} to 10^{-5} A/cm^2. Both cases of n produce a small range variation in J_0, thus choosing any of this n would still provide a fair judgement for GaInP. The J_0 for AlInP shows lower results than GaInP, which is true due to its wider bandgap. Both compositions conclude that J_0 decreases with aluminium content, but increase with temperature.

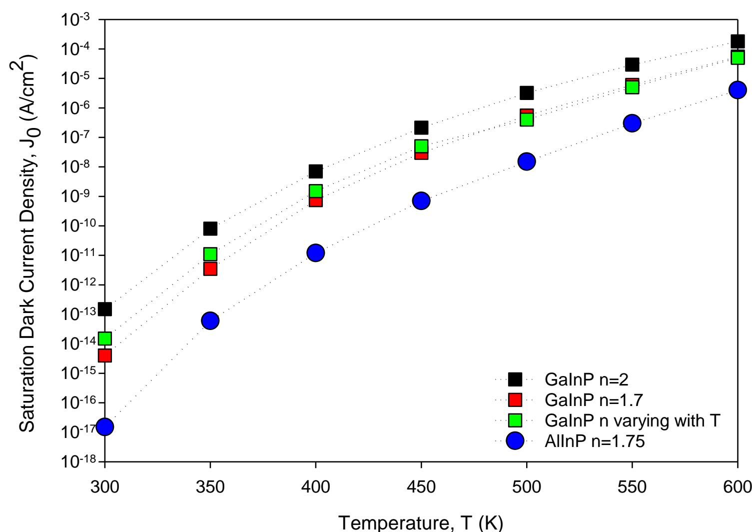

Figure 6-11 Temperature dependence of J_0 for GaInP and AlInP

6.2 Arrhenius plot

The Arrhenius Law is widely used in multitude systems to interpret the sensitivity of any constant rate in studies due to thermally activated process. The Arrhenius relation is governed by the thermal dependence parameter of activation energy, E_a as shown in Equation 6.1[154]. The C_T is the constant of the pre-exponential factor, k is the Boltzmann constant, and T is the diode temperature in Kelvin. The equations shows that any reaction rate in studies is exponentially proportional to the temperature[155].

$$J_T = C_T \cdot exp\left(-\frac{E_a}{kT}\right)$$ **Equation 6.1**

In a semiconductor material, the activation energy can be described as the minimum energy needed for electrons to be excited into the conduction band, at a particular temperature. The comparability of the Arrhenius equation to the diode equation leads to the relation of the E_a and E_g as shown in Equation 6.2[156]. The existence of the ideality factor in the equation provides the magnitude of the effects of temperature towards the deviation from ideal-diode characteristic.

$$\frac{E_a}{kT} = \frac{E_g - qV}{nkT}$$ **Equation 6.2**

To obtain the activation energy, the temperature dependence of dark current density as a function of voltage is first extracted as in Figure 6-12. The analysis was carried on devices of both ends of composition. The extrapolation to the y-axis gives the 0V dark current, whereas the extrapolation to higher voltages shows an intersection point of all linear plots. The converging points are positioned at ~2V for GaInP and ~2.25V for AlInP. These intersecting points give a good sense of temperature measurement as the values are close to the bandgap values for respective materials. The voltages from 0V to 1.2V with increment of 0.2V at each temperature are then used for Arrhenius plot, shown in Figure 6-13.

Voltages for Arrhenius plot

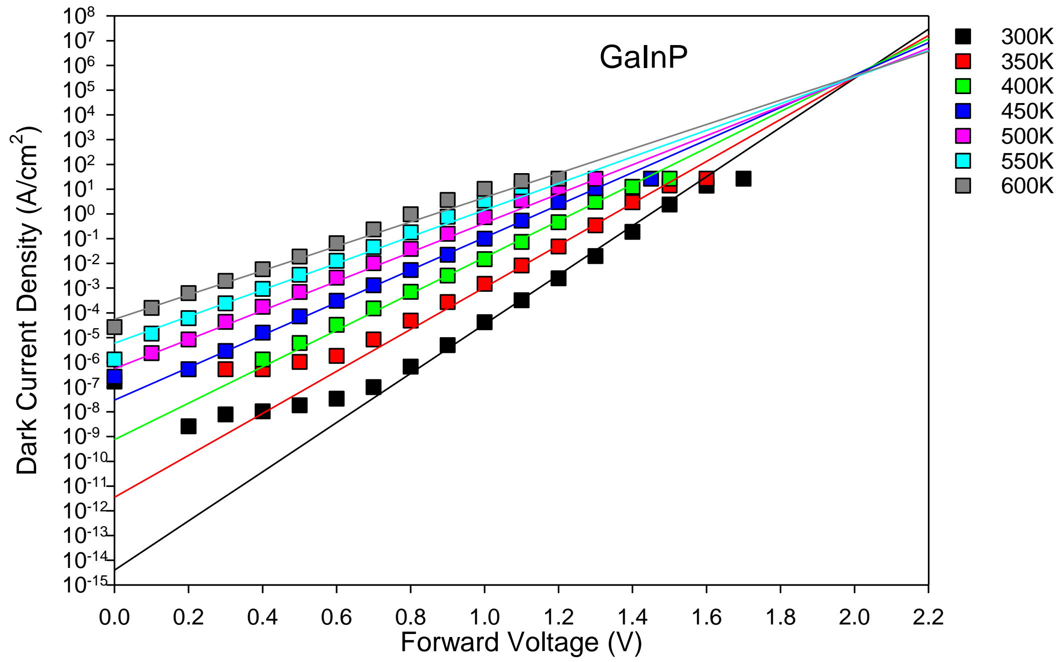

Voltages for Arrhenius plot

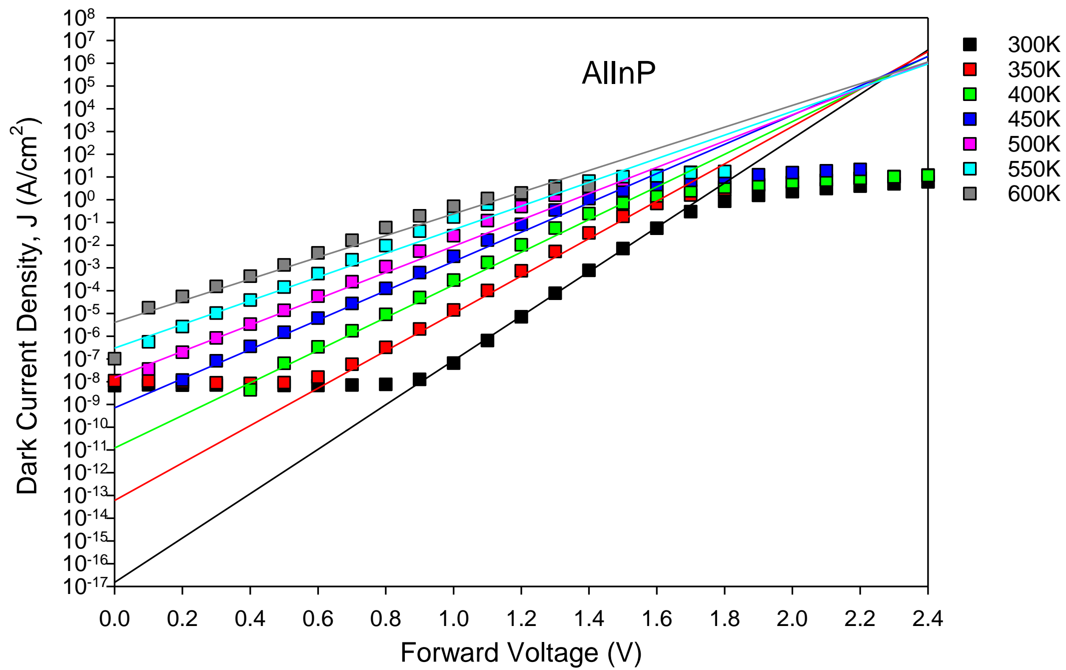

Figure 6-12 Fitting lines based on diode equation with ideality factor of 1.70 and 1.75 for GaInP and AlInP respectively

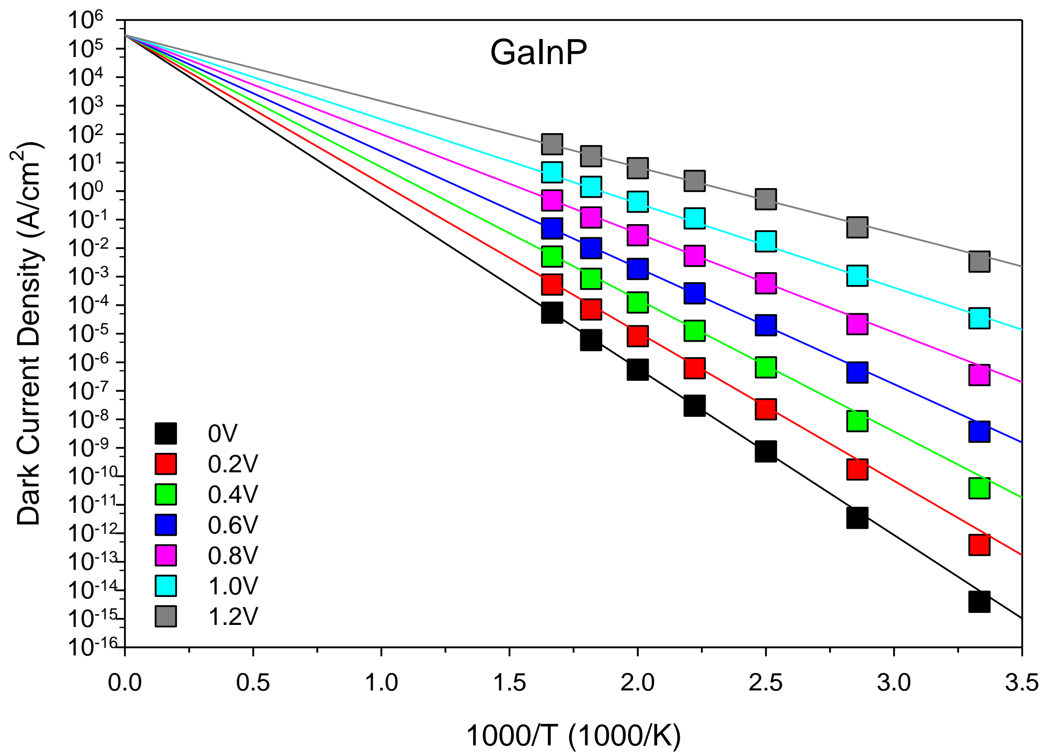

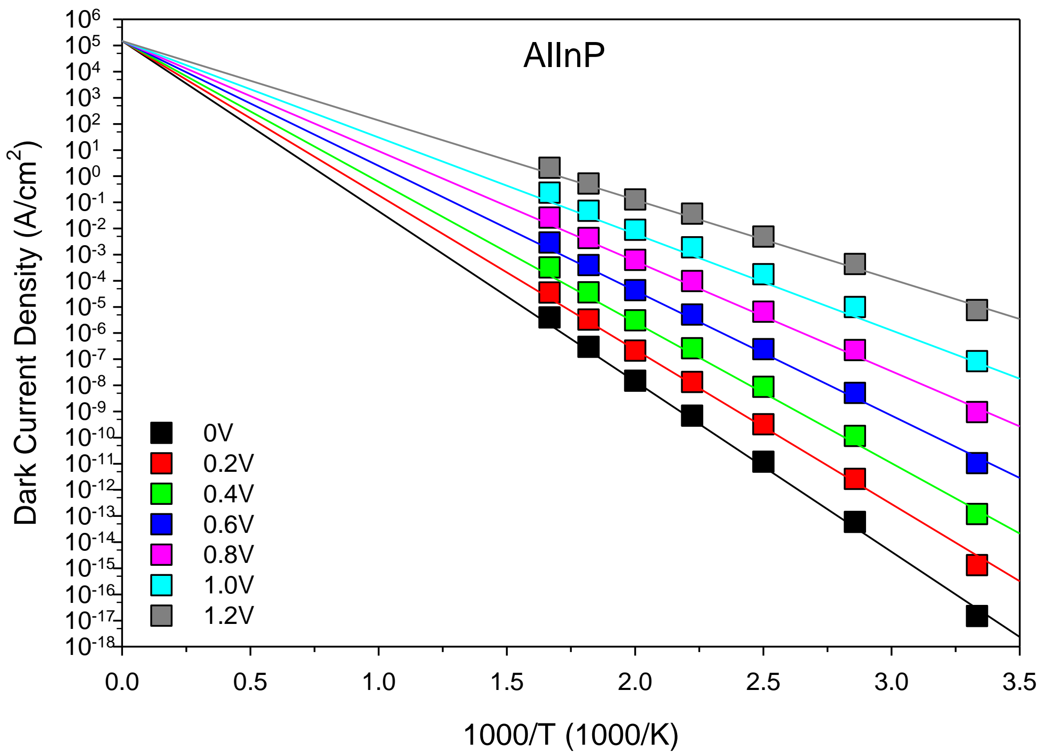

Figure 6-13 Arrhenius plots of GaInP and AlInP

Figure 6-13 shows the rate of change in voltage associated to the temperature. For each constant voltage plots, the linear fit is made through the increase in temperatures, and extrapolated to the y-axis, using the J_T and E_a relation. The plots keep bending downward with voltages, indicating a significant decrease of gradient. This causes the extrapolation of constant C to come closer to one another, and eventually overlap at the constant value of T=0. Therefore, the dependency of the dark current towards temperature reduces as voltage increases. The slopes are governed by the I-V characteristics; thus it varies between GaInP and AlInP.

Figure 6-12 shows that the extended lines through the I-V curves for temperatures of 300K to 600K converge to a common focal point equivalent to the bandgap voltage. Similar behaviour has been seen in the forward I-V characteristics of silicon p-n junction at different temperatures by Widenhorn et. al[156] and Qinghai et.al[157].

Widenhorn et. al showed the forward converging point corresponds to the bandgap of the silicon with the assumptions that the material bandgap is temperature independent. The behaviour of the samples was shown to satisfy the Meyer-Neldel Rule (MNR). Qinghai et. al related the point of convergence to the summation of material bandgap value and $\frac{nkT\gamma}{q}$. The second term however is very small in proportion to the forward voltage, where γ is a constant of ≥2.5.

The occurrence of focal points in MNR is natural, and can be found in most electrical characterisation. It is called positive MNR when the cumulative point occurrs at T≥0 in the positive abscissa, or called negative MNR if otherwise[156]. Studies suggest that universal behaviour of MNR in semiconductors are due to the temperature effects towards the multiple excitations, or towards the fermi level, or both processes that take place simultaneously[158].

6.3 Activation Energy

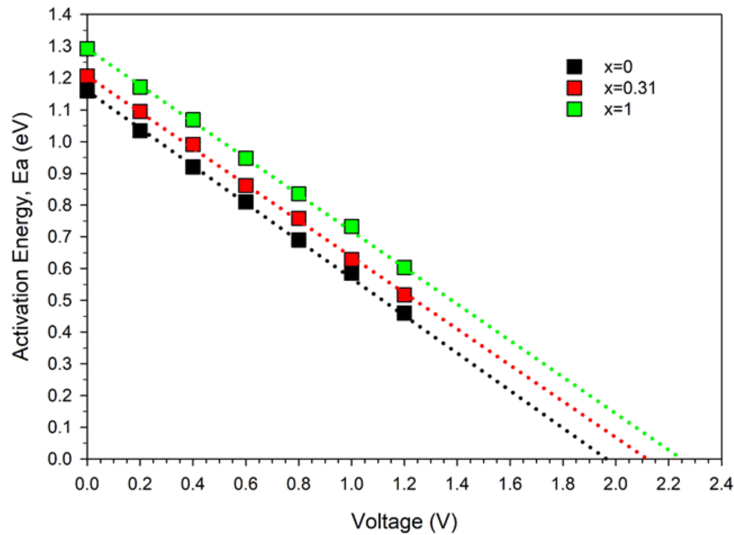

Figure 6-14 Activation energy as a function of forward voltages

When the product of $E_g \approx E_a$ is at zero bias[159], the dark current can be concluded to be dominated by bulk diffusion current. This leads to non-voltage dependant current. The ideal case for AlInP would be $E_a = 2.2eV$ at 0V, and reaches $E_a = 0$ at 2.2V. Devices with defects or mid band traps would normally have the $E_a \approx ½E_g$. The AlGaInP under this study however shows activation energy slightly higher than half of the bandgap. Nevertheless, the extrapolation still results in the x-intercepts value to be approximately equal to the bandgap value. It is proven experimentally that the materials under this study are dominated by the recombination current.

When the voltage is at 0V, the y-intercept value is approximately half of the material bandgap. This suggests that there exists a trap located near the middle band as demonstrated in Figure 6-15, creating an easier path for more minority carriers to cross to the other junction.

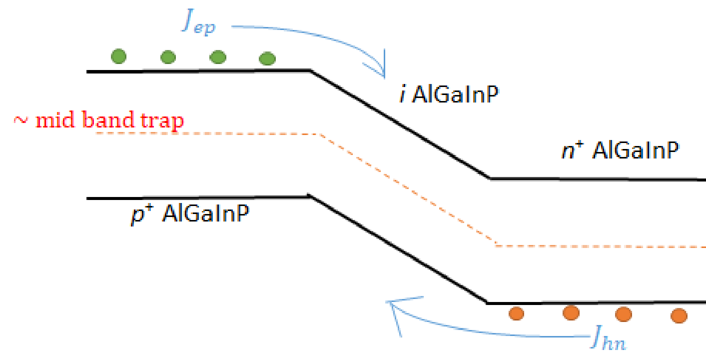

Figure 6-15 Band structure at 0V

However, as the forward bias increases, the barrier height as illustrated in Figure 6-16 for majority carriers to flow reduces . Once the applied voltage is equal to the built-in voltage, the barrier height and activation energy becomes zero.

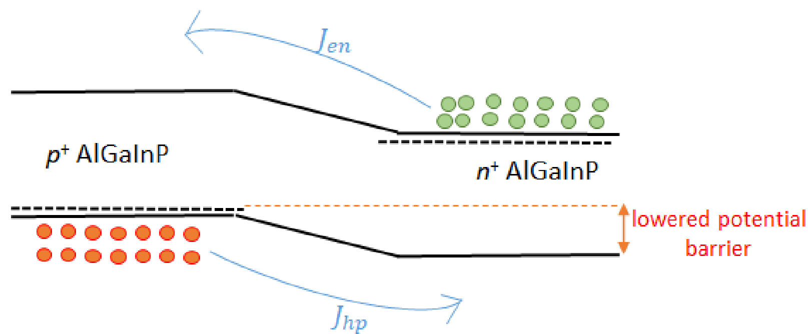

Figure 6-16 Forward biased band structure

Figure 6-14 shows the correlation of activation energy and forward bias being applied. Based on the Arrhenius plots, the curves with steeper slopes yield higher activation energy compared to the flatter slopes. Within the same temperature range, dark current at low voltages is more sensitive towards change in temperature. The E_a of GaInP becomes zero at V≈1.95, while the E_a of AlInP is extrapolated to be at V≈2.25. The activation energies can also be strongly affected by the existence of defects and impurities. Thus, the E_a is normally low in doping semiconductor, and constant in intrinsic semiconductor[158].

Theoretically, when ideality factor is 2, the traps are assumed to be in the middle of the bandgap while $n = 1$ for non-existant traps. However, this is not always true as AlGaInP ideality factor are neither 1 or 2 specifically. It is possible to say, even at higher injection bias, there is enough component of diffusion current that reduces the ideality factor to 1.7 instead of $n = 2$.

The argument on how to locate the exact position of traps is still ongoing. Thus, the relation of $E_g = n \times E_a$ is used as a basis for the correct estimation of E_a. Table 6-1 shows the relation of n, E_a and E_g for both compositions. By observation, higher aluminium content with wider bandgap material yields higher E_a. The bandgap at 0V, calculated by the Arrhenius analysis is comparable with the bandgap measured at 300K by photocurrent measurement. Study by Chen on forward I-V characteristics of AlGaInP LED also shows a similar relation, where $n \times E_a = 2.2eV$[160].

Table 6-1 Relation of n, Ea and Eg for GaInP and AlInP

Aluminium composition, $\boldsymbol{x}$	Ideality Factor, $\boldsymbol{n}$	Activation Energy at 0V, $\boldsymbol{E_a}$ (eV)	Bandgap by I-V measurement $\boldsymbol{E_g = n \times E_a}$ (eV)	Bandgap by Photocurrent measurement, $\boldsymbol{E_g}$ (eV)
0	1.7	1.16	1.97	1.89
1	1.75	1.29	2.26	2.26

6.4 Reverse Current-Voltage Characterisation

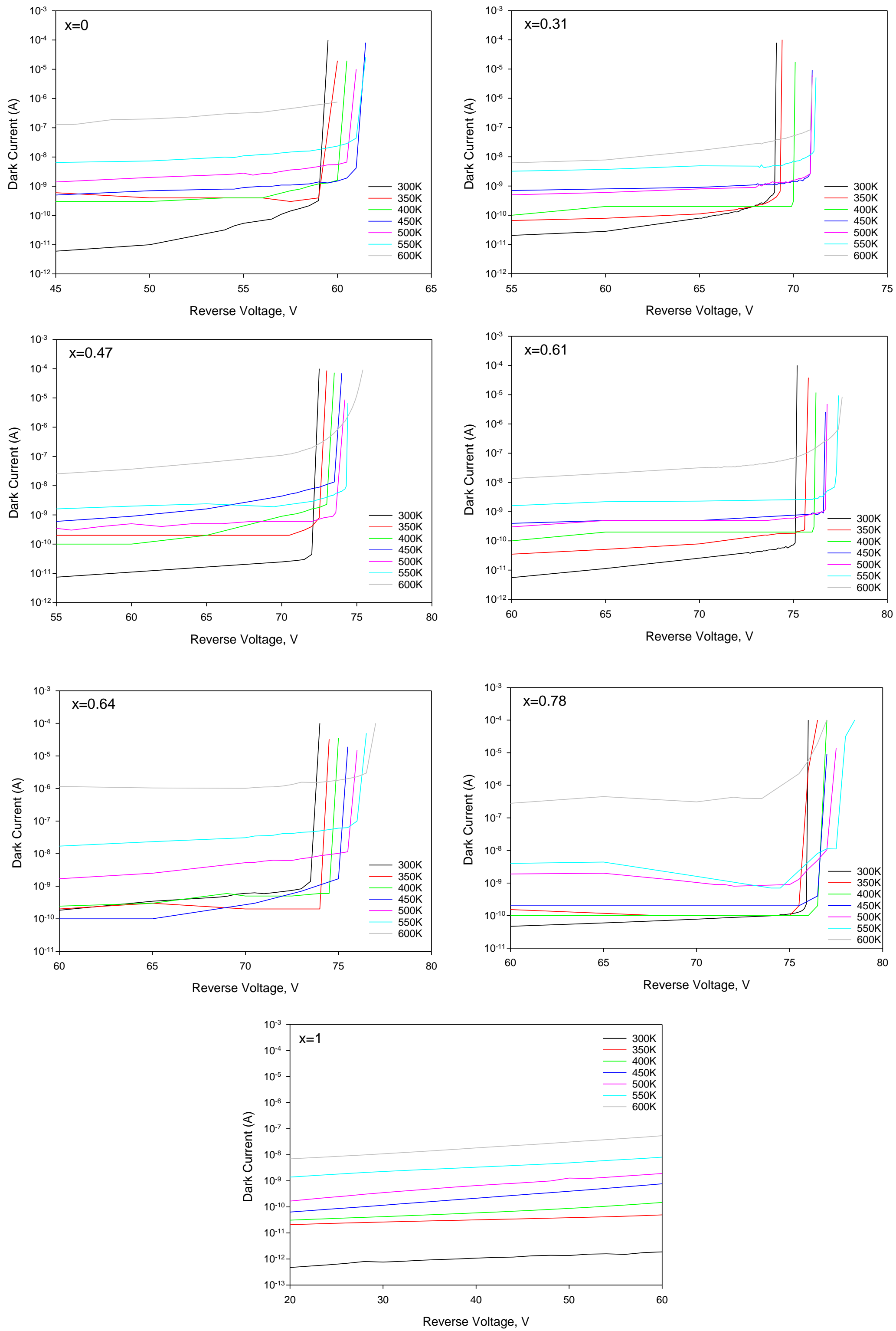

Figure 6-17 Temperature dependence of reversed dark current

Figure 6-17 shows the dark current characteristic as a function of reverse biased. Every measurement was tested on 110µm radius devices, from 300K to 600K. Initially, a gradual increase in dark current is recorded for all composition. Then, they start showing a rapid increase in small voltage increments, indicating a breakdown voltage region. Despite the temperature being increased to 600K, the devices still managed to maintain reasonably low I-V characteristics. Since the bulk dark current is very low, the surface leakage current determines the reverse current-voltage characteristics.

The breakdown voltage relation with aluminium content is summarised in Figure 6-18. The trends of breakdown voltages shifting to higher bias with increase in temperature are observed in all compositions. Studies on the ionisation coefficient on the same material have been published by Lewis, where the ionisation coefficient reduces with increase in aluminium composition[161]. Subsequently, the breakdown voltages increase with aluminium composition. When the dark current increases with temperature, more scattering occurs, and carriers cannot gain enough energy to be ionised. Thus, more electric fields are needed to reach the breakdown voltage as the temperatures increases.

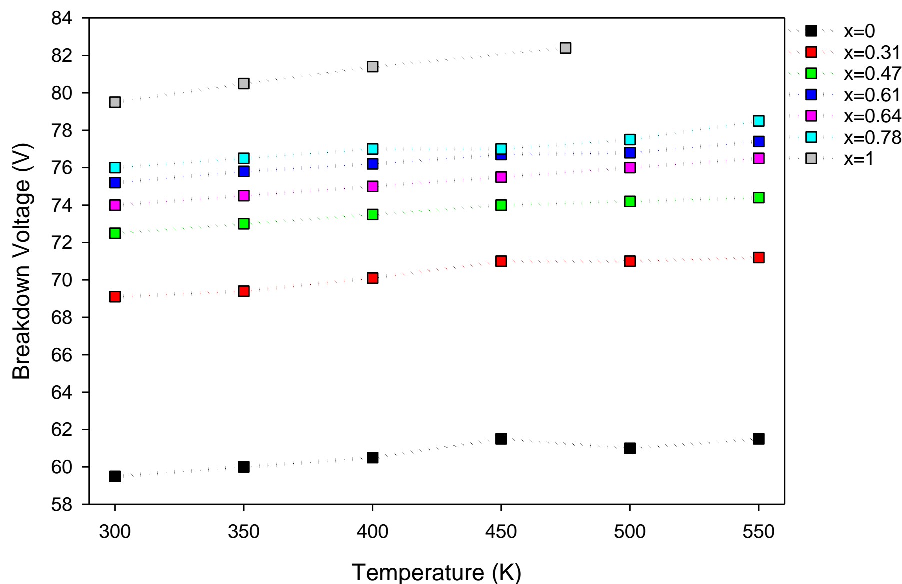

Figure 6-18 Breakdown voltage of AlGaInP with respect of temperature, where the data of AlInP is from Liang's[162]

The accuracy of breakdown voltage can be achieved by repeating the measurement. However, only few runs of experiment were done for each composition. This is done to prevent the devices from deteriorating, and to preserve them for further characterisation. For x=1, the measurement was carried out up to -60V only, due to the limited working devices. The breakdown voltage for x=1 is from Liang's work, measured on the same fabricated sample from 300K to 475K[162]. Most measurements at 600K show an early breakdown voltage. Thus, the results of 600K are omitted from the plots to avoid underestimation of the results.

6.4.1 Reverse Activation Energy

Since the measurement at each temperature was done singularly, the accuracy of the data is arguable. Despite the probable inaccuracy, the attempts in obtaining the activation energy were carried out by performing the following; firstly, the J_o are extrapolated from the current-reverse voltage characteristics shown in dotted line in Figure 6-19. The result is then compared with the forward biased J_o extracted earlier in this chapter. The analysis was done only on AlInP device.

The J_o for 500K, 550K and 600K show comparable results between forward and reverse biased. This similarity indicates a bulk current flowing through the junction. However, significant differences in J_o are shown for temperature between 300K to 450K. Much lower dark current is expected at this region, but it is below the capabilities of the equipment to measure that low. On the other hand, such low dark current in forward bias is extrapolated using the diode equation. This extrapolation can only be done provided more experimental data are available for the fitting.

Through reverse I-V measurement, the surface dark current measured is much larger compared to bulk current at up to 450K. This large surface current is due to the tunnelling effect and shunt resistance. Therefore, the measured dark currents below 500K are not realistic for further analysis on activation energy. Only data from 500K, 550K, and 600K are used on Arrhenius plot as shown in Figure 6-20.

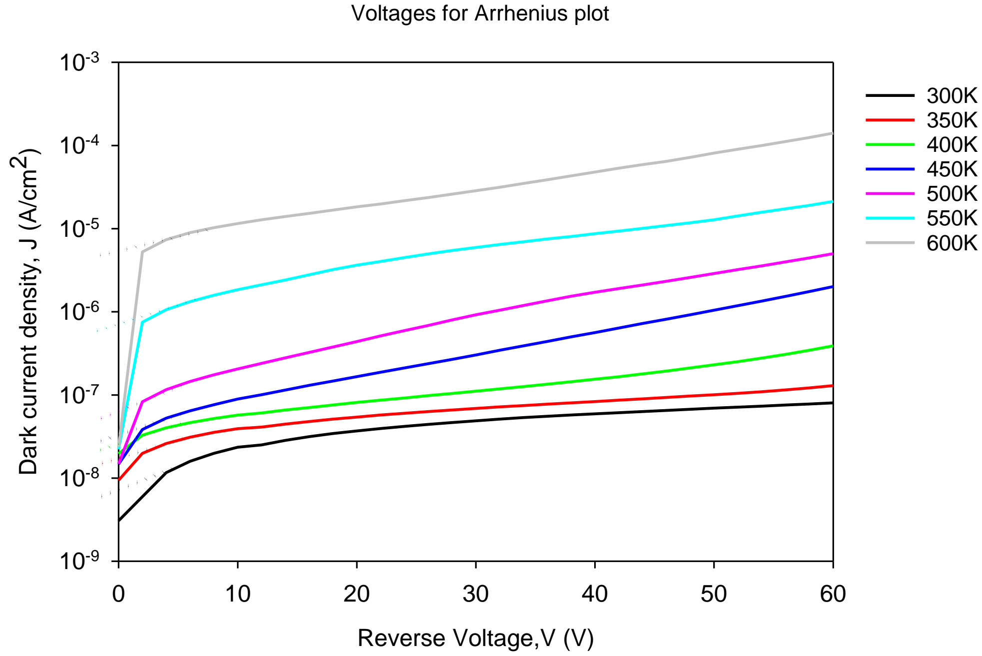

Figure 6-19 Reversed J-V of AlInP with voltages marks shown for Arrhenius plot

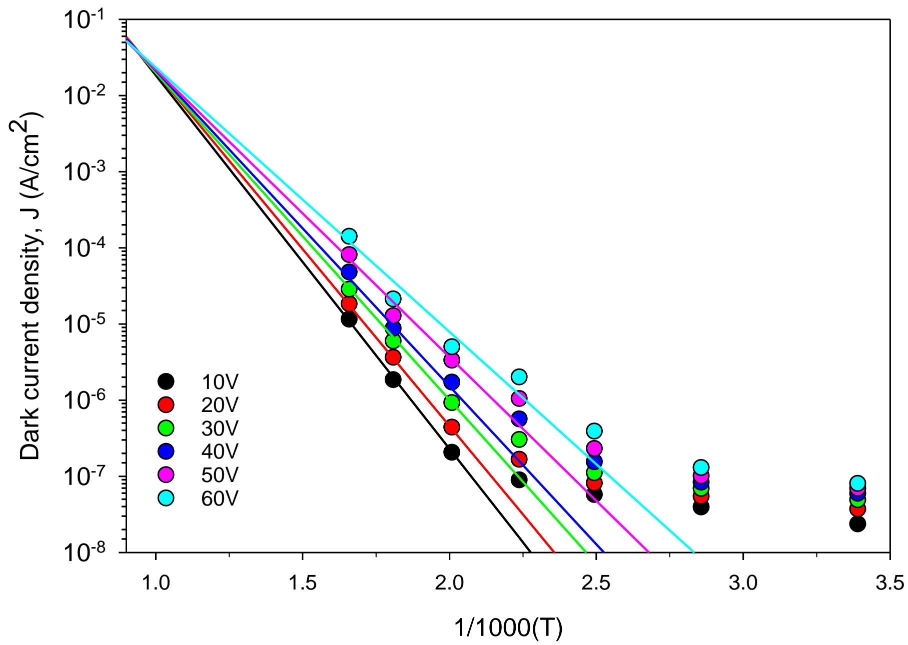

Figure 6-20 Arrhenius plots of reverse voltages for AlInP

The expectation of fitting through the 300K to 600K in reverse I-V is quite complicated. However, the best effort produces the linear plot to fit only on 500K to 600K. Meanwhile, the voltages where the surface leakage dominate are not following the linear trends. This low temperature region is unable to be fitted with the same gradient as the higher temperature. All plots accumulated at T≈$1x10^{-3}T^{-1}$ whereas in forward bias, the merging point resulted at T=0. The activation energies extracted from the gradient of each linear plots are registered in Table 6-2.

Table 6-2 Activation Energy of AlInP as a function of reverse voltage

Reverse Voltage, V (V)	Activation Energy, Ea (±2 meV)
-10	0.97
-20	0.92
-30	0.85
-40	0.82
-50	0.75
-60	0.69

The activation energy reduces with increase in reverse voltage, associated to the reduction in the gradient of the Arrhenius plot. If the extrapolation through the -10V to -60V activation energy is made, the E_a at 0V will be 1.1eV. This value of activation energy is close to half of the bandgap of 2.2eV, indicating the existence of the middle band traps. Studies on commercial semiconductor of Si have shown the activation energy due to the leakage current of up to 300°C are varied from half of the Si bandgap, 0.6eV to as close as Si bandgap, 1.2eV[159].

Meanwhile, the forward bias activation energy of AlInP is 1.29eV at 0V. This dissimilarity between forward and reverse activation energy of <0.2eV is considered small and qualitatively similar. The inabilities of the equipment to measure very low dark current contributed to the limited measured data. The reverse bias analysis could be improvised, provided more data could be measured. Although this reverse I-V analysis is interesting and could be done, the effort towards this area is not continued due to devices limited supply, equipment capability and time constraint. The characterisation of the reverse activation energy would benefit studies on detectors.

6.5 Summary

In this chapter, the forward current voltage characteristics are done on all compositions from room temperature to 600K. All dark currents are scaled with area, and there exists a sign of increase in series resistance with temperature. The uniformity in multiple devices' results give confidence in their I-V characteristics. The variations of the ideality factor are shown and $n = 1.7$ and $n = 1.75$ are used as a single ideality factor to represent GaInP and AlInP respectively. The Arrhenius plot across each voltage from 300K to 600K gives the gradient value for activation energy. The slope gradient reduces from 0V to 1.2V, indicating weak current-voltage temperature dependence. The 0V activation energies for GaInP and AlInP are 1.16eV and 1.29eV respectively. This concludes that the factors contributing to the dark current are slightly above half of the bandgap. The same analysis in attempts on extracting the activation energy for reverse bias are carried out on AlInP. The reverse dark currents are very low, causing the Arrhenius plot to only fit several measurement data. Even so, the activation energy of AlInP extracted from reverse voltage measurement produces 1.1eV, which is close to half of the bandgap.

Chapter 7 Conclusions and Future Work

7.1 Conclusions

This is the first study on absorption characterisation for this balance of alloy system across the entire composition range at room temperature. This work demonstrated the accurate results of absorption coefficient of AlGaInP, extracted through photocurrent measurement. The absorption coefficient follows the trend seen in many different materials, with spectrum shifting to the blue region as aluminium decreases. With this precise and careful extraction of optical properties, it is useful for designing and tailoring photodiodes to cope with any region of visible spectrum.

With advantages of wide bandgap material, the low dark current enables the measurement to be taken down to 3 orders of magnitude from the peak photocurrent. This combination of alloy becomes direct to indirect at x=0.48, about the same as GaAs/AlGaAs. Even though the starting point of GaAs bandgap value is located at lower energy, the rate of increase of valleys are similar, where the curve shifts up for AlGaInP.

All seven compositions of x=0, 0.31, 0.47, 0.61, 0.64, 0.78 and 1.0 were grown with nominal i-region thickness of 1µm. The device processing with standard metallisation stages and etching technique were used for the fabrication of the p-i-n photodiode of AlGaInP. Even without proper surface passivation, devices are able to withstand repeated temperature cycling with slight degradation in the dark current measurement. Nevertheless, the fabrication stages prove to work for the characterisation up to 600K, without severe degradation on the devices. If higher temperature testing is needed, optimisation on fabrication stages is recommended.

The activation energy due to forward and reverse bias have shown the capabilities of devices as a temperature dependant photodiode. The activation energies are 1.16eV and 1.29eV for GaInP and AlInP respectively, which are about half of the bandgap, similar to Si. Despite their advances in technology, the Si semiconductor however is restricted by its narrow bandgap indirect properties. Therefore, AlGaInP benefiting from its wide bandgap properties is capable in maintaining reasonably low dark current, even lower and better than Si at room temperature and more robust towards radiation and temperature hardness.

The AlGaInP has been proven to be a promising material system that can be grown lattice matched to GaAs with high quality. Even though the wide bandgap technology has been dominated by GaN and SiC, a simpler structure such as AlGaInP would be valuable for detector applications. Optimisation of this material system to aim for visible wavelength detection or any specific wavelength region would be beneficial for the multi-junction solar cell. Considerable rise in attention has been paid on AlGaInP as a solar cell material, either for terrestrial and industrial application or high temperature invention.

To fulfil the full potential of AlGaInP, the midband defects and traps have to be removed from the substrate, which is very difficult for III-V material. However, growth of higher doping in either n or p-type junction for this mature non-nitride material system are practical and feasible. The dark currents are not optimised yet in these samples, but with better quality of growth and fabrication, even lower dark currents can be expected. The bandgap of the material can be engineered with respect to the aluminium content, with assurances of low dark current as the bandgap increases. As a conclusion, the ternary alloy of GaInP and AlInP, with the conjunction of quaternary alloy of AlGaInP, have wide opportunities in tailoring the spectral responses to any intended visible wavelength.

7.2 Future work

7.2.1 2° and 10° Ordering of GaInP

Instead of variations of aluminium composition, different ordering of wafer substrate can perform the same function of bandgap tailoring. Reduce in number of ordering can increase the bandgap energy, while maintaining the material optical properties. Preliminary work has been done throughout the study on 2° and 10° of GaInP samples. Both are grown at the same time, with the same growth procedure and temperature. The Nomarski image of wafers are shown in Figure 7-1, where 2° samples show more surface roughness compared to 10°. The QE spectral responses converted from photocurrents are shown in Figure 7-2. The 10° samples record 32% efficiency at 672nm peak, and the spectrum efficiency reduces to 30% efficiency at 656nm peak for 2° sample. Further characterisation on these samples would be interesting for many applications exploiting the benefits of wide bandgap material.

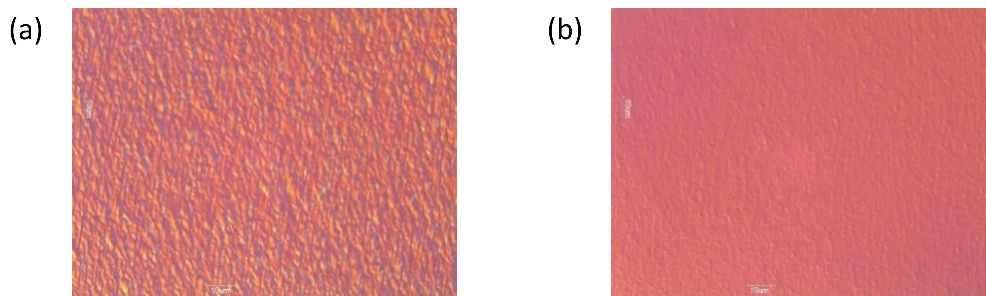

Figure 7-1 Nomarksi image of (a) 2° and (b) 10° GaInP wafers surface

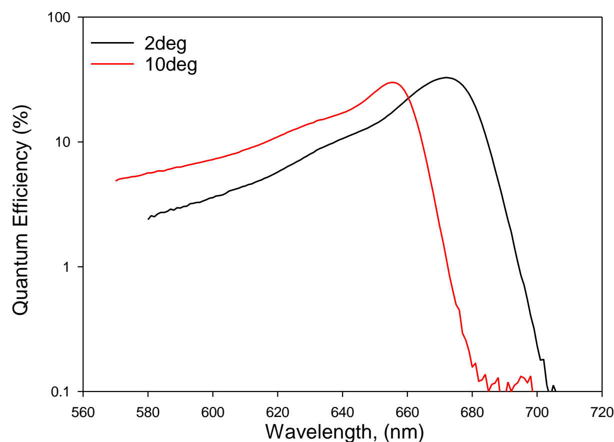

Figure 7-2 Quantum efficiency of 2° and 10° GaInP

7.2.2 Gallium Phosphide

Gallium Phosphide, GaP is another alternative for very short wavelength region detection from 350nm to 550nm. Figure 7-3 shows the spectral response for p-i-n and n-i-p GaP plotted together with AlGaInP responses, and high temperature QE up to 600K. The combination spectrum gives a very thorough coverage on visible light spectrum. The p-i-n GaP shows higher efficiency of 39% with broader spectrum compared to 19% efficiency in n-i-p device. The device thickness recorded consists of 2µm i-region sandwiched in between 0.5µm p^+ and n^+ cladding layer. The devices growth reports however are not to be found; thus, many measurements have to be taken for further characterisation.

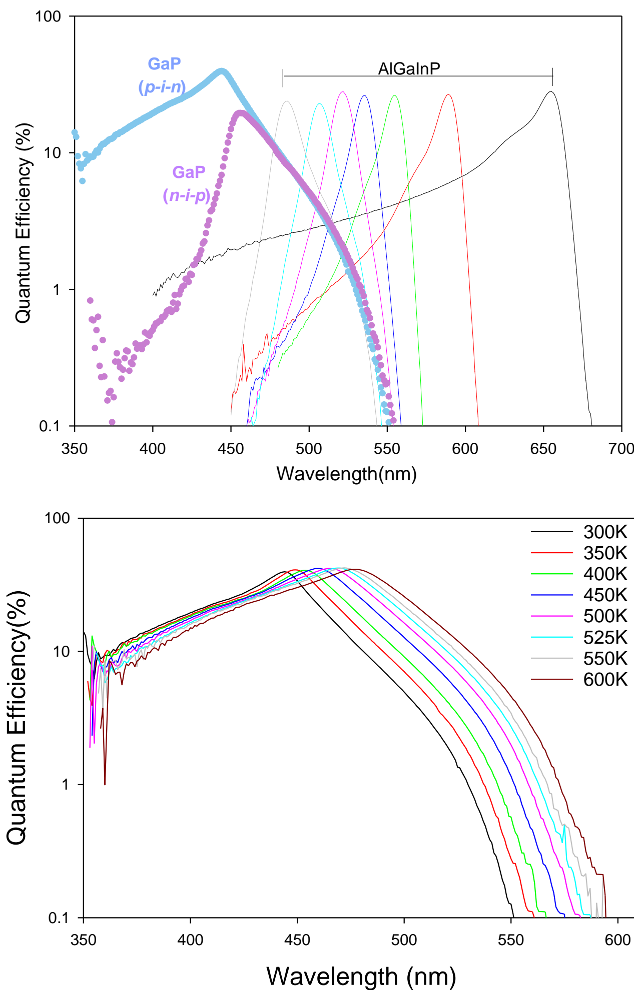

Figure 7-3 QE for GaP (top graph) p-i-n and n-i-p shown in blue and purple dotted-lines. The QE (bottom graph) of p-i-n GaP as a function of temperature

Chapter 8 Appendices

8.1 XRD

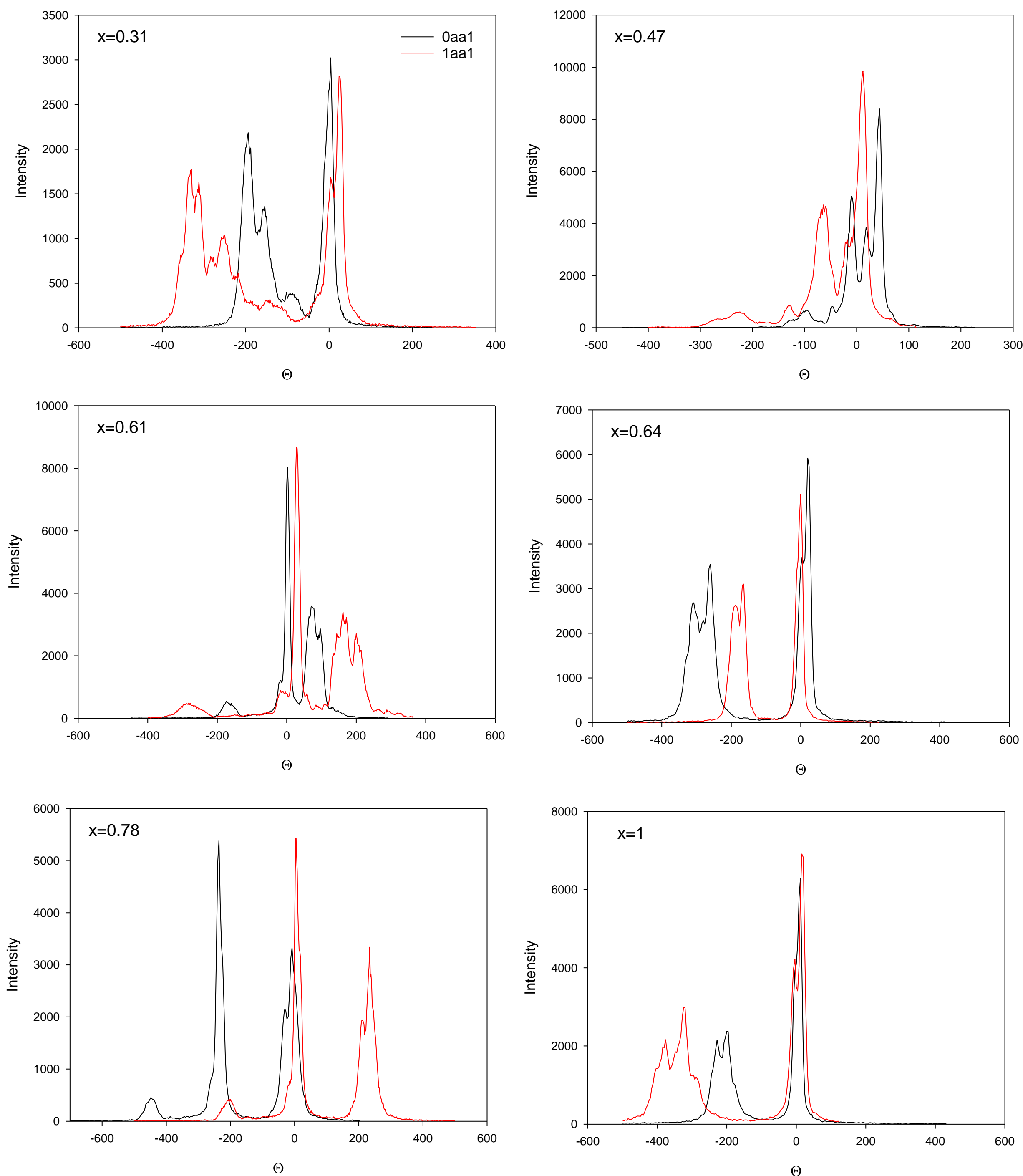

Figure 8-1 XRD results for x=0.31,0.47,0.61,0.64,0.78 and 1

8.2 Temperature Dependence of Photocurrent

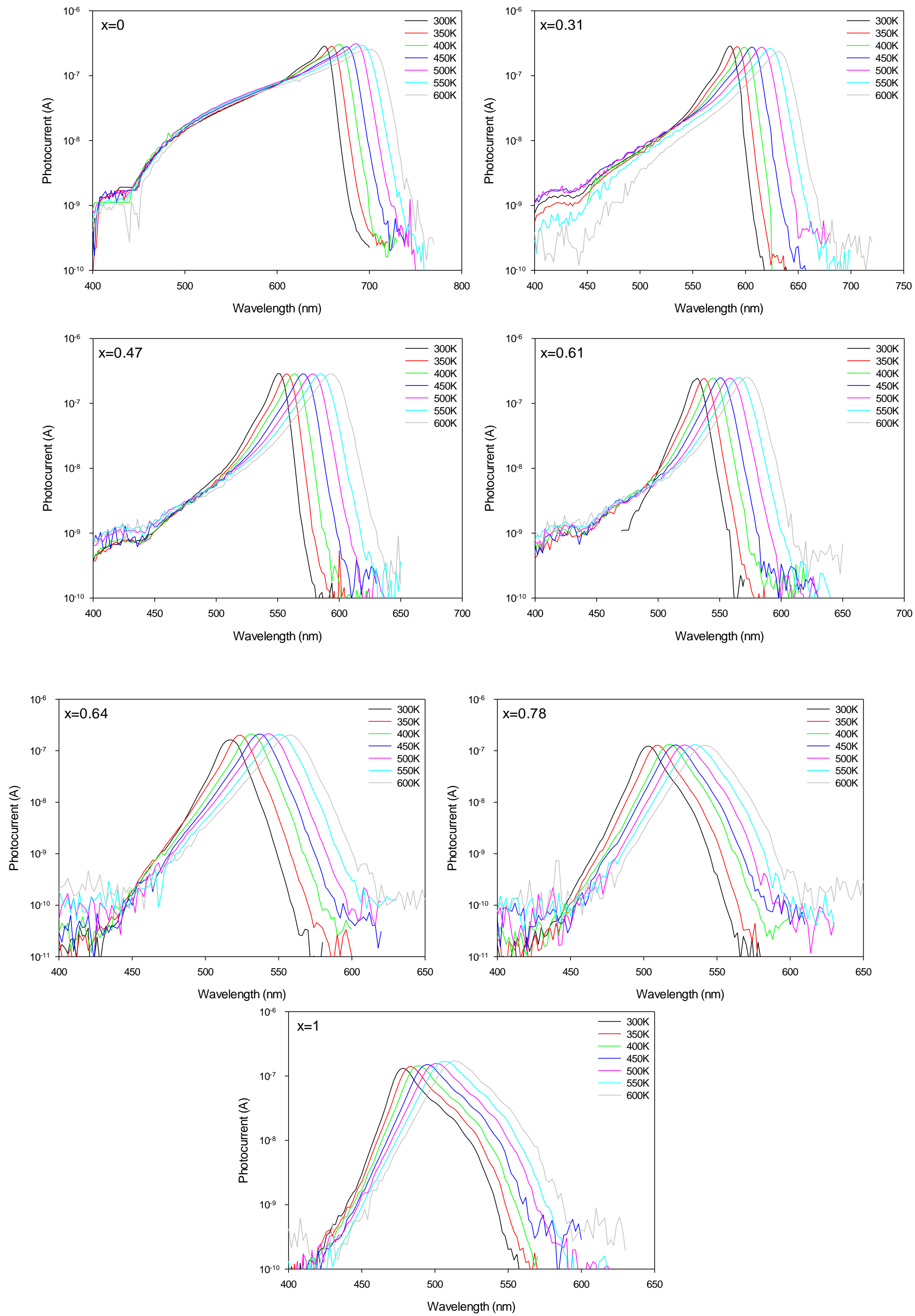

Figure 8-2 Photocurrent of AlGaInP as a function of temperature

8.3 Temperature Dependence of Quantum Efficiency

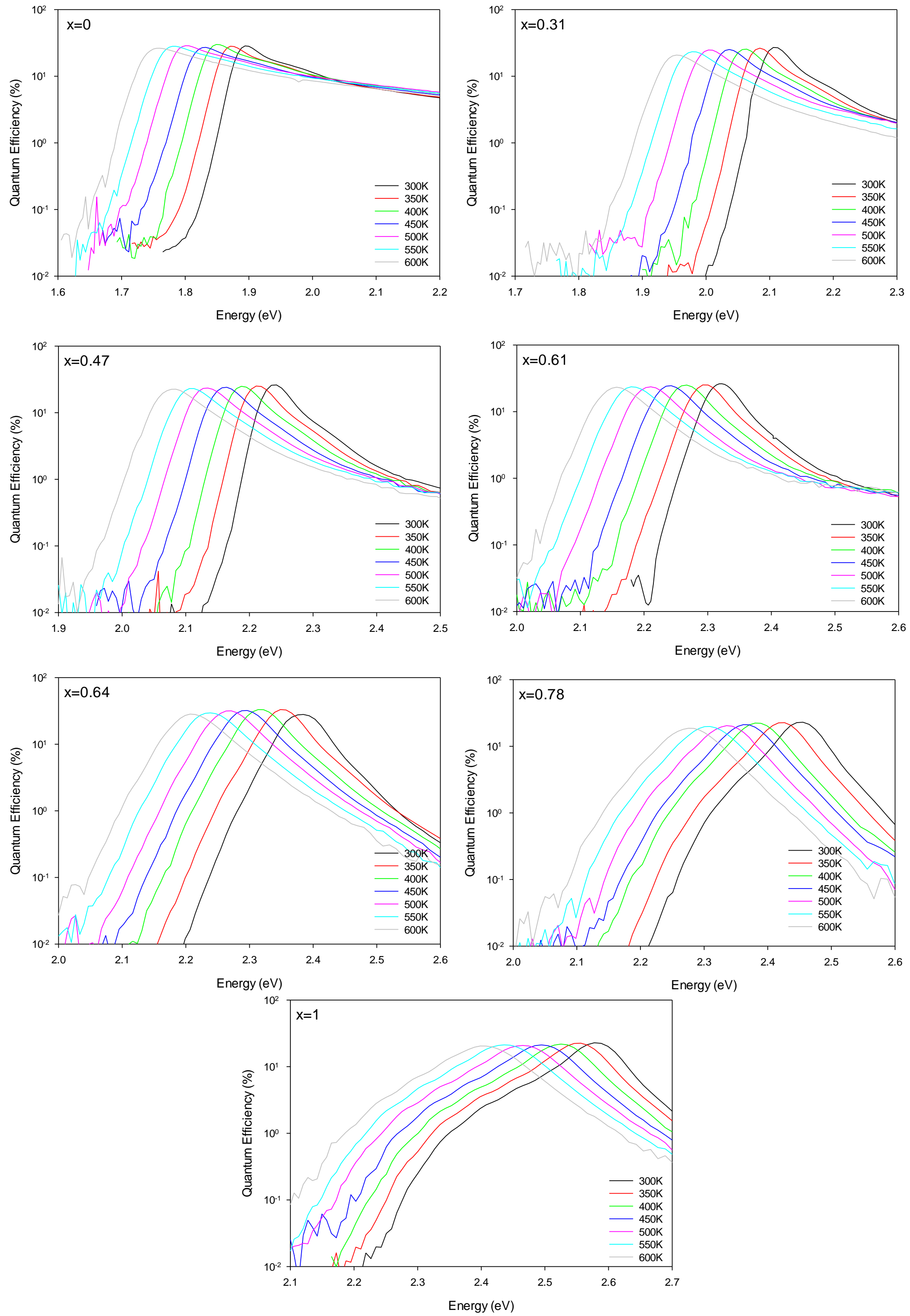

Figure 8-3 Quantum efficiency of AlGaInP as a function of temperature

8.4 Temperature Dependence of Bandgap

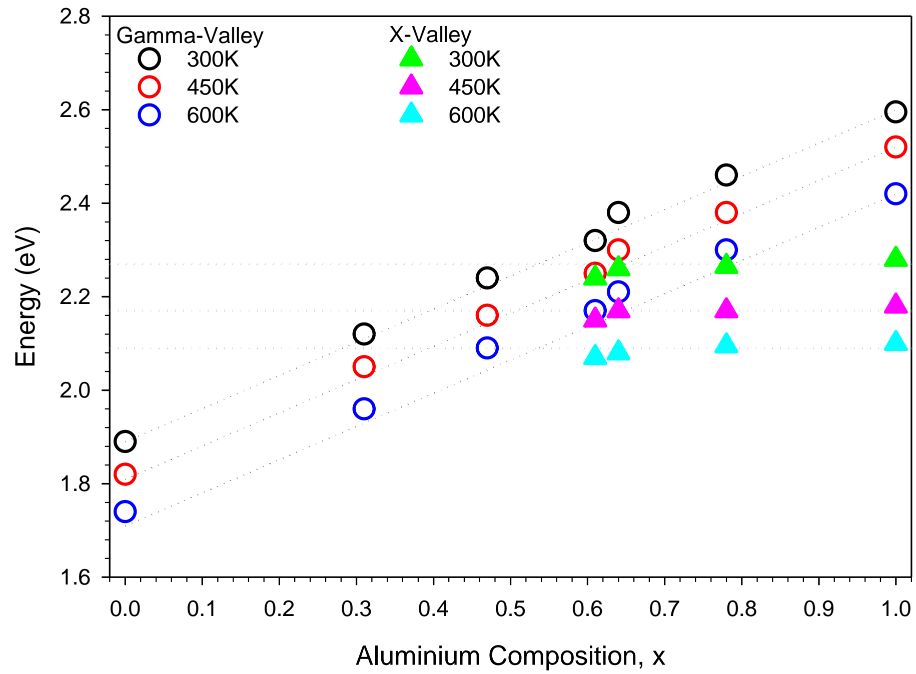

Figure 8-4 Direct and indirect bandgap energy for of AlGaInP versus the aluminium composition for temperature of 300K, 450K and 600K

References

1. NASA. Introduction to the Electromagnetic Spectrum | Science Mission Directorate. 1 https://science.nasa.gov/ems/01_intro (2020).

2. Owens, A. & Peacock, A. Compound semiconductor radiation detectors. *Nucl. Instruments Methods Phys. Res. Sect. A Accel. Spectrometers, Detect. Assoc. Equip.* **531**, 18–37 (2004).

3. Zaletin, V. M. & Varvaritsa, V. P. Wide-bandgap compound semiconductors for x-or gamma-ray detectors. *Russ. Microelectron.* **40**, 443–452 (2011).

4. McLaren, I. A. & Wayne, R. P. Germanium detector for the near infrared. *J. Photochem.* **16**, 9–18 (1981).

5. Harkness-Brennan, L. J. *et al.* An experimental characterisation of a Broad Energy Germanium detector. *Nucl. Instruments Methods Phys. Res. Sect. A Accel. Spectrometers, Detect. Assoc. Equip.* **760**, 28–39 (2014).

6. Hamamatsu. Infrared Detectors. www.hamamatsu.com (2020).

7. Sun, K. & Beling, A. High-speed photodetectors for microwave photonics. *Appl. Sci.* **9**, (2019).

8. Zong, L. *et al.* Nanopurification of silicon from 84% to 99.999% purity with a simple and scalable process. *Proc. Natl. Acad. Sci. U. S. A.* **112**, 13473–13477 (2015).

9. Spaziani, L. & Lu, L. Silicon, GaN and SiC: There's room for all: An application space overview of device considerations. *Proc. Int. Symp. Power Semicond. Devices ICs* **2018-May**, 8–11 (2018).

10. Sellai, A. Temperature dependence of dark current in a Si-pin photodiode. *IEEE Int. Conf. Semicond. Electron. Proceedings, ICSE* 267–270 (2008) doi:10.1109/SMELEC.2008.4770321.

11. Morkoç, H. *et al.* Large-band-gap SiC, III-V nitride, and II- VI ZnSe-based semiconductor device technologies Cite. **1363**, (2005).

12. Szweda, R. GaN and SiC detectors for radiation and medicine. *III-Vs Rev.* **18**, 40–41 (2005).

13. Guo, X. *et al.* Study of reverse dark current in 4H-SiC avalanche photodiodes. *IEEE J. Quantum Electron.* **41**, 562–567 (2005).

14. Yang, B ; Li, T ; Heng, K ; Collins, C ; Wang, S ; Carrano, J.C ; Dupuis, R.D ; Campbell, J.C ; Schurman, M.J ; Ferguson, I. . Low Dark Current GaN Avalanche Photodiodes. *IEEE J. Quantum Electron.* **36**, 1389–1391 (2000).

15. Shen, S. C. *et al.* Performance of deep ultraviolet gan avalanche photodiodes grown by MOCVD. *IEEE Photonics Technol. Lett.* **19**, 1744–1746 (2007).

16. Whitaker, M. D. C., Lioliou, G., Butera, S. & Barnett, A. M. Al0.2Ga0.8As X-ray photodiodes for X-ray spectroscopy. *Nucl. Instruments Methods Phys. Res. Sect. A Accel. Spectrometers, Detect. Assoc. Equip.* **840**, 168–173 (2016).

17. Barnett, A. M., Lioliou, G. & Ng, J. S. Characterization of room temperature AlGaAs soft X-ray mesa photodiodes. *Nucl. Instruments Methods Phys. Res. Sect. A Accel. Spectrometers, Detect. Assoc. Equip.* **774**, 29–33 (2015).

18. Mowbray, D. J., Kowalski, O. P., Hopkinson, M., Skolnick, M. S. & David, J. P. R. Electronic band structure of AlGaInP grown by solid-source molecular-beam epitaxy. *Appl. Phys. Lett.* **65**, 213–215 (1994).

19. Schubert, E. F. Visible-spectrum LEDs. in *Light-Emitting Diodes* 201–221 (Cambridge University Press, 2006). doi:10.1017/CBO9780511790546.

20. Olson, J. M., Kurtz, S. R., Kibbler, A. E. & Faine, P. A 27.3% efficient Ga0.5In0.5P/GaAs tandem solar cell. *Appl. Phys. Lett.* **56**, 623–625 (1990).

21. Conrad, B., Lochtefeld, A., Gerger, A., Barnett, A. & Perez-Wurfl, I. Optical characterisation

of III-V alloys grown on Si by spectroscopic ellipsometry. *Sol. Energy Mater. Sol. Cells* **162**, 7–12 (2017).

22. Ochoa-Martínez, E. *et al.* Refractive indexes and extinction coefficients of n- and p-type doped GaInP, AlInP and AlGaInP for multijunction solar cells. *Sol. Energy Mater. Sol. Cells* **174**, 388–396 (2018).

23. Strategy, D. for B. E. & I. 2020 UK greenhouse gas emissions, provisional figures. *Natl. Stat.* 1–19 (2021).

24. Rayner, T. UK power generation in 2020 : Renewables up to 43%. *PV Magazine International* 1–8 (2021).

25. Smith, W. Effect of Light on Selenium During the Passage of an Electric Current. 303 (1873).

26. Adams, W. G. & Day, R. E. The Action of Light on Selenium. *Proc. R. Soc. London* **25**, 113–117 (1876).

27. Fritts, C. E. On a new form of selenium cell, and some electrical discoveries made by its use. *Am. J. Sci.* **s3**-**26**, 465–472 (1883).

28. Scheiman, D. A., Landis, G. A. & Weizer, V. G. High-bandgap solar cells for near-sun missions. *AIP Conf. Proc.* **616**, 616–620 (1999).

29. Scharber, M. C. & Sariciftci, N. S. Efficiency of bulk-heterojunction organic solar cells. *Prog. Polym. Sci.* **38**, 1929–1940 (2013).

30. Green, M. A. *et al.* Solar cell efficiency tables (version 56). *Prog. Photovoltaics Res. Appl.* **28**, 629–638 (2020).

31. Yastrebova, N. V. High-efficiency multi-junction solar cells : Current status and future potential. *Cent. Res. Photonics, Univ. Ottawa* (2007).

32. Milichko, V. A. *et al.* Solar photovoltaics: current state and trends. *Physics-Uspekhi* **59**,

727–772 (2016).

33. Dimroth, F., Baur, C., Bett, A. W., Meusel, M. & Strobl, G. 3-6 Junction Photovoltaic Cells for Space and Terrestrial Concentrator Applications. *Conf. Rec. Thirty-first IEEE Photovolt. Spec. Conf. 2005.* 525–529 (2005) doi:10.1109/PVSC.2005.1488185.

34. King, R. R. *et al.* Metamorphic III-V Materials , Sublattice Disorder , and Multijunction Solar Cell Approaches With Over 37 % Efficiency. *Proc. 19th Eur. Photovolt. Sol. Energy Conf. Exhib.* 7–11 (2004).

35. Aho, A., Isoaho, R. & Raappana, M. Wide spectral coverage (0.7–2.2 eV) lattice-matched multijunction solar cells based on AlGaInP, AlGaAs and GaInNAsSb materials Arto. 1–7 (2021) doi:10.1002/pip.3412.

36. Isoaho, R. *et al.* Photovoltaic properties of low-bandgap (0.7–0.9 eV) lattice-matched GaInNAsSb solar junctions grown by molecular beam epitaxy on GaAs. *Sol. Energy Mater. Sol. Cells* **195**, 198–203 (2019).

37. Zhang, X. *et al.* Research on monolithic AlGaInP/AlGaInAs/GaInAs/Ge quadruple-junction solar cell for high efficiency lattice-matched tandem photovoltaic device. *Appl. Phys. Express* **13**, (2020).

38. Huang, X. *et al.* Flexible four-junction inverted metamorphic AlGaInP/AlGaAs/ In0.17Ga0.83As/In0.47Ga0.53As solar cell. *Sol. Energy Mater. Sol. Cells* **208**, 110398 (2020).

39. Chiu, P. T. *et al.* Direct semiconductor bonded 5J cell for space and terrestrial applications. *IEEE J. Photovoltaics* **4**, 493–497 (2014).

40. Geisz, J. F. *et al.* Six-junction III–V solar cells with 47.1% conversion efficiency under 143 Suns concentration. *Nat. Energy* **5**, 326–335 (2020).

41. Bernardes, S., Lameirinhas, R. A. M. & Torres, J. P. N. Characterization and Design of

Photovoltaic Solar Cells That Absorb Ultraviolet , Visible and Infrared Light. 1–16 (2021).

42. Farr, N. *et al.* Optical modem technology for seafloor observatories. in *OCEANS 2006* (2006). doi:10.1109/OCEANS.2006.306806.

43. Giles, J. W. & Bankman, I. N. Underwater optical communications systems. http://ieeexplore.ieee.org.eresources.shef.ac.uk/xpls/icp.jsp?arnumber=1605919.

44. Lanzagorta, M. *Underwater Communications*. vol. 1 (Morgan & Claypool Publishers, 2012).

45. Larson, A. Identifying Elements in the Sun Using Spectral Lines. *Columbia State Univ. Website* 1–2 (2013).

46. Jerlov, N. G. *Marine Optics*. (Elsevier Scientific Publishing Company, 1976).

47. Morel, A. & Prieur, L. Analysis of variations in ocean color. *Limnology and Oceanography* vol. 22 709–722 (1977).

48. Overview of Optical Oceanography Classification Schemes. http://www.oceanopticsbook.info/view/overview_of_optical_oceanography/classification_schemes.

49. Bertuccio, G., Puglisi, D., Pullia, A. & Lanzieri, C. X- Ray Spectroscopy With Semi-Insulating 4H-Silicon Carbide. **60**, 1436–1441 (2013).

50. Barnett, A. M. Characterization of GaAs mesa photodiodes with X-ray and γ-ray photons. *Nucl. Instruments Methods Phys. Res. Sect. A Accel. Spectrometers, Detect. Assoc. Equip.* **756**, 39–44 (2014).

51. Auckloo, A. & Cheong, J. S. Al 0 . 52 In 0 . 48 P avalanche photodiodes for soft X-ray. (2016).

52. Gobain, S. BGO - Bismuth Germanate Scintillation Material. 1–2 https://www.crystals.saint-gobain.com/sites/imdf.crystals.com/files/documents/bgo-material-data-sheet.pdf (2004).

53. Nestor, O. H. & Huang, C. Y. Bismuth Germanate: A High-Z Gamma-Ray and Charged Particle Detector. 68–71 (1975).

54. Smith, D. M. Hard X-ray and Gamma-ray Detectors. *Obs. Photons Sp.* 367–389 (2013) doi:10.1007/978-1-4614-7804-1_21.

55. Rehan, N., Abidin, Z. & Lockman, Z. Material Selection for High Temperature Electronic Devices and Its Potential Applications. 39–42 (2009).

56. Tajima, M. Research Activity on High Temperature Electronics and Its Future Application in Space Exploration in Japan. 177–182 (1994).

57. Ferron, A. *et al.* Discussion about photodiode architectures for space applications. **10563**, 206 (2017).

58. Bernardes, S., Marques Lameirinhas, R. A., Torres, J. P. N. & Fernandes, C. A. F. Characterization and design of photovoltaic solar cells that absorb ultraviolet, visible and infrared light. *Nanomaterials* **11**, 1–16 (2021).

59. Waltereit, P. *et al.* High efficiency X-band AlGaN/GaN MMICs for space applications with lifetimes above 105 hours. *Eur. Microw. Week 2012 'sp. Microwaves', EuMW 2012, Conf. Proc. - 7th Eur. Microw. Integr. Circuits Conf. EuMIC 2012* 123–126 (2012).

60. Banu, V. *et al.* High temperature SiC Schottky diodes with stable operation for space application. *Proc. Int. Semicond. Conf. CAS* **2**, 397–400 (2010).

61. Metcalfe, A. *et al.* Diamond based detectors for high temperature, high radiation environments. *J. Instrum.* **12**, (2017).

62. Zimmermann, C. G., Nomayr, C., Kolb, M. & Rucki, A. A mechanism of solar cell degradation in high intensity, high temperature space missions. *Ieee Trans Fuzzy Syst* **20**, 1114–1129 (2012).

63. Tighe, A., Bras, B., Hołyńska, M., Noemayr, C. & Zimmermann, C. High-intensity high-

temperature testing of materials for the Bepi Colombo MPO and MTM solar arrays. *CEAS Sp. J.* **13**, 475–492 (2021).

64. Landis, G. a, Merritt, D., Raffaelle, R. P. & Scheiman, D. High-temperature Solar Cell Development. *Nasa/Cp—2005-213431* **CP**-**2005**-**21**, 241–247 (2005).

65. Ostling, M., Ghandi, R. & Zetterling, C.-M. SiC power devices - Present status, applications and future perspective. *Power Semicond. Devices ICs (ISPSD), 2011 IEEE 23rd Int. Symp.* 10–15 (2011) doi:10.1109/ISPSD.2011.5890778.

66. Neudeck, P., Okojie, R. & Chen, L. High-temperature electronics-a role for wide bandgap semiconductors. *Proc. IEEE* **90**, 1065–1076 (2002).

67. Eisenman, W. L., Merriam, J. D., Potter, R. F. & Bratt, P. R. *Semiconductors and Semimetals Volume 12 Infrared Detectors II*. (1977).

68. Sze, S. M. & Ng, K. K. Semiconductor Devices: Physics and Technology. *Technology* (John Wiley & Sons, INC Publication, 2006).

69. Bandyopadhyay, J. P. *Solid State Electronics Devices*. (Vikas Publishing House, 2010).

70. Sapoval, B., Hermann, C. & Hermann, C. *Physics of Semiconductors*. (Springer Science & Business Media, 2003).

71. PVEducation. http://pveducation.org/.

72. Hummel, R. E. *Electronic Properties of Materials*. (Springer Science&Business Media, 2011).

73. Jr., N. H. *Solid State Physical Electronic Series*. (Prentice-Hall, 1971).

74. Benda, V. *A Comprehensive Guide to Solar Energy Systems*. (2018). doi:10.1016/C2016-0-01527-9.

75. Pankove, J. I. *Optical processes in semiconductors*. (Courier Corporation, 1975).

76. Piprek, J. *Semiconductor Optoelectronic Devices*. (Academic Press, 2003). doi:10.1016/B978-0-08-046978-2.50028-4.

77. Ingersoll, L. R. & Littleton, J. T. A new method of determining the optical constants of metals, and the optical constants of silicon. *Phys. Rev. (Series I)* **31**, 489–499 (1910).

78. 78. & Azzam, R. M. A. The intertwined history of polarimetry and ellipsometry. *Thin Solid Films* **519**, 2584–2588 (2011).

79. Gonçalves, D. & Irene, E. A. Fundamentals and applications of spectroscopic ellipsometry. *Quim. Nova* **25**, 794–800 (2002).

80. Aspnes, D. E. Spectroscopic ellipsometry - Past, present, and future. *Thin Solid Films* **571**, 334–344 (2014).

81. Kato, H., Adachi, S., Nakanishi, H. & Ohtsuka, K. Optical Properties of (AlxGa 1- x) 0 . 5 In 0 . 5 P Quaternary Alloys. *Japanese J. Appl. Phys. 33* **186**, 186–192 (1993).

82. Macfarlane, G. G. & Roberts, V. Infrared Absorption of Germanium near the Lattice Edge. **97**, (1955).

83. Philipp, H. R. & Taft, E. A. Optical constants of Germanium in the Region 1 to 10 ev. *J. Appl. Phys.* **1**, 775–777 (1960).

84. Macfarlane, G. G. & Roberts, V. Infrared Absorption of Silicon near the Lattice Edge. 1–2 (1955).

85. Philipp, H. R. & Taft, E. A. Optical Constants of Silicon in the region 1 to 10ev. *Rev. Lit. Arts Am.* **120**, (1960).

86. Barnes, R. B. & Czerny, M. Concerning the reflection power of metals in thin layers for the infrared. *Phys. Rev.* **38**, 338–345 (1931).

87. Brattain, W. H. & Briggs, H. B. The optical constants of germanium in the infra-red and

visible. *Phys. Rev.* **75**, 1705–1710 (1949).

88. Cheong, J. S., Ng, J. S., Krysa, A. B., Ong, J. S. L. & David, J. P. R. Determination of absorption coefficients in AlInP lattice matched to GaAs. *J. Phys. D. Appl. Phys.* **48**, 405101 (2015).

89. Su, L. C., Ho, I. H. & Stringfellow, G. B. Effects of substrate misorientation and growth rate on ordering in GaInP. *J. Appl. Phys.* **75**, 5135–5141 (1994).

90. Shin, Y. C., Kim, B. J., Kang, D. H., Kim, Y. M. & Kim, T. G. Investigation of Zn diffusion by SIMS and its effects on the performance of AlGaInP-based red lasers. *Semicond. Sci. Technol.* **21**, 35–39 (2006).

91. Nishikawa, Y., Ishikawa, M., Tsuburai, Y. & Kokubun, Y. Lattice Constant Shift in Zn-Doped InGaAlP Grown by Low Pressure Metalorganic Chemical Vapor Deposition. *J. Cryst. Growth* **100**, 63–67 (1990).

92. Matthews, J. W. & Blakeslee, A. E. Defects in epitaxial multilayers: Misfit dislocations. *J. Cryst. Growth* **27**, 118–125 (1974).

93. Ong, S. Impact Ionisation in AlInP Photodiodes. (PhD Thesis, The University of Sheffield, 2012).

94. Sanada, T. & Wada, O. Ohmic Contacts to p-GaAs with Au / Zn / Au Structure. *Jpn. J. Appl. Phys.* **19**, L491–L494 (1980).

95. HP4140B Picoammeter/DC Voltage Source. http://www.siliconinvestigations.com/hprep/hp4140/04140-app238.pdf.

96. Ochoa, M., Algora, C., Garcia, I. & Barrigón, E. Analysis of perimeter recombination in the subcells of GaInP / GaAs / Ge triple-junction solar cells.

97. Multi-Frequency LCR Meters. http://www.testequipmentdepot.com/usedequipment/pdf/427475A.pdf.

98. Monemar, B. Determination of band gap and refractive index of AIP from optical absorption. *Solid State Commun.* **8**, 1295–1298 (1970).

99. Bhalla, A. S. & Cross, L. E. Temperature dependence of the dielectric constant of InP. *Ferroelectr. Lett. Sect.* **9**, 161–164 (1989).

100. z100., Lockwood, D. J., Yu, G. & Rowell, N. L. Optical phonon frequencies and damping in AlAs, GaP, GaAs, InP, InAs and InSb studied by oblique incidence infrared spectroscopy. *Solid State Commun.* **136**, 404–409 (2005).

101. Halogen Light Sources. http://www.dmf.unisalento.it/LaureeScientificheFisica/Download/fisicamoderna/LQ_Operating_tungsten_halogen_lamps_eu.pdf.

102. Fowler, M., Hanson, D. M. & Flowers, P. 1 . 1 : Blackbody Radiation Cannot Be Explained lassically. https://chem.libretexts.org/Courses/Pacific_Union_College/Quantum_Chemistry/01%3A_The_Dawn_of_the_Quantum_Theory (2020).

103. Yvon, J. SPEX 1681 Monochromator User Manual. (1980).

104. Hamamatsu. Si PIN photodiode. 1–5 https://www.hamamatsu.com/resources/pdf/ssd/s5971_etc_kpin1025e.pdf.

105. Lu, H. *et al.* A 2.05 eV AlGaInP sub-cell used in next generation solar cells. *J. Semicond.* **35**, (2014).

106. Perl, E. E. *et al.* Development of a 2.0 eV AlGaInP solar cell grown by OMVPE. *2015 IEEE 42nd Photovolt. Spec. Conf. PVSC 2015* (2015) doi:10.1109/PVSC.2015.7356336.

107. Coronel, E. & Hultqvist, A. Waferbonded four-junction GaInP/GaAs//GaInAsP/GaInAs concentrator solar cells with 44.7% efficiency. *Prog. Photovolt Res. Appl.* **17**, 115–125 (2009).

108. Masuda, T., Tomasulo, S., Lang, J. R. & Lee, M. L. Comparison of single junction AlGaInP and GaInP solar cells grown by molecular beam epitaxy. *J. Appl. Phys.* **117**, (2015).

109. Perl, E. E. *et al.* Development of high-bandgap AlGaInP solar cells grown by organometallic vapor-phase epitaxy. *IEEE J. Photovoltaics* **6**, 770–776 (2016).

110. Faucher, J. *et al.* High-efficiency AlGaInP solar cells grown by molecular beam epitaxy. *Appl. Phys. Lett.* **109**, (2016).

111. Neville, R. C. *Solar Energy Conversion (Second Edition)*. *Elsevier Science* (1995). doi:10.1016/b978-044489818-0/50006-5.

112. Vaillon, R., Parola, S., Lamnatou, C. & Chemisana, D. Solar Cells Operating under Thermal Stress. *Cell Reports Phys. Sci.* **1**, 1–20 (2020).

113. Properties of Si, Ge, and GaAs at 300K. 1–2 https://eesemi.com/sigegaas.htm (2021).

114. Electrical properties of Silicon (Si). *Springer Series in Materials Science* vol. 104 35–78 http://www.ioffe.ru/SVA/NSM/Semicond/Si/electric.html (2008).

115. Electrical properties of Indium Phosphide (InP). *Springer Series in Materials Science* vol. 104 35–78 http://www.ioffe.ru/SVA/NSM/Semicond/InP/electric.html (2008).

116. Electrical properties of Gallium Arsenide (GaAs). *Springer Series in Materials Science* vol. 104 35–78 http://www.ioffe.ru/SVA/NSM/Semicond/GaAs/electric.html (2008).

117. Schultes, F. J. *et al.* Temperature dependence of diffusion length, lifetime and minority electron mobility in GaInP. *Appl. Phys. Lett.* **103**, (2013).

118. McIntosh, K. R., Altermatt, P. P. & Heiser, G. Depletion-Region Recombination in Silicon Solar Cells: When Does mdr = 2? *16th Eur. Photovolt. Sol. Energy Conf.* 250–253 (2000).

119. Dimroth, F., Schubert, U., Schienle, F. & Bett, A. W. High C-doping of MOVPE grown thin AlxGa1-xAs layers for AlGaAs/GaAs interband tunneling devices. *J. Electron. Mater.* **29**, 47–

52 (2000).

120. Masui, H. Diode ideality factor in modern light-emitting diodes. *Semicond. Sci. Technol.* **26**, (2011).

121. Fong, K. C., McIntosh, K. R. & Blakers, A. W. Accurate series resistance measurement of solar cells. *Ieee Trans Fuzzy Syst* **20**, 490–499 (2011).

122. Sze, S. M. & Irvin, J. C. Resistivity, mobility and impurity levels in GaAs, Ge, and Si at 300°K. *Solid State Electron.* **11**, 599–602 (1968).

123. Bertness, K. A., Kurtz, S. R., Asher, S. E. & R.C. Reedy, J. AlInP benchmarks for growth of AlGaInP compounds by organometallic vapor-phase epitaxy. *J. Cryst. Growth* **196**, (1999).

124. Hinojosa, M., Garcia, I., Dadgostar, S. & Algora, C. Point-Defects Assisted Zn-Diffusion in AlGaInP/GaInP Systems during the MOVPE Growth of Inverted Multijunction Solar Cells. *IEEE J. Photovoltaics* **11**, 429–436 (2021).

125. GaxIn1-xP - Basic Parameters at 300 K. http://www.ioffe.ru/SVA/NSM/Semicond/GaInP/basic.html (2008).

126. Ong, J. S. L., Ng, J. S., Krysa, A. B. & David, J. P. R. Impact Ionization Coefficients in Al0.52In0.48P. *IEEE Electron Device Lett.* **32**, 1528–1530 (2011).

127. Ohba, Y., Nishikawa, Y., Nozaki, C., Sugawara, H. & Nakanisi, T. A study of p-type doping for AlGaInP grown by low-pressure MOCVD. *J. Cryst. Growth* **93**, 613–617 (1988).

128. Al-Jabr, A. A. *et al.* Large bandgap blueshifts in the InGaP/InAlGaP laser structure using novel strain-induced quantum well intermixing. *J. Appl. Phys.* **119**, (2016).

129. Mowbray, D. J., Kowalski, O. P., Hopkinson, M., Skolnick, M. S. & David, J. P. R. Electronic band structure of AlGaInP grown by solid-source molecular-beam epitaxy. *Appl. Phys. Lett.* **65**, 213–215 (1994).

130. Adachi, S., Kato, H., Moki, A. & Ohtsuka, K. Refractive index of $(Al_x Ga_{1-x})_{0.5} In_{0.5} P$ quaternary alloys. *J. Appl. Phys.* **75**, 478–480 (1994).

131. Adachi, S. Optical dispersion relations for GaP, GaAs, GaSb, InP, InAs, InSb, Al xGa1-xAs, and In1-xGaxAs yP1-y. *J. Appl. Phys.* **66**, 6030–6040 (1989).

132. Schultes, F. J. *et al.* Temperature dependence of diffusion length, lifetime and minority electron mobility in GaInP. *Appl. Phys. Lett.* **103**, (2013).

133. Aspnes, D. E. Recombination at semiconductor surfaces and interfaces. *Surf. Sci.* **132**, 406–421 (1983).

134. Gudovskikh, A. S. *et al.* Properties of interfaces in GaInP solar cells. *Semiconductors* **43**, 1363–1368 (2009).

135. Radamson, H. & Thylen, L. *Monolithic Nanoscale Photonics-Electronics Integration in Silicon and Other Group IV Elements*. (Ringgold, Inc, 2015).

136. Schubert, M., Gottschalch, V. & Herzinger, C. M. Optical constants of Ga x In 1- x P lattice matched to GaAs. 4–9 (1995).

137. Hooft, G. W., Van Opdorp, C., Veenvliet, H. & Vink, A. T. Minority carrier lifetime and luminescence in MOVPE-grown (Al,Ga)As epilayers and DH lasers. *J. Cryst. Growth* **55**, 173–182 (1981).

138. Zarem, H. A., Lebens, J. A. & Nordstrom, K. B. Effect of Al mole fraction on carrier diffusion lengths and lifetimes in AlxGa1−xAs. **2622**, (1989).

139. Urbach, F. The long-wavelength edge of photographic sensitivity and of the electronic Absorption of Solids. *Phys. Rev.* **92**, 1324 (1953).

140. Photodiode Rise Time Increases with Wavelength of Incident Light. *Thorlabs* 10–11 https://www.thorlabs.com/newgrouppage9.cfm?objectgroup_id=14218.

141. Aspnes, D. E. & Studna, A. A. Dielectric functions and optical parameters of Si, Ge, GaP, GaAs, GaSb, InP, InAs, and InSb from 1.5 to 6.0 eV. *Phys. Rev. B* **27**, 985–1009 (1983).

142. Green, M. A. Self-consistent optical parameters of intrinsic silicon at 300 K including temperature coefficients. *Sol. Energy Mater. Sol. Cells* **92**, 1305–1310 (2008).

143. Aspnes, D. E., Kelso, S. M., Logan, R. A. & Bhat, R. Optical properties of Al x Ga1−x As. *J. Appl. Phys.* **60**, 754 (1986).

144. Tauc, J. Optical properties and electronic structure of amorphous Ge and Si. *Mater. Res. Bull.* **I**, 1–21 (1968).

145. Feng, Y., Lin, S., Huang, S., Shrestha, S. & Conibeer, G. Can Tauc plot extrapolation be used for direct-band-gap semiconductor nanocrystals? *J. Appl. Phys.* **117**, (2015).

146. Makuła, P., Pacia, M. & Macyk, W. How To Correctly Determine the Band Gap Energy of Modified Semiconductor Photocatalysts Based on UV-Vis Spectra. *J. Phys. Chem. Lett.* **9**, 6814–6817 (2018).

147. Di, M. *et al.* Comparison of methods to determine bandgaps of ultrathin HfO 2 films using spectroscopic ellipsometry . *J. Vac. Sci. Technol. A Vacuum, Surfaces, Film.* **29**, 041001 (2011).

148. Yuan, L. D., Deng, H. X., Li, S. S., Wei, S. H. & Luo, J. W. Unified theory of direct or indirect band-gap nature of conventional semiconductors. *Phys. Rev. B* **98**, 1–10 (2018).

149. Beaton, D. A. *et al.* Determination of the direct to indirect bandgap transition composition in AlxIn1-xP. *J. Appl. Phys.* **114**, (2013).

150. Donati, G. P., Kaspi, R. & Malloy, K. J. Interpolating semiconductor alloy parameters: Application to quaternary III-V band gaps. *J. Appl. Phys.* **94**, 5814–5819 (2003).

151. Adachi, S. *Properties of Semiconductor Alloys: Group-IV, III-V and II-VI Semiconductors*. (2009). doi:10.1002/9780470744383.

152. Perl, E. *et al.* Measurements and modeling of III-V solar cells at high temperatures up to 400°C. *2017 IEEE 44th Photovolt. Spec. Conf. PVSC 2017* **6**, 1–14 (2017).

153. Delong, M. C., Mowbray, D. J., Hogg, R. A. & Skolnick, M. S. Band gap of '"completely disordered"' Ga 0.52 In 0.48 P. **66**, 3185–3187 (1995).

154. Luque, A. & Hegedus, S. S. *Handbook of photovoltaic science and engineering*. (2003). doi:10.1002/9780470974704.

155. Dittrich, T. *Materials Concepts for Solar Cells*. (World Scientific, 2018). doi:10.1142/q0131.

156. Widenhorn, R., Fitzgibbons, M. & Bodegom, E. The Meyer-Neldel rule for diodes in forward bias. *J. Appl. Phys.* **96**, 7379–7382 (2004).

157. Qinghai, M., Shuojin, L., Xinghua, Z., Fujian, Z. & Yangjun, Z. The Convergence Characteristics of the Forward I-V Characteristics Curves of a Semiconductor Silicon Barrier at Different Temperatures. *J. Semicond.* **4**, (2008).

158. Widenhorn, R., Rest, A. & Bodegom, E. The Meyer-Neldel rule for a property determined by two transport mechanisms. *J. Appl. Phys.* **91**, 6524–6528 (2002).

159. Obreja, V. V. N. & Obreja, A. C. Activation energy values from the temperature dependence of silicon PN junction reverse current and its origin. *Phys. Status Solidi Appl. Mater. Sci.* **207**, 1252–1256 (2010).

160. Chen, N. C., Yang, Y. K., Lien, W. C. & Tseng, C. Y. Forward current-voltage characteristics of an AlGaInP light-emitting diode. *J. Appl. Phys.* **102**, (2007).

161. Lewis, H. I. J. *et al.* Impact Ionization Coefficients in $(Al_xGa_{1-x})0.52In0.48P$ and $Al_xGa_{1-x}As$ Lattice-Matched to GaAs. *IEEE Trans. Electron Devices* **PP**, 1–6 (2021).

162. Qiao, L. Methodologies for low excess noise measurement in wide bandgap materials. (PhD Thesis, The University of Sheffield, 2017).